APPLICATION OF NOVEL CELLULAR BIOLOGY TECHNIQUES TO UNDERSTANDING THE PHYSIOLOGY AND PATHOPHYSIOLOGY OF THE DEVELOPING LUNG

By

Dina Rashad Mohamed Ali Johar

A thesis submitted to the Faculty of Graduate Studies of the University of Manitoba in partial fulfillment of the requirements for the degree of

DOCTOR OF PHILOSOPHY

Department of Physiology and Pathophysiology
Max Rady College of Medicine
Rady Faculty of Health Sciences
University of Manitoba
Winnipeg, Canada

ABSTRACT

Events at the level of cellular physiology are important to both pulmonary vascular development and in the pathophysiological processes that lead to pulmonary diseases of the newborn. Cell remodelling throughout development is a disorder of abnormal lung growth due to tissue hypoplasia or pulmonary artery hyperplasia. My thesis addresses two diseases of the lung: congenital diaphragmatic hernia (CDH) and persistent pulmonary hypertension of the newborn (PPHN). Nitrofen, a teratogen, induces CHD in rats and human, however, the mechanism is not fully known and there is no specific gene mutation associated with nitrofen-induced CDH. PPHN is a respiratory failure during circulatory transition because the lung fails to replace fluids and blood with inspired gases. As a result, the pulmonary artery pressure remains high due to hypertensive remodeling where a higher than normal Filamentous:Globular (F:G-actin) ratio increases stiffness, resulting in a thicker vessel diameter.

The overall hypothesis that was examined was that methods such as Next Generation Sequencing (NGS) and Laser Scanning Cytometry (LSC) can provide novel insights to encompass both embryonic lung toxicity and the effect of unabated stress on development and on pathophysiological lung conditions postnatally. The primary objective was to evaluate the utility of two new methods to investigate CDH and PPHN.

The research undertaken was able to identify changes in miRNA levels in the nitrofen rat model of CDH using NGS. A total of 186 known mRNA and 100 miRNAs were diferentially expressed in nitrofen-induced hypoplastic lungs. Sixty-four rat miRNAs homologous to known human miRNAs were identified. A subset of these genes may promote lung hypoplasia in rats and/or humans. Potential miRNA pathways relevant to nitrofen-induced lung hypoplasia include PI3K, TGF-β, Wnt and cell cycle kinases. Also, the research demonstrated that LSC can be used to image and quantify cytoskeletal alterations in the form of the F:G-actin ratio at the cellular level. Furthermore, the observations obtained with the LSC *in vitro* are amenable to validation in any *in vivo* model of interest. The research undertaken supports the proposal that NGS and LSC can open new avenues for research of CDH and PPHN.

ACKNOWLEDGEMENTS

A warm and grateful thank you to all those who contributed, in their own invaluable way, to the award of my PhD degree. In particular I would like to thank:

My family for all their support and their unwavering faith in me; Mother, Father who is laying in peace thank you for well raising me, and my siblings Rusha and Hesham, your encouragement and prayers helped me all the way through.

My gratitude and respect goes to Dr. Edwin Kroeger, Associate Dean of Research in Medicine, for his continuous support and for his role as a liaison until this work ended.

My gratitude and sincere thanks go to my supervisor, Dr. Peter Zahradka, for his time in review, critical evaluation of my thesis proposal, for guiding me through organizing and writing my thesis and preparing for my defence. It has been a pleasure working under his supervision.

Dr Larry Howard Bernstein: without his insight and experience, I would have wasted a huge amount of time stressing over temperamental challenges. I thank him for his dedication and help, for his offer to supervise my thesis despite the challenges, for his pertinent comments, encouragement, words of advice and help, and for making me laugh during the tough times. I cannot thank him enough for being there for me without return.

Special thanks goes to Mr. Gerald Stelmack, from the Children's Hospital Research Institute of Manitoba (CHRIM), who trained me and assisted me with the Laser Scanning Cytometery technique; Dr. Debourah Tsuyuki from the Next Generation Sequencing NGS platform at the Manitoba Institute of Cell Biology (MICB), who helped me with the microRNA/mRNA sequencing experiments. Their help was very much appreciated. Also, Dr. Wayne Xu from the NGS platform who was instrumental in guiding me through the bioinformatics analysis of the NGS data.

My friends from Ontario; Ms. Elaine Harvey, Ms. Barbara Schlafer, Gamela, Lisa, Karen and everyone at the Queen's University Ban Righ Center for Continuing Women's University Education, for their financial support and encouragement throughout my years at Queen's graduate school that continued over my time in Ontario. My big family's love and support mean the life for me, and I could not have done it without their help.

The funders of this PhD thesis, namely The Egyptian Minsitry of Higher Education and Egyptian Mission Affairs; P.E.O International Peace Scholearship, USA and The University of Manitoba Faculty of Graduate Studies funded the years of my education in Canada. Without this fund, the study would have not been feasible.

TABLE OF CONTENTS

LIST OF TABLES

LIST OF FIGURES

ABBREVIATIONS

AD	Adaptor
Ago	Argonaute
AKT	Protein kinase B
AMPK	5' AMP-activated protein kinase
Ang II	Angiotensin II
ANOVA	Analysis of variance
Apaf-1	Apoptotic protease activating factor 1
APLN	Apelin
AT I	Angiotensin I
ATF4	Activating transcription factor 4
ATF6	Activating transcription factor 6
ATM	Ataxia-telangiectasia mutated
Bad	Bcl-2-associated death promoter
Bax	Bcl-2-associated X protein
Bcl-XL	B-cell lymphoma-extra large
Bcl2	B-cell lymphoma-2
BDGFRB	Platelet-derived growth factor receptor B
BDNF	Brain derived neurotrophic factor
BEAS-2B	Bronchial epithelial cells
BHRF1	Epstein–Barr virus (EBV)-encoded proteins
Bmp4/Rb	Bone morphogenic protein 4/Retinoblastoma
BNIP3	BCL2/adenovirus E1B 19 kDa protein-interacting protein 3
c-fos	The transforming gene of the FBJ MSV (Finkel–Biskis–Jinkins murine osteogenic sarcoma virus)
c-jun	The putative transforming gene of avian sarcoma virus 17
c-myc	Avian myelocytomatosis viral oncogene homolog
c-src	Cellular src kinase
CaMK	Ca+2/calmodulin-dependent protein kinase
Caspase	Cysteine-dependent aspartases
CDH	Congenital diaphragmatic hernia
CDK	Cyclin dependent kinase
CDKI	Cyclin dependent kinase inhibitor
cDNA	Complementary DNA
CED	Caenorhabditis elegans
CF	Cystic fibrosis

cGMP	Cyclic guanosine monophosphate
ChIP	Chromatin immunoprecipitation
CHK2	Checkpoint kinase 2
CHOP	C/EBP homologous protein
COPD	Chronic obstructive pulmonary disease
Coup-TFII	Chicken ovalbumin upstream promoter transcription factor 2
CRABPs	Cellular RA-binding proteins
CREB	Cyclic AMP response element binding protein
CT	Cycle threshold
DCF-DA	2',7'-dichlorodihydrofluorescein diacetate
DHE	Dihydroethidium
DEG	Differentially Expressed Genes
DNMT-1	DNA methyltransferase-1
E19	Embryonic day 19
E2F	Transcription factors in higher eukaryotes
ECM	Extracellular matrix
ECMO	Extracorporial membrane oxygenation
Egr1	Early growth response protein 1
eIF4E	Eukaryotic initiation factor
4EBP1	Eukaryotic initiation factor binding protein1
Elf5	Ets domain transcription factor
EMT	Epithelial to mesenchymal transition
eNO synthase	Endothelial NO synthase
ERK1/2	Extracellular activated kinases 1/2
ET_A	Endothelin A
ET	Endothelin
F-actin	Filamentous actin
FAK	Focal adhesion kinase
FBS	Fetal bovine serum
FC	Fold change
FeTTPs	5,10,15,20-tetrakis (4-sulfonatophenyl) porphyria to-iron (III) chloride
FETO	Fetoscopic endotreacheal occlusion
FGF	Fibroblast growth factor
FGFR	Fibroblast growth factor receptor
Fog2	Friend of Gata2
Fwd	Forward
G actin	Globular actin
GADD45α	Growth arrest and DNA-damage-inducible protein GADD45 α
GDP-Rho	Guanosine-5'-diphosphate Rho
GEFH1	Guanosin nucleotide exchange factor H1

GFP	Green fluorescent heterologous protein
GI	Gastrointestinal viscera
GJIC	The gap junctional intercellular communication
GO	Gene ontology
GPCR	G protein coupled receptor
GrB2	Growth factor receptor-bound protein-2
GRP78	78 kDa glucose-regulated protein
GSK	Glycogen synthase kinase 3
GTP-Rho	Guanosine-5'-triphosphate Rho
hsa	Homosapiens = humans
hASMCs	Human airway smooth muscle cells
HAT	Histone acetyltransferase
hBECs	Human bronchial epithelial cells
HDACs	Histone deacetylases
HEPES	4-(2-hydroxyethyl)-1-piperazineethanesulfonic acid
hESCs	Human embryonic stem cells
HIF1α	Hypoxia-inducible factor 1α
Hix	Homeobox transcription factor
HMGA2	TGF-β and high-mobility group activator
HNF3α	Hepatocyte nuclear factor α
HO-1	Heme oxygenase-1
Hoxb5	Homeobox protein 5
IGF	Insulin-like growth factor
IL-8	Interleukin-8
IPA	Ingenuity pathway analysis
IPF	Idiopathic pulmonary fibrosis
IRE1α	Inositol-requiring enzyme 1α
ISH	*In situ* hybridization
KEGG	Kyoto Encyclopedia of Genes and Genomes
KLF5	Krüppel-like factor
KO	Knockout
KRAS	Kirsten rat sarcoma virus
LNA	locked nucleic acid
lncRNAs	lncRNAs
LPA	Lysophosphatidic acid
LPS	Lipopolysaccharides
LRAT	Lecithin-retinol acyltransferase (phosphatidylcholine-retinol-O acyltransferase)
LSC	Laser scanning cytometry
MAPK14	Mitogen activated protein kinase 14

MDM2	Mouse double minute 2 homolog
MEF	Mouse embryonic fibroblasts
miR	Micro RNA
miRNA	MicroRNA
MiSeq	Micro RNA sequencing
MRTFA	Myocardin-related transcription factor A
mTOR	The mechanistic target of rapamycin
MYC	Myelocytomatosis oncogene
NADPH	Nicotinamide adenine dinucleotide phosphate
NCBI	National Centre for Biotechnology Information
ncRNA	Noncoding RNA molecules
NF-KB	Nuclear factor-kappa B
NGS	Next generation sequencing
NHE1	Sodium hydrogen exchanger1
Nix	Mammalian NIP3-like protein X
NM	NCBI Identification number of mRNA
NSCLC	Non-small cancer lung cells
P0	Passage 0
p16INK4a	Cyclin-dependent kinase inhibitor 2A, multiple tumor suppressor 1
P21	Cyclin dependent kinase inhibitor 1A
P27	Cyclin-dependent kinase inhibitor 1B
PAECs	Pulmonary arterial endothelial cells
PAH	Pulmonary artery hypertension
PARP	Poly (ADP-ribose) polymerse
PASM	Pulmonary artery smooth muscle
PDE5	Phosphodiesterase 5
PEG-catalase	Polyethylene glycol-conjugated catalse
pFDR	Alpha associated with the False Doscovery Rate
$(ONOO-)^{\bullet}$	Peroxy nitrite radical
PGI2	Prostaglandin I 2
PH	Pulmonary hypoplasia
PHN	Pulmonary hypertension
pI	Isoelectric point
PI/BrdU	Propidium iodide/5-Bromo-2´-Deoxyuridine
PI3K	Phosphatidylinositol-4,5-bisphosphate 3-kinase
PKC	Protein kinase C
PML	Promyelocytic leukemia protein
PMT	Photomultiplier
Pol II	RNA Polymerase II
PPHN	Persistent pulmonary hypertension

PTEN	Phosphatase and tensin homolog
RA	Retinoic acid
Rac1	Ras-related C3 botulinum toxin substrate 1
RAF	Rapidly accelerated fibrosarcoma
RALDH2	Retinal dehydrogenase 2
RAREs	Retinoic acid response elements
RARs	Retinoic acid receptors
Rb	Retinoblastoma
RBI2	Retinoblastoma-like 2
Rev	Reverse
Rho	Small G protein
RhoA	Ras homolog gene family, member A
RISC	RNA-induced silencing complex
rno	Rattus norvegicus
RNS	Reactive nitrogen species
ROI	Region of interest
ROS	Reactive oxygen species
RPKM	Kilobase per million reads
RT	Room temperature
RT-qPCR	Real time quantitative PCR
RTK	Receptor tyrosine kinase
RVH	Right ventricular hypertrophy
RXRs	Retinoid X receptors
SA β-gal	SA β-galactosidase
SASP	Senescence associated secretory phenotype
SCARE	Segments with chromatin alterations reinforcing senescence
SDS-PAGE	Sodium dodecyl sulfate-polyacrylamide gel electrophoresis
SH1P1	Src homology 2 domain-containing inositol 5 phosphatase 1
Shc	Src homology 2 domain-containing transforming protein Shc
SHH	Sonic hedgehog
shRNA	Small hairpin RNA
siRNA	Small interference RNA
Skp2	S-phase kinase-associated protein 2
SM	Smooth muscles
snoRNA	Small nucleolar RNA
SnRNA	Small nuclear RNA
SOD	Superoxide dismutase
SOLiD	Oligonucleotide ligation and detection
SRF	Serum response factor
STAT3	Signal transducer and activator of transcription 3

TAFs	TBP-associated factors
Tar	Target
TBP	TATA box binding protein
TCF	Ternary complex factor
TGF-R1	Tumour growth factor receptor alpha
TGF-β	Transforming growth factor β
Th-2	T type lymphocyte response
TM	Transmembrane domain
TOP	Terminal Oligo Pyrimidine
TR	Thromboxane receptor
Trx1	Thioredoxin 1
TSC1	Tuberous sclerosis 1
TUSC2P	Tumour suppressor candidate-2 pseudogene
Ub	Ubiquitin
UCSC	The University of California Santa Cruz
UPR	Unfolded protein response
UTR	Untranslated region
VEGFR2	Vascular epithelial growth factor receptor 2
WNT	Wingless-type MMTV integration site family
Wt1	Wilms tumor suppressor gene 1
XBP1	X-box-binding protein 1
XO	Xanthine oxidase
γ-H2AX	Gamma-histone 2A phosphorylated variant

LIST OF COPYRIGHTED MATERIAL

CHAPTER 1: OVERVIEW

1.1. Introduction

Exposure of the fetus to environmental stressors during intrauterine life is of potential importance in chronic lung pathogenesis. Lung toxic effects throughout development are associated with heightened multiple interacting stressors in the lung. Lung tissues can respond to stress in ways that range from the activation of survival pathways to the initiation of cell death (1, 2). Whether cells mount a protective or destructive stress response depends to a large extent on the nature and duration of the stress as well as the cell type (2). Toxic effects on the lung by teratogens, as well as oxidative-, mechanical- or hypoxia-induced stress, result in pathophysiological conditions that range from lung hypoplasia, impaired vascular function, persistent hypoxemia to arterial hypertension. While stress stimulates cells to mount protective responses to counteract the effect of the stress on cellular processes, either cell death or proliferation occurs if the stress still is unresolved. This chapter will overiew the clinical background and animal models of CDH, the lack of therapeutic strategies, the gaps in research as well as will briefly introduce the causative agents of persistent pulmonary hypertension of the newborn (PPHN).

1.2. Lung morphogenesis in humans versus rats

Lung development extends from the embryonic period through the fetal period up to birth and afterwards. Human lung buds form in the first four weeks of

fetal development in response to signals from the mesenchyme, including fibroblast growth factors. During the pseudoglandular stage of organogenesis, weeks five through sixteen, these cues lead to formation of the bronchial tree and parts of the parenchyma. This is followed by a differentiation phase, characterized by three stages, the canalicular, the saccular, and the alveolar. During the canalicular stage, from weeks 16 through 24, the lung periphery fully forms, epithelial cells differentiate, and the air-blood barrier starts to build up. In the saccular stage, from weeks 24 through 36, air spaces expand and surfactant forms. Lastly, active alveolar formation via secondary septation occurs throughout the alveolar stage, from 36 weeks of gestation till birth and afterwards. The distal tips of the embryonic lung accommodate undifferentiated progenitors that differentiate into a versatile range of specialized epithelial cells. All cellular differentiation programs require the cell to exit the cell cycle at some stage and turn some genes on and other genes off. Apoptosis is fundamental to many cellular processes including differentiation. To proliferate, lung cells must escape apoptosis and vice versa. MiRNAs play a significant role in various cell physiological processes and contribute to pulmonary diseases and lung development (3-8). Table 1.1. compares the stages of lung morphogenesis in humans and rats.

The broncheal tree arises from the sequential use of three modes of branching: Planar bifurcation; orthogonal bifurcation and domain branching. A complex epithelial-to-mesenchymal interaction is required for tip split formation (9). The most important regulators are fibroblast growth factor 10 (FGF10), Sonic

Hodgehog (SHH), bone morphogenic protein 4 (BMP4) and FGF receptor 2b. SHH inhibits FGF10 expression in mesenchyme, whereas FGF10 induces SHH-dependent epithelial growthand chemotactic in a negative feedback loop. Two models explained FGF10 AND SHH-mediated tip split regulation in the lung as follows: 1) growth is proportional to FGF10 concerntation; 2) chemotactic functions are proportional to FGF10 difusion gradient. Alveolar differentiation occurs in late lung development and the distal tip dilates and epithelium disappears. The septum is formed in the dilated cyst to form alveoli after birth. This septation is regulated by platelet-derived growth factor (PDGF), and correlates with the local SM density at the cleft (9), Table 1.1.

Table 1.1. Milestone of lung development in huamns versus rats.

Weeks of gestation (humans)	Days of gestation (rats)	Morphogenesis events (humans)	Morphogenesis events (rats)
Branching			
2-16	E9.5	*The embryonic and pseudoglandular stages:* • Formation of major airways • Formation of bronchial tree and portions of respiratory parenchyma • Birth of the acinus • Development of mesenchymal cell lineage: smooth muscle cells; lymphatic cells; endothelial cells; nerve cells; chondrocytes. • Development of epithelial cell lineage: Basal cells; ciliated cells; secretory cells.	*The pseudoglandular stage:* • Development of mesenchymal cell lineage: smooth muscle cells; lymphatic cells; endothelial cells; nerve cells; chondrocytes. • Development of epithelial cell lineage: Basal cells; ciliated cells; secretory cells.
Differentiation			
16-24	E16.5	*The canalicular stage:* • Last generations of the lung periphery formed • Epithelial differentiation • Air-blood barrier formed • Capillary formation • Libofibroblast • Alveolar type I and II	*The canalicular stage:* • Capillary formation • Libofibroblast • Alveolar type I and II
24-36	E17.5	*The Sacualr stage:* • Expansion of air spaces • Surfactant detectable in amniotic fluid • Expansion of capillary and lymphatic netwrok	*The Sacualr stage:* • Alveolar sac formation • Surfactant production • Expansion of capillary and lymphatic netwrok
36-birth-3-8 years	Postnatal day 5-30	*The alveolar stage:* • Secondary septation • Microvascular maturation • Alveolar myofibroblast	*The alveolar stage:* • Secondary septation • Microvascular maturation • Alveolar myofibroblast
Adulthood		• Alveolar type I and II • Libofibroblast (progenitor) • Macrophage • Resident fibroblast • Elastin • Capillary	

Source: (4, 9-11)

1.3. The clinical background of CDH

CDH is a developmental disorder of unknown cause. CDH-babies are born with a hole in the diaphragm through which part of the gastrointestinal (GI) viscera herniates into the chest. The distention of GI viscera compresses the lung parenchyma leading to pulmonary hypoplasia, less airway branching and consequently respiratory insufficiency, thick fibroblast layer compared to normal, and failure of alveolarization post delivery.

Surgery can be used to fix the hole, however, the baby continues to suffer persistent pulmonary hypertension throughout infancy (Figure 1.1). There is a high rate of hearing loss, neurodevelopmental delay, higher metabolic rate, and failure to thrive. Blood biochemistry changes include glucose and Ca^{2+} dishomeostasis (12). CDH constitutes about 8% of major congenital anomalies, with the highest death rate among neonates afflicted by the disease (13). Single gene mutations have only been reported in 20% of symptomatic CDH cases (14), whereas the majority of cases are of unknown etiology (15), suggesting epigenetic factors and gene-environment interactions as potential regulatory mechanisms. Karyotype abnormalities reported in CDH cases include trisomy 13 and 18 and tetrasomy 12p mosaicism (16, 17).

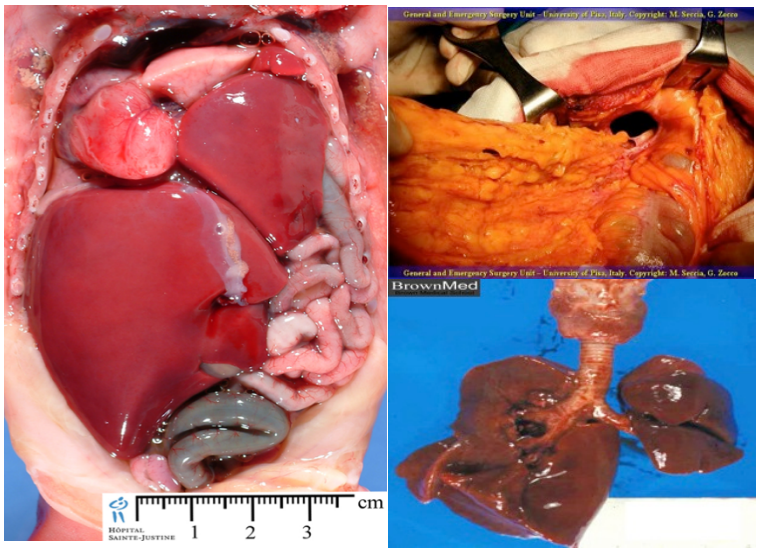

Figure 1.1. Human CDH showing lung hypoplasia and herniation of the GI organs into the chest cavity, and surgical closure of the diaphragmatic hole, unilateral hypoplasia. Photo at the lower right from (18). Photos at the upper right and left are available online from https://www.slideshare.net/FTmed38/topic-cdh as of April 18, 2018.

1.4. Animal models for CDH

To date, four animal models have been developed to study the defects associated with CDH and lung hypoplasia.

1.4.1. The surgical model

In this model, hernia is induced surgically in the diaphragm of the fetus. The animals typically used are sheep, followed by dogs and then rabbits (19, 20). This model is useful in demonstrating the impact of the sequence of events following the induction of CDH on lung development, such as compression of the lung and dysfunction of the diaphragm, as it allows prediction of the mechanics of the lung and treatment strategies outcome, but it does not enable an exploration of the

etiological causes of CDH (21). A second defect linked to the treatment of this model is the development of tracheal occlusion (21).

1.4.2. The teratogenic model

Nitrofen (2,4-diclorophenyl-p-nitrophenyl ether) is an aromatic herbicide that induces the most common form of CDH known as Bochdalek CDH (occurs in the dorsolateral region of the diaphragm), and bilateral pulmonary hypoplasia in rodents that shares many similarities with the phenotype in humans (22, 23). In the nitrofen model, 60% of the offspring will have CDH and 100% pulmonary hypoplasia after administration of nitrofen to pregnant rats on E9. Lung hypoplasia precedes the diaphragmatic defect that develops on E13 (24-27). Nitrofen is similar in its structure to thyroid hormone (28). To date, the mechanisms underlying nitrofen-induced lung hypoplasia in this rodent model of CDH are poorly understood. Accumulated evidence suggests that nitrofen-induced CDH occurs through the inhibition of the retinoic acid (RA) pathway (29). The limitations of using the nitrofen rat model include i) a direct link between nitrofen, abnormal lung development and CDH in humans has never been established; and ii) nitrofen induces a CDH-like lung in up to 100% of E13.5 rats which is not at the genetic level and therefore of uncertain phenotype.

1.4.3. The nutritional model

Retinoic acid signaling regulates normal diaphragm specification and lung development. Research has shown three key pieces of evidence for a role in these processes. The first relates to the fact that the retinol-deficient animal model exhibits teratogenic defects including CDH, that are rescued by vitamin A supplementation.

Similarly, authors have found that nitrofen-induced CDH diaphragmatic malformation, cardiogenic anomalies and lung hypoplasia are reversed by vitamin A supplementation to fetuses (30). Secondly, Nitrofen blocks the conversion and activation of the inactive retinal to the active retinoid acid through the inhibition of the enzyme retinal dehydrogenase 2 (RALDH2) (31). Thirdly, RA receptors RARα and RARβ2 knockout mice (KO) manifest diaphragmatic malformations (32, 33).

1.4.4. The genetic model

The genetic mouse model is the most suitable for the study of etiology, however, a small number of malformations induced by gene mutations that are created in mice link perfectly to the phenotype manifested by humans. Among the common mutations is the conditional deletion of the Chicken ovalbumin upstream promoter transcription factor 2 (Coup-TFII) (34). Coup-TFII is a transcription factor in the thyroid/steroid family of hormone receptors and is a commonly deleted region on chromosome 15q26 that is also commonly deleted in CDH (35). Friend of Gata 2 (Fog2) and its cofactor (Gata4) play key roles in lung and diaphragm development in human (36, 37), In humans, a coding mutation by translocation or deletion of the Fog2 locus is associated with asymptomatic CDH (37, 38). Gata4, is located on the CDH-cytogenic region on humans chromosome 8p (39) and contributes to CDH diaphragmatic defects in Gata4-mutant mice (36). The Wilms tumor suppressor gene (Wt1) mutation in mice is associated with posterior defects in the diaphragm and abnormal structured primordial diaphragm pleuriperitoneal folds (40), although Wt1 mutation has not been found in human cohorts with asymptomatic CDH cases.

Mutation of the homeobox transcription factor Hix has been suggested as a CDH candidate, however, sequence variants cause abnormal diaphragmatic changes in mice (41) and are not well characterized in patients.

1.5. Gaps in knowledge

The mechanism of CDH pathogenesis or etiology is poorly understood. A number of reports have provided evidence on nitrofen's potential effects during diaphragm development in rodents embryos, but whether the nitrofen-rat model shares the same pathological signaling with humans remains to be determined. Herniation can be reproduced in surgical models using rabbits, lambs and primates. However, the associated malformations are absent in these mechanical models, which limits their validity as a research tool. Using the teratogenic model, the dual hit hypothesis suggested that lung hypoplasia and congenital changes of the lung occur earlier than diaphragmatic changes and herniation begins, and that the development of the dipharagmatic changes promotes herniation, while the decreased airway pressure in the lung contributes to lung hypoplasia (27).

1.6. Therapeutic options in CDH

CDH is associated with 50% mortality and has no standard guidelines for treatment (42). The gold standard in treatment of CDH is respiratory support at birth such as mechanical ventilation with positive respiratory pressure or Extracorporeal Membrane Oxygenation (ECMO), followed by closure of the diaphragmatic defect.

This intervention involves placing the abdominal organs into their correct locations, which provides room for the lungs to grow. Relocating the liver has disadvantages because the umbilical vein and inferior vena cava become occluded, resulting in the death of the fetus. A more advantegous and minimally invasive technique was developed using a fetoscope and hence its name Fetoscopic Endotreacheal Occlusion (FETO). FETO manitpulates the mechanical forces through production of lung fluid that distends the lung airway. FETO is limited by the toxicity from the fluids. This developed into the tracheal occlusion scope that inflates a ballon in the trachea of the fetus or the newborn by a perfusion scope and then the ballon is detached at birth. This procedure, although minimally invasive, results in scars and tracheal stenosis. FETO-treated babies have better respiration but a similar mortality rate (43).

1.7. How the clinical problem can be treated

Validating the obtained data with clinical samples and demonstrating a correlation between the miRNA level of deregulation and the disease progression is required. One of the recent therapeutic approaches (44) investigated prenatal transplacental microRNA (miRNA) miR 200 b as a therapeutic modality to improve lung hypoplasia and lung deformation with CDH, however, this approach has been studied in the nitrofen-induced CDH rat model and was not validated in human pre-clinical trials for its side effects. The possible pitfalls are the potential off-target effects with rescuing selectively an individual miRNA. Also, the model did not identify

the therapeutic dose or timing or the other side effects on the body organs or extraembryonic tissues. Studies of early lung development on human embryos or pregnant dams are not permitted.

1.8. Current and new approaches to studying CDH

CDH is a malformation of lung and alveolarization. Exposure to teratogens such as nitrofen can promote lung dysgenesis and dysfunction throughout development and postpartum. MiRNAs are putative epigenetic targets of such stressors. MiRNAs are viewed as negative posttranscriptional regulators of gene expression (45). Studies also indicated that miRNAs operate as negative or positive transcriptional regulators of gene expression by targeting the promoter sequence. Converging lines of evidence have suggested a role for miRNA silencing in endoplasmic reticulum (ER) stress signaling (45).

Interesting mRNA targets of relevance to lung development can be validated for their protein expression and interactions using proteomics approaches in nitrofen and control E13 rat embryonic fibroblasts (EF), such as quantitative mass spectrometry-based proteomics in combination with affinity purification (46), or prediction approaches (47). Epithelial cells from normal and abnormal lungs can be separated and characterized and used to study the identified pathways and crosstalk between mRNA reads, using molecular biology and biochemistry approaches (48). Functional analysis can also be achieved by immunoblotting to validate the identified pathways and how mRNA differences translate to changes in protein structure and

function. Targeting selected mRNA reads by siRNA approaches *in vitro* will allow a demonstration of their physiological relevance to lung development.

Chromatin immunoprecipitation (ChIP) (49) is an epigenetic approach that can be used to examine mouse embryonic fibroblasts (MEFs) treated with RA and look at markers of lung fibroblast cell differentiation.

Other approaches include studying the regulation of a specific miRNAs of interest using mimics or inhibitors (50, 51) *in vitro* using human broncheal epithelial cell line (BEAS-2B).

Similar structure of miRNAs means similar function. Hence, perhaps those reads that are upregulated by nitrofen treatment in rats have the same function in humans or if the miRNAs are upregulated in rats and are closely related to humans they could be also upregulated in humans miRNA. Phylogeny identifies what genes are closely related relative to others. It therefore becomes possible to compare sequences of the primary structure without external information, where these genes sit on the chromosome and what they do. By comparing phyologeny trees, the optimal tree can be identified by assigning scores to all possible trees and then choosing the highest score. Through a phylogenetic inference analysis approach (52), it is possible to analyze and understand the similarity in structure and function of mRNA reads between i) human and other species, ii) between members of the same miRNA family, iii) between important mRNA reads and genes that are proved in the literature to have developmental regulatory function. For this purpose, gene and

species trees that were assigned the highest scores can be used to study conservation in structure and function, to distant rat from human in terms of the response to nitrofen and its effect on the relationship between genes.

The Hox cluster (miR 10; miR 196 a-1 and 2; miR 10-a; miR 196-b; miR 99-a; miR 99-b; miR 100) is an example of miRNAs that we can use as an evidence from the literature when we construct the phylogeny. HOX genes are direct targets of RA (53). RA, synthesized intracellularly from circulating retinol or diffusing from an adjacent cell, eventually reaches the nucleus. Cellular RA-binding proteins (CRABPs) may be involved in this transfer. Dimers of RA receptors (RARs) and retinoid X receptors (RXRs), termed RAR/RXR, are able to bind to RA-response elements (RAREs) in their target genes in the absence of ligand, interacting with protein complexes (co-repressors) that stabilize the chromatin nucleosomal structure and prevent access to the promoter (53). Upon RA binding, a conformational change in the helicoidal structure of the RAR ligand-binding domain changes its protein-protein interaction properties, releasing the co-repressors and recruiting co-activator complexes that destabilize the nucleosomes and/or facilitate assembly of the transcription pre-initiation complex, which contains RNA polymerase II (Pol II), TATA-binding protein (TBP) and TBP-associated factors (TAFs). In the absence of RA the heterodimer represses transcription through histone deacetylation. The direct targets of RA are HOX genes, TFs (HNF3α) (53).

The miR 10 family is of particular importance for their conservation, their position within the HOX clusters of developmental regulators. It regulates the

translation of HOX transcripts (54). Their deregulations leads to the development of cancer and reflect general down regulation during differentiation. They regulate ribosomal biogenesis and global protein synthesis, embryonic development, differentiation and inflammation. miR 10-a copurifies with the 5'UTR of TOP transcripts (55). These proteins are characterized by having their 5'UTR downstream from the 5' Terminal Oligo Pyrimidine TOP found in many elongation factors and other proteins associated with the translational apparatus. These TOP proteins respond to several stimuli such as amino acid starvation and stressors. The upstream signals regulating TOP translations involve the phospatidylinositol 3-kinase (PI3K) and mTOR, however, the exact wiring is still not known. miR 10-a-mediated targeting of TOP mRNA is independent on the complete base pairing with the seed region (55).

miR 10-a contributes to lung dysgenesis throughout the course of lung development in response to nitrofen in rats. A proposed approach can be based on miR 10-a to characterize miR 10-a expression and activity and to examine if RA contributes to miR 10-a regulation throughout the course of lung development in response to nitrofen in lung extracts at developmental stages E13, E15 and E18. If miR 10-a was upregulated by the treatment, *in situ* hybridization (ISH) experiments can be conducted to localize the expression of miR 10-a spatially and temporally in embryonic rat fibroblasts throughout the course of lung development. The pattern of expression can be compared between nitrofen and control lungs.

Determination of RARE-luciferase activity in normal and miR 10-a knockout (KO) immortalized human broncheal epithelial cell lines (BEAS) is warranted. The

latter looks at how RARE-luciferase activity reads in nitrofen treated miR 10-a KO cells change from control (Figure 1.2). It is possible to view luciferase in response to SMAD phosphorylation as a function of the activity of TGFβ signaling in response to nitrofen in the presence and absence of miR 10-a mimics and inhibitors.

The miRNA 200 b family plays a pivotal role in regulating epithelial to mesenchymal transition, lung fibrosis by targeting the transcription factors ZEB1 and 2 (56), and lung hypoplasia by downregulating SMAD/TGFβ signaling and branching of the elongating airway (44). The expression of miR 200 b depends on the degree of lung hypoplasia and is upregulated in less hypoplastic, non-CDH pups' lungs prenatally compared to CDH-hypoplastic lungs. Nitrofen abrogated such increases and consequently, stimulated SMAD/TGFβ cascade in lung epithelium (44).

SMAD luciferase activity assay can be applied to demonstrate the effect of loss and gain of function of miR 200 b. Authors treated immortalized bronchial epithelial cells (BEAS-2B) with nitrofen or control. Cells were then co-transfected with SMAD reporter construct and LNA-miR 200 b inhibitor, mimic or scrambled *in vitro* by *in situ* hybridization (44). Nitrofen-induced miR 200 b inhibition upregulated SMAD luciferase activity, while miR 200 b mimics abrogated such inhibition and rescued the the normal morphogenesis in *ex vivo* lung explants (44).

In vivo studies on miR 200 b mimics administered prenatal to dams intravenously after nitrofen gavage reduced the incidence of CDH in neonatal pups compared to scrambled mimics (44).

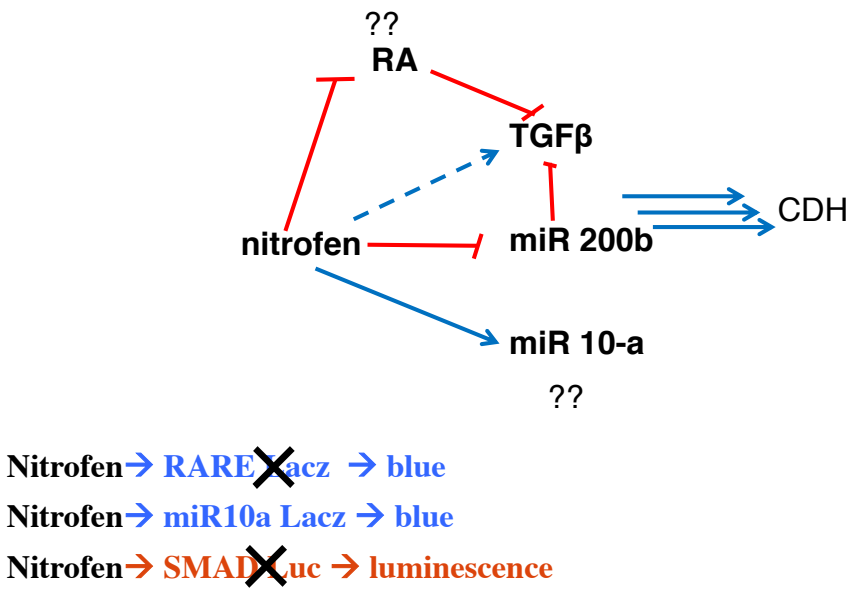

Figure 1.2. Transforming growth factorβ (TGFβ) is targeted by miR 200 b. Using a heat map, Keijzer and Puri (14) performed a microarray screen with 317 microRNAs comparing human control and CDH lungs. They observed higher levels of miR 200b and miR 10-a in human hypoplastic CDH lungs compared to age-matched controls and that was controversial to the scenario that occurs in rats when the expression was reduced early throughout development and then increased towards term. Nitrofen-induced miR-200b inhibition was associated with reduced airway branching morphogenesis. Eventually, this led to our thinking about exploring what nitrofen does to the transcriptome as primary to further explore its mechanism. Nitrofen promotes TGFβ signaling and it does this through abolishing miR 200 b expression. Others observed that RA regulates miR 10-a expression and is important to CDH progression. It also blocks TGFβ. In using RARELacZ, every cell that responds to RA is blue. Therefore, if RA miR 200 b LacZ is blocked, every cell that responds to miR 200 b is blue. Upon blockage of RA SMADLuc, everycell that responds to TGFβ is luminescent. Consequently, if these promoters are suppressed it becomes possible to see the total effect on the expression and function of miR 10-a or 200 b, which could be informative of their role throughout development.

New research can examine the role TGFβ in early and late endoderm development. RT-qPCR can be used to examine expression in E13 lungs of control and nitrofen treated rats. Also, frozen paraffin embedded lung tissues (ISH) can be used to see markers such as HNF4α (a late endodermal marker that regulates endoderm specification) and Gata6. These genes are down regulated in early lung but then the pattern changes throughout development.

Human miRNAs could function similarly to their orthologs in rats. Searching for orthologs can enable us to see the effect of nitrofen on the entire gene that encodes for the miRNA, not only on the mature structure of miRNA, because nitrofen could do something different that changes the gene sequence or changes how genes interrelate in the chromosome. New bioinformatic approaches based on miR 10-a include miR 10-a target prediction using miR Tar and Target scan databases.

1.9. Hypothesis, experimental approach, and objectives

I approached the subject of lung developmental diseases using an epigenetic approach combined with strategies based on miRNAs and cytometry to evaluate the role of environmental stress in developmental vascular disease. My major goal was to develop methods to study lung responses to high levels of cytotoxic stressors in two model diseases of developmental lung disorders which continue to impair lung function postpartum and cause high mortality rates among neonates. Specifically, I aim to examine nitrofen-induced CDH and PPHN of the newborn. The overall

Hypothesis explored is: Aberrant cellular remodeling during development leads to abnormal lung growth and occurs via changes in miRNA and cytoskeletal modifications.

I initially conducted a review of the literature on the signaling associated with chronic lung diseases including, but not limited to, CDH (chapter 2) and PPHN (chapter 4). Two research projects were subsequently postulated (chapters 3 and 5), each based on new experimental trends, models, and methodology. In chapters 3 and 5, lung toxicity was examined, and this involved observing transcriptome changes, apoptosis, proliferation and cytoplasmic changes of key cytoskeletal proteins. The major objective was to develp methods to study lung responses to high levels of cytotoxic stressors using the two models (nitrofen-CDH lung and PPHN).

In the first case, I used Nitrofen (2,4-dichlorophenyl-p-nitrophenyl ether) which is a pesticide to induce CDH and pulmonary hypoplasia in rodents, and I gave it orally to pregnant rats and then dissected the embryo's intact lungs early on at E13 since miRNA expression profile changes largely by time. Possible factors in this process are miRNAs, which are small (17-24 bp), stable, noncoding RNAs that modulate mRNA production and stability at post-transcriptional levels (57). The advancement of miRNA deep sequencing technology has become a platform for the discovery of important miRNAs and their regulatory signaling that control pivotal processes of all tissues, including development and differentiation (58, 59). I used next generation sequencing (NGS) technology and I anticipated collecting big data. This was expected to give better insights into the pathogenesis of nitrofen-induced

pulmonary hypoplasia. This should then result in translating this information to human pulmonary hypoplasia and CDH in future studies.

Studying how miRNAs are differentially regulated in lung development and lung diseases in response to epigenetic changes provides new insights for their versatile role in various physiological and pathological processes in the lung. In this context, I discuss the contribution of miRNAs to lung development and diseases and possible future implications in the field of lung pathophysiology.

What I proposed to address through the first project was:

1. To profile the differential expression of RNA subclasses in embryonic nitrofen-induced CDH lungs in rats.
2. To analyze the similarity in structure and function of mRNA and miRNA reads between i) human and other species; ii) members of the same family of mRNA in rats.
3. to identify the regulatory miRNA networks and interactions with mRNA networks or those that are associated with nitrofen-CDH lungs in rats.

Cell structure indicates the behaviour of the cells during stretch and I can compare that to the behaviour of the arterial wall *in vivo*. This work is original in demonstrating a Laser Scanning Cytometry (LSC) method that utilizes a fluidic matrix to grow cells and to describe the role of pulsatile stretch in pulmonary artery hypertension (PAH) tissue remodeling. These LSC experiments should provide pivotal data necessary to characterize, in broad terms, hypoxia and mechanical strain-

induced regulation of the PPHN phenotypic vasculature in an animal model that manifests the disease in a similar pattern to human babies. The findings obtained by LSC *in vitro* are amenable to validation in any *in vivo* model of interest.

In the second project I proposed a role for F:G-actin ratio as a measurable endpoint for cytoskeletal reorganization upon exposure of PASM or hASM cells to hypoxia together with or independent on strain. My major objectives were:

1. to develop an LSC method to image and quantify the altered cytoskeleton.
2. to show that an application for LSC by two different methods can result in the same F:G-actin ratios, i.e. the data can be reproducible.

CHAPTER 2: LITERATURE REVIEW

New insights into lung development and diseases: the role of miRNAs

In this chapter, I review the role of miRNAs in lung biology and their potential contribution to lung development, homeostasis and inflammatory diseases.

Biochem. Cell Biol. 93: 139–148
dx.doi.org/10.1139/bcb-2014-0103.

2.1. Contribution statement

I, Dina Johar, made the following contributions to this study:

- I contributed to conception of idea, review literature synthesis, actual writing of the manuscript, reviewing and editing.
- I guided and enriched other's understanding the implication of miRNA in various lung diseases through discussions and presentations that contributed to the progression of this article.
- I wrote 70% of the manuscript that was edited later by Vinaya Siragam, such that we were listed as first co-authors.

Other contributors:

- Vinayakumar Siragam
- Thomas H. Mahood
- Richard Keijzer

2.2. Introduction

MiRNAs are short endogenous noncoding RNA molecules (~22 nucleotides) that can regulate gene expression at the post-transcription level. Research interest in the role of miRNAs in lung biology is emerging. MiRNAs have been implicated in a range of processes such as development, homeostasis, and inflammatory diseases in lung tissues and are capable of inducing differentiation, morphogenesis, and apoptosis. In recent years, several studies have reported that miRNAs are differentially regulated in lung development and lung diseases in response to epigenetic changes, providing new insights for their versatile role in various physiological and pathological processes in the lung. In this review, I discuss the contribution of miRNAs to lung development and diseases and possible future implications in the field of lung biology.

MiRNAs are highly conserved single-stranded RNA molecules (~22 nucleotides) derived from endogenous transcripts regulating gene expression. MiRNAs regulate mRNA translation or degradation via partial complementarity with the 3'-untranslated region (UTR) of target mRNAs (60) and thereby repress gene expression (61). Mature miRNAs are processed by cleavage of endogenous primary RNA transcripts (pri-miRNA) through RNA polymerase II/III enzymes (62). MiRNAs (63) regulate many biological processes such as development and cell differentiation (64-68). To date, more than 2000 human miRNAs have been reported for their implications in various diseases (3, 69) throughout development, for example, sparse functional data confirming the epigenetic regulation that may alter miRNA-mediated

regulation of gene expression programs. Limited information is available regarding the regulation of miRNA expression and their potential role in lung pathophysiology, despite several studies addressing the involvement of miRNAs in lung development and disease (70-73). Therefore, understanding the miRNA regulatory network and the physiological role of miRNAs in lung development and disease can provide new insights into lung biology.

2.3. MiRNA biogenesis and biological function

MiRNAs are derived from introns of protein-coding genes or exons of noncoding genes of the genome. Figure 2.1 represents a schematic overview of miRNA biogenesis. Briefly, miRNAs are transcribed from primary miRNAs (pri-miRNAs) in two stages. The first step involves the nuclear cleavage of the pri-miRNA post-transcription by RNA polymerase II. Subsequently, this liberates stem loop-like structures (60–70 nucleotides) known as the miRNA precursor, or the pre-miRNA. The Drosha-DGCR8 complex regulates this step. Next, the precursor of a mature miRNA (pre-miRNA) is actively transported from the nucleus to the cytoplasm by the GTP-binding nuclear protein Ran through the help of Exportin5 (74, 75). The second step involves the formation of a miRNA duplex in the cytoplasm by Drosha from pre-miRNA to mature miRNA (76). One of the strands of the miRNA duplex ("guide" strand) is incorporated into the RNA-induced silencing complex (RISC) and functions to guide the RISC complex to its targets, whereas the other strand ("passenger" strand) of the miRNA duplex is degraded (63).

Based on the degree of complementarity between the miRNA to 3'-UTR of target mRNAs, the mature miRNA negatively regulates expansion of the gene by two mechanisms: (i) degradation of mRNA and (ii) inhibition of translation initiation. Degradation of the mRNA occurs based on the perfect complementarity between miRNA with target mRNA (77, 78). Secondly, translation repression occurs if the target mRNA has partial complementarity to the miRNA (79-81). MiRNAs can also be transported to different cells providing an interesting mechanism for intercellular regulation and cross-talk between the cells (65, 82). This suggests that miRNAs can influence gap junctional intercellular communication (GJIC) between proliferation and differentiation during lung development. However, the regulatory mechanism of miRNAs through GJIC in lung development is poorly understood.

2.4. Noncoding regions of the genome can regulate the activity of miRNAs

Noncoding RNA transcripts (transcription products of pseudogenes) have multiple binding sites attracting specific miRNAs to direct target mRNA repression (83, 84). Recently, Rutnam et al. (85) investigated the functional role of noncoding RNA molecules (ncRNA) in breast cancer cell lines to understand the regulatory role of pseudogenes on gene expression. These studies showed overexpression of tumour suppressor candidate-2 pseudogene (TUSC2P) and the TUSC2 3'-UTR in breast cancer cell lines results in downregulation of various cell physiological activities regulating miRNA function. Further, they have demonstrated that the overexpression of 3'-UTR can modulate the endogenous miRNA (85) in promoting the translation of TUSC2

function. Limited information is available with respect to the role of long noncoding RNA (lncRNAs) functions in lung development. LncRNAs are expressed in the lung and have a variety of biological roles, including differentiation and proliferation (86-88). However, the mechanisms underlying lncRNA regulation in lung development and disease are still unknown.

2.5. MiRNA regulation of proliferation and differentiation in embryonic lung tissues

In normal development, the translational machinery is controlled by a number of miRNA families. Lu et al. (89) addressed the function of miRNAs during the late canalicular stage of lung development. They compared the expression profiles of miRNAs between E11.5 (pseudoglandular stage) and E17.5 (late canalicular stage) in mice. MiR-17 was highly expressed at E11.5, while at E17.5 let-7 was the most abundant miRNA (90). The miR-17-92 family can regulate cell survival and proliferation in early and late stages of lung development; for example, miR-17-92 deficient mice show lung-related embryonic lethality (91, 92). The miR-17-92 family also has been implicated in lung cancer via activation of the pro-apoptotic protein Bim and loss of B cell lineage (89, 93, 94). Hayashita et al. (95) demonstrated that the overexpression of miR-17-92 could lead to the proliferation of lung epithelial progenitors in lung cancer cells.

Less attention has been given to signaling that regulates growth of progenitor cells and their lineages or fates in the epithelium or mesenchyme before or after birth. Such research is particularly important for lung regeneration after damage or

insufficient growth. Ras, downstream of tyrosine kinase fibroblast growth factor receptor (FGFR) signaling, has been identified as a potential target of the miR-17-92 cluster, allowing progenitor self-renewal and eliminating differentiation programs in the adult lung (96). Whether the effect of mir-17-92 on progenitor expansion is cell type-specific or multicellular requires more investigation.

2.6. Animal models and the role of miRNAs in lung development

Animal models demonstrate that miRNAs are involved in lung development, and that dysregulation of miRNAs can lead to postnatal diseases. Lu et al. (89) addressed the importance of the specific miRNA-processing proteins Argonaute (Ago) 1-4 and Dicer in developing lung epithelium and mesoderm. Functional defects of Dicer in lung epithelium can lead to poor branching of airways in lung development, suggesting a regulatory role for miRNAs in lung morphogenesis (97). In the lung epithelial branching region during embryonic stage 11.5 (E11.5), Ago1 and Ago2 are highly expressed in epithelial and mesenchymal regions, demonstrating the pivotal role of miRNA regulation in lung remodeling (98). Bhaskaran et al. (7) reported the differential expression of 27 miRNAs at different phases of lung development. For example, miR-29a has been shown to limit lung proliferation during development (7), and over-expression in lung cancer cells appears to inhibit the tumorigenicity (99).

In recent years, more attention has been given to the regulatory role of the miR 17-92 locus in lung development. For instance, the miRNAs in this locus are

overexpressed in undifferentiated lung progenitor epithelial cells, regulating the key cell cycle gene Retinoblastoma-like 2 (RBl2) for cell proliferation (89). Differential expression of miR-127 and miR-351 has been observed in the saccular–alveolar region of the mesenchymal zone and later expressed in lung epithelial cells, providing a regulatory role for mesenchymal to epithelial transition (7). MiR-17, miR-20a, and miR-106b were demonstrated to regulate E-cadherin expression in epithelium and mesenchyme during the pseudoglandular stage of lung development via targeting signal transducer and activator of transcription 3 (STAT3) and mitogen activated protein kinase (MAPK14) downstream of FGF-10-FGFR-2b cues and consequently modulate timing of sprouty-induced bud morphogenesis (93). Taking into account the aforementioned studies in lung development, miRNAs are believed to participate in a complex regulatory circuit that allows rapid and dynamic lung developmental changes from proliferation to differentiation. The above examples provide an overview of expression profiles of miRNAs between mouse and human lungs hinting at the evolutionary conserved roles of miRNAs as mediators of lung development processes.

2.7. Epigenetic regulation of miRNAs in lung development

Epigenetic regulation involves a series of heritable changes that control phenotype and gene expression without altering the DNA sequence. In recent years, the importance of miRNAs in lung development has emerged, but the genetic mechanism that controls the expression of miRNAs in lung is poorly understood (4).

Histone modifications control lung development and gene regulation through epigenetic mechanisms that involve primarily histone acetylation (100, 101). These mechanisms operate through histone acetyltransferase (HAT) in enhancing transcription and histone deacetylases (HDACs) by silencing the gene function through a histone tail cleavage. Histone acetylation also controls protein function through epigenetic factors (101) that regulate lung pathologies such as chronic obstructive pulmonary disease (COPD) and asthma (102, 103). Wang et al. (104) determined the activity of HDAC1 and HDAC2 in promoting lung proliferation and airway differentiation through bone morphogenic protein 4/retinoblastoma (Bmp4/Rb) pathways. Further, decreased activity of HDAC1/2 during neonatal development leads to improper alveolarization causing hypoxia and hypoplasia (105, 106). Although the functional role of miRNAs to the regulation of histone acetylation in lung development is not clearly understood, epigenetic complexes might play a significant role in lung development. For example, during hypoxia, methyltransferases Suv39H1 and Suv39H2 induce transcriptional silencing via histone H3 lysine 9 methylation, causing repression of gene expression leading to reduced surfactant protein SP-A expression (107). Likewise, Dakhlallah et al. (108) reported the repression of miR-17-92 cluster function in lung development through DNA methylation by DNA methyltransferase (DNMT)-1 in pulmonary fibrosis. These observations suggest methyltransferases have a regulatory role during early lung development.

MiR-10a contributes to multiple cellular processes such as differentiation, apoptosis (109-111), cell survival, replication, and senescence in embryonic development (57, 112). MiR-24 and miR-10a target genes have been demonstrated to inhibit endodermal differentiation of human embryonic stem cells (hESC) (110). Developmental regulatory circuitry of hESCs work synergistically with miR-10a in modulating smooth muscle cell differentiation from ESC by repressing histone deacetylase 4 (HDAC4) and thus preventing its undesirable vascular effects in pathologies, such as hypertension (113).

Taking the above examples into consideration, it certainly emphasizes that histone acetylation occupies a central role in epigenetic mechanisms regulating lung development and diseases. However, the underlying mechanisms that control these epigenetic factors during lung development and disease states warrant further investigation. In addition, epigenetic factors also influence the regulatory role of miRNAs in lung development, either by promoting or repressing lung proliferation and differentiation. Table 2.1 provides a list of miRNAs that are epigenetically regulated in lung development (3, 4, 89, 93, 108, 114-121).

2.8. MiRNAs and lung diseases

MiRNAs are critical for normal lung development and homeostasis. Aberrant expression profiles of certain miRNAs in the lung can impair lung cellular processes and may contribute to lung diseases (reviewed in Table 2.2) (94, 95, 122-136). The

following section will give insights into miRNA signaling that contributes to the deregulation in lung pathologies.

2.9. Lung cancer and bronchopulmonary dysplasia

Lung cancer leads cancer mortality worldwide (137). Some miRNAs function as oncogenes, while others are considered tumor suppressors (95, 138, 139). To become tumorigenic, epithelial cells need to acquire the ability to migrate and metastasize, i.e. EMT. Members of the miR-200 family regulate EMT in lung tumor metastasis. In this regard Pacurari et al. (124) reported the potential role for the miR-200 family to serve as prognostic markers for non-small cancer lung cells (NSCLC) using H1299 and BEAS-2B cells. Dysregulation of the enzyme Dicer in miRNA biogenesis pathways can also lead to lung tumor development (140, 141). Taking the above examples into consideration, miRNAs might have the potential for new therapy development or as biomarkers for the diagnosis of lung or metastasized cancers. Vascular endothelial growth factor (VEGF), insulin-like growth factor (IGF), fibroblast growth factor (FGF), Wnts (142), and (SHH) (96) have all been implicated in abnormal signaling that ultimately causes defective gas exchange at birth, a process termed bronchopulmonary dysplasia (BPD). The opposing properties of the angiostatic miR-221 and the angiogenic miR-130a coordinated airway branching in *ex vivo* mouse. Fetal lung cultures by altering total VEGFR2-expressing endothelial cells (143).

2.10. Idiopathic pulmonary fibrosis

Idiopathic pulmonary fibrosis (IPF) is a chronic lung disease of unknown cause, characterized by interstitial fibrosis impairing lung function. Accumulating evidence suggests that upregulating genes of the TGF-β, SHH, and Wnt/β-catenin signaling cascades advances IPF (144-146). Willis and Borok (147) reported the involvement of TGF-β and high-mobility group activator HMGA2 as key players in the pathogenesis of pulmonary fibrosis. Yang et al. (a) (125) suggested the involvement of the mir-200 family (miR-200a, miR-200b, and miR-200c) in regulating pulmonary fibrosis through EMT. Let-7d has been identified as a key miRNA involved in the pathogenesis of IPF (148). TGFβ-mediated let-7d inhibition triggers an EMT phenotype in patients with IPF. Let-7d, miR-29, and miR-155 all have been implicated in the pathogenesis of pulmonary fibrosis. For example, Let-7 has been shown to suppress genes such as HMGA2 (TGFβ-activator), Kirsten rat sarcoma virus (KRAS), Myelocytomatosis oncogene (MYC), cyclins such as D2 and cyclin-dependent kinase 6 (CDK6) Pandit (149), implicating the anti-fibrotic role in pulmonary fibrosis.

MiR-21 is expressed in pulmonary myofibroblasts and augments TGFβ-R1 signaling, the latter in turn stimulates miR-21-mediated SMAD2/3 phosphorylation and lung fibrosis progression in a feed-forward loop-dependent manner (150).

Recent studies (151) indicated that administration of bleomycin to mice triggered symptoms of pulmonary fibrosis by up-regulating miR-199a-5P expression and regulating TGFβ-induced lung fibrosis by targeting caveolin-1. In early lung development, BMP4 signaling is required for the proliferation of anterior foregut

mesenchyme and later in epithelial tube elongation (152, 153). SHH signaling is required for mesenchymal proliferation and specification, lung branching, and smooth muscle cell (SMC) formation (154, 155). BMP and SHH signaling coordinate the separation of the trachea and the esophageal tube (156). Radzikinas et al 2011 (155) demonstrated a mechanism of miR-206-mediated regulation of SHH BDNF (brain-derived neurotrophic factor) interaction in airway SMC innervation during airway branching, thus supporting a mechanism whereby miR-206 targets BDNF in early lung bud formation. Manipulating and designing novel therapeutics for specific miRNAs in lung diseases will help us to understand disease pathogenesis.

2.11. Inflammatory airway conditions, cystic fibrosis, and asthma

In recent years, many studies have addressed the role of miRNAs in allergic diseases. Lung injury induced by sensitizing cells with aerosolized lipopolysaccharides (LPS) in vitro induces an inflammatory lung condition and dysregulation of a versatile group of miRNAs: miR-146, miR-125b, miR-21, miR-25, miR-27b, miR-100, miR-140, miR-142, miR-3p, miR-181c, miR-187, miR-194, miR-214, miR-223, and miR-224 (157-159). These findings suggest that these miRNAs are important modulators of lung inflammation, likely through the upregulation of the pro-inflammatory cytokine TNF-β (159). Interestingly, LPS-mediated regulation of Kappa B kB-Ras2 also abolished the miR-125b effects and blocked IkB signaling (157, 160, 161) during pulmonary inflammation. The transcription factor E74-like factor 5 (Elf5; Ets domain transcription factor) coordinates embryonic lung cell shape and polarity in response

to FGF-10-mediated activation of phosphatidylinositol-4,5-bisphosphate 3-kinase/protein kinase B (PI3K/Akt) signaling in distal epithelium (162). PI3K/Akt signaling is upregulated in cystic fibrosis (CF), a condition of heightened inflammation due to bacterial infections, neutrophil recruitment, and lung tissue breakdown in the airway. Findings suggest that IL-8 expression is upregulated by miR-155-mediated inhibition of phosphatidylinositol-3,4,5-trisphosphate 5-phosphatase 1 transcription, an event that results in PI3K/Akt signaling activation (163). Similarly, in airway hyper-responsiveness conditions such as asthma, SMC of the lung contract after stimuli resulting in increased cytokine secretion and epithelial hyperplasia. A recent study (164) demonstrated that in an *in vitro* stretch system, miR-155 expression significantly increased due to the inflammatory response of human bronchial epithelial cells (hBEC) as a result of 24 h mechanical stretch. They demonstrated that the higher expression levels of miR-155 upon hyperstretch repress Src homology 2 domain-containing inositol 5-phosphatase 1 (SHIP1) and promote c-Jun N-terminal kinase (JNK) phosphorylation. MiR-10a regulates PI3K signaling by repressing PI3KCA (catalytic subunit alpha) expression in human airway smooth muscle cells (hASM). PI3KCA inhibition by miR-10a further abrogates AKT phosphorylation and cyclin expression required for hASM proliferation. This suggests that miR-10a could potentially have a therapeutic role in controlling the abnormal ASM proliferation (165). Dysregulation of miRNAs has been reported in different experimental asthma models. For example, miR-21 deletion in mice challenged with ovalbumin elevates the allergic immune response by repressing interleukin 12 (IL-12) expression and

promoting a T helper-2 (Th-2) type lymphocyte response (166). Considering SMC, miR-133a promotes the expression of the small G protein RhoA by increasing bronchial hyperactivity in an asthma animal model (167). MiR-126 has also been reported to play a key role in the development of allergic airway disease (130). This study found that blocking miR-126 could repress the airway inflammatory disease of the lung by downregulating the Th-2 response that mediates the inflammation. However, the definitive mechanisms that contribute to the Th-2 responses in asthmatics remain unclear at this point.

2.12. Pulmonary hypertension

Pulmonary hypertension (PH) is a severe disease of pulmonary arteries resulting in right ventricular hypertrophy (RVH), increased fibrosis, and heart failure leading to morbidity and mortality (168, 169). This disease affects primarily pulmonary arterial endothelial cells (PAECs) and pulmonary artery smooth muscle cells (PASMC). However, the key factors that regulate these events in the pathogenesis of PH are currently unknown. Dysregulation of miRNAs might play a significant role in the development of PH. For example, repression of miR-204 is observed in the PASMCs through STAT3 and SRC kinase (170). Similarly, miR-424/503 expression is inhibited in PAECs disease by downregulating apelin (APLN) and stimulating proliferation through FGF2 (135). These studies suggest that both APLN and FGF2 play a significant role in mediating the miRNA function in pulmonary vascular homeostasis. MiR-21 and miR-145 occupy a central role in understanding

the pathobiology of pulmonary arterial hypertension (PAH). For example, downregulation of miR-21 is observed in the monocrotaline-injected rat model with hypoxia exposure (171).

Similarly, miR-21 null mice showed severe disease pathogenesis in PAH with increased expression of Rho B and Rho-kinase activity (172). MiR-145 is a phenotypic marker for SMC and regulates SMC function through Krüppel-like factor-5 (KLF-5) and myocardin (173, 174). Repression of miR-145 has been reported to play a role in the re-modelling of vascular homeostasis in mice (174). Caruso et al. (175) have demonstrated that miR-145 inhibition in a mouse model protects against PAH development. This group also demonstrated that the mice exposed to hypoxia exhibit elevated expression of miR-145 and observed this pathological condition in lung tissues from patients with PAH. Further, Fichtlscherer et al. (176) have identified a role for circulatory miRNAs in coronary artery disease patients, but limited information is available in PH patients. Recently, Wei et al. (177) determined the expression patterns of miRNAs in the blood of PH human subjects and identified novel miRNAs in the circulation of PH subjects. Additionally, they validated and identified miRNAs that were upregulated (miR-23b, miR-130a, and miR-191), or downregulated (miR-451 and miR-1246) in the circulation of PH subjects. These dysregulated miRNAs link directly to the degree of pathogenesis of PH and might be considered as potential biomarkers in PH disease for therapeutic intervention. However, it is still unclear how the dysregulated circulating miRNAs in the blood of PH patients influence the target genes.

2.13. Limitations of lung tissue heterogeneity and available animal models

Two major limitations of existing efforts are the lack of multiple time points in development and the lack of combined analysis of mRNA genes in parallel with an analysis of miRNAs. Such factors are important to identify dynamic changes. Available data do not always reflect cell-specific changes in gene expression, since the available studies have been utilizing whole lung tissues, a very heterogeneous and complex organ. Thus, the use of different methods that rely on spatial micro-analysis of lung tissues such as laser capture microdissection or cell sorting is emphasized. Demonstrating such approaches allows for novel markers that will have a significant impact on disease gene–epigenetics interaction discovery. Animal studies on specific miRNA inhibitors or mimics lack clinical efficacy and unlikely trigger exactly the same symptoms in patients. Armed with this challenge, one miRNA could regulate a number of adverse scenarios resulting from indiscriminate targeting of multiple transcripts or pathways. The spatial and temporal regulation that controls such complex crosstalk is obscure in such cases, and the application of one therapy could provoke undesired effects. Moreover, a number of the animal models that are currently available are not fully characterized at the molecular level, and therefore they do not assimilate the players in the human disease. Understanding the molecular mechanisms responsible for miRNA-associated diseases is extremely important. The studies reported to date have only assessed the short-term impact of miRNA inhibition or overexpression. Although many approaches using miRNA inhibitors or mimics showed significant results, the constituents used in these studies

are not suitable for *in vivo* miRNA inhibition or ectopic expression. New strategies based on improving penetration, pharmacokinetics, coupling to carrier molecules, antibody conjugates, membrane permeable peptides, colloidal particles, or gene transfer is warranted.

2.14. MiRNAs as targets for therapeutic strategy

MiRNAs have been employed as potential therapeutic targets in the treatment of various lung diseases. Recently, molecular strategies have emerged to increase the therapeutic function of miRNAs in diseased tissues. Accordingly, two approaches have been developed for miRNA-based therapeutics: miRNA antagonists and miRNA mimics. MiRNA antagonists inhibit endogenous miRNA function contributing to the gain-of-function in pathological states or inflammatory conditions. This therapeutic approach is compared to other inhibitory therapeutics that target individual gene products as well as short interfering RNAs (siRNAs).

MiRNA mimics restore a loss of function and are considered "miRNA replacement therapy", introducing therapeutic miRNAs targeting diseased cells in the patients (178). For example, therapeutic delivery of a let-7 mimic inhibited tumour growth in human NSCLC xenografts and in a transgenic mouse model of RAS-G12D (179). Similarly, miR-34 mimics therapeutically blocked lung tumour growth in a mouse model (180).

Anti-miRNA oligonucleotides (antagomir oligos) are modified chemically to increase their stability and to silence the miRNA functions *in vivo* (181). More

research studies are warranted to understand the impact of anti-miR treatment on miRNA–miRNA interaction networks. Recently, more attention has been focused on the locked nucleic acid (LNA) strategy to understand the mechanism of miRNA-mediated gene regulation. Using this strategy, the LNA approach has potential for application in human trials considering their increased specificity versus conventional approaches, theoretically reducing off-target effects (182). For example, LNA antagomirs against miR-33 proved to be beneficial for the treatment of atherosclerosis by regulating the lipoprotein levels (120, 143, 183). Mutation of this oncogene has been implicated in adenocarcinoma of the lung.

Liu et al. (a) (150) reported that miR-21 regulates the fibrogenic activity in lung fibrosis through TGF-1 and Smad/Smad7 pathways. Further, this group addressed the elevated expression of miR-21 in the lungs of mice having lung fibrosis and in patients with IPF. Similarly, anti-miR-21 has been reported to extra therapeutic effect in the treatment of lung fibrosis (150). Mir-29 also protects lungs against bleomycin-induced lung fibrosis in mice (184). Mujahid et al. (143) recently addressed the specific role of anti-angiogenic miR-221 and pro-angiogenic miR-130a effects on airway and vascular development in fetal lungs. These studies have found that lungs treated with anti-miR 221 resulted in increased branching with overexpression of Hoxb5 and VEGFR2 around the airways. Alternatively, miR-221 mimic had opposite effects on treated lungs with respect to airway branching, defining the regulator effects of miR-221 and miR-130a on vascular remodelling of the developing lung. Engineering novel therapeutics against the potential target miR-

21 provides better treatment for the pathogenesis of lung fibrosis. Molecular approaches or strategies, applied in miRNA biology to understand the potential interaction between miRNAs and their targets, will guide us in the development of new effective therapeutics and therapies for the treatment of lung diseases. However, the adverse effects of nonspecific miRNA inhibitor/mimic-based therapeutics can damage normal proliferating cells. Preliminary and pilot experiments will be required to examine such cycling effects on normal cells of the lung microenvironment. This approach is limited by the lack of miRNA inhibitors/mimics that selectively target the cell cycle of damaged cells or compounds that preferentially arrest normal lung cells at the S phase. These approaches are difficult to exploit clinically.

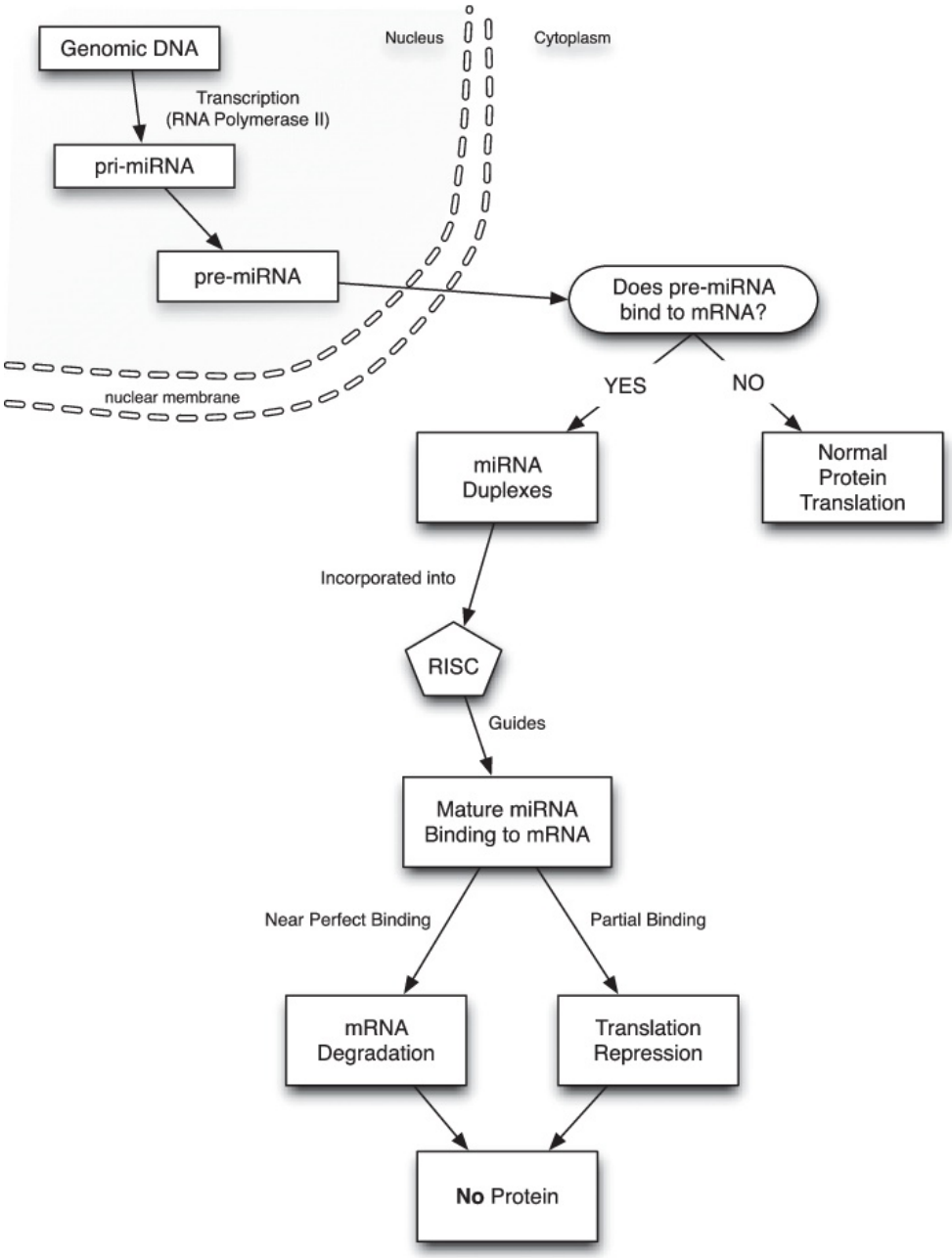

Figure 2.1. A schematic overview of miRNA biogenesis pathways. Shown are two pathways for miRNA function: degradation of mRNA and normal mRNA functions (185).

Table 2.1. Epigenetic regulation of miRNAs in lung development.

miRNA	Target genes	Function	References
miR-302/367	GATA6	Controls lung endoderm progenitor proliferation, differentiation and apical-basal polarity. The cluster also plays a role in lung homeostasis.	(Tian et al. 2011; Zhang et al. 2008).
miR-17–92 family	RAB14, BMP4, FGF-10, DNMT-1	Regulates early lung development by promoting proliferation and inhibiting differentiation of lung epithelium.	(Carraro et al. 2009; Dakhlallah et al. 2013; Herriges and Morrisey 2014; Khoshgoo et al. 2013; Lu et al. 2007)
miR-34/449	CCNE1, CCND2, E2F1	Role in the development of multiciliogenesis and inhibits lung proliferation through p53 (Trp53) acetylation and activation. The cluster also regulates airway epithelial cells.	(Lize et al. 2010*a*, 2010*b*; Marcet et al. 2011)
miR-375	FZD8	Controls epithelial cell differentiation through WNT/β-catenin pathway.	(Wang et al. 2013*a*)
miR-200 and 205	ZEB1, ZEB2	Role in epigenetic silencing by promoting epithelial-to-mesenchymal transition (EMT) process in human lung epithelial cells.	(Tellez et al. 2011).
let-7 family	RAS, KRAS	Role in sacculo-alveolar stage of lung development and promotes lung tumor development.	(Khoshgoo et al. 2013; Johnson et al. 2005; Kumar et al. 2008)

Source (185).

Table 2.2. Implications of miRNAs in lung disease.

miRNA	Target genes	Functional role in lung diseases	References
miR-200 family (miR-200b, miR-200a, miR-429, miR-200c and miR-141)	ZEB1, ZEB2, HNRNPR3, HFE ATRX and TGF-β1	Regulates epithelial-mesenchymal transition (EMT) and metastasis in lung cancers.	(Pieraccioli et al. 2013; Li et al. 2014; Pacurari et al. 2013; Yang et al. 2012*a*)
miR-17-92 cluster	PTEN and RB2	Over expressed in human lung cancers and also contributes to uncontrolled inflammation.	(Hayashita et al. 2005; Ventura et al. 2008)
miR-155	SOCS1	Over expression in lung cancer with poor survival rate. Promotes acute lung inflammatory lung injury.	(Rodriguez et al. 2007; Rao et al. 2014)
let-7	RAS	Low expression in human lung cancer with poor prognosis and functions as a tumor suppressor in human lung cells.	(Johnson et al. 2007; Takamizawa et al. 2004)
miR-126	POU3F1, PU.1 and GATA3	Regulates the asthma pathogenesis by altering the immune response of helper T2 cells (TH2). miR-155 elevates the cyclooxygenase expression and PGE2 secretion on in asthmatic airway smooth muscle cells.	(Mattes et al. 2009; Comer et al. 2014)
miR-155	COX2, PGE2		
miR-154	SMAD3, Laminins	Regulates fibroblast migration and proliferation in pulmonary fibrosis.	(Milosevic et al. 2012; Cushing et al. 2011; Yang et al. 2013)
miR-29	Integrins and TGF-β1	Role in the pathogenesis of pulmonary fibrosis.	
miR-424 and 503	APLN, FGF2, BMPR2 and WWP1	Role in the maintenance of pulmonary vascular homeostasis.	(Kim et al. 2013; Yang et al. 2012*b*)
miR-21 SATB1 and YOD1		Role in the pathogenesis of chronic hypoxia-induced pulmonary vascular remodeling.	

Source (185).

CHAPTER 3

The transcriptome of nitrofen-induced pulmonary hypoplasia in the rat model of congenital diaphragmatic hernia

In this chapter, I elucidate the utility of next generation sequencing (NGS) technology in characterizing transcriptome changes that contribute to abnormal lung development in the nitrofen rat model of CDH. Specifically, I used NGS technology to characterize the transcriptomic differences between control lungs and nitrofen-induced hypoplastic lungs in embryonic lung tissues prior to the development of the diaphragmatic defect (Figure 3.1). I examined the hypothesis that transcriptome changes contribute to abnormal lung development in the nitrofen rat model of CDH. Exploring such phenotypic mechanisms in rats could help improve our understanding of abnormal lung development in human CDH.

3.1. Contribution statement

I, Dina Johar, made the following contributions to this study:

- extracted the total RNA for running the validity check of the NGS data by dPCR and RT-qPCR.
- conducted the bioinformatic analysis of NGS source files including identification and annotation of miRNA, mRNA, GO terms and pubmed IDs. I generated tables 3.2 and 3.3 and the discussions corresponding to them.
- conducted the similarity check using Blastin and filtered out 64 rat miRNAs species homologous to known human miRNAs and generated table 3.4 and its discussion.
- conducted the bioinformatics analysis of miRNA rat orthologs to human based on stem loop structure and similarity and generated table 3.5 and its discussion.
- discussed the above miRNA interactions with organogenesis network associated with nitrofen-induced lung hypoplasia presented in table 3.5.
- conducted multiple sequence alignments and structure conservation of functionally relevant embryonic and fetal miRNA ortholog sequences cross species. Identified species ID by mirOrtho database for figure 3.7.
- contributed to the primers' design used for dPCR and RT-qPCR.
- performed statistical analyses for above-mentioned data.
- interpreted results together with those from other contributors.
- I wrote 100% of the manuscript that was edited later on by Thomas Mahood, such that we were listed as co-first authors.

Other contributors:

- Thomas H. Mahood
- Wayne Xu
- Richard Keijzer
- Debourah Tsuyuki

3.2. Rationale

Babies with CDH have a hole in their diaphragm and abnormal lung development resulting in lung hypoplasia and PPHN. CDH constitutes about 8% of major congenital anomalies and has the highest mortality rate (14). In rodents, nitrofen-induces CDH and lung hypoplasia similar to the phenotype observed in humans (186). Whether the nitrofen-rat model shares the same pathogenesis with human CDH remains to be determined. Some hypotheses suggest that nitrofen influences diaphragm and lung development in rodent embryos similar to the human condition (27, 187, 188). Thus far, the transcriptomic changes associated with nitrofen-modulated developmental signaling have not been characterized in the lung.

We currently do not know how the herbicide nitrofen induces lung hypoplasia and CDH in rats. MiRNAs are small (17–24 bp), noncoding RNAs that regulate different biological functions by modulating expression and stability of target genes post-transcriptionally (189, 190). The role of miRNAs in lung development is currently poorly defined. Deregulation of miRNAs, and consequently, loss of fine adjustments to target genes can lead to lung diseases (185).

My aim was to compare the differentially expressed transcriptome of nitrofen-induced hypoplastic lungs to control lungs in E13 rat embryos before the development of embryonic diaphragmatic defects. Using next-generation sequencing technology (NGS), I identified the expression profile of miRNA and mRNA genes (191).

Once the dataset was validated by both real time quantitative polymerase chain reaction (RT-qPCR) and digital-PCR, I conducted gene ontology (GO), miRNA target analysis, and orthologous miRNA sequence matching for the deregulated miRNAs in silico. The study identified 186 known mRNA and 100 miRNAs which were differentially expressed in nitrofen-induced hypoplastic lungs. Sixty-four rat miRNAs homologous to known human miRNAs were identified. A subset of these genes may promote lung hypoplasia in rat and/or human, and I discuss their associations. Potential miRNA pathways relevant to nitrofen-induced lung hypoplasia include PI3K, TGF-β, and cell cycle kinases. Nitrofen-induced hypoplastic lungs have an abnormal transcriptome that may lead to impaired development. This knowledge may have implications for diagnosis and possible treatment of the disease in the future.

3.3. Methods

3.3.1. Animals, nitrofen administration and sample preparation

The University of Manitoba Animal Care Committee approved all animal care protocols. A total of two pregnant dams were included in each group. E13.5 lungs were isolated and snap frozen in liquid nitrogen (Figure 3.1). The diaphragmatic changes associated with the nitrofen model were validated by former studies (192-194) and the model was standardized (27). Total RNA was extracted from pools of four lungs for each sample using the mirVana extraction kit (ThermoFisher, Waitman, MA). DNA contamination was removed with a DNase treatment kit (Ambion Life Technologies, Carlsbad, CA) before yield was determined spectrophotometrically.

RNA quality was assessed using a Bioanalyzer (Agilent Technologies, Santa Clara, CA) with RNA integrity values of greater than 9 used for further analysis (Figure 3.2).

3.3.2. Small RNAseq (miRNA) library preparation and sequencing

Total RNA (1 µg) was quantified by the Qubit fluorometer (ThermoFisher). After 5′ and 3′ adapter ligation, transcripts were amplified with barcoded primers for parallel sample sequencing. Samples were combined and run on a polyacrylamide gel and miRNAs and piwi interacting RNAs were cut out of the gel and purified using standard molecular biology techniques. Briefly the excised gel bands are eluted in elution buffer overnight and small RNAs are released into the supernatant. RNAs are then extracted in phenol:chloroform, then in chloroform, and finally are precipitated in ethanol. RNAs are then resuspended in H_2O and quantified by incorporation of label or by A260 if necessary. The purified miSeq library was then validated by RT-qPCR before running on an Illumina MiSeq NGS instrument (Illumina, San Diego, CA) using 50 base pairs single end reads.

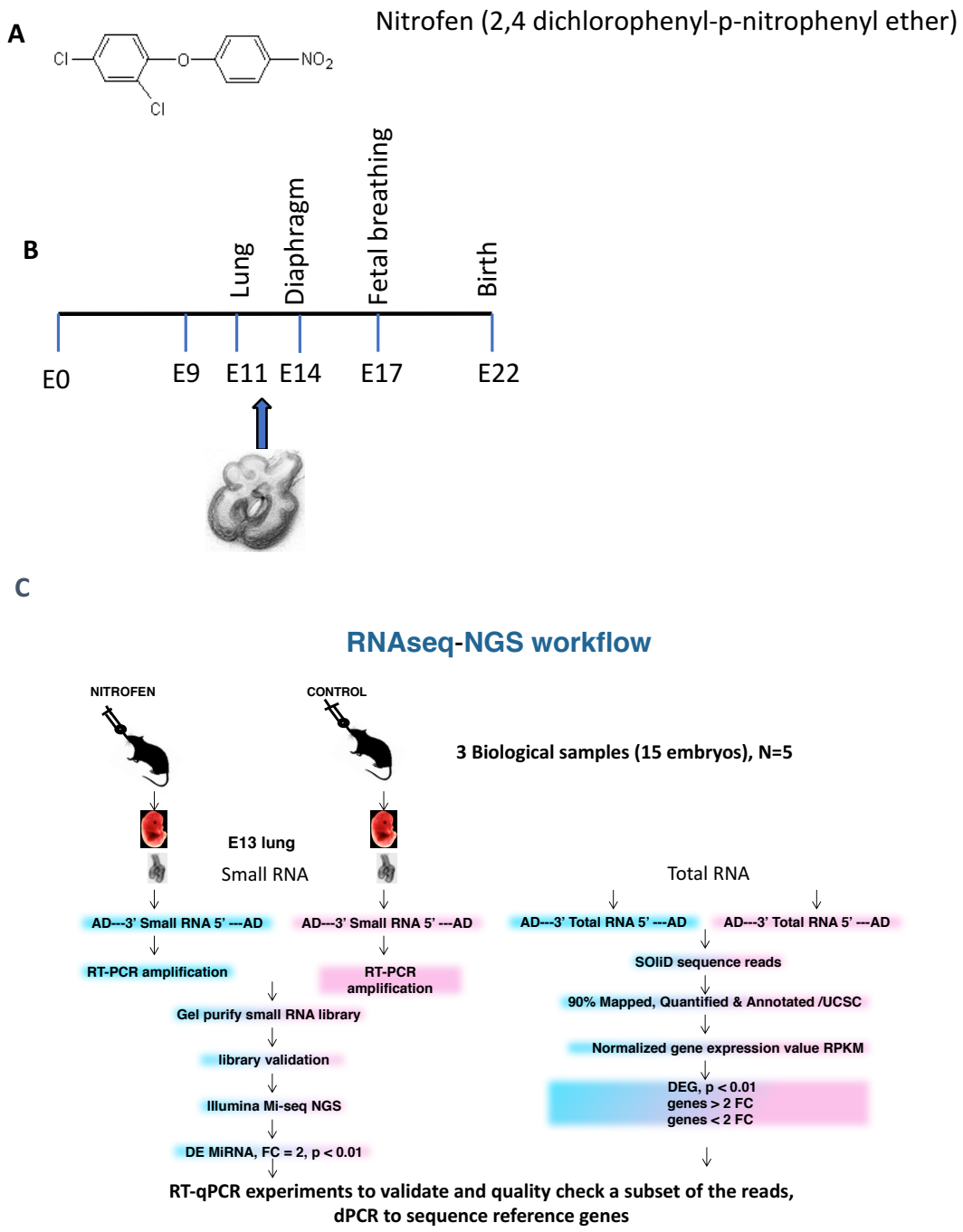

Figure 3.1. The nitrofen rat model. A. The chemical structure of nitrofen. B. E13 lung provides the phenotype characteristics of 80% CDH and 100% pulmonary hypoplasia (PH). C. RNAseq-NGS workflow. N= number, AD= Adaptor, DEG= Differentially expressed genes, FC=Fold Change, UCSC= The University of California Santa Cruz-annotated refGenes, RPKM= Kilobase Per Million Reads.

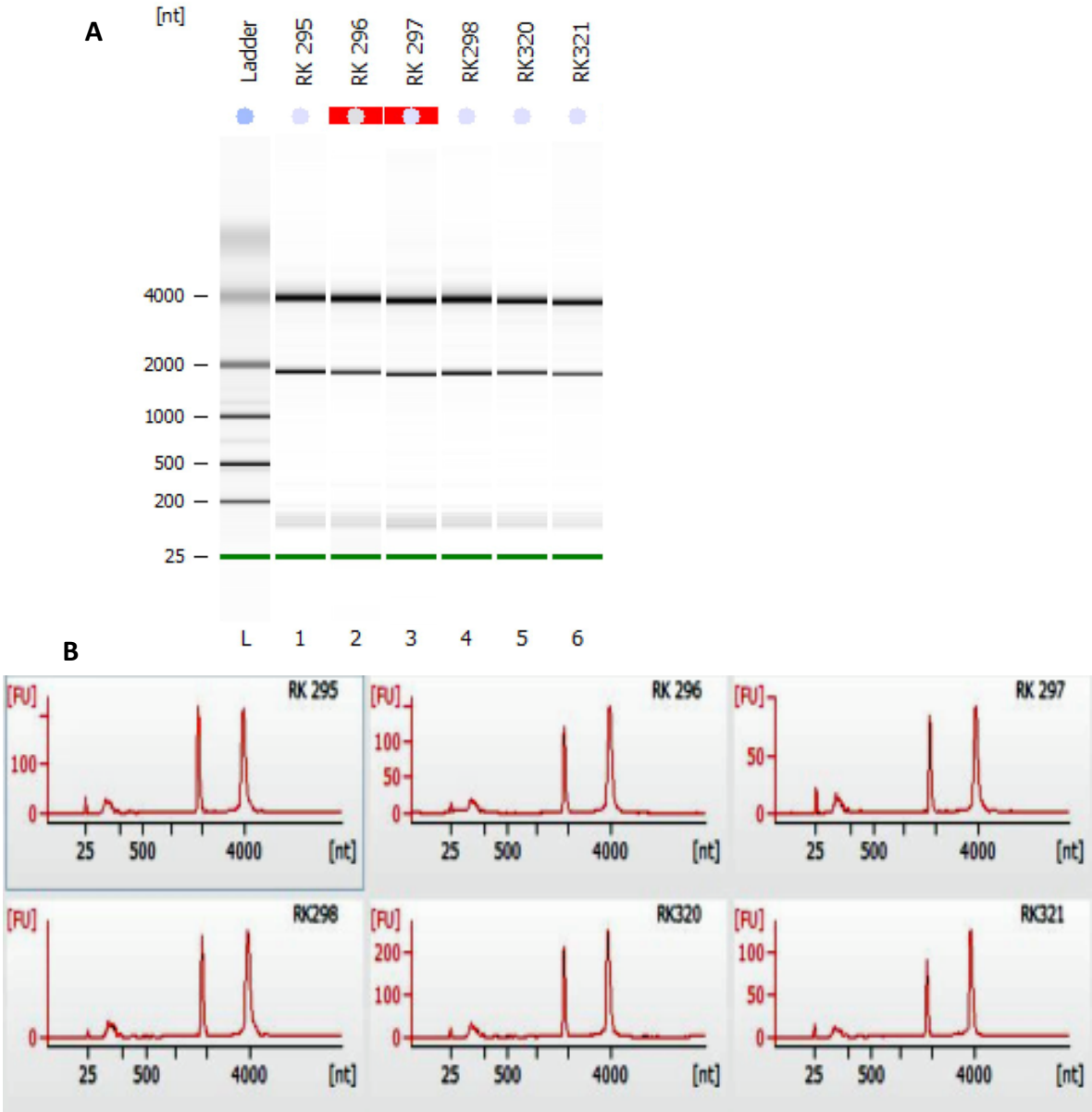

Figure 3.2. RNA quality check of pooled total RNA extracts in triplicate samples of nitrofen treated and control E13.5 embryos before sequencing. A) Capillary based gel electrophoresis and B) electrophoretagram using a BioAnalyzer 2100 (Agilient), version 2.6, sensitivity in picograms.

3.3.3. Total RNAseq library preparation and sequencing

Using 5 µg of ribosomal depleted total RNA (Epicenter Ribo-Zero, Illumina), the total RNA library was created using the SOLiD total RNA-Seq kit (ThermoFisher). Briefly, the RNA was fragmented to 100–200 bp using RNAse III before being hybridized and ligated to SOLiD adapters. The library was reverse transcribed to cDNA before being size selected using AmPure XP beads (Beckman Coulter, Mississauga, Canada). Once cDNA libraries were barcoded (SOLiD primers, ThermoFisher) and assessed (Agilent Technologies), libraries were pooled and run for NGS on the SOLiD 5500 xl instrument (ThermoFisher).

3.3.4. Bioinformatics and statistical analysis

SOLiD RNAseq data were mapped to the Rattus norvegicus (rno) reference genome (rn5) using Lifescope v2.5.1 software (ThermoFisher) with the two-mismatch settings. The mapped reads were quantified against the UCSC and normalized gene expression profiles, reads RPKM, were generated. The bioconductor package edgeR (195) based on a negative binomial model was used to infer the differentially expressed genes between the treated and control samples. MiSeq sequence reads were used for miRNA profiling. After adaptor removal and quality check, the differentially expressed mature miRNAs were analyzed using the mirTools 2.0 pipeline (195). The rno mirBase v16 with “best match” setting was used. I detected 100 miRNAs by a cutoff of $P \leq 0.01$ and fold change (FC) ≥ 1.5 and their mature sequences were further identified using mirBase. The miRNA and mRNA expression data files of the nitrofen-treated and control lung tissue samples were loaded into

the Partek Genomics Suite v6.6 (Partek Inc, St Louis, MO). The Pearson correlations of the miRNAs and their target mRNAs were analyzed against the rno-miR database using the miRNA integration module. For differentially expressed miRNAs, all sequence reads in rat and mRNA targets overlapping with differentially expressed genes were used to perform IPA pathway analysis to obtain a list of enriched pathways (Ingenuity Systems, Redwood City, CA). I identified human ortholog sequences by mapping the short rno reads to a known miRNA database (mir-Base) using BLASTN and other tools from the mirOrtho database (196). Homolog sequences of selected miRNAs were identified among different species using the stem loop structure. Consequently, the aligned sequence conservation of miRNAs was compared across species (Figure 3.7). Differential expression of miRNA between paired samples was measured using a Chi-squared statistic. P values were calculated for the null hypothesis that no differential expression existed between the two samples. Final P values are corrected using the Bonferroni correction for multiple hypothesis testing.

3.3.5. Endogenous control TaqMan assay

Embryonic rat lungs E21 were isolated from three different dams, and total RNA was extracted and reverse transcribed as described previously. A rat endogenous control plate (ThermoFisher) was seeded with cDNA (25 ng RNA input per reaction), TaqMan Fast Advanced Master Mix (ThermoFisher), and water to 10 µL. The plates were run on a CFX96 thermocycler (Bio-Rad, Mississauga, Canada) using the recommended cycling parameters and Raw Cycle Threshold (Ct) values

were reported along with m-value analysis provided by the accompanied software (CFX Manager 3.1; Bio-Rad). Total RNA input equivalent to 1 µg were reverse-transcribed (Bio-Rad). Reverse-transcribed products were amplified and quantitated using rat gene-specific forward and reverse primers. Supermix-based assays were performed using the thermal cycler, with an initial denaturation at 95°C for 30 s, followed by 40 cycles of denaturation at 95°C for 15 s; annealing/extension accompanied with plate read at 60°C for 60 s. All reverse transcribed reactions were performed with three different RNA inputs, and all qPCR reactions were carried out in triplicate. Primers against rat β-actin, TATA-box binding protein and β-2-microglobulin were used as internal references for target genes. All mRNA values were normalized to β-actin mRNA levels, which were identical for nitrofen and control lungs. The mean threshold cycle was determined and used for analysis.

3.3.6. Primer design and optimization

Primers were designed using Primer Quest (Integrated DNA Technologies, Coralville, IA) and verified for specificity using UNAFold (IDT), and Primer-Blast (197) software. Primer specificity was verified using conventional molecular techniques before being optimized for SYBR Green annealing temperature and melting curve specificity using gradient RT-qPCR and also determined with dPCR (Table 3.1).

3.3.7. Digital PCR

Samples were diluted to an optimal concentration (1.6 copies/µL in water) using

Table 3.1. Primers used for digital and RT-qPCR validation of the NGS dataset.

Gene Symbol (rno)	Gene Name	Entrez Gene ID / mRNA Accession		Primer Sequence 5'-3'
Gapdh	glyceraldehyde-3-phosphate dehydrogenase	24383	Fwd	TGTGAAGCTCATTTCCTGGTAT
		NM_017008.4	Rev	GTGGTCCAGGGTTTCTTACTC
Abl1	ABL proto-oncogene 1, non-receptor tyrosine kinase (Abl1)	311860	Fwd	CTCGATGGAACTCCAAGGAAA
		NM_001100850.1	Rev	AGCTTCTCGCCTTTAGTGATG
Ephx3	Epoxide hydrolase 3	366836	Fwd	CCTGGGATTTCTCAGTCTACTTC
		XM_006241083.1	Rev	TGGCGGGTTGAGTATTCTTG
Car7	Carbonic anhydrase 7	291819	Fwd	GTTCGGTTTAAGGACACCAAAG
		XM_006255051.1	Rev	TGGTTAGGGAGCCAGGATA
Wnt3	Wingless-type MMTV integration site family, member 3	24882	Fwd	CAGGCCGAACGACCATC
		XM_006247489.1	Rev	CGTACTTGTCCTTGAGGAAGTC
Psg19	pregnancy specific glycoprotein 19	24256	Fwd	TCTTTTCGTCTGTGGGCGTCCT
		NM_001270654.1	Rev	GCGTTCGTAGATTCTCTGGAAGATTG
Nol3	Nucleolar protein 3 (apoptosis repressor with CARD domain)	85383	Fwd	CTCGAAGCCCAAATGGGTAA
		XM_006255539.1	Rev	AGTCAGCCTGCAATGTTTCTA
Id4	Inhibitor of DNA binding 4	291023	Fwd	CTGACCTAGATGGGAACCTTTG
		NM_175582.1	Rev	CCCTCACGCACTTAATTCTTTAT
Cdt1	Chromatin licensing and DNA replication factor 1	292071	Fwd	GCCTTGTCCTACCATACAAGT
		NM_001106192.1	Rev	CTTCAAAGCGCTTGCGTATC
Chrna4	Cholinergic receptor, nicotinic, alpha 4 (neuronal)	25590	Fwd	GACTCTTCTCCGGTTACAACAA
		NM_024354.1	Rev	GTTCTTCTCGTCCACGTCAAT

Source: (191).

an Early Access dPCR Experiment Design application (ThermoFisher). Each sample was combined with Quant Studio 3D Master Mix (ThermoFisher), SYBR I (ThermoFisher), primers (500 nM each) and built up to 14.5 µL with water.

Reactions were loaded, filled, and sealed on separate QuantStudio 3D dPCR 20k Chips (ThermoFisher) and run on a QuantStudio 3D chip reader (ThermoFisher) with data analysis completed using the associated online software (Figure 3.3).

3.3.8. RT-qPCR

Using Sso Advanced SYBR green supermix (Bio-Rad), each reaction well was loaded with primers (500 nM each), along with 10 Nanogram (ng) of template and built up to 20 µL with water. Samples were run using a CFX 96 thermocycler with the following cycling parameters: 95 ^{o}C 30 second (s), 40 cycles of 95 ^{o}C for 15 s and annealing at 59 ^{o}C for 30 s after which a melting curve was performed. Two endogenous controls as determined by the TaqMan assay were used to calculate changes in expression (CFX Manager 3.1, Bio-Rad).

3.4. Results

A total of 5,045,279 single-end (50 base pairs (bp)) miRNA sequence (MiSeq) reads were generated and 153,253,385 pair-end (50 base pairs) Sequencing by Oligonucleotide Ligation and Detection (SOLiD) sequence mRNA reads were generated from nitrofen-treated and control lung samples. Over 90% of the mRNA, reads were mapped on the rno reference genome (rn5; rno) using Lifescope v2.5.1 software (ThermoFisher, Grand Island, NY) with two-mismatch settings.

3.4.1. MiRNA and mRNA profile induced by nitrofen

Once the MiSeq sequences were normalized, a large number of unaligned sequences were identified possibly due to the low abundance of embryonic RNA. Due to the nature of working with limited material derived from embryonic animals, a pooled sample collection was analyzed to strengthen our alignment profile. To compensate for the pooled effects of the data, a strict statistical filtering of the raw miRNA dataset provided a focused approach identifying differentially expressed miRNAs in the nitrofen-induced hypoplastic lungs. The dataset resulted in 100 significantly upregulated miRNAs ($P < 0.01$) that were differentially induced by a fold change > 1.5 (Table 3.2).

The sequences of other small RNA species including ribosomal (rRNA), small nuclear, small nucleolar and transfer were annotated against the UCSC genome browser (198) (Figure 3.4). Analysis of the mRNA transcriptome identified 186 mRNA coding genes that had significantly altered abundance relative to control ($P < 0.01$) (Table 3.3). Nitrofen treatment induced 80 mRNA genes by > 2 fold while 106 genes were downregulated by < 1 fold relative to controls.

3.4.2. Functional enrichment analysis of mRNA

The differentially expressed transcript datasets were entered into QIAGEN's Ingenuity Pathway Analysis (IPA, QIAGEN Redwood City, CA) for mRNA and miRNA pathway analysis PANTHER Gene Ontology classification system (199) for functional gene expression analysis (Figure 3.5). Finally differentially expressed genes were mapped to the Kyoto Encyclopedia of Genes and Genomes (KEGG)(200). IPA analysis

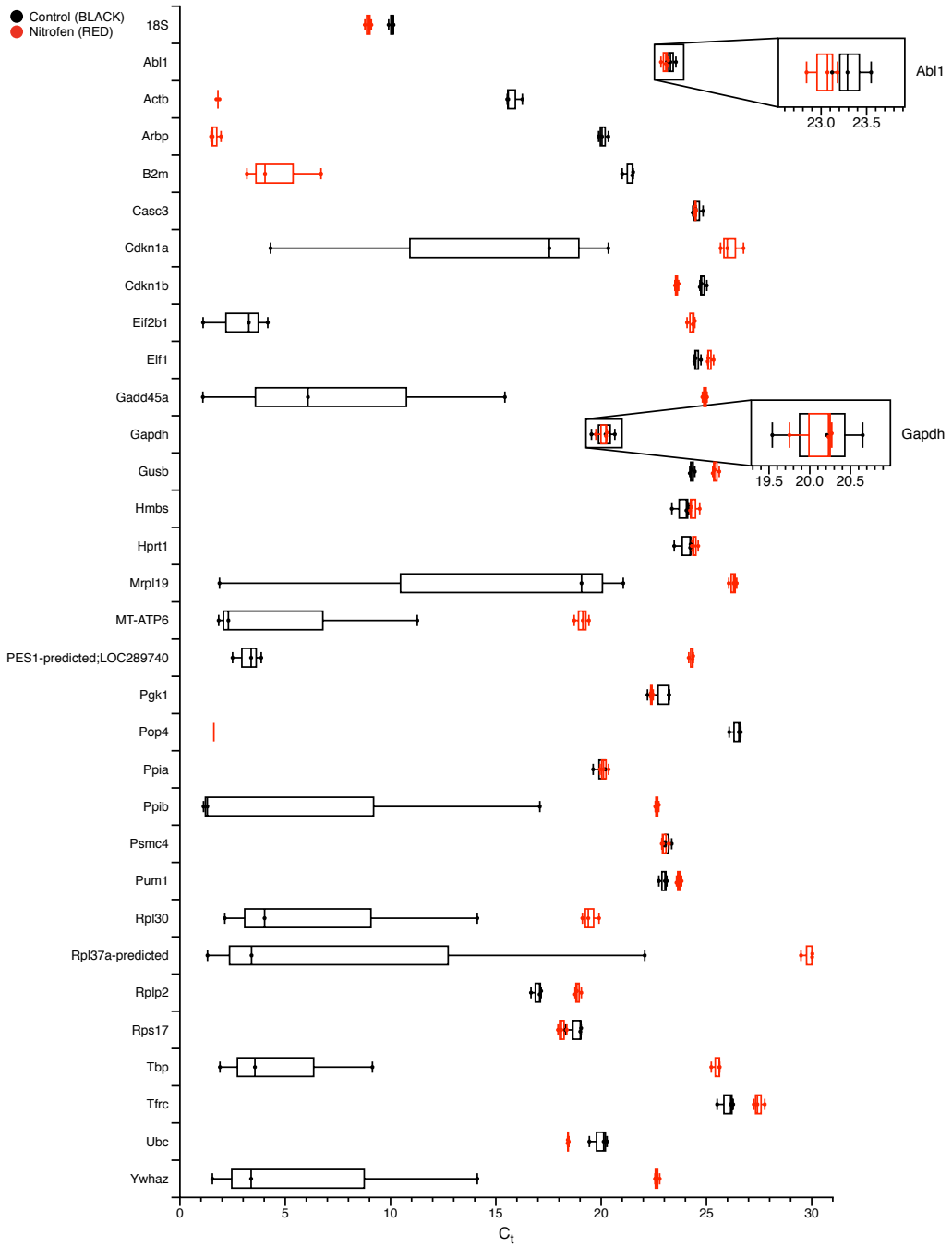

Figure 3.3. TaqMan Assay Validation. Endogenous genes tested (y-axis) were compared to their Ct (x-axis). Box plots show distribution of true biological replicates at E21 from nitrofen and control treated rat lungs. Best candidates, ABLT1 and GAPDH, were selected based upon coefficient of variance and m-fold calculations. CV: 0.0769, M-value: 0.2221 (191).

Table 3.2. Nitrofen-induced differential expression of miRNAs.

mirBase ID (rno)	Mature sequence	Accession number of mature sequence (mirBase)	P-value	FC	miRNA Family (rno)
rno-miR-216a-3p	CACAGUGGUCUCUGGGAUUAUG	MIMAT0017160	0	14.91	216
rno-miR-216b-3p	AAAUCUCUGCAGGCAAAUGUGA	MIMAT0017846	0	5.15	216
rno-miR-216b-5p	AAAUCUCUGCAGGCAAAUGUGA	MIMAT0017846	0.01	1.71	216
rno-miR-3075	UGUCUGGGAGCAGCCAAGGACAAG	MIMAT0025057	0	12.88	3075
rno-miR-325-5p	CCUAGUAGGUGCUCAGUAAGUGU	MIMAT0000557	0	10.3	325
rno-miR-135b-3p	AUGUAGGGCUAAAAGCCAUGGG	MIMAT0017043	0	8.29	135
rno-miR-881-3p	UAACUGUGGCAUUUCUGAAUAG	MIMAT0005289	0	8.29	881
rno-miR-24-1-5p	GUGCCUACUGAGCUGAUAUCAG	MIMAT0003153	0	7.73	24
rno-miR-505-5p	GGGAGCCAGGAAGUAUUGAUGUU	MIMAT0017226	0	7.71	505
rno-miR-377-5p	AGAGGUUGCCCUUGGUGAAUUC	MIMAT0017203	0	6.2	154
rno-miR-539-3p	CAUACAAGGGUAAUUUCUUUUC	MIMAT0017212	0	4.66	154
rno-miR-369-3p	AAUAAUACAUGGUUGAUCUUU	MIMAT0003207	0	2.12	154
rno-miR-337-3p	UUCAGCUCCUAUAUGAUGCCUUU	MIMAT0000577	0	6.2	337
rno-miR-370-5p	CAGGUCACGUCUCUGCAGUUACAC	MIMAT0017202	0	6.2	370
rno-miR-466b-5p	UAUGUGUGUGUGUAUGUCCAUG	MIMAT0005278	0	6.2	467
rno-miR-132-3p	UAACAGUCUACAGCCAUGGUCG	MIMAT0000838	0	5.78	132
rno-miR-212-5p	ACCUUGGCUCUAGACUGCUUACUG	MIMAT0017158	0	5.15	132
rno-miR-291a-5p	CAUCAAAGUGGAGGCCCUCUCU	MIMAT0000894	0	5.15	290
rno-miR-3594-3p	CACACCGCCUCUGCCCGCUAGU	MIMAT0017899	0	5.15	3594
rno-miR-380-5p	AUGGUUGACCAUAGAACAUGCG	MIMAT0005308	0	5.15	397
rno-miR-130a-5p	GCUCUUUUCACAUUGUGCUACU	MIMAT0017121	0	5.14	130
rno-miR-130b-3p	CAGUGCAAUGAUGAAAGGGCAU	MIMAT0000837	0	1.68	130
rno-miR-501-3p	AAUGCACCCGGGCAAGGAUUUGG	MIMAT0017198	0	4.67	500
rno-miR-500-3p	AAUGCACCUGGGCAAGGGUUCA	MIMAT0005321	0	2.33	500
rno-miR-181b-2-3p	CUCACUGGUCAAUGAAUGCAAA	MIMAT0017140	0	4.66	181
rno-miR-181b-1-3p	CUCACUGAACAAUGAAUGCAA	MIMAT0017139	0	2.01	181
rno-miR-490-5p	CCAUGGAUCUCCAGGUGGGU	MIMAT0017356	0	4.66	490
rno-miR-592	AUUGUGUCAAUAUGCGAUGAUGU	MIMAT0012834	0	4.5	592
rno-miR-193-3p	AACUGGCCUACAAAGUCCCAGU	MIMAT0000868	0	4.45	193
rno-miR-200b-5p	CAUCUUACUGGGCAGCAUUGGA	MIMAT0017152	0	4.04	8
rno-miR-200c-5p	CGUCUUACCCAGCAGUGUUUG	MIMAT0017150	0	3.11	8
rno-miR-200c-3p	UAAUACUGCCGGGUAAUGAUG	MIMAT0000873	0	2.03	8
rno-miR-877	GUAGAGGAGAUGGCGCAGGG	MIMAT0005285	0	3.99	877
rno-let-7b-5p	UGAGGUAGUAGGUUGUGUGGUU	MIMAT0000775	0	3.89	let 7
rno-let-7d-3p	CUAUACGACCUGCUGCCUUUCU	MIMAT0000563	0	2.27	let 7
rno-miR-340-3p	UCCGUCUCAGUUACUUUAUAGCC	MIMAT0000585	0	3.5	340
rno-miR-140-5p	CAGUGGUUUUACCCUAUGGUAG	MIMAT0000573	0	3.48	140
rno-miR-101a-5p	UCAGUUAUCACAGUGCUGAUGC	MIMAT0004726	0	3.47	101
rno-miR-101a-3p	UACAGUACUGUGAUAACUGAA	MIMAT0000823	0	1.59	101
rno-miR-215	AUGACCUAUGAUUUGACAGACA	MIMAT0003118	0	3.43	192
rno-miR-582-5p	UACAGUUGUUCAACCAGUUACU	MIMAT0012833	0	3.38	582
rno-miR-450a-3p	UAUUGGGAACAUUUUGCAUAA	MIMAT0017183	0	3.11	450
rno-miR-450a-5p	UUUUGCGAUGUGUUCCUAAUGU	MIMAT0001547	0	1.6	450
rno-miR-384-5p	UGUAAACAAUUCCUAGGCAAUGU	MIMAT0005309	0	3.11	384

rno-miR-384-3p	AUUCCUAGAAAUUGUUCACAAU	MIMAT0005310	0	1.52	384
rno-miR-185-5p	UGGAGAGAAAGGCAGUUCCUGA	MIMAT0000862	0	3.11	185
rno-miR-1843-5p	UAUGGAGGUCUCUGUCUGACU	MIMAT0024847	0	3.06	1843
rno-miR-488-3p	UUGAAAGGCUGUUUCUUGGUC	MIMAT0005341	0	3.04	488
rno-miR-27a-5p	AGGGCUUAGCUGCUUGUGAGCA	MIMAT0004715	0	2.91	27
rno-miR-3585-5p	UUCACAAGAAGGUGUCUUUCAU	MIMAT0017878	0.01	2.9	506
rno-miR-10b-5p	CCCUGUAGAACCGAAUUUGUGU	MIMAT0000783	0	2.71	10
rno-miR-100-3p	CAAGCUUGUGUCUAUAGGU	MIMAT0017112	0	2.02	10
rno-miR-338-3P	UCCAGCAUCAGUGAUUUUGUUGA	MIMAT0000581	0	2.59	338
rno-miR-484	UCAGGCUCAGUCCCCUCCCGAU	MIMAT0005319	0	2.38	484
rno-miR-667-5P	CGGUGCUGGUGGAGCAGUGAGCAC	MIMAT0017369	0	2.33	667
rno-miR-330-3P	GCAAAGCACAGGGCCUGCAGAGA	MIMAT0000568	0	2.33	330
rno-miR-615	GGGGGUCCCCGGUGCUCGGAUC	MIMAT0012835	0	2.33	615
rno-miR-879-5P	AGAGGCUUAUAGCUCUAAGCC	MIMAT0005287	0	2.25	879
rno-miR-376a-5p	GGUAGAUUCUCCUUCUAUGAG	MIMAT0003197	0	2.16	368
rno-miR-598-3p	UACGUCAUCGUCGUCAUCGUUA	MIMAT0005325	0	2.14	598
rno-miR-144-5p	GGAUAUCAUCAUAUACUGUAAGU	MIMAT0017130	0	2.13	144
rno-miR-666-3p	GGCUGCAGCGUGAUCGCCUGCUC	MIMAT0017371	0	2.07	666
rno-miR-339-5P	UCCCUGUCCUCCAGGAGCUCACG	MIMAT0000583	0	2.04	339
rno-miR-6329	AAUGUGACUCAGCUAUCUGAACA	MIMAT0025068	0	2	6329
rno-miR-214-5p	AGAGUUGUCAUGUGUCU	MIMAT0017159	0	1.98	214
rno-miR-93-3p	ACUGCUGAGCUAGCACUUCCCGA	MIMAT0017109	0	1.97	17
rno-miR-423-5p	UGAGGGGCAGAGAGCGAGACUUUU	MIMAT0017305	0	1.86	423
rno-miR-293-5p	ACUCAAACUGUGUGACACUUU	MIMAT0012847	0	1.82	290
rno-miR-6331	CUUUGGUGGCUUAGUUCUUUGUGC	MIMAT0025070	0	1.81	6331
rno-miR-493-5p	UUGUACAUGGUAGGCUUUCAUU	MIMAT0017217	0	1.8	493
rno-miR-325-3p	UUUAUUGAGCACCUCCUAUCAA	MIMAT0004639	0	1.8	325
rno-miR-541-5p	AAGGGAUUCUGAUGUUGGUCACACU	MIMAT0003177	0	1.8	541
rno-miR-675-3p	UGUAUGCCCUAACCGCUCAGU	MIMAT0017363	0	1.77	675
rno-miR-21-3p	CAACAGCAGUCGAUGGGCUGUC	MIMAT0004711	0	1.73	21
rno-miR-323-3p	CACAUUACACGGUCGACCUCU	MIMAT0000550	0	1.71	154
rno-miR-382-3P	AAUCAUUCACGGACAACACUU	MIMAT0003202	0	1.63	154
rno-miR-341	UCGGUCGAUCGGUCGGUCGGU	MIMAT0000587	0	1.7	341
rno-miR-351-3p	GGUCAAGAGGCGCCUGGGAAC	MIMAT0017041	0	1.69	351
rno-miR-194-5p	UGUAACAGCAACUCCAUGUGGA	MIMAT0000869	0	1.67	194
rno-miR-136-5p	ACUCCAUUUGUUUUGAUGAUGGA	MIMAT0000842	0	1.65	136
rno-miR-210-3p	CUGUGCGUGUGACAGCGGCUGA	MIMAT0000881	0	1.65	210
rno-miR-322-3p	AAACAUGAAGCGCUGCAACA	MIMAT0000547	0	1.64	322
rno-miR-145-3p	GGAUUCCUGGAAAUACUGUUC	MIMAT0017131	0	1.62	145
rno-miR-145-5p	GUCCAGUUUUCCCAGGAAUCCCU	MIMAT0000851	0	1.56	145
rno-miR-136-3p	CAUCAUCGUCUCAAAUGAGUCU	MIMAT0004733	0	1.62	136
rno-miR-125b-2-3p	ACAAGUCAGGCUCUUGGGACCU	MIMAT0026467	0	1.6	10
rno-miR-99b-3p	CAAGCUCGUGUCUGUGGGUCCG	MIMAT0004725	0	1.53	10
rno-miR-6324	UCAGUAGGCCAGACAGCAAGCAC	MIMAT0025063	0	1.6	6324
rno-miR-203a-3p	GUGAAAUGUUUAGGACCACUAG	MIMAT0000876	0	1.59	203
rno-miR-296-3p	GAGGGUUGGGUGGAGGCUCUCC	MIMAT0004742	0	1.59	296
rno-miR-504	AGACCCUGGUCUGCACUCUGUC	MIMAT0012830	0	1.58	504
rno-miR-142-5p	CAUAAAGUAGAAAGCACUACU	MIMAT0000847	0	1.58	142
rno-miR-370-3p	GCCUGCUGGGGUGGAACCUGGU	MIMAT0003122	0	1.55	370
rno-miR-222-3p	AGCUACAUCUGGCUACUGGGU	MIMAT0000891	0	1.55	221
rno-miR-25-3p	CAUUGCACUUGUCUCGGUCUGA	MIMAT0000795	0	1.52	25
rno-miR-433-5P	UACGGUGAGCCUGUCAUUAUUC	MIMAT0017192	0.01	1.52	433

rno-miR-328a-3p	CUGGCCCUCUCUGCCCUUCCGU	MIMAT0000564	0	1.51	328
rno-miR-24-2-5p	GUGCCUACUGAGCUGAAACAGU	MIMAT0005441	0	1.5	24
rno-miR-222-5p	GGCUCAGUAGCCAGUGUAGAU	MIMAT0005287	0.01	1.5	879
rno-miR-217-5P	UACUGCAUCAGGAACUGACUGG	MIMAT0000887	0	1.5	217

Source (191).

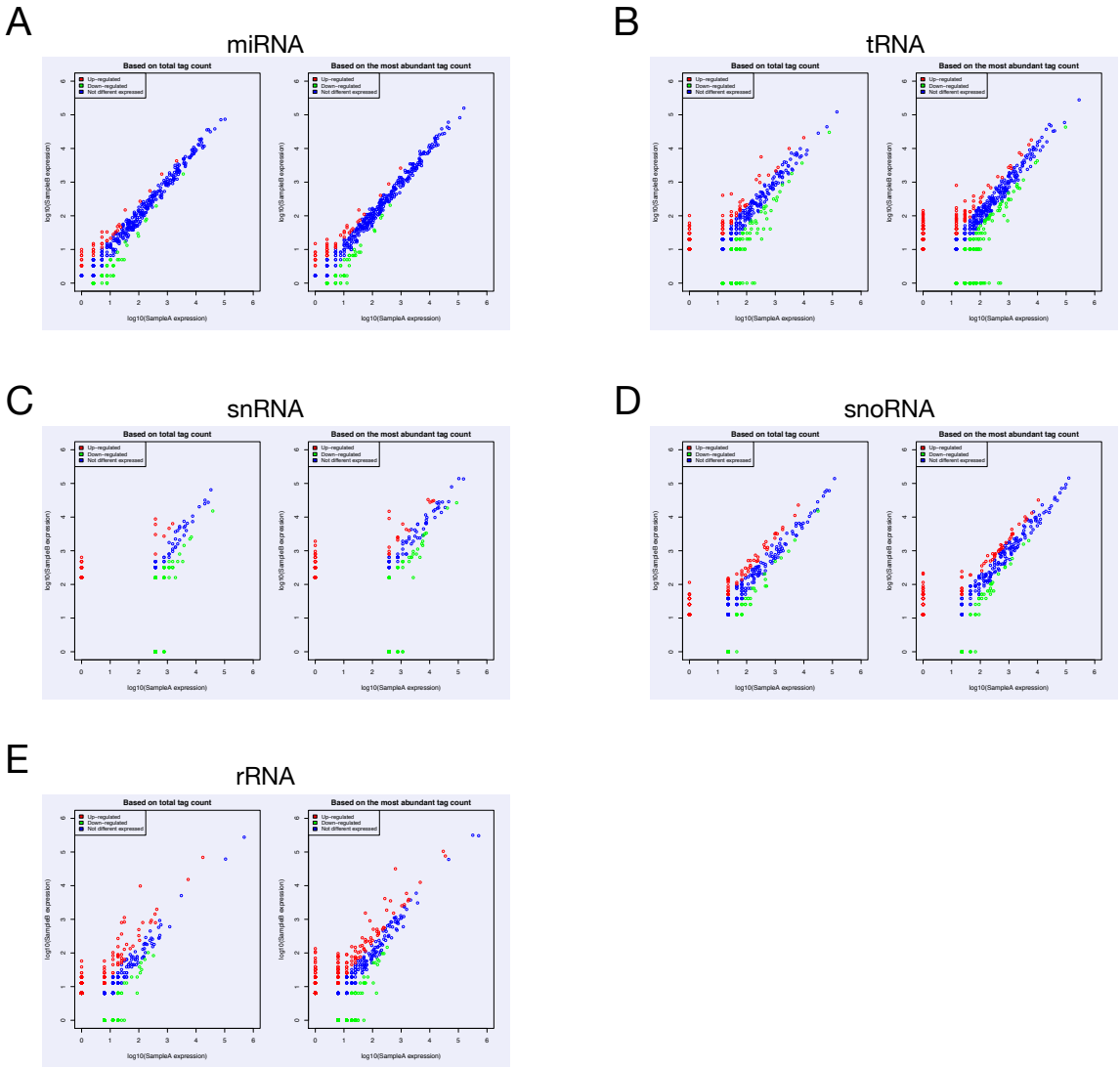

Figure 3.4. Changes in small RNA abundance due to nitrofen. Scatter blots represent the differential expression between nitrofen and control. Left panel: Based on total tag count (pre-normalization) and right panel: based on the most abundant tag count (post normalization) populations were presented for individual small RNA species. The X-axis represents the normalized expression levels of the control, and the scale is log 10. The Y-axis represents the normalized expression levels of nitrofen. Each point in the scatter represents an individual small RNA. The points on both sides on the diagonal line represent a ratio of the normalized expression of nitrofen/ the normalized expression of the control. SnRNA= Small Nuclear RNA, snoRNA=Small Nucleolar RNA.

Table 3.3. Nitrofen-induced differential expression of mRNA.

Up-regulated to Control	Gene symbol	FC	P value	pFDR	Tissue Expression*	NCBI Accession	NCBI Evidence
Epoxide hydrolase 3	EPHX3	159.355	0	0	embryonic, spleen, other tissues	NM_001108988.1	provisional
Pregnancy specific glycoprotein 19	PSG19	17.652	0	0	embryonic, placenta, other tissues	NM_001270654.1	validated
Hepatocyte nuclear factor 4-alpha isoform 1	HNF4A	11.683	0	0	kidney, liver, other tissues	NM_022180.2	validated
Carbonic anhydrase 7	CAR7	7.192	0	0	embryonic, brain, other tissues	NM_001106165.1	provisional
Potassium voltage-gated channel, subfamily H (eag-related), member 7	KCNH7	6.808	0	0	Brain	NM_131912.1.	provisional
ATP synthase, H+ transporting, mitochondrial Fo complex, subunit B1	ATP5F1	5.666	0	0.009	embryonic, lung	NM_134365.2	provisional
Similar to kinesin-like protein (103.5 kD)	KLP-6	5.409	0	0.015	liver	NM_001270385	validated
Ankyrin repeat and sterile alpha motif domain containing 1B	ANKS1B	5.218	0	0.005	adult, brain	NM_001271371	provisional
Biphenyl hydrolase-like (serine hydrolase), breast epithelial mucin-associated antigen	BPHL	4.996	0	0.024	adult, lung	NM_001037206.1	validated
Calcyphosine-like	CAPSL	4.792	0	0.04	adult, lung	NM_001106417.1	provisional
CD99 molecule-like 2	CD99	4.138	0	0.019	embryonic, adult, lung	NM_134459.1	provisional
Ribosomal protein S19	RPS19	3.617	0	0.003	adrenal, brain, other tissues	NM_001037346.2.	provisional
Wingless-type MMTV integration site family, member 3	WNT3	3.229	0	0.038	adult, brain, other tissues	NM_001105715.1.	validated
Thymidine phosphorylase	TYMP	3.173	0.001	0.152	juvenile, adult, lung	NM_001012122.1.	provisional
Myosin VIIb	MYO7B	3.14	0	0.065	liver, colon, other tissues	NM_001191941.1	provisional
MORN repeat containing 1	MORN1	3.103	0.002	0.2	liver, kidney, brain, other tissues	NM_001005544.1.	inferred
Pygopus 2	PYGO2	3.082	0	0.005	embryonic, lung	NM_001106447.1.	provisional
Transmembrane protein 205	TMEM205	3.068	0	0.332	pancreas, liver	NM_001106804.1.	provisional
Ceroid-lipofuscinosis, neuronal 3	CLN3	3.062	0.002	0.206	juvenile, adult, lung	NM_001006971.1.	provisional
Transketolase-like 1	TKTL1	2.998	0	0.079	testis, other tissues	NM_001109534.1	provisional
Mitochondrial intermediate peptidase	MIP	2.955	0.003	0.267	embryonic, lung	NM_031052.1.	provisional
Growth arrest and DNA-damage-inducible, gamma	GADD45G	2.893	0	0.063	adult, lung	NM_001077640.1.	validated

Fibroblast growth factor receptor 4	FGFR4	2.883	0.001	0.134	juvenile, adult, lung	NM_001109904.1.	provisional
Coagulation factor III (thromboplastin, tissue factor)	F3	2.883	0	0.033	juvenile, adult, lung	NM_013057.2.	validated
ATPase, Ca++ transporting, plasma membrane 2	ATP2B2	2.802	0.001	0.111	brain, eye, other tissues	NM_012508.5.	provisional
Dynein, axonemal, light chain 1	DNAL1	2.791	0.001	0.121	kidney, eye, brain, other tissues	NM_001109477.2.	provisional
Phosphodiesterase 1B, calmodulin-dependent	PDE1B	2.734	0.003	0.267	adipose, brain, other tissues	NM_022710.1.	validated
2-aminoethanethiol (cysteamine) dioxygenase	ADO	2.674	0.003	0.27	eye, other tissues	NM_001107626.2.	provisional
Growth differentiation factor 6	GDF6	2.665	0.006	0.377	eye, other tissues	NM_001013038.1.	validated
Tektin 1	TEKT1	2.661	0	0.088	juvenile, adult, lung	NM_053508.2.	provisional
Growth arrest and DNA-damage-inducible, beta	GADD45B	2.61	0.003	0.258	juvenile, adult, lung	NM_001008321.1.	predicted
Fin bud initiation factor homolog (zebrafish)	FIBIN	2.603	0.001	0.157	juvenile, adult, lung	NM_001025042.2.	provisional
Paired related homeobox 2	PRRX2	2.593	0	0.079	adult, brain, other tissues	NM_001105739.1.	validated
Mannan-binding lectin serine peptidase 1	MASP1	2.59	0.004	0.293	adipose, brain, other tissues	NM_022257.1.	provisional
Chemokine (C-X-C motif) ligand 2	CXCL2	2.577	0.001	0.134	adult, connective tissues, other tissues	NM_053647.1	provisional
Ribosomal protein S2	RPS28	2.573	0	0.066	adult, lung	NM_001105730.1.	provisional
Family with sequence similarity 213, member B	FAM213B	2.551	0.001	0.157	heart, prostate, other tissues	NM_001108697.1	provisional
Aldehyde dehydrogenase family 1, subfamily A7	ALDH1A7	2.546	0.003	0.258	adult, lung	NM_017272.15.	provisional
Transmembrane protein 243, mitochodrial	TMEM243	2.486	0.007	0.395	juvenile, adult, lung	NM_001109219.1.	provisional
Cholesterol 25-hydroxylase	CH25H	2.454	0.005	0.352	adult, lung	NM_001025415.1.	provisional
Nucleolar protein 3 (apoptosis repressor with CARD domain	NOL3	2.452	0.007	0.389	juvenile, adult, lung	NM_053516.2	provisional
BTB (POZ) domain containing 16	BTBD16	2.447	0.009	0.45	adult, lung	NM_001017464.2.	provisional
LSM domain containing 1	LSMD1	2.41	0.001	0.134	brain, connective tissues, other tissues	NM_001105794.2.	provisional
Dicarbonyl L-xylulose reductase	DCXR	2.392	0.009	0.45	eye, heart	NM_134387.1.	validated
Tctex1 domain containing 2	TCTEX1D2	2.373	0.001	0.149	braine, kidney, other tissues	NM_001109054.1.	provisional
Coiled-coil domain containing 126	Ccdc126	2.349	0.003	0.237	embryonic, adult, lung	NM_001109232.2	provisional
Acyl-CoA synthetase bubblegum family member 2	ACSBG2	2.317	0.006	0.368	Testis	NM_001080096.1.	provisional
Ankyrin repeat domain 37	ANKRD37	2.316	0.005	0.352	connective tissue, eye	NM_001108400.2.	provisional
Cytochrome c oxidase subunit VIb polypeptide 2	COX6B2	2.298	0.006	0.366	brain, nerve, other tissues	NM_001039085.1.	provisional
Kelch domain containing 8A	KLHDC8A	2.29	0.001	0.113	brain, connective tissues, other tissues	NM_001100683.1.	validated
Zinc finger protein 13	ZFP13	2.275	0.007	0.411	Kidney	NM_001105765.1.	validated
AlkB, alkylation repair homolog 7	ALKBH7	2.268	0.005	0.352	brain, connective tissues, other tissues	NM_001109384.1.	provisional

Acetylserotonin O-methyltransferase-like	ASMTL	2.258	0.007	0.389	adipose, brain, other tissues	NM_001105915.2.	provisional
Syntaxin binding protein 6	STXBP6	2.252	0.005	0.352	embryonic, adult, lung	NM_001191872.1.	validated
SLIT and NTRK-like family, member 5	SLITRK5	2.25	0.001	0.134	Brain	NM_001107284.1.	provisional
Autophagy related 16-like 2 (S. cerevisiae)	ATG16l2	2.234	0.009	0.46	brain, liver	NM_001191560.1.	provisional
Ribosomal protein S12	RPS12	2.233	0.001	0.135	juvenile, adult, lung	NM_031709.3.	inferred
ATP synthase, H+ transporting, mitochondrial Fo complex, subunit E	ATP5I	2.222	0.001	0.152	fetus, juvenile, adult, lung	NM_080481.1.	validated
Ankyrin repeat domain 16	ANKRD16	2.212	0.009	0.45	brain, prostate	NM_001033698.1.	predicted
Mitochondrial ribosomal protein S25	MRPS25	2.208	0.002	0.191	brain, ganglion	NM_001025408.1.	provisional
Phosphopantothenoylcysteine synthetase	PPCS	2.206	0.005	0.352	brain, ganglion	NM_001039010.2	provisional
Histone cluster 1, H2aa	HIST1H2AA	2.194	0.003	0.267	mammalian spermatogenesis	NM_021839.1.	validated
Family with sequence similarity 111, member A	FAM111A	2.188	0.001	0.156	fetus, juvenile, adult, lung	NM_001109163.1.	provisional
Coiled-coil domain containing 150	CCDC150	2.168	0.005	0.332	unknown	NM_001191806.1.	provisional
Ribosomal protein L35a	RPL35A	2.141	0.003	0.237	embryonic, fetus, juvenile, adult, lung	NM_021264.3.	inferred
Cytochrome c oxidase assembly factor 4	COA4	2.136	0.004	0.321	brain, adrenal	NM_001127655.1	provisional
DCN1, defective in cullin neddylation 1, domain containing 2 (S. cerevisiae)	DCUN1D2	2.102	0.007	0.389	brain, connective tissues	NM_001134798.1.	predicted
Tankyrase, TRF1-interacting ankyrin-related ADP-ribose polymerase 2	TNKS2	2.099	0.007	0.395	embryonic, fetus, juvenile, adult, lung	NM_001107607.2.	inferred
Nucleotide binding protein-like	NUBPL	2.089	0.005	0.352	kidney, other tissues	NM_001185025.1	provisional
Thiopurine S-methyltransferase	TPMT	2.075	0.01	0.46	embryonic, adult, lung	NM_001079531.1	validated
Inhibitor of DNA binding 4	ID4	2.071	0.006	0.376	embryonic, juvenile, adult, lung	NM_175582.1	provisional
DNA-damage inducible transcript 3	DDIT3	2.071	0.006	0.386	juvenile, adult, lung	NM_024134.2	provisional
Ring finger protein 113A1	RNF113A1	2.067	0.006	0.386	brain, connective tissues, other tissues	NM_001014791.1.	validated
Gamma-aminobutyric acid (GABA) B receptor 2	GABBR2	2.051	0.004	0.29	brain, testis	NM_031802.1.	provisional
Centromere protein K	CENPK	2.029	0.006	0.376	brain, adrenal	NM_001106407.1.	provisional
Ribosomal protein L36	RPL36	2.029	0.005	0.363	brain, adrenal	NM_022504.1.	provisional
Ribosomal protein S3a	RPS3A	2.014	0.004	0.304	embryonic, fetus, juvenile, adult, lung	NM_017153.1	provisional
Phosphodiesterase 12	PDE12	2.014	0.007	0.411	adult, juvenile, lung	NM_001013998.2	provisional
Docking protein 1	DOK1	2.008	0.01	0.46	brain, connective tissues, other tissues	NM_001025416.1	provisional
Proteasome (prosome, macropain) subunit, alpha type 6	PSMA6	2.007	0.004	0.328	fetus, juvenile, adult, lung	NM_017283.3.	provisional

Protocadherin gamma subfamily B, 5	PCDHGA8	0.498	0.006	0.375	embryonic, fetus, juvenile, adult, lung	NM_001012215.1	provisional
Leucine rich repeat neuronal 1	LRRN1	0.497	0.01	0.46	adult, juvenile, lung	NM_001037363.1	provisional
Signal-regulatory protein alpha	SIRPA	0.491	0.01	0.46	embryonic, juvenile, adult, lung	NM_013016.2.	provisional
Zinc finger and BTB domain containing 25	ZBTB25	0.489	0.007	0.411	prostate, spleen	NM_199496.1.	provisional
Bromodomain adjacent to zinc finger domain, 2A	BAZ2A	0.487	0.005	0.352	embryonic, juvenile, adult, lung	NM_001107158.1.	provisional
Actin, gamma 2, smooth muscle, enteric	ACTG2	0.486	0.005	0.36	embryonic, juvenile, adult, lung	NM_012893.1.	provisional
Abhydrolase domain containing 2	ABHD2	0.484	0.005	0.352	embryonic, fetus, juvenile, adult, lung	NM_001106275.1	provisional
Transforming growth factor, beta receptor III	TGFBR3	0.484	0.008	0.415	adult, lung	NM_017256.1.	provisional
Apolipoprotein L, 3	APOL3	0.477	0.006	0.388	adult, juvenile, lung	NM_001013175.1.	provisional
Protocadherin 20	PCDH20	0.472	0.004	0.293	brain, heart	NM_001107280.1	provisional
Roundabout, axon guidance receptor, homolog 1 (Drosophila)	ROBO1	0.471	0.003	0.266	brain, ganglion	NM_022188.1	provisional
1-acylglycerol-3-phosphate O-acyltransferase 1	AGPAT1	0.469	0.006	0.389	adipose, brain	NM_212458.1	provisional
Protocadherin 12	PCDH12	0.468	0.003	0.266	juvenile, lung	NM_053944.1.	validated
Rap1 GTPase-activating protein	RAP1GAP	0.466	0.009	0.46	embryonic, juvenile, adult, lung	NM_001100713.1	validated
CDGSH iron sulfur domain 3	CISD3	0.462	0.009	0.452	brain, colon	NM_001105835.1	validated
Potassium voltage-gated channel, Shal-related subfamily, member 3	KCND3	0.462	0.003	0.267	adult, lung	NM_031739.3	provisional
Guanine nucleotide binding protein, alpha 14	GNA14	0.461	0.009	0.46	adult, lung	NM_001013151.1	validated
Porcupine homolog (Drosophila)	PORCN	0.46	0.006	0.376	juvenile, adult, lung	NM_001173355.1.	provisional
R3H domain containing 1	R3HDM1	0.459	0.002	0.228	adipose, brain	NM_001134867.1.	validated
Netrin 4	NTN4	0.459	0.01	0.46	kidney, other tissues	NM_001106780.1	provisional
Proline and serine rich 1	PROSER1	0.459	0.007	0.389	juvenile, adult, lung	NM_001107676.1.	provisional
ADP-ribosyltransferase 4 (Dombrock blood group)	ART4	0.458	0.004	0.304	embryonic, adult, lung	NM_001173509.1.	provisional
Adenylate cyclase 5	ADCV5	0.457	0.007	0.411	embryonic, juvenile, adult, lung	NM_022600.1	validated
Leucine rich repeat containing 9	LRRC9	0.456	0.008	0.415	Eye	NM_001191613.1.	provisional
Glucosaminyl (N-acetyl) transferase 2, I-branching enzyme	GCNT2	0.453	0.01	0.46	adult, lung	NM_001001511.2.	provisional
Aquaporin 1	AQP1	0.452	0.003	0.267	embryonic, juvenile, adult, lung	NM_012778.1.	provisional
Trafficking protein, kinesin binding 1	TRAK1	0.452	0.002	0.218	brain, connective tissues	NM_001134565.1.	provisional
Phosphate regulating endopeptidase homolog, X-linked	PHEX	0.45	0.002	0.237	muscle, connective tissues	NM_013004.1.	provisional

Eukaryotic translation initiation factor 4E family member 3	EIF4E3	0.448	0.004	0.314	juvenile, adult, lung	NM_001106612.1.	provisional
AarF domain containing kinase 2	ADCK2	0.447	0.004	0.29	adult, lung	NM_001107855.1.	provisional
Coiled-coil domain containing 67	CCDC67	0.446	0.007	0.407	juvenile, adult, lung	NM_001014087.1	provisional
Wolfram syndrome 1 (wolframin)	WFS1	0.446	0.009	0.46	embryonic, juvenile, adult, lung	NM_031823.1.	validated
Protein tyrosine phosphatase, receptor type, C	PTPRC	0.445	0.005	0.352	embryonic, juvenile, adult, lung	NM_138507.2	provisional
Kelch-like family member 31	KLHL31	0.445	0.006	0.388	heart, nerve	NM_001108170.1.	validated
Phospholipase C, gamma 2	PLCG2	0.441	0.002	0.206	adipose, connective	NM_017168.1.	unknown
IKAROS family zinc finger 2	IKZF2	0.44	0.009	0.454	Eye	NM_001106916.1.	provisional
Nhibin beta-A	INHBA	0.44	0.006	0.375	connective tissues	NM_017128.2	provisional
Zinc finger, MIZ-type containing 2	ZMIZ2	0.439	0.009	0.45	embryonic, juvenile, adult, lung	NM_001100507.1.	validated
TOX high mobility group box family member 3	TOX3	0.438	0.003	0.27	embryonic, adult, lung	NM_001106171.1	validated
Chloride intracellular channel 5 (Clic5), nuclear gene encoding mitochondrial protein	CLIC5	0.436	0.007	0.389	embryonic, fetus, juvenile, adult, lung	NM_053603.2.	provisional
Inositol-trisphosphate 3-kinase B	ITBKP	0.435	0.004	0.321	brain, heart	NM_019312.2.	validated
Dual-specificity tyrosine-(Y)-phosphorylation regulated kinase 3	DVRK3	0.432	0.004	0.321	brain, heart	NM_001024767.1	validated
Myosin, heavy chain 11, smooth muscle	MYH11	0.432	0.001	0.111	embryonic, fetus, juvenile, adult, lung	NM_001170600.1.	provisional
Forkhead box N3	FOXN3	0.428	0.001	0.133	brain, colon	NM_001108047	provisional
Smooth muscle alpha-actin	ACTA2	0.428	0.001	0.129	embryonic, fetus, juvenile, adult, lung	NM_019183.1.	provisional
FCH and double SH3 domains 1	FCHSD1	0.426	0.001	0.151	brain, connective tissues	NM_001109881.1	validated
AT hook, DNA binding motif, containing 1	AHDC1	0.424	0.001	0.113	nerve, ovary	NM_001134956.1.	inferred
SLIT-ROBO Rho GTPase activating protein 1	SRGAP1	0.424	0.002	0.163	pituitary	NM_001191784.1.	provisional
Calponin 1, basic, smooth muscle	CNN1	0.419	0.001	0.118	embryonic, juvenile, adult, lung	NM_031747.1	provisional
Nucleolar protein 4	NOL4	0.416	0.01	0.46	brain, testis	NM_001107401.1.	provisional
Neuroblastoma 1, DAN family BMP antagonist	NBL1	0.416	0.005	0.352	adult, juvenile, lung	NM_031609.1	provisional
Protocadherin beta 20	PCDHB20	0.416	0.004	0.317	pancreas	NM_001109395.1	provisional
WNK lysine deficient protein kinase 2	WNK2	0.416	0.003	0.268	brain-connective tissues	NM_001191556.1.	provisional
Sprouty homolog 4 (Drosophila)	SPRV4	0.416	0.002	0.218	adult, lung	NM_001106150.1	provisional
Phosphatidylinositol-4-phosphate 3-kinase, catalytic subunit type 2 beta	PIK3C2B	0.415	0.001	0.134	embryonic, placenta	NM_001105951.1.	provisional
Zinc finger protein 777	ZFP777	0.409	0.001	0.141	embryonic, adult, lung	NM_001109348.1	provisional

MicroRNA mir-671	MIR671	0.405	0.01	0.46	unknown	NR_032287.1	provisional
PYD and CARD domain containing	PVCARD	0.405	0.01	0.46	juvenile, adult, lung	NM_172322.1.	unknown
Zyxin	ZYX	0.405	0	0.074	embryonic, fetus, juvenile, adult, lung	NM_053761.1.	provisional
Chromatin licensing and DNA replication factor 1	CDT1	0.399	0.001	0.118	embryonic, juvenile, adult, lung	NM_001106192.1.	validated
Ring finger protein 44	RNF44	0.398	0.001	0.156	embryonic, fetus, juvenile, adult, lung	NM_001024795.1.	provisional
Rho GTPase activating protein 20	ARHGAP20	0.398	0.002	0.212	brain, eye	NM_213629.1.	provisional
Ring finger protein 26	RNF26	0.398	0.001	0.156	brain, ganglion	NM_001113748.1	provisional
Stam binding protein	STAMBP	0.396	0.005	0.352	juvenile, adult, lung	NM_138531.2.	provisional
Fatty acid synthase	FAS	0.394	0.002	0.175	embryonic, fetus, juvenile, adult, lung	NM_017332.1.	provisional
Prostate androgen-regulated mucin-like protein 1	PARM1	0.393	0.01	0.46	heart, eye	NM_173114.1.	provisional
Tropomodulin 1	TMOD1	0.393	0.002	0.202	embryonic, fetus, juvenile, adult, lung	NM_013044.2	provisional
Sodium channel, voltage gated, type VIII, alpha subunit	SCN8A	0.39	0.001	0.121	dorsal, brain, other tissues	NM_019266.2.	provisional
UDP-GlcNAc:betaGal beta-1,3-N-acetylglucosaminyltransferase 7	B3GNT7	0.387	0.004	0.321	colon, heart, other tissues	NM_001012134.1.	provisional
Family with sequence similarity 210, member B	FAM210B	0.382	0	0.079	embryonic, juvenile, adult, lung	NM_001106547.2.	provisional
Glycoprotein (transmembrane) nmb	GPNMB	0.381	0.003	0.27	juvenile, adult, lung	NM_133298.1	provisional
Sulfotransferase family, cytosolic, 1C, member 3	SULT1C3	0.378	0	0.066	liver	NM_031732.2.	provisional
Dehydrogenase/reductase (SDR family) member 3	DHRS3	0.378	0	0.033	juvenile, adult, lung	NM_001037199.3.	provisional
Mastermind like 1 (Drosophila)	MAML1	0.377	0	0.065	adipose, connective tissues, other tissues	NM_001106997.1.	provisional
Gremlin 2	GREM2	0.372	0.001	0.111	adult, lung	NM_001105974.1.	provisional
G protein-coupled receptor 155	GPR155	0.369	0.004	0.293	fetus, juvenile, adult, lung	NM_001107811.1	provisional
Sprouty-related, EVH1 domain containing 2	SPRED2	0.36	0.001	0.134	Brain	NM_001047094.1	provisional
Tetratricopeptide repeat domain 38	TTC38	0.358	0.001	0.107	heart, kidney	NM_001130499.1	provisional
Protein kinase, AMP-activated, alpha 2 catalytic subunit	PRKAA2	0.351	0	0.062	brain, ganglion	NM_023991.1.	provisional
Guanine nucleotide binding protein (G protein), alpha z polypeptide	GNAZ	0.344	0.001	0.139	brain, pancreas	NM_013189.2	provisional
Inhibin alpha	INHA	0.341	0.001	0.118	colon, connective tissues	NM_012590.2	provisional
Cytochrome P450, family 26, subfamily b, polypeptide 1	CYP26B1	0.34	0	0.051	embryonic, adult, lung	NM_181087.2.	provisional
ATP-binding cassette, subfamily C (CFTR/MRP), member 2 (Abcc2)	CFTR	0.337	0	0.033	brain, kidney	NM_012833.1	provisional

Lymphoid enhancer binding factor 1	LEF1	0.336	0.001	0.113	embryonic, juvenile, adult, lung	NM_130429.1	provisional
Mir451 microRNA mir-451	MIR451	0.335	0.001	0.138	unknown	unknown	provisional
Transcribed locus, strongly similar to NP_714942.1 Itgb3 gene product	ITAB3	0.333	0	0.033	Testis	UniGene 1829900	unknown
Serine (or cysteine) peptidase inhibitor, clade B, member 6b	SERPINB6B	0.329	0.001	0.134	fetus, juvenile, adult, lung	NM_001012214.1.	unknown
Myosin, light chain 2, regulatory, cardiac, slow	MYL2	0.328	0.001	0.12	embryonic, eye	NM_001035252.2	provisional
Calsequestrin 2 (cardiac muscle)	CASQ2	0.326	0	0.02	embryonic, juvenile, adult, lung	NM_017131.2	provisional
Nuclear receptor subfamily 5, group A, member 2	NR5A2	0.326	0	0.056	fetus, adult, lung	NM_021742.1	validated
1-acylglycerol-3-phosphate O-acyltransferase 9	AGPAT9	0.32	0	0.051	adipose, liver	NM_001025670.1.	provisional
ArsA arsenite transporter, ATP-binding, homolog 1 (bacterial)	ARSA	0.318	0	0.04	juvenile, adult, lung	NM_001100505.1.	provisional
Cortexin 1	CTXN1	0.318	0	0.078	embryonic, brain	NM_001109935.1	validated
Charged multivesicular body protein 4C	CHMP4c	0.318	0	0.047	adult, lung	NM_001017466.2	validated
Musculoskeletal, embryonic nuclear protein 1	MUSTN1	0.315	0.001	0.107	embryonic, brain	NM_181368.3.	validated
Spire homolog 2 (Drosophila)	SPIRE2	0.303	0	0.04	brain, pancreas	NM_001127538.1	provisional
Solute carrier family 29 (nucleoside transporters), member 3	SLC29A3	0.299	0	0.091	fetus, juvenile, adult, lung	NM_181639.3.	provisional
Aldo-keto reductase family 1, member C14	AKR1C14	0.295	0	0.066	fetus, juvenile, adult, lung	NM_138547.2.	provisional
Aldehyde dehydrogenase 1 family, member L2	ALDH1L2	0.287	0	0.017	adipose, brain, other tissues	NM_001191778.1	provisional
Lecithin-retinol acyltransferase (phosphatidylcholine-retinol-O-acyltransferase)	LRAT	0.283	0	0.005	fetus, adult, lung	NM_022280.2.	provisional
Erythrocyte membrane protein band 4.9 (dematin)	EPB49	0.268	0	0.024	brain, ganglion	NM_001108385.1	provisional
Cholinergic receptor, nicotinic, alpha 4 (neuronal)	CHRNA4	0.204	0	0.017	Brain	NM_024354.1.	provisional
Wnt inhibitory factor 1	WIF1	0.2	0	0.005	embryonic, juvenile, adult, lung	NM_053738.1	provisional
Family with sequence similarity 189, member B	FAM189B	0.184	0	0.006	heart, dorsal ganglion	NM_001107690.1	predicted
Coiled-coil domain containing 60	CCDC60	0.112	0	0	Testis	NM_001034945.1	provisional
Down syndrome cell adhesion molecule-like 1	DSCAML1	0.105	0	0	brain, eye	NM_001108141.1.	provisional

pFDR=Alpha associated with False Discovery Rate; NCBI= National Center for Biotechnology Information; NM= NCBI identification number of mRNA (191).

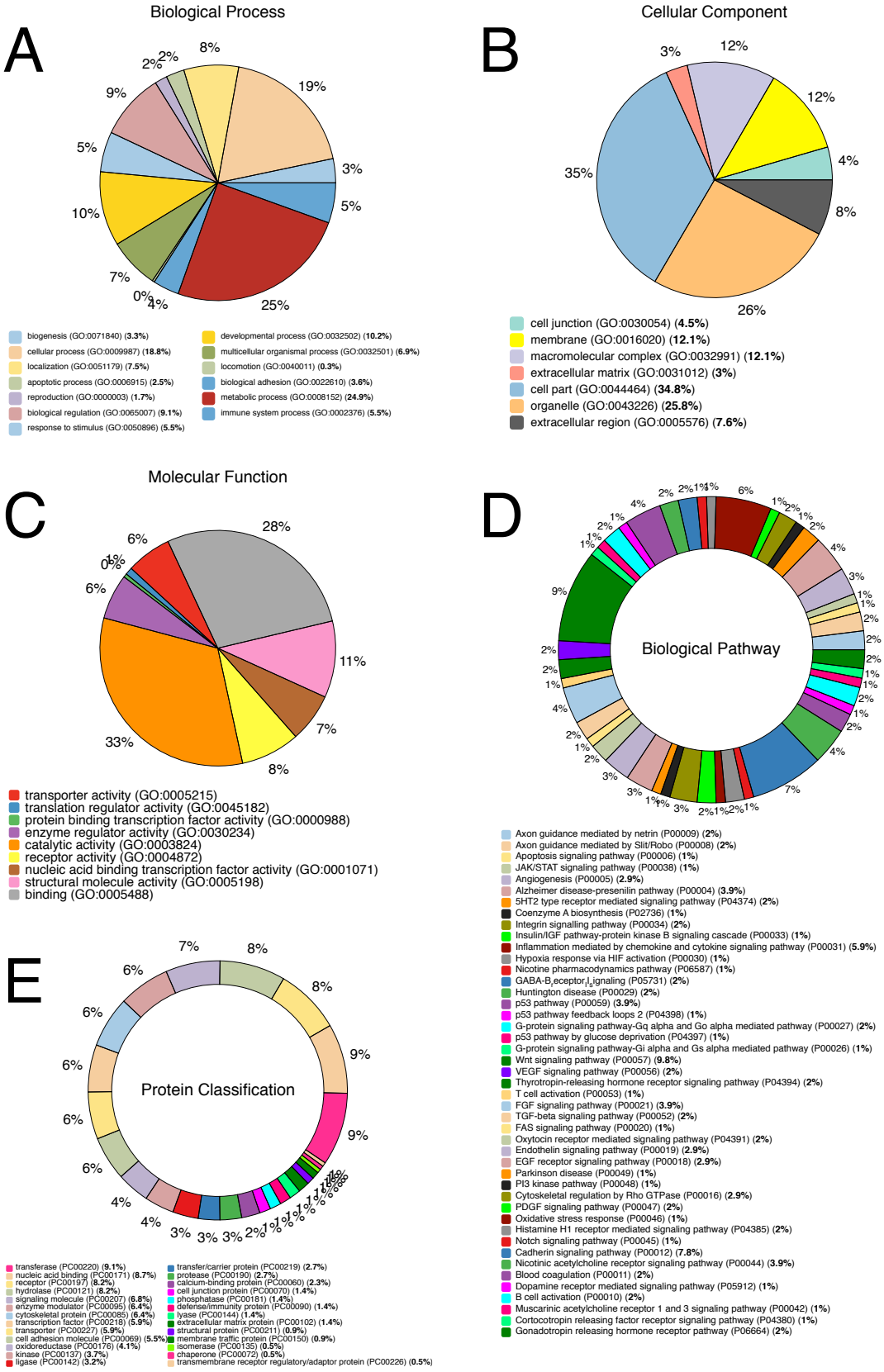

Figure 3.5. Transcript gene functional analysis was conducted using the PANTHER GO database. GO has been categorized into A) biological processes, B) cellular components, C) molecular function, D) biological pathways, and E) protein classification (191).

identified several signaling pathways including cell survival mechanisms, lipid metabolism, cellular movement and more tissue-specific mechanisms such as connective tissue development. Using PANTHER transcript classification, processes such as metabolism, protein binding, catalytic activity, WNT signaling pathway and protein functions such as transferase activity and nucleic acid binding were most apparent. Using a binomial distribution and logarithmic (Log2) conversion of the gene expression data, genes were entered into KEGG (200) and set to a binomial distribution of expression (upregulation, red, downregulation, green). Pathways of significant interest included WNT, TGF-β signaling and retinol metabolism (Figure 3.6). I grouped the identified miRNAs on the basis of their sequence similarity into 83 families (Table 3.4). Sequence comparison revealed 64 human orthologs to previously described rat miRNAs (mirBase release 21 (201)) (Table 3.5). I identified 10 miRNA families with at least 10 sequence reads at the embryonic stage in human that are potentially relevant to the nitrofen-induced lung pathology in the rat (Figure 3.7). I identified 19 putative interacting miRNA–mRNA pairs highly relevant to nitrofen-induced lung development (Table 3.6). This linkage between miRNAs and mRNA was also statistically linked using IPA software.

3.4.3. Nitrofen-induced changes in miRNA expression affect gene transcription

From the differentially expressed miRNAs and mRNA genes, I identified 78 differentially correlated pairs of miRNAs and mRNAs. The assessment of miRNA and mRNA expression levels revealed significant positive and negative correlations in 8 and 11% of the identified pairs, respectively (Table 3.5). The correlations suggest

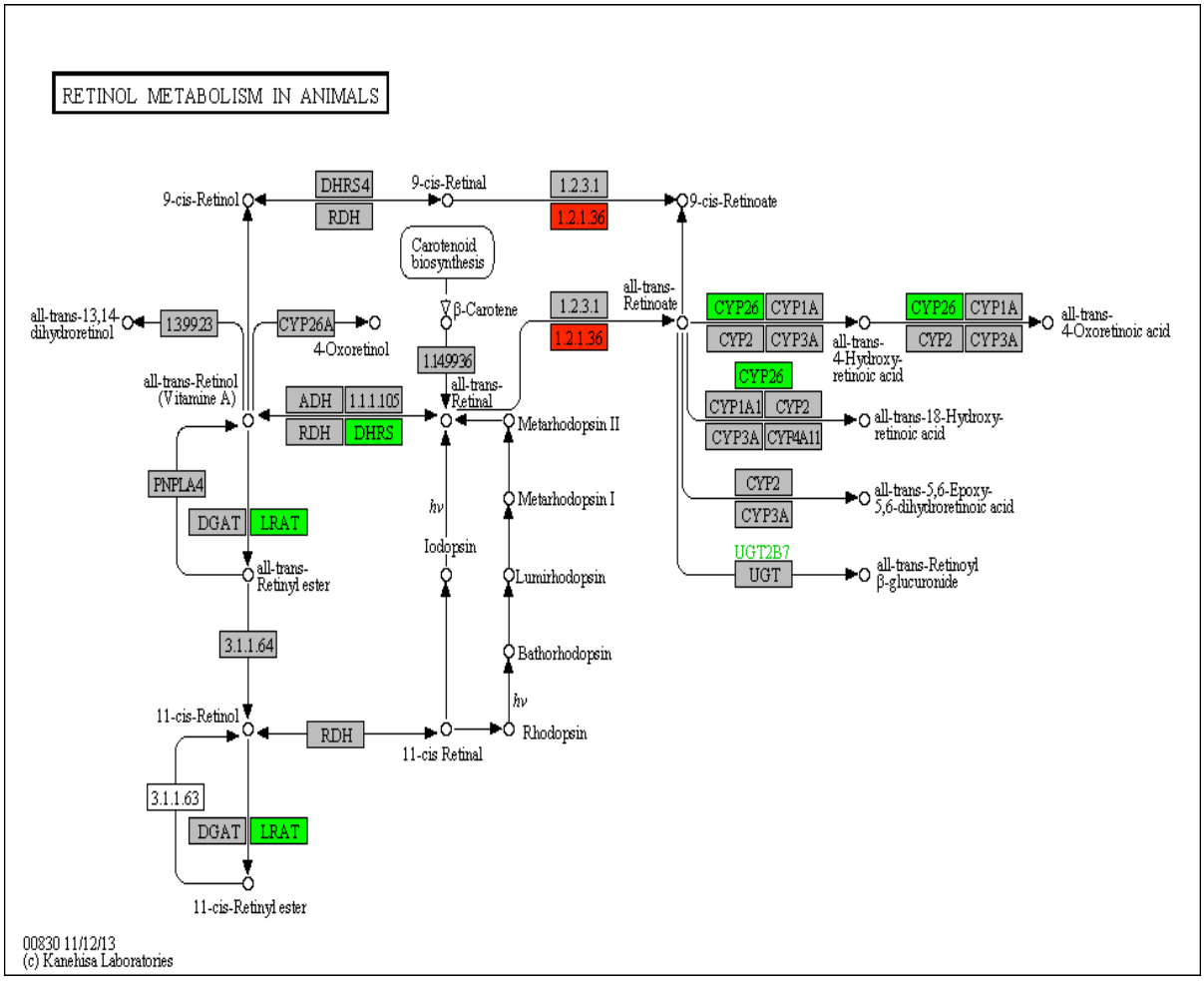

Figure 3.6. Gene expression analysis comparing control and nitrofen-treated rat embryonic lungs as conducted through KEGG. Differentially expressed genes and enzymes are binomially labeled based upon their expression. Green indicates downregulated compared to control, while red indicates genes which are upregulated in the nitrofen-treated samples. Reprinted with permission from KEGG/Genome Net (http://www.kegg.jp/pathway/map00830) (191).

Table 3.4. Multiple sequence alignments and structure conservation of functionally relevant embryonic and fetal miRNA ortholog sequences cross species. CLUSTAL format for T-COFFEE version 6.92 [http://www.tcoffee.org]. Sequence conservation is represented by asterisks and shaded red, mature miRNAs are underlined. Species ID are provided by mirOrtho database.

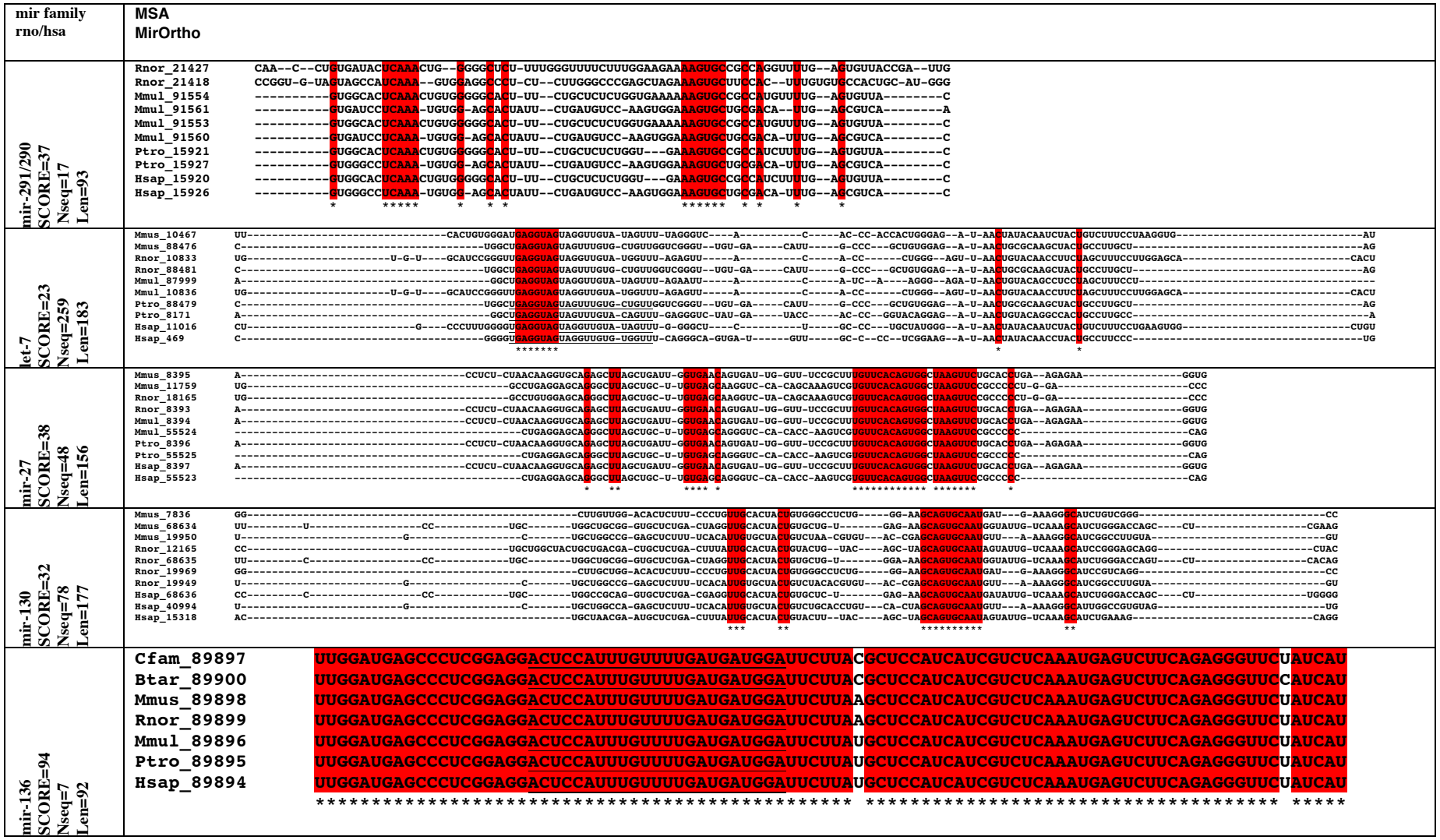

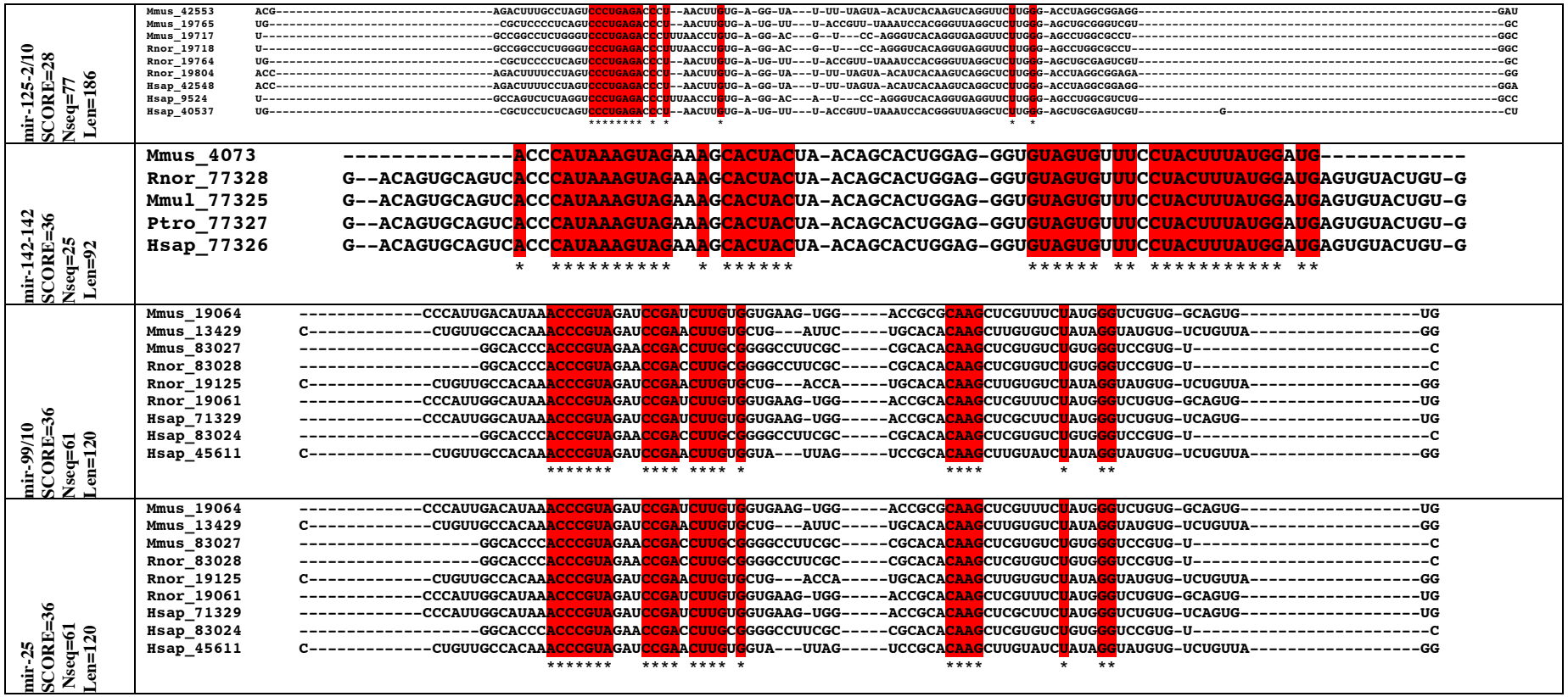
mir-125-2/10
SCORE=28
Nseq=77
Len=186
mir-142-142
SCORE=36
Nseq=25
Len=92
mir-99/10
SCORE=36
Nseq=61
Len=120
mir-25
SCORE=36
Nseq=61
Len=120

Source (191).

Table 3.5. Pairwise sequence identity of rat and human miRNA orthologs. The pairwise sequence identity of homologs is constructed for mature miRNAs. Among 84 identified families, the highest scores were presented.

No.	Fold	mirBase ID (rno)	Score (mirBase)	evalue (mirBase) Cutoff 10	Pairwise Alignment Number of comparisons =100 Search algorithm BLASTN Mismatch Penalty -4
1	8.29	rno-miR-136-5p	115	2e-04	**UserSeq 1 acuccauuuguuuugaugaugga 23** |||||||||||||||||||||||| **hsa-miR-136-5p 1 acuccauuuguuuugaugaugga 23**
2	8.29	rno-miR-135b-3p	110	6e-04	**UserSeq 1 auguagggcuaaaagccauggg 22** |||||||||||||||||||||||| **hsa-miR-135b-3p 1 auguagggcuaaaagccauggg 22**
3	6.2	rno-miR-377-5p	110	5e-04	**UserSeq 1 agagguugcccuuggugaauuc 22** |||||||||||||||||||||||| **hsa-miR-377-5p 1 agagguugcccuuggugaauuc 22**
4	6.2	rno-miR-370-5p	110	6e-04	**UserSeq 1 caggucacgucucugcaguuac 22** |||||||||||||||||||||||| **hsa-miR-370-5p 1 caggucacgucucugcaguuac 22**
5	5.78	rno-miR-132-3p	110	5e-04	**UserSeq 1 uaacagucuacagccauggucg 22** |||||||||||||||||||||||| **hsa-miR-132-3p 1 uaacagucuacagccauggucg 22**
6	5.15	rno-miR-216b-3p	110	5e-04	**UserSeq 1 aaaucucugcaggcaaauguga 22** |||||||||||||||||||||||| **hsa-miR-216b-5p 1 aaaucucugcaggcaaauguga 22**
7	5.15	rno-miR-380-5p	105	0.001	**UserSeq 2 ugguugaccauagaacaugcg 22** |||||||||||||||||||||| **hsa-miR-380-5p 1 ugguugaccauagaacaugcg 21**
8	4.67	rno-miR-501-3p	100	0.003	**UserSeq 1 aaugcacccgggcaaggauu 20** |||||||||||||||||||| **hsa-miR-501-3p 1 aaugcacccgggcaaggauu 20**
9	4.5	rno-miR-592	110	6e-04	**UserSeq 2 uugugucaauaugcgaugaugu 23** |||||||||||||||||||||||| **hsa-miR-592 1 uugugucaauaugcgaugaugu 22**
10	4.45	rno-miR-193-3p	110	5e-04	**UserSeq 1 aacuggccuacaaagucccagu 22** |||||||||||||||||||||||| **hsa-miR-193a-3p 1 aacuggccuacaaagucccagu 22**
11	4.04	rno-miR-200b-5p	110	5e-04	**UserSeq 1 gagcuuuuggcccgggguuauac 22** |||||||||||||||||||||||| **hsa-miR-208a-5p 1 gagcuuuuggcccgggguuauac 22**
12	3.99	rno-miR-877	110	5e-04	**UserSeq 1 guagaggagauggcgcaggg 20** |||||||||||||||||||| **hsa-miR-877-5p 1 guagaggagauggcgcaggg 20**

13	3.89	rno-let-7b-5p	110	6e-04	**UserSeq**	**1**	**ugagguaguagguuguugugguu**	**22**
							||||||||||||||||||||	
					hsa-let-7b-5p	**1**	**ugagguaguagguuguugugguu**	**22**
14	3.48	rno-miR-140-5p	110	5e-04	**UserSeq**	**1**	**caguggguuuacccuaugguag**	**22**
							||||||||||||||||||||	
					hsa-miR-140-5p	**1**	**caguggguuuacccuaugguag**	**22**
15	3.38	rno-miR-582-5p	110	5e-04	**UserSeq**	**1**	**uacaguuguucaaccaguuacu**	**22**
							||||||||||||||||||||	
					hsa-miR-582-5p	**2**	**uacaguuguucaaccaguuacu**	**23**
16	3.11	rno-miR-185-5p	110	5e-04	**UserSeq**	**1**	**uggagagaaaggcaguuccuga**	**22**
							||||||||||||||||||||	
					hsa-miR-185-5p	**1**	**uggagagaaaggcaguuccuga**	**22**
17	3.04	rno-miR-488-3p	96	0.007	**UserSeq**	**1**	**uugaaaggcuguuucuugguc**	**21**
							|||||||||| |||||||||	
					hsa-miR-488-3p	**1**	**uugaaaggcuauuucuugguc**	**21**
18	2.91	rno-miR-27a-5p	110	5e-04	**UserSeq**	**1**	**agggcuuagcugcuugugagca**	**22**
							||||||||||||||||||||	
					hsa-miR-27a-5p	**1**	**agggcuuagcugcuugugagca**	**22**
19	2.71	rno-miR-10b-5p	105	0.002	**UserSeq**	**1**	**cccuguagaaccgaauuugug**	**21**
							||||||||||||||||||	
					hsa-miR-10b-5p	**3**	**cccuguagaaccgaauuugug**	**23**
20	2.59	rno-miR-338-3p	115	2e-04	**UserSeq**	**23**	**uccagcaucagugauuuuguuga**	**1**
							||||||||||||||||||||	
					hsa-miR-3065-5p	**1**	**uccagcaucagugauuuuguuga**	**23**
			110	6e-04	**UserSeq**	**1**	**uccagcaucagugauuuuguug**	**22**
							||||||||||||||||||||	
					hsa-miR-338-3p	**1**	**uccagcaucagugauuuuguug**	**22**
21	2.33	rno-miR-615	110	6e-04	**UserSeq**	**1**	**gggggucccccggugcucggauc**	**22**
							||||||||||||||||||||	
					hsa-miR-615-5p	**1**	**gggggucccccggugcucggauc**	**22**
22	2.33	rno-miR-330-3P	106	0.001	**UserSeq**	**1**	**gcaaagcacagggccugcagaga**	**23**
							|||||||||| |||||||||||	
					hsa-miR-330-3p	**1**	**gcaaagcacacggccugcagaga**	**23**
23	2.27	rno-let-7d-3p	110	6e-04	**UserSeq**	**1**	**cuauacgaccugcugccuuucu**	**22**
							||||||||||||||||||||	
					hsa-let-7d-3p	**1**	**cuauacgaccugcugccuuucu**	**22**
24	2.16	rno-miR-376a-5p	100	0.004	**UserSeq**	**2**	**guagauucuccuucuaugag**	**21**
							||||||||||||||||||	
					hsa-miR-376a-5p	**1**	**guagauucuccuucuaugag**	**20**
25	2.13	rno-miR-144-5p	110	6e-04	**UserSeq**	**1**	**ggauaucaucauauacuguaag**	**22**
							||||||||||||||||||||	
					hsa-miR-144-5p	**1**	**ggauaucaucauauacuguaag**	**22**
26	2.12	rno-miR-369-3p	105	0.002	**UserSeq**	**1**	**aauaauacaugguugaucuuu**	**21**
							|||||||||||||||||||	
					hsa-miR-369-3p	**1**	**aauaauacaugguugaucuuu**	**21**

27	2.04	rno-miR-339-5p	115	2e-04	**UserSeq**	**1**	**ucccuguccuccaggagcucacg**	**23**
							||||||||||||||||||||	
					hsa-miR-339-5p	**1**	**ucccuguccuccaggagcucacg**	**23**
28	2.03	rno-miR-200c-3p	105	0.002	**UserSeq**	**1**	**uaauacugccggguaaugaug**	**21**
							|||||||||||||||||||	
					hsa-miR-200c-3p	**1**	**uaauacugccggguaaugaug**	**21**
29	2.01	rno-miR-181b-3p	105	0.002	**serSeq**	**1**	**cucacugaacaaugaaugcaa**	**21**
							|||||||||||||||||||	
					hsa-miR-181b-3p	**1**	**cucacugaacaaugaaugcaa**	**21**
30	1.97	rno-miR-93-3p	110	6e-04	**UserSeq**	**1**	**acugcugagcuagcacuucccg**	**22**
							|||||||||||||||||||	
					hsa-miR-93-3p	**1**	**acugcugagcuagcacuucccg**	**22**
31	1.86	rno-miR-423-5p	115	2e-04	**UserSeq**	**1**	**ugaggggcagagagcgagacuuu**	**23**
							||||||||||||||||||||	
					hsa-miR-423-5p	**1**	**ugaggggcagagagcgagacuuu**	**23**
			115	2e-04	**UserSeq**	**1**	**ugaggggcagagagcgagacuuu**	**23**
							||||||||||||||||||||	
					hsa-miR-3184-3p	**1**	**ugaggggcagagagcgagacuuu**	**23**
32	1.8	rno-miR-493-5p	110	6e-04	**UserSeq**	**1**	**uuguacaugguaggcuuucauu**	**22**
							|||||||||||||||||||	
					hsa-miR-493-5p	**1**	**uuguacaugguaggcuuucauu**	**22**
33	1.71	rno-miR-216b-5p	110	6e-04	**UserSeq**	**1**	**aaaucucugcaggcaaauguga**	**22**
							|||||||||||||||||||	
					hsa-miR-216b-5p	**1**	**aaaucucugcaggcaaauguga**	**22**
34	1.71	rno-miR-323-3p	105	0.001	**UserSeq**	**1**	**cacauuacacggucgaccucu**	**21**
							||||||||||||||||||	
					hsa-miR-323a-3p	**1**	**cacauuacacggucgaccucu**	**21**
35	1.68	rno-miR-130b-3p	110	6e-04	**UserSeq**	**1**	**cagugcaaugaugaaagggcau**	**22**
							|||||||||||||||||||	
					hsa-miR-130b-3p	**1**	**cagugcaaugaugaaagggcau**	**22**
36	1.67	rno-miR-194-5p	110	5e-04	**UserSeq**	**1**	**uguaacagcaacuccaugugga**	**22**
							|||||||||||||||||||	
					hsa-miR-194-5p	**1**	**uguaacagcaacuccaugugga**	**22**
37	1.65	rno-miR-210-3p	110	5e-04	**UserSeq**	**1**	**cugugcgugugacagcggcuga**	**22**
							|||||||||||||||||||	
					hsa-miR-210-3p	**1**	**cugugcgugugacagcggcuga**	**22**
38	1.63	rno-miR-382-3P	105	0.002	**UserSeq**	**1**	**aaucauucacggacaacacuu**	**21**
							||||||||||||||||||	
					hsa-miR-382-3p	**1**	**aaucauucacggacaacacuu**	**21**
39	1.62	rno-miR-145-3p	105	0.001	**UserSeq**	**1**	**ggauuccuggaaauacuguuc**	**21**
							||||||||||||||||||	
					hsa-miR-145-3p	**1**	**ggauuccuggaaauacuguuc**	**21**
40	1.6	rno-miR-125b-2-3p	100	0.004	**UserSeq**	**1**	**acaagucaggcucuugggac**	**20**
							|||||||||||||||||	
					hsa-miR-125b-2-3p	**3**	**acaagucaggcucuugggac**	**22**
41	1.59	rno-miR-203a-3p	110	6e-04	**UserSeq**	**1**	**gugaaauguuuaggaccacuag**	**22**
							|||||||||||||||||||	
					hsa-miR-203a-3p	**1**	**gugaaauguuuaggaccacuag**	**22**

			105	0.002	**UserSeq 21 gugaaauguuuaggaccacua 1** |||||||||||||||||||| **hsa-miR-203b-5p 1 gugaaauguuuaggaccacua 21**
42	1.59	rno-miR-296-3p	110	6e-04	**UserSeq 1 gaggguuggguggaggcucucc 22** |||||||||||||||||||| **hsa-miR-296-3p 1 gaggguuggguggaggcucucc 22**
43	1.59	rno-miR-101a-5p	105	0.001	**UserSeq 2 caguuaucacagugcugaugc 22** |||||||||||||||||||| **hsa-miR-101-5p 1 caguuaucacagugcugaugc 21**
44	1.59	rno-miR-101a-3p	105	0.002	**UserSeq 1 uacaguacugugauaacugaa 21** |||||||||||||||||||| **hsa-miR-101-3p 1 uacaguacugugauaacugaa 21**
45	1.58	rno-miR-142-5p	105	0.002	**UserSeq 1 cauaaaguagaaagcacuacu 21** |||||||||||||||||||| **hsa-miR-142-5p 1 cauaaaguagaaagcacuacu 21**
46	1.58	rno-miR-504-5p	101	0.004	**UserSeq 1 agacccuggucugcacucuguc 22** |||||||||||||||||| || **hsa-miR-504-5p 1 agacccuggucugcacucuauc 22**
47	1.56	rno-miR-145-5p	115	2e-04	**UserSeq 1 guccaguuuucccaggaaucccu 23** ||||||||||||||||||||| **hsa-miR-145-5p 1 guccaguuuucccaggaaucccu 23**
48	1.55	rno-miR-370-3p	110	5e-04	**UserSeq 1 gccugcugggguggaaccuggu 22** |||||||||||||||||||| **hsa-miR-370-3p 1 gccugcugggguggaaccuggu 22**
49	1.55	rno-miR-222-3p	105	0.002	**serSeq 1 agcuacaucuggcuacugggu 21** |||||||||||||||||||| **hsa-miR-222-3p 1 agcuacaucuggcuacugggu 21**
50	1.53	rno-miR-99b-3p	110	6e-04	**UserSeq 1 caagcucgugucuguggguccg 22** |||||||||||||||||||| **hsa-miR-99b-3p 1 caagcucgugucuguggguccg 22**
51	1.52	rno-miR-25-3p	110	6e-04	**UserSeq 1 cauugcacuugucucggucuga 22** |||||||||||||||||||| **hsa-miR-25-3p 1 cauugcacuugucucggucuga 22**
52	1.52	rno-miR-433-5P	110	6e-04	**UserSeq 1 uacggugagccugucauuauuc 22** |||||||||||||||||||| **hsa-miR-433-5p 1 uacggugagccugucauuauuc 22**
53	1.51	rno-miR-328a-3p	110	5e-04	**UserSeq 1 cuggcccucucugcccuuccgu 22** |||||||||||||||||||| **hsa-miR-328-3p 1 cuggcccucucugcccuuccgu 22**

Source (191).

Table 3.6. Human orthologs to mature (rno) miRNA reads. The 64 candidate miRNAs formed hairpins. Embryonic rno-miRNAs are underlined. miRNAs that are significantly correlated with mRNAs are in bold. Sequences represent the longest of each miRNA identified that matches the greatest extent with available rat or human genome sequence. The mature structure has been taken from the mirBase registry release 21 (http://www.mirbase.org).

FC	MiRNA annotation (miRBase, rno)	Mature sequence (mirBase)	Accession number of mature sequence (miRBase)	MiRNA annotation (miRBase, hsa)	Family (hsa)	Chromosome (hsa)	Strand	Mature sequence (mirBase)	Accession number of mature sequence (miRBase)	experimental evidence in human
8.29	rno-miR-135b-3p	AUGUAGGGCUAAAAGCCAUGGG	MIMAT0017043	hsa-miR-135b-3p	mir 135	1	-	AUGUAGGGCUAAAAGCCAUGGG	MIMAT0004698	(202)
7.73	rno-miR-24-1-5p	GUGCCUACUGAGCUGAUAUCAG	MIMAT0003153	hsa-miR-24-1-5p	mir 24	9	+	UGCCUACUGAGCUGAUAUCAGU	MIMAT0000079	(202, 203)
6.2	rno-miR-377-5p	AGAGGUUGCCCUUGGUGAAUUC	MIMAT0017203	hsa-miR-377-5p	mir 154	14	+	AGAGGUUGCCCUUGGUGAAUUC	MIMAT0004689	(204)
6.2	rno-miR-337-3p	UUCAGCUCCUAUAUGAUGCCUUU	MIMAT0000577	hsa-miR-337-3p	mir 337	14	+	CUCCUAUAUGAUGCCUUUCUUC	MIMAT0000754	(108)
6.2	rno-miR-370-5p	CAGGUCACGUCUCUGCAGUUACAC	MIMAT0017202	hsa-miR-370-5p	mir 370	14	+	CAGGUCACGUCUCUGCAGUUAC	MIMAT0026483	(205)
5.78	rno-miR-132-3p	UAACAGUCUACAGCCAUGGUCG	MIMAT0000838	hsa-miR-132-3p	mir 132	17	+	UAACAGUCUACAGCCAUGGUCG	MIMAT0000426	(206)
5.15	rno-miR-216b-3p	AAAUCUCUGCAGGCAAAUGUGA	MIMAT0017846	hsa-miR-216b-5p	mir 216	2	-	AAAUCUCUGCAGGCAAAUGUGA	MIMAT0004959	(207)
5.15	rno-miR-291a-5p	CAUCAAAGUGGAGGCCCUCUCU	MIMAT0000894	hsa-miR-371b-5p	mir 290	19	+	ACUCAAAAGAUGGCGGCACUUU	MIMAT0019892	(203)
				hsa-miR-371b-3p	mir 290	19	+	AAGUGCCCCCACAGUUUGAGUGC	MIMAT0019893	
				hsa-miR-371a-5p	mir 290	19	+	ACUCAAACUGUGGGGGCACU	MIMAT0004687	
				hsa-miR-371a-3p	mir 290	19	+	AAGUGCCGCCAUCUUUUGAGUGU	MIMAT0000723	
				hsa-miR-372-3p	mir 290	19	+	AAAGUGCUGCGACAUUUGAGCGU	MIMAT0000724	
				hsa-miR-372-5p	mir 290	19	+	CCUCAAAUGUGGAGCACUAUUCU	MIMAT0026484	
5.15	rno-miR-380-5p	AUGGUUGACCAUAGAACAUGCG	MIMAT0005308	hsa-miR-380-5p	mir 380	14	+	UGGUUGACCAUAGAACAUGCGC	MIMAT0000734	(208)
4.67	rno-miR-501-3p	AAUGCACCCGGGCAAGGAUUUGG	MIMAT0017198	hsa-miR-501-5p	mir 500	x	+	AAUCCUUUGUCCCUGGGUGAGA	MIMAT0004774	(202)
4.5	rno-miR-592	AUUGUGUCAAUAUGCGAUGAUGU	MIMAT0012834	hsa-miR-592	mir 592	7	-	UUGUGUCAAUAUGCGAUGAUGU	MIMAT0003260	(209)
4.45	rno-miR-193-3p	AACUGGCCUACAAAGUCCCAGU	MIMAT0000868	hsa-miR-193a-3p	mir 193	17	+	AACUGGCCUACAAAGUCCCAGU	MIMAT0000459	(124)
4.04	rno-miR-200b-5p	CAUCUUACUGGGCAGCAUUGGA	MIMAT0017152	hsa-miR-200b-5p	mir 8	1	+	CAUCUUACUGGGCAGCAUUGGA	MIMAT0004571	(210)
3.99	rno-miR-877	GUAGAGGAGAUGGCGCAGGG	MIMAT0005285	hsa-miR-877-5p	mir 877	6	+	GUAGAGGAGAUGGCGCAGGG	MIMAT0004949	(202)
3.89	rno-let-7b-5p	UGAGGUAGUAGGUUGUGUGGUU	MIMAT0000775	hsa-let-7b-5p	let 7b	22	+	UGAGGUAGUAGGUUGUGUGGUU	MIMAT0000063	(211)
3.5	rno-miR-340-3p	UCCGUCUCAGUUACUUUAUAGCC	MIMAT0000585	hsa-miR-340-3p	mir 340	5	-	UCCGUCUCAGUUACUUUAUAGC	MIMAT0000750	(202)
3.48	rno-miR-140-5p	CAGUGGUUUUACCCUAUGGUAG	MIMAT0000573	hsa-miR-140-5p	mir 140	16	+	CAGUGGUUUUACCCUAUGGUAG	MIMAT0000431	(212)
3.47	rno-miR-101a-5p	UCAGUUAUCACAGUGCUGAUGC	MIMAT0004726	hsa-miR-101-5p	mir 101	1	+	CAGUUAUCACAGUGCUGAUGCU	MIMAT0004513	(213)
3.43	rno-miR-215	AUGACCUAUGAUUUGACAGACA	MIMAT0003118	hsa-miR-192-3p	mir 192	11	-	CUGCCAAUUCCAUAGGUCACAG	MIMAT0004543	(214)
3.38	rno-miR-582-5p	UACAGUUGUUCAACCAGUUACU	MIMAT0012833	hsa-miR-582-5p	mir 582	5	-	UUACAGUUGUUCAACCAGUUACU	MIMAT0003247	(215)

3.11	rno-miR-200c-5p	CGUCUUACCCAGCAGUGUUUG	MIMAT0017150	hsa-miR-200c-5p	mir 8	12	+	CGUCUUACCCAGCAGUGUUUGG	MIMAT0004657	(205)
3.11	rno-miR-185-5p	UGGAGAGAAAGGCAGUUCCUGA	MIMAT0000862	hsa-miR-185-5p	mir 185	22	+	UGGAGAGAAAGGCAGUUCCUGA	MIMAT0000455	(108)
3.04	rno-miR-488-3p	UUGAAAGGCUGUUUCUUGGUC	MIMAT0005341	hsa-miR-488-3p	mir 488	13	-	UUGAAAGGCUAUUUCUUGGUC	MIMAT0004763	(202)
2.91	rno-miR-27a-5p	AGGGCUUAGCUGCUUGUGAGCA	MIMAT0004715	hsa-miR-27a-5p	mir 27	17	-	AGGGCUUAGCUGCUUGUGAGCA	MIMAT0004501	(216)
2.71	rno-miR-10b-5p	CCCUGUAGAACCGAAUUUGUGU	MIMAT0000783	hsa-miR-10b-5p	mir 10	2	+	UACCCUGUAGAACCGAAUUUGUG	MIMAT0000254	(58)
2.59	rno-miR-338-3P	UCCAGCAUCAGUGAUUUUGUUGA	MIMAT0000581	hsa-miR-3065-5p	mir 3065	17	+	UCAACAAAAUCACUGAUGCUGGA	MIMAT0015066	(217)
				hsa-miR-338-3p	mir 338	17	-	UCCAGCAUCAGUGAUUUUGUUG	MIMAT0000763	(218)
2.38	rno-miR-484	UCAGGCUCAGUCCCCUCCCGAU	MIMAT0005319	hsa-miR-484	mir 484	16	+	UCAGGCUCAGUCCCCUCCCGAU	MIMAT0002174	(177)
2.33	rno-miR-500-3p	AAUGCACCUGGGCAAGGGUUCA	MIMAT0005321	hsa-miR-502-3p	mir 500	x	+	AAUGCACCUGGGCAAGGAUUCA	MIMAT0004775	(4)
2.33	rno-miR-330-3P	GCAAAGCACAGGGCCUGCAGAGA	MIMAT0000568	hsa-miR-330-3p	mir 330	19	-	GCAAAGCACACGGCCUGCAGAGA	MIMAT0000751	(173)
2.33	rno-miR-615	GGGGGUCCCCGGUGCUCGGAUC	MIMAT0012835	hsa-miR-615-5p	mir 615	7	+	GGGGGUCCCCGGUGCUCGGAUC	MIMAT0004804	(219)
2.27	rno-let-7d-3p	CUAUACGACCUGCUGCCUUUCU	MIMAT0000563	hsa-let-7d-3p	let 7	9	+	CUAUACGACCUGCUGCCUUUCU	MIMAT0004484	(220)
2.16	rno-miR-376a-5p	GGUAGAUUCUCCUUCUAUGAG	MIMAT0003197	hsa-miR-376a-5p	mir 368	14	+	GUAGAUUCUCCUUCUAUGAGUA	MIMAT0003386	(202)
2.13	rno-miR-144-5p	GGAUAUCAUCAUAUACUGUAAGU	MIMAT0017130	hsa-miR-144-5p	mir 144	17	-	GGAUAUCAUCAUAUACUGUAAG	MIMAT0004600	(221)
2.12	rno-miR-369-3p	AAUAAUACAUGGUUGAUCUUU	MIMAT0003207	hsa-miR-369-3p	mir 154	14	+	AAUAAUACAUGGUUGAUCUUU	MIMAT0000721	(124)
2.04	rno-miR-339-5P	UCCCUGUCCUCCAGGAGCUCACG	MIMAT0000583	hsa-miR-339-5p	mir 339	7	-	UCCCUGUCCUCCAGGAGCUCACG	MIMAT0000764	(222)
2.03	rno-miR-200c-3p	UAAUACUGCCGGGUAAUGAUG	MIMAT0000873	hsa-miR-200c-3p	mir 8	12	-	UAAUACUGCCGGGUAAUGAUGGA	MIMAT0000617	(223)
2.01	rno-miR-181b-1-3p	CUCACUGAACAAUGAAUGCAA	MIMAT0017139	hsa-miR-181b-3p	mir 181	1	-	CUCACUGAACAAUGAAUGCAA	MIMAT0022692	(202)
1.97	rno-miR-93-3p	ACUGCUGAGCUAGCACUUCCCGA	MIMAT0017109	hsa-miR-93-3p	mir 17	7	-	ACUGCUGAGCUAGCACUUCCCG	MIMAT0004509	(224)
1.86	rno-miR-423-5p	UGAGGGGCAGAGAGCGAGACUUUU	MIMAT0017305	hsa-miR-423-5p	mir 423	17	+	UGAGGGGCAGAGAGCGAGACUUU	MIMAT0004748	(58)
				hsa-miR-3184-3p	mir 3184	17	-	AAAGUCUCGCUCUCUGCCCCUCA	MIMAT0022731	
1.8	rno-miR-493-5p	UUGUACAUGGUAGGCUUUCAUU	MIMAT0017217	hsa-miR-493-5p	mir 493	14	+	UUGUACAUGGUAGGCUUUCAUU	MIMAT0002813	(204)
1.71	rno-miR-323-3p	CACAUUACACGGUCGACCUCU	MIMAT0000550	hsa-miR-323a-3p	mir 154	14	+	CACAUUACACGGUCGACCUCU	MIMAT0000755	(132)
1.71	rno-miR-216b-5p	AAAUCUCUGCAGGCAAAUGUGA	MIMAT0017846	hsa-miR-216b-5p	mir 216	2	-	AAAUCUCUGCAGGCAAAUGUGA	MIMAT0004959	(202)
1.68	rno-miR-130b-3p	CAGUGCAAUGAUGAAAGGGCAU	MIMAT0000837	hsa-miR-130b-3p	mir 130	22	+	CAGUGCAAUGAUGAAAGGGCAU	MIMAT0000691	(203)
1.67	rno-miR-194-5p	UGUAACAGCAACUCCAUGUGGA	MIMAT0000869	hsa-miR-194-5p-1	mir 194	1	+	UGUAACAGCAACUCCAUGUGGA	MIMAT0000460	(214)
				hsa-miR-194-5p-2	mir 194	19	+	UGUAACAGCAACUCCAUGUGGA	MIMAT0000460	
1.65	rno-miR-136-5p	ACUCCAUUUGUUUUGAUGAUGGA	MIMAT0000842	hsa-miR-136-3p	mir 136	14	+	CAUCAUCGUCUCAAAUGAGUCU	MIMAT0004606	(202)
1.65	rno-miR-210-3p	CUGUGCGUGUGACAGCGGCUGA	MIMAT0000881	hsa-miR-210-3p	mir 210	11	-	CUGUGCGUGUGACAGCGGCUGA	MIMAT0000267	(225)
1.63	rno-miR-382-3P	AAUCAUUCACGGACAACACUU	MIMAT0003202	hsa-miR-382-3p	mir 154	14	+	AAUCAUUCACGGACAACACUU	MIMAT0022697	(202)
1.62	rno-miR-145-3p	GGAUUCCUGGAAAUACUGUUC	MIMAT0017131	hsa-miR-145-5p	mir 145	5	+	GUCCAGUUUUCCCAGGAAUCCCU	MIMAT0000437	(206)
1.62	rno-miR-136-3p	CAUCAUCGUCUCAAAUGAGUCU	MIMAT0004733	hsa-miR-136-3p	mir 136	14	+	CAUCAUCGUCUCAAAUGAGUCU	MIMAT0004606	(226)
1.6	rno-miR-450a-5p	UUUUGCGAUGUGUUCCUAAUGU	MIMAT0001547	hsa-miR-450a-5p	mir 450	x	-	UUUUGCGAUGUGUUCCUAAUAU	MIMAT0001545	(175)
1.6	rno-miR-125b-2-3p	ACAAGUCAGGCUCUUGGGACCU	MIMAT0026467	hsa-miR-125b-2-3p	mir 10	21	+	UCACAAGUCAGGCUCUUGGGAC	MIMAT0004603	(202)
1.59	rno-miR-203a-3p	GUGAAAUGUUUAGGACCACUAG	MIMAT0000876	hsa-miR-203a-3p	mir 203	14	+	GUGAAAUGUUUAGGACCACUAG	MIMAT0000264	(202)
				hsa-miR-203b-5p	mir 203	14	-	UAGUGGUCCUAAACAUUUCACA	MIMAT0019813	

1.59	rno-miR-296-3p	GAGGGUUGGGUGGAGGCUCUCC	MIMAT0004742	hsa-miR-296-3p	mir 296	20	-	GAGGGUUGGGUGGAGGCUCUCC	MIMAT0004679	(227)
1.59	rno-miR-101a-3p	UACAGUACUGUGAUAACUGAA	MIMAT0000823	hsa-miR-101-3p	mir 101	1	-	UACAGUACUGUGAUAACUGAA	MIMAT0000099	(228)
1.58	rno-miR-504	AGACCCUGGUCUGCACUCUGUC	MIMAT0012830	hsa-miR-504-5p	mir 504	x	-	AGACCCUGGUCUGCACUCUAUC	MIMAT0002875	(202)
1.58	rno-miR-142-5p	CAUAAAGUAGAAAGCACUACU	MIMAT0000847	hsa-miR-142-5p	mir 142	17	-	CAUAAAGUAGAAAGCACUACU	MIMAT0000433	(202)
1.56	rno-miR-145-5p	GUCCAGUUUUCCCAGGAAUCCCU	MIMAT0000851	hsa-miR-145-5p	mir 145	5	+	GUCCAGUUUUCCCAGGAAUCCCU	MIMAT0000437	(202)
1.55	rno-miR-370-3p	GCCUGCUGGGGUGGAACCUGGU	MIMAT0003122	hsa-miR-370-3p	mir 370	14	+	GCCUGCUGGGGUGGAACCUGGU	MIMAT0000722	(202)
1.55	rno-miR-222-3p	AGCUACAUCUGGCUACUGGGU	MIMAT0000891	hsa-miR-222-3p	mir 221	x	-	AGCUACAUCUGGCUACUGGGU	MIMAT0000279	(202)
1.53	rno-miR-99b-3p	CAAGCUCGUGUCUGUGGGUCCG	MIMAT0004725	hsa-miR-99b-3p	mir 10	19	+	CAAGCUCGUGUCUGUGGGUCCG	MIMAT0004678	(202)
1.52	rno-miR-25-3p	CAUUGCACUUGUCUCGGUCUGA	MIMAT0000795	hsa-miR-25-3p	mir 25	7	-	CAUUGCACUUGUCUCGGUCUGA	MIMAT0000081	(202)
1.52	rno-miR-433-5P	UACGGUGAGCCUGUCAUUAUUC	MIMAT0017192	hsa-miR-433-5p	mir 433	14	+	UACGGUGAGCCUGUCAUUAUUC	MIMAT0026554	(202)
1.51	rno-miR-328a-3p	CUGGCCCUCUCUGCCCUUCCGU	MIMAT0000564	hsa-miR-328-3p	mir 328	16	-	CUGGCCCUCUCUGCCCUUCCGU	MIMAT0000752	(202)

Source (191).

Table 3.7. Correlations of the miRNA-mRNA pairs. Genes expressed in the lung are in bold. The P value indicates the likelihood of the focus genes in a network being found together by random chance. The same computation was used for GO analysis of the initial gene list. The columns are sorted in descending order of P value.

Pearson correlation coefficient	miRNA annotation (mirBase)	Fold Change (Nitrofen/Control)	p-value	Gene
1	rno-miR-3585-5p	2.90	0.01	TPD52L1
1	rno-miR-142-5p	0.63	0.00	**ABHD2**, **BAZ2A**, **CYP26B1**, EIF4E3, HIPK2, IKZF2, **LRAT**, MAML1, ROBO1, SRGAP1
1	rno-miR-504	0.63	0.00	RNF44
1	rno-miR-325-3p	0.55	0.00	B3GNT7, CFTR, **CNN1**, FAM189B, FAM189B, FOXN3, **GPR155**, IKZF2, INHA, LRRN1, MAML1, MUSTN1, **NR5A2**, TRAK1,
1	rno-miR-615	0.43	0.00	IKZF2
1	rno-miR-384-5p	0.32	0.00	GCNT2, HIPK2, IKZF2, ITGB3, MAML1, **MYH11**, **NR5A2**, PCDH20, R3HDM1, **RNF44**, SBK1, SCN8A
1	rno-miR-216b-3p	0.19	0.00	FOXN3, IKZF2, SPRED2
1	rno-miR-291a-5p	0.19	0.00	**BAZ2A**, PARM1, PRKAA2, TGFBR3
-1	rno-miR-592	4.50	0.00	**CYP26B1**
-1	rno-miR-877	3.99	0.00	FOXN3
-1	rno-miR-215	3.43	0.00	**ABHD2**
-1	rno-miR-3585-5p	2.90	0.01	**BAZ2A**, IKZF2, ITGB3, **SIRPA**, SPRY4, SRGAP1, TGFBR3
-1	rno-miR-484	2.38	0.00	FOXN3, **PCDHGA8**, TGFBR3
-1	rno-miR-369-3p	2.12	0.00	**ADCY5**, AHDC1, CYP26B1, FOXN3, GREM2, IKZF2
-1	rno-miR-142-5p	0.63	0.00	DNAL1
-1	rno-miR-504	0.63	0.00	PDE1B
-1	rno-miR-325-3p	0.55	0.00	FIBIN, GADD45G, MASP1, MRPS25, MYO7B, PDE1B, PPCS, TMEM205
-1	rno-miR-384-5p	0.32	0.00	ADO, ATP2B2, DCUN1D2
-1	rno-miR-216b-3p	0.19	0.00	ID4

Source (191).

potential functional relationships that contribute to the pathogenesis of lung hypoplasia upon nitrofen treatment. Of the identified mRNA reads, EPHX3, PSG19, HNF4a, CAR7 and KCNH7 displayed the highest significant differentially expression (FC >6). Amongst the next 82 mRNAs that had a more moderate yet substantial upregulated expression during embryonic and fetal lung development, (CF >2) were 14 genes: ATP5F1, CD99, PYGO2, MIP, CCDC126, STXBP6, ATP5I, FAM111A, RPI35A, TNKS2, TPMT, ID4, RPS3A, PSMA6. Also, 34 genes were downregulated (FC <0.5) during embryonic and fetal lung development.

3.4.4. PCR validation of the differential mRNA transcripts

Due to the variable nature of gene expression in developmental tissues along with the significant phenotypic changes altered by nitrofen treatment in embryonic rats, a survey of 32 commonly used endogenous genes was performed. Comparing both nitrofen and control E21 lungs, I identified both ABL and GAPDH as excellent endogenous control genes for RT-qPCR (CV: 0.0769, M value: 0.2221). These two genes were used in tandem through a geometric normalization approach for all functional gene expression analysis (dPCR and RT-qPCR) (Figure 3.7). Two-way Analysis of Variance (ANOVA) of results run in Prism (ver 6.0) using a Sidak repeated measures test showed that only PSG19 was significantly upregulated compared to control (P = 0.001).

Chromatin licensing and DNA replicating factor 1 (CDT1) was significantly downregulated due to nitrofen treatment (two-tailed unpaired t-test, P = 0.0420). Using the same cDNA samples and primer sets from the dPCR, RT-qPCR was also conducted. As expected, a similar trend in gene expression was observed. However,

no significant changes were shown for PSG19 when compared to control (two-way unpaired t-test, P = 0.0558). Using the calculated fold change in gene expression from both dPCR and RT-qPCR, a linear regression was constructed to determine the correlation between RNA-sequencing and gene expression validation. Using these methods, dPCR (slope = 0.592, R2 = 0.34) was shown to be a more accurate method to assess changes in gene expression to that of RT-qPCR (slope = 0.457, R2 = 0.11). Furthermore, large changes in gene expression were more strongly correlated between dPCR and RNA sequencing compared to smaller changes (Figure 3.7).

3.5. Discussion

The purpose of this study was to determine which mRNAs and miRNAs are differentially expressed in the embryonic rat lung after nitrofen treatment and which developmental signaling pathways are affected. Large changes in our gene expression data show a similar trend between NGS and functional analysis, however, smaller changes in gene expression are lost amongst the gene expression variability in this embryonic treatment despite identifying key endogenous control genes that are stable after embryonic nitrofen treatment.

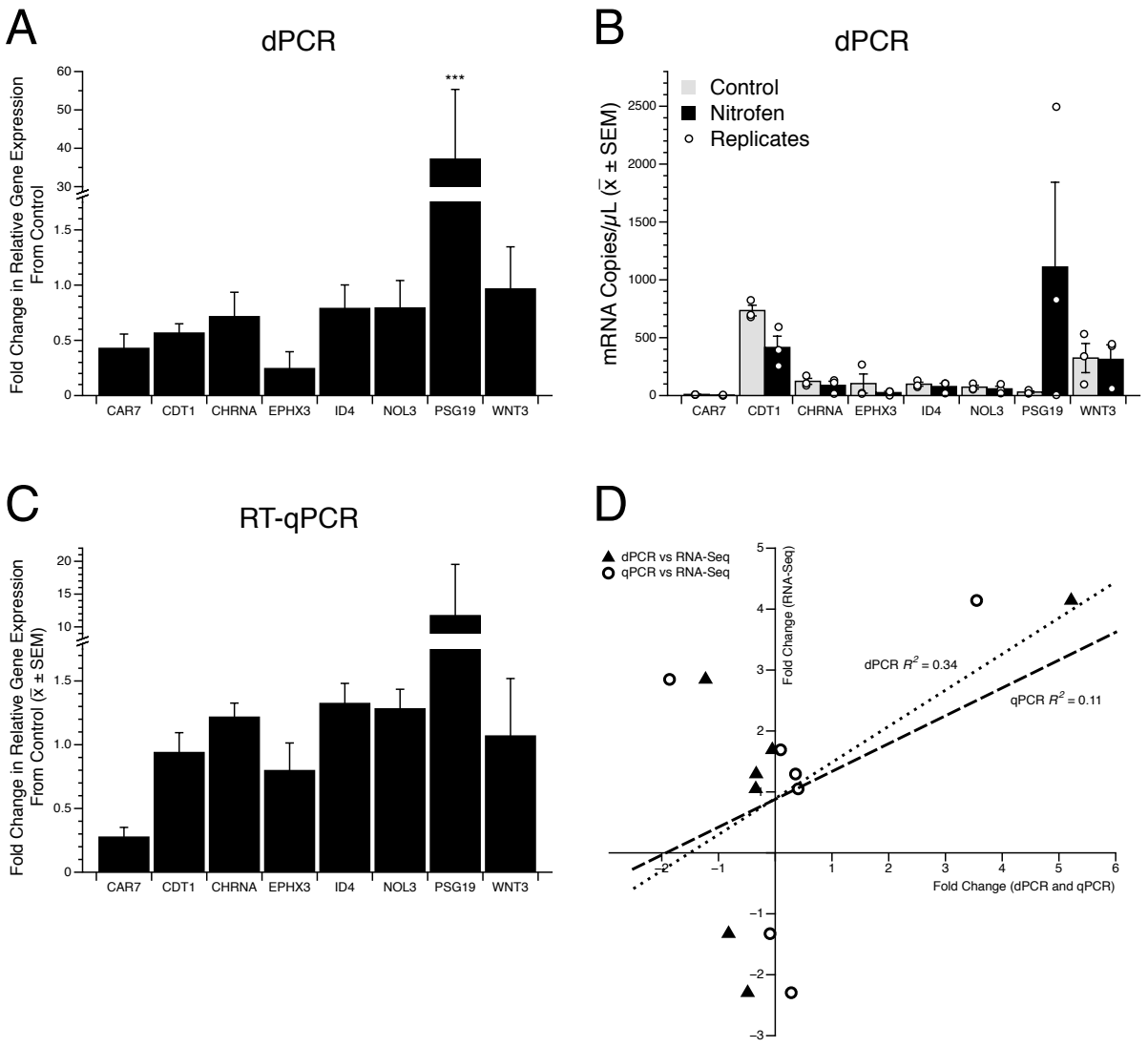

Figure 3.7. NGS Validation by dPCR and RT-qPCR. Validation of the expression of a subsample of genes by dPCR. Two-way ANOVA (***, P < 0.001) (A, B). RT-qPCR of the selected NGS transcripts with no significant changes were shown (PSG19 two tailed t-test (P=0.0558) (C). (D) Linear regression correlation of RNA-seq (Y axis) with dPCR and qPCR data (X axis) using a log2 mean fold change measure of the genes differentially expressed across the two gene-expression platforms under correlation analysis. Outliers (Ephx3) were identified and removed as having 1.5 standard deviations or larger (191).

3.5.1. Conservation in structure and function of RNA-coding genes can be used to distinct rat from human in terms of their responses to nitrofen

Using NGS sequencing technology, I obtained reads from both the 5' and 3' arms of the pre-miRNAs. The identified rat miRNAs showed strong conservation with known human miRNAs in mirBase with only three unique miRNA seeds missing from known vertebrate homologs. Although these are unique and represent rat-specific sequences, I cannot exclude the possibility that they are unique in humans or remain to be detected in other species.

Interestingly, the density of miRNA genes is remarkably similar across the rat and human lineages. Putative miR-290, -500, -194 and -203 families in human tend to be organized in clusters, with large proportions having multiple isoforms and/or copies in their vicinity in the genome, suggesting that many of them could be a result of gene duplications or act redundantly. The rat gene encoding miR-291a: a gene linked to negative regulation of apoptotic processes and SMAD signaling (homologs of both the Drosophila protein, mothers against decapentaplegic (MAD) and the Caenorhabditis elegans protein SMA (from gene sma for small body size) has been previously identified as pluripotent embryonic stem cell-specific in mouse, rat, and in human, known as miR-hes-1, -2, -3 plays a role in embryonic stem cell differentiation (203). Our finding of a redundant expression of the six homologous hsa-290 isoforms that are orthologous to rat miRNA suggests that they are pluripotent embryonic stem miRNAs with crucial regulatory differentiation roles in early human development. One exception is the density of miRNA genes. The above

results demonstrate that sequence conservation may point to conservation in function of human miRNAs that are not validated experimentally.

3.5.2. Rat miRNAs and their target mRNAs could function similarly to their human homologs in response to nitrofen

MiRNAs are derived from larger precursors that have the capacity to form stem-loop structures from either side of the strand. Existing evidence based on the hairpin fold structure suggests phylogenetic conservation of our rno-miRNA data (229). For example, the orthologous hsa-miR-200c-3p that was enriched in the rat lung tissues and upregulated upon nitrofen treatment exhibited seed conservation with its host gene. Our findings, with regard to lung development, are consistent with increasing evidence from human studies on the effects of teratogenic and toxic triggers on miRNA profiling, and reconcile with orthologous studies matching the nitrofen-mediated upregulation of rat miR-101a-5p, -3p and human miR-144-5p *in vivo* in human airway epithelial cells exposed to cigarette smoke (221). Both of these miRNAs are also known to target genes associated with lung diseases such as the cystic fibrosis transmembrane conductor regulator gene in human (221). I also reported the upregulation of rat miR-193b after nitrofen exposure. Others attributed cystic fibrosis transmembrane conductor regulator replenishment and cancer regression to the upregulation of miR-193b in human (206). Thus, miR-193b may rescue cystic fibrosis transmembrane conductor regulator downstream of nitrofen in rat lung hypoplasia; a finding that warrants further investigation. I report a 4.04-fold increase in rno-miR-193-3p after nitrofen treatment and a high level of conservation with its human ortholog, demonstrating hsa-miR-193-3p to be a putative

antiproliferative molecule that may play a role in CDH progression by a similar mechanism in human.

I report a greater than two fold increase in the expression of another highly conserved miRNA; let-7d-3p in nitrofen-induced hypoplastic lungs. This result is in contrast to Pandit and colleagues (148), who demonstrated that a lack of let-7d promotes alveolar thickening of alveolar compartments exclusively. The latter study demonstrated that a lack of let-7d causes epithelial-to-mesenchymal transition in lung epithelial cells from IPF patients, mediated by TGF-β by a SMAD-dependent mechanism. Nitrofen induced rno-let-7b-5p by 3.89-fold and -7d-3p by 2.27-fold, that target the Ras transcripts downstream of the fibroblast growth factor receptors (120) thus downregulating lung branching and epithelial cell proliferation. Mir-145 consists of a specific miRNA signature associated with pulmonary hypertension and regulates ASM cell differentiation according to previous studies (230). Our results indicate that miRNA rno-miR-145-3p and -5p is a putative component in CDH abnormal lung development in both rat and humans, corroborating the results from others (230). Consequently, future studies should target miR-145 to investigate if it plays a role in PPHN in CDH.

3.5.3. MiRNAs mediate nitrofen-induced cell cycle arrest and proliferation inhibition

Most differentially expressed genes from the nitrofen lungs are clustered, demonstrating a strong expression profile in the developing lung. Nitrofen persists in the lung at elevated levels for 3 days and hence a single dose is enough for inducing intense irreversible damage to the cells (186). Nitrofen induces genotoxicity that modulates several miRNAs, and thereby alters critical cell cycle control signaling

networks. Studies have previously reported in both the nitrofen rat and mouse model that cell cycle-associated proteins are downregulated in nitrofen-induced lung hypoplasia (27, 188, 231). Nitrofen has been demonstrated to suppress cell proliferation by inhibiting regulators of DNA replication (27), activation of the mitochondrial apoptosis axis Bcl2, Bax, and Bak, inhibition of Bcl-xl, and executing the activation of p38-mitogen-activated protein kinase (p38-MAPK) in cultured type II pneumocytes (232). Abhydrolase domain containing 2 (ABHD2) plays an important role in maintaining lung structure integrity and is expressed in alveolar type II cells in mice lungs. In mouse pulmonary SM cells, ABHD2 triggers the differentiation of monocytes to macrophages. Its deficiency often presents emphysema-like symptoms including increased macrophage infiltration, increased inflammatory cytokines, a protease/anti-protease imbalance and enhanced apoptosis in a strikingly similar fashion to human pathology (233). Here, I identified a nitrofen-perturbed immune response pattern in the lung and implicated a role for ABHD2. Similarly to nitrofen, the lung carcinogen benzo(a)pyrene downregulates miR-142-5p significantly (234).

In the current study, rno-miR-325-3p positively correlated with nitrofen-induced GPR155 and NR5A2. GPR155 is an integral membrane protein related to G-protein-coupled receptors. The mRNA for GPR155 is widely located in adult mouse tissues and during the development of the lung and brain. Rno miR-384-5p and NR5A2 expressions correlate positively upon nitrofen exposure. MiR-384-5p is a marker of neurotoxicity and regulates apoptotic cell death in myocardial ischemia by modulating PIK3CD pathway (224). Myosin heavy chain 11 is a component of the contractile apparatus of aortic smooth muscle cells and is expressed in neonatal lung

SMC (235). RNF44 is a poorly understood protein that is encoded by a gene and contains a RING finger motif, a motif often present on proteins involved in protein–protein and protein–DNA interactions. In the current study, nitrofen induced both myosin heavy chain 11 and RNF44 in embryonic lungs, and their expression positively correlated with miR-384-5P expression. These data suggest a potential role for this pathway in the vascular remodeling observed in CDH-associated pulmonary hypertension.

3.5.4. MiRNAs regulate nitrofen-induced ASM cell dysfunction

ASMC progenitors in the embryonic lung mesenchyme produce fibroblast growth factor-10 required for epithelial cell morphogenesis. Fibroblast growth factor-10 expression is crucial for fine tuning the spatiotemporal ASMC activity early in human development. The relationship between lung hypoplasia, fibroblast growth factor-10 deficiency, and dysfunctional ASMC from birth onward is critical for early development (236), and perturbation of this relationship by nitrofen results in abnormal SM relaxation near term. Calponin (CNN1), a multifunctional orthologous protein in both rats and humans in ASMC, is tightly restricted to differentiated ASMC lineages including those in the lung during embryonic and postnatal life. In the current study, nitrofen downregulates CNN1, and this correlates with upregulation of miR-504 upregulated expression.

3.5.5. E-cadherin and integrin are major components of the extracellular matrix

Loss of E-cadherin is a hallmark of epithelial- to-mesenchymal transition and synergizes the dedifferentiation capacity of the cell. From my study, I identified a

nitrofen-induced upregulation of rno-miR-296-3p. MiR-192/215 has been shown to mediate changes in E-cadherin expression by targeting the ZEB2 family of transcriptional repressors downstream of TGF-β (220). In addition, our study showed downregulation of members of the miR-200 family (rno-miR-200c-3p, rno-miR-200c-5p, and rno-miR-200b-5p) upon nitrofen treatment by more than two fold relative to the control. Expression of miR-200 and ZEB1/2 is linked to a negative feedback loop (56) that may involve crosstalk of rno-miR-200c-3p and -200b-5p with TGF-β. A previous study from Xu et al. (237) using immunohistochemistry in the nitrofen rat model demonstrated that TGF-β1 protein was stronger in CDH lungs.

Retinoic acid (RA) signaling is essential for fetal lung development and postnatal alveolar septation (11). Nitrofen suppresses the retinoid response element by a mechanism yet to be identified (238) and this suppression is reversible by RA supplementation. CYP26B1 gene encodes an RA metabolizing cytochrome P450 enzyme that is expressed in embryonic lung tissues undergoing morphogenesis. CYP26B1 fine tunes the activity of RA. The primary function of lecithin retinol acyltransferase is to convert retinol to the more functional retinyl esters. I report that nitrofen inhibits CYP26B1 and lecithin retinol acyltransferase. Studies have shown that inhibiting CYP26 augments RA function in human epidermal keratinocytes (239).

The above data corroborates previous findings that RA is diminished upon nitrofen exposure. I found that CYP26B1 and lecithin retinol acyltransferase correlate positively with miR-142-5p expression, whereas miR-592 negatively correlates with CYP26B1 expression. These results confirm the previous evidence from clinical studies that showed retinol levels to be lower in babies born with CDH (240). MiR-

10a is an RA target (241) and is localized in the vicinity of the Homeobox (HOXB) cluster of chromosome 17 in humans. The HOXB locus is involved in lung branching morphogenesis and has a putative role in determining cell fate decision in the lung (242). Our study identified nitrofen-mediated upregulation of rno-miR-10b. MiR-10a (a close homolog of MiR-10b) is a known mediator of RHOC that functions through the upstream axis TWIST-miR-10b-HOXD10-RHOC (243). PI3K/mTOR signaling is required for miR-10 activity and depends on their interactions with 5'-oligopyrimidine tract at their 5' termini (5'TOP-mRNAs) and cell type (244). Doi et al. (245) previously reported that PI3K mRNA is decreased in E21 nitrofen-induced hypoplastic lungs. They also showed with immunohistochemistry that PI3K protein was diminished in the distal epithelium of E18 CDH lungs and that PI3K overall intensity was decreased in E21 CDH lungs (245).

Our NGS analysis demonstrated that rno-miR-142-5p and -291a-5p are differentially expressed and correlate positively with BAZ2A, a chromatin-dependent transcriptional regulator; an integral component of chromatin re-modeling complexes. I report that rno-miR-3585-5p negatively alters two genes; BAZ2A and SIRPA; however, the exact mechanism is poorly understood. It has been shown that SIRPA, a member of the signal regulatory-protein family, can interact with surfactant proteins A and D to suppress alveolar phagocytosis without triggering an inflammatory response (246). This protein can be phosphorylated by tyrosine kinases and is found to participate in signal transduction triggered by CD47 and mediated by various growth factor receptors.

3.6. Limitations

One of the limitations of our study is the use of the teratogen nitrofen to induce lung hypoplasia and CDH. Even though this model has been widely used and accepted to study the pathogenesis of abnormal lung development and CDH (reviewed by van Loenhout et al. (186)), a direct link between nitrofen use and abnormal lung development and CDH in humans has never been established.

When performing a transcriptomic analysis, there are limitations that are inherent to the design of such a study. I have shown that several genes and miRNAs are involved in nitrofen-induced abnormal lung development and CDH. How these transcript differences translate to changes in protein structure and function remains unknown. A high-throughput proteomic survey combined with immunoblotting candidate proteins would be ideal to assess these differences. It is possible that the sampling differences between the NGS study and that conducted by the biological replicates could be the strongest effect being shown. The RNA used for the experiment was pooled from multiple dams whereas RNA used for the functional gene expression analysis was true biological replicates derived from multiple dams. These biological replicates are essential as nitrofen induces a CDH-like lung phenotype in up to 100% of E13.5 rats. Due to this uncertainty in the developmental phenotype, the variability that would be induced at the genetic level due to nitrofen would be more pronounced than shown in the phenotypic presentation of nitrofen-induced CDH. This biological bias combined with the technical variability in NGS complicates the functional assessment of the NGS results. Further extrapolations into the transcriptomic effects of nitrofen warrant a stronger presence of biological

diversity amongst samples. An important follow up study would be a combined miRNA and mRNA sequencing experiment across consecutive stages of lung development. In our study, the age-matched embryonic tissues and the nature of the collected samples limited our primary material and thus I had to pool multiple lungs for analysis. This approach did not permit the proper assessment of biological variation. Additionally, using a mixed sample approach studying a highly heterogeneous organ such as the lung does not permit focusing on functionally distinct regions or substructures, making the establishment of expression profiles less informative. I could not confirm tissue-specific, strain-specific or cell-specific differential miRNA or gene expression pattern for all reads analyzed. This would have been an important step in elucidating miRNA functions. Future studies analyzing cell type differences across the various tissues and linking cell types to transcriptome changes would provide a better understanding at which level these changes have an effect.

3.7. Closing Remarks

My study characterizes the transcriptome associated with nitrofen-induced abnormal lung development using NGS technology. I identified several miRNAs, including members of the miR-290, -500, -194, -203, -200c, -200b, -101a, -144, -193, -145, -142, -215, -384, -504, -10a and -296 families, that deserve further investigation. Our data highlight the importance of PI3K, TGF-β, RA, Wnt and cell cycle kinase signaling in nitrofen-induced rat lung hypoplasia.

CHAPTER 4

Application of laser scanning cytometry in vascular smooth muscle remodeling

In this chapter, the first section reviews the current research methods, models and markers of PPHN relevant to oxidative and nitrosative stress as well as cell fate commitment, with an emphasis on apoptosis and proliferation. In the second section, I establish that LSC, a method that utilizes a fluidic matrix to grow cells, is appropriate for exploring the integrated role of pulsatile stretch and hypoxia in PAH oxidative environment and the resultant tissue remodeling. I describe how the LSC method is suitable for monitoring arterial cytoskeletal remodeling in vitro, a process closely associated with PHN. I hypothesize that: (a) LSC is a valid method that can be used in the analysis of nuclear and cytosolic fluorescence, and (b) the cumulative effects of mechanical strain together with hypoxia promote ROS formation. The molecular events that are triggered in response to hypoxia and mechanical overload of the pulmonary circuit can be demonstrated *in vitro* by subjecting hypoxic cultured PASM cells to repetitive stretch-relaxation cycles at rates comparable to dynamic stretch *in vivo*. The altered cytoskeleton in the form of filamentous to globular actin (F: G-actin) ratio can be imaged and quantitated at the cellular level by LSC. LSC can remove the nuclear G-actin fluorescence from the total G-actin fluorescence. The findings obtained by LSC *in vitro* are amenable to validation in any *in vivo* model of interest.

4.1. Cytoskeletal remodeling and regulation of cell fate in the hypertensive neonatal pulmonary artery in response to stress: Contribution Statement

I, Dina Johar, made the following contributions to this study:

- Conceived of, designed, developed the search strategy, and conducted the literature review
- wrote the manuscript

Section 4.1 is reprinted with permission from: J of Cellular Physiology. Copyright (2017); 9999:1–16. https://doi.org/10.1002/jcp.25950

Section 4.1. covers a range of subsections 4.3 to 4.14

4.2. The application of LCS in cytoskeletal remodeling: Contribution statement

I, Dina Johar, made the following contributions to this study:
- contributed to the conception and design of the manuscript.
- tested protocols to optimize experimental conditions of the LSC experiments.
- conducted the LSC experiments and generated all the figures included in the manuscript.
- conducted the western blot experiments on the expression of SM markers.
- conducted the DCF and DHE assays for quantification of oxidative stress markers.
- performed statistical analysis of the above mentioned data.
- interpreted the results and wrote the complete manuscript and submitted the manuscript.
- supported the publication and software charges associated with this work, read and approved the work for publication.

Other contributors:

- Gerald Stelmack

Section 4.2 covers a range of subsections from 4.15 to 4.21.

4.3. Abstract

Neonatal pulmonary hypertension (PHN) is a lethal progressive disease that occurs in prenatal circulatory transition. Mechanical wall strain caused by cardiac pulsation integrates with hypoxia to generate rapidly progressive myocyte cytoskeleton disassembly and failure to exert force generation. The physiological responses to such an interaction have not been investigated. The persistent phenotype does not respond to traditional vasodilator therapy; hence, there is a need for new treatment strategies to improve the morbidity and mortality outcomes. I reviewed the current research methods, models and markers of PPHN relevant to oxidative and nitrosative stress as well as cell fate commitment, with an emphasis on apoptosis and proliferation. I surveyed potential investigations into the role of senescence in neonatal PHN cell fate decision programming during vasodilator treatment and suggested putative drug targets to improve clinical outcomes. I identified important signaling intermediates of senescence and cell cycle entry regulation in hypertensive pulmonary arterial tissues (247).

At term, fluids and blood in neonatal lung alveoli are replaced with inspired gases resulting in reduced alveolar pressure and relaxed pulmonary artery pressure, which allows inspiration. Persistent PHN is a sporadic vascular disease that begins in the hypoxic intrauterine environment and progresses throughout the perinatal circulatory transition (248, 249). The pulmonary vasculature fails to relax due to perinatal hypoxia, inflammation or direct lung injury (248, 250). The incidence is 1-6 per 1000 births in North America of whom 30% die or require ventilator assistance (251). Persistent PHN is associated with hypoxemia, endothelial and SM dysfunction,

pulmonary vascular constriction and arterial remodeling (252). Hypoxia-induced hyperproliferative signaling promotes vascular fibrosis; that is, thickening of the arterial wall, which in turn increases stiffness and resistance to vasodilator therapy such as nitric oxide (NO) (253). Hypoxia promotes the excessive proliferation of arterial media and adventitia, rendering PHN difficult to treat or persistent. The latter is characterized by impaired arterial distensibility and results in fixed and irreversible pulmonary vascular resistance. SMC undergo cyclic mechanical stretch during the cardiac cycle. In unresolved PHN, the pulsatile stretch is exacerbated, and it alters myocyte phenotype commitment (253-255) and induces ROS, causing significant damage to the cytoskeletal structures of the vessel (256).

Various models of neonatal PPHN have been studied to assess the physiological response to individual stressors (256-261), but the integrated physiological response of concurrent multiple etiological effectors has not been investigated. The initial sections of this chapter (to 4.17) aim to review the current research methods and markers of neonatal PPHN. I limit the discussions to current methods, markers, and signaling that are relevant to oxidative and nitrosative stress. Additionally, I refer to the current therapies and connect known pathways of reactive oxygen and nitrogen species (ROS/RNS) generation with biomechanical signaling and uncover new targets for therapy. Subsequent sections of the chapter (4.16.4 and beyond) describe the use of laser scanning cytometry for examining the cellular remodelling that accompanies PPHN. In combination, this chapter will provide a new perspective on the cellular mechanisms associated with the onset of PPHN and novel

approaches for monitoring some of the critical changes that can be quantified as cell changes ensue.

4.4. Persistent PHN and the cell cycle

The progression of pulmonary arterial proliferation requires the normally quiescent PASM cells to enter and pass through the cell cycle. Cell cycle progression depends on the regulation of cyclin proteins and their associated CDKs. These complexes regulate proliferation by phosphorylating and deactivating the transcriptional repressor Retinoblastoma (Rb) and allowing the expression of genes that are required for cell cycle entry (Figure 4.1). Different cell fate decisions are implicated in the pathogenicity of PPHN including an imbalance in autophagy, proliferation, and resistance to apoptosis to varying degrees throughout phenotype progression (252, 255, 262, 263). Senescence is a permanent cell cycle arrest and typically depends on the cell cycle regulators p53 and pRb functions to sustain cell survival in response to DNA damage or constitutive environmental insults (Figure 4.1). The attributes of senescent cells include a flattened cytoplasm, inhibition of proteasomal and lysosomal pathways (264), accumulation of lipofuscin pigment, lipid vacuole formation, nuclear pyknosis, expression of cyclin-dependent kinase inhibitors (CDKI), loss of ribosomal RNA, decline in transcription, decline in energy production, decline in protein synthesis, accumulation of calcium ions, changes in plasma membrane permeability, degeneration of mitochondria, the formation of senescence-associated heterochromatin foci, and the senescence-associated secretory phenotype (SASP) (265). Senescent cells, however, are metabolically active.

The function of the cell is altered by the increased secretion of inflammatory factors such as interleukin IL-6 and IL-8 produced by the secretory cells as well as other factors and cells of the innate and acquired immune system. These secretions influence the interaction of senescent cells with the microenvironment via autocrine or paracrine loops. SASP is implicated in chronic obstructive pulmonary disease (COPD) (266) and IPF via a mechanism that involves the loss of regulatory autophagy (267). In pulmonary endothelial senescence (262), telomere length shortening secondary to ROS-induced genotoxicity was suggested as a putative senescence mechanism (268). Whether SASP contributes to the onset of arterial wall fibrosis in hypoxic PPHN, and an immune/inflammatory mechanism secondary to SASP contributes to arterial wall dishomeostasis and a specific cell fate decision has not been explored. Future research explores the putative role of senescence or SASP and associated alternative pathways in pulmonary hypertensive vasculature remodeling in the newborn.

4.5. The role of senescence in the modulation of the cell fate decision during PPHN treatment

P53 is a key regulator of the DNA damage response and a mediator of cell fate decision. Intensive DNA damage can trigger either cell fate; apoptosis or necrosis. When the ability to proliferate is completely lost due to p53 dysfunction, subsequently, the stem cell pool and microenvironment are depleted. The cell is then instructed to undergo senescence or autophagy, and the loss of p53 function augments proliferation. It is not clearly demonstrated if current PPHN therapy, i.e., NO, in a hypoxic environment can induce senescence in PASM cells.

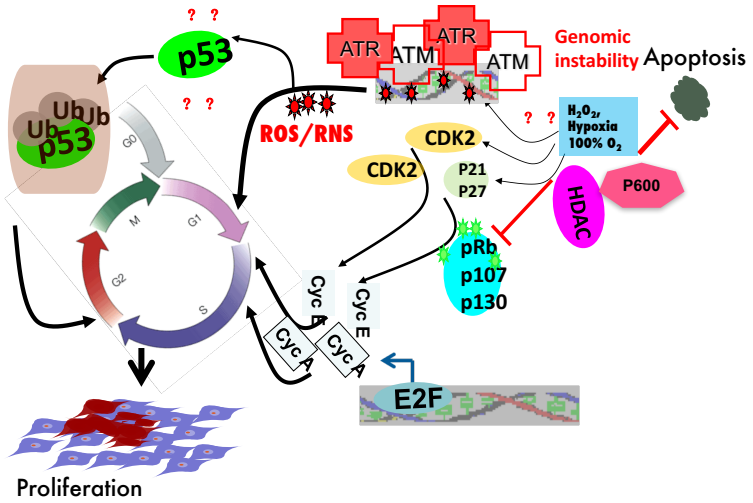

Figure 4.1. Hypoxia integrates with oxidative and nitrosative stress signaling to induce the cell cycle by a mechanism that is yet to be identified. p16, p21, and p27 are three CDKI that associate with and inactivate CDK, which results in growth arrest. Hypoxia promotes PASM proliferation by p27 protein degradation. p27 regulates SM proliferation in vitro. P27(Kip1) is a member of the Cip/Kip family of CDK inhibitors. p27 binds to G1 cyclin/CDK complexes (cyclin D/CDK4, cyclin E/CDK2, and cyclin A/CDK2) to inhibit their kinase activity and negatively regulate the cell cycle by blocking the cell at the G1:S transition. One of the mechanisms through which hypoxia maintains the proliferative ability include the E2F family of transcription factors, that is essential for cell cycle progression. Of the eight family members, E2F1, is a downstream effector of cell cycle regulators that plays a critical role in governing DNA synthesis. p27 is an upstream factor of E2F1, Cyclin D1 is downstream effector of p27 and upstream factor of E2F1 and is downregulated in PASM isolated from NHE1-deficient mice with decreased hypoxic PHN. E2F1 regulates CDK that are responsible for G1:S transition. NHE1 knockout significantly decreases the expression of Rho kinase 1 and 2. In hypoxia, what disrupts Rb-E2F complexes, resulting in the constitutive expression of E2F-responsive genes and promotes premature S phase entry and DNA synthesis is currently unknown. What hypoxia does so that it affects the expression of S phase genes by directly interacting with E2F factors is currently unknown. Normally p53 is required for p21 (Cip1) inhibition of cell cycle progression and transcriptional suppression of E2F gene activation of cell cycle progression. The Rb protein is a negative regulator of E2F1 and is controlled by the activity of upstream CDK that are activated during transition from Go:G1. ROS induce a DNA damage response that triggers DNA repair and cell cycle checkpoints, which in turn, maintain the integrity of the genome via p53 and Rb. P53 and Rb promote cell fates such as transient cell cycle arrest and DNA repair, cell death, that is, apoptosis, or permanent cell cycle arrest, that is, senescence or an imbalanced combination between apoptosis, senescence, and proliferation in the PHN SM. The induction of p21 and p27 results in Rb phosphorylation and Rb-E2F-mediated transcriptional repression. HDAC, histone deacetylase; Ub, ubiquitin (247).

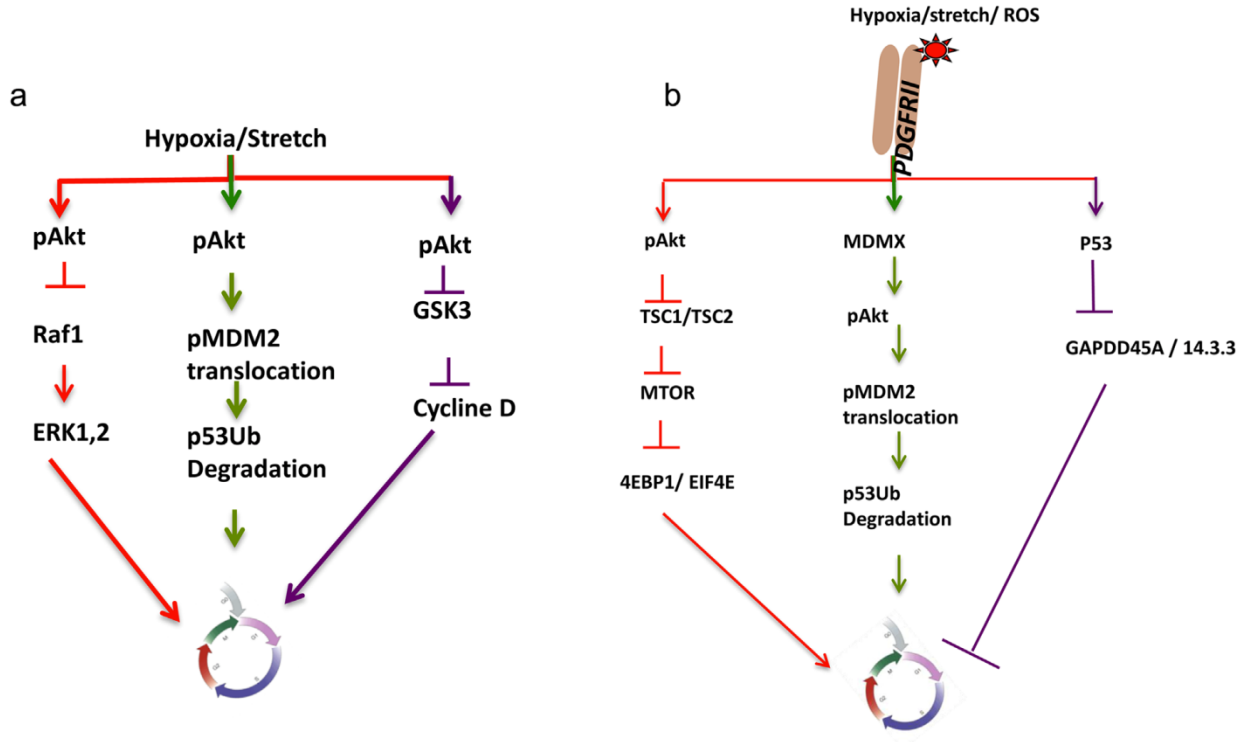

Figure 4.2. Putative models that may contribute to biomechanical signaling upstream of p53 are shown. (a) The AKT/MDM2 (Mouse double minute 2 homolog) model: Future investigations need to determine whether the phosphorylation of AKT triggers the activation and translocation of MDM2 to the nucleus and thus targets p53 for ubiquitination and degradation, which promotes cell cycle progression. The glycogen synthase kinase 3 (GSK) pathway is another putative pathway. Further investigations need to determine whether activation of AKT elicits inhibition of GSK3 and therefore the downregulation of cyclin D and cell cycle progression. (b) Future research is required to investigate the effect of hypoxia and stretch on the regulation of the TSC1/TSC2 (tuberous sclerosis) complex, which may elicit the mechanistic target of rapamycin (mTOR) inhibition and block eukaryotic initiation factor (eIF)4E-binding protein 1 (4EBP1/eIF4E) and protein synthesis and, thereby, indirectly affect G1:S transition. Downstream of platelet derived growth factor receptor B (PDGFRB), it is unknown whether MDMX upstream of AKT is activated, which eventually activates MDM2 to trigger p53 ubiquitination and translocation to the cytosol for degradation and promotion of death. The effect of hypoxia and stretch on growth arrest and DNA-damage-inducible protein GADD45 α (GADD45 α) and 14.3.3 may inhibit the G2:M transition downstream of p53 and arrest cell growth (247).

Whether PASM cells can undergo multiple different cell fates in response to treatment is unclear. Whether the cell fate decision can be switched to senescence in a subset of airway cells is also not clear. Assuming this hypothesis is true, remodeling molecular switches such as p53 to change cell fate from proliferative or senescence to apoptosis may reduce resistance to vasodilator therapy. A putative approach would be to characterize senescence in PASM cells and use such a culture to evaluate the potential of cells to undergo senescence after oxidant-induced DNA damage. This model is an ideal resource to identify mechanisms of resistance to current therapies. I outline two models involving these mechanisms in (Figure 4.2). Characterization of the *in vitro* model is required to ensure the inclusion of i) a positive control of senescence with the functional expression of p53+/+; ii) a negative control of senescence p53+/- mutant; iii) p53 null mutant -/-, and iv) a cell line that is resistant to telomere shortening, i.e., immortalized human ASM (hASM) cell line HC82.

4.6. Unfolded protein response (UPR) to oxidative and nitrosative stress

Nitric oxide is a known vasodilator that is exogenously inhaled to reduce pulmonary vascular resistance. Depending on the concentration, >10 particles per million worsens arterial oxygenation. Higher doses are potentially toxic. NO-derived toxic nitrogen oxides, hydroxyl, and peroxynitrite radicals elicit pulmonary cellular injury (269). The accumulation of misfolded proteins in the ER constitutes a form of cellular stress termed the UPR (270). SMC undergo cyclic mechanical stretch during the cardiac beat. Mechanical stretch has been implicated in the generation of ROS

(254), increased mobilization of calcium (271) and initiation of ER stress (272). Current strategies study ER stress in contractile SM that is challenged by hypoxia and pulsatile stretch.

Previously, marked alteration of the ROS environment and antioxidant enzyme function in hypoxic myocytes was reported and included increased cytosolic and mitochondrial ROS (273), altered mitochondrial permeability, nitration of mitochondrial membrane proteins, and downregulation of the oxidoreductases, namely superoxide dismutase (SOD) activity (269) and activation of cytosolic catalase (274). Biomechanical signaling crosstalks with high levels of intracellular ROS in hypoxic myocytes to cause vascular contraction (275, 276). The mechanism has yet to be resolved. In unresolved PAH, pulsatile stretch becomes a strain due to the stiffness of the artery and induces apoptosis in stressed vascular myocytes (255). Apoptosis can be activated by the release of pro-apoptotic factors from the mitochondria or via UPR (274, 277, 278). Hypoxia and strain can activate UPR signaling (277). Prolonged ER stress promotes apoptosis (279). The SM composition of the hypoxic pulmonary arterial wall is influenced by selective cell cycle re-entry and initiation of apoptotic signaling (280, 281).

4.7. The role of integrins and focal adhesion kinases (FAK) in arterial remodeling

Previous studies showed that wall strain induces integrins and FAK to activate early gene transcription of SM (282) via extracellular activated kinases (ERK1/2) (283). Strain activates small G protein (Ras homolog gene family member A (RhoA)

and its associated downstream Rho kinase to converge with ERK1/2 and protein kinase AKT and promotes cell cycle progression by downregulating p27 (254, 283, 284). Rho kinase regulates actin polymerization (285, 286). Stretch-induced ERK1/2 activation is modulated by the state of actin polymerization. However, mechanisms that link hyperplasia to actin disassembly have been uncovered (287). Rho acts through several pathways to polymerize and stabilize actin filaments, which may explain the more pronounced effect of Rho inhibition than of its kinase. The integrity of the cytoskeleton is essential for ERK-dependent gene transcription in response to stretch (Figure 4.3). Both angiotensin II (AT2) and endothelin A (ET_A) cause ERK phosphorylation in SM via a mechanism involving protein kinase C (PKC) and cellular src kinase (c-src). The mechanisms activating the Rho and ERK pathways exhibit crosstalk at the level of SRF. SRF controls the transcription of immediate-early genes and SM differentiation genes. At the Ca^{2+} level, Ca^{2+} regulates both immediate early gene expression via Ca^{2+}/calmodulin-dependent protein kinase (CaMK) and cAMP response element-binding protein (CREB) and differentiation genes in a Rho kinase/myocardin/SRF-dependent mechanism (Figure 4.3).

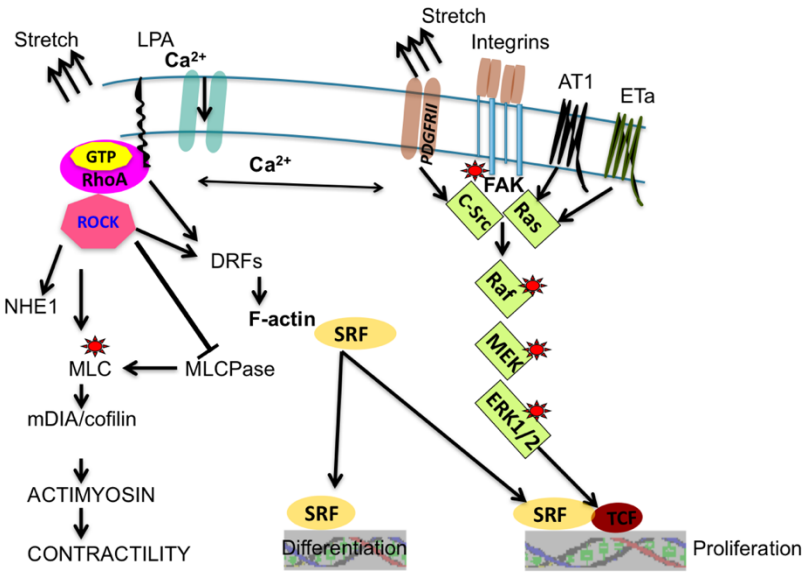

Figure 4.3. The small G protein coupled receptor (Rho) mediates the assembly and disassembly of actin filaments and ensures the integrity of the cytoskeleton which is essential for ERK-dependent gene transcription in response to stretch. Absence of stretch causes actin depolymerization, and loss of contractile phenotype, whereas growth factor stimulation of dissociated SM cells causes proliferation but with loss of contractility. Regulation of contractility and proliferation of SM by integrins and ET_A in normal vascular biology is shown. Mechanical forces are provided via interactions of extracellular matrix proteins with integrins in the cell membrane, activating the phosphorylation of FAK, which stimulates the rapidly accelerated fibrosarcoma RAF-MEK (MAP-ERK Kinase)-ERK 1/2 pathway and thus immediate early gene expression. Another cascade is triggered by factors that activate G protein coupled receptors (GPCR) such as angiotensin I (ATI), ET_A receptors, and tyrosine kinases, for example, PDGFR. Once phosphorylated, ERK is capable of entering the nucleus and phosphorylating ternary complex factors (TCF), which bind to SRF and activate the transcription of immediate early genes such as the transforming gene of the FBJ MSV (Finkel–Biskis–Jinkins murine osteogenic sarcoma virus), c-fos, and the putative transforming gene of avian sarcoma virus 17 (c-jun), and the early growth response protein 1 (Egr1). Integrins regulate the Ras homolog gene family, member A (RhoA) but how this regulation affects proliferation upon hypoxia and/or stretch has not been investigated. RhoA activation and its downstream effector Rho kinase were suggested in many studies to be involved in stretch-induced SM proliferation and inhibition of this pathway completely inhibited pulsatile stretch induced SM proliferation. Although the upstream signals responsible for the activation of Rho/Rho kinase signaling in mechanical hypoxic–induced PHN is unknown, this pathway is a convergent point for several vasoconstrictor signals such as those signals mediated by GPCR, receptor tyrosine kinase (RTK) and integrin clustering. Rho kinase inhibitors are more effective vasodilators in rat models of PHN, and this family includes compounds such as tyrosine kinase inhibitor Gleevec that inhibits PASM proliferation and reverses PAH in the monocrotaline and in chronic hypoxic injury rat models. Inhibition of Rho kinase inhibits ERK's translocation to the nucleus without affecting ERK's phosphorylation in SM. Both AT2 and ET_A cause ERK phosphorylation in SM by a mechanism involving PKC and c-src (247).

Growth factors (288) and integrins (289) can induce FAK-mediated cell survival (290) (Figure 4.3). However, if growth factors are limiting, the main signaling pathway to convey growth signals is through the ERK cascade. FAK and Src homology 2 domain-containing transforming protein (Shc), through integrin-activated Shc phosphorylation, can contribute to the activation of ERK/MAPK. It appears that Shc is responsible for the initial high-level activation of ERK, and FAK sustains ERK activation (291-295). Activated FAK binds many molecules (296), mediating integrin- (289) or serum-induced (297) activation of the MAPK pathways, which promote cell proliferation.

The absence of stretch causes actin depolymerization and loss of the contractile phenotype. This is studied using two methods as follows: 1) fractionation by ultra centrifugation; and 2) confocal microscopy of tissue sections selectively labeled for filamentous (F) and globular (G) actin by phalloidin and DNAse I (298). Both methods indicate a lower F:G-actin ratio in unstretched vs. stretched veins. Integrins regulate RhoA; however, how this regulation affects proliferation when hypoxia is coupled together with or independent of stretch cues has not been investigated in PPHN. Johar and Bernstein (299) recently proposed a role for the RhoA/Rho kinase pathway in cytoskeletal reorganization in association with integrins upon exposure of SM cells to hypoxia coupled with or independent of stretch.

Another degree of regulation for integrins involves ligation of its vascular component αvβ3 that promotes cell survival during angiogenesis through the

suppression of the key cell cycle regulator p53 and increased CDK inhibitor 1A (p21) expression, which suppresses the Bcl-2-associated X protein (Bax) cell death pathway (300). Activation of Shc by the integrin vascular components α1β1, α5β1 and αvβ3 may be protective against apoptosis (292, 294). These and other findings demonstrate that integrins can mediate cell survival at various levels of the apoptotic pathways, indicating that maybe one or more of these pathways are triggered under various conditions.

The extracellular matrix (ECM)-derived signals transmitted by integrins are in part responsible for either the proliferation of cells or the exiting of the cell cycle for differentiation. A loss of this attachment causes healthy cells to enter apoptosis (301). The latter is an important process in tissue homeostasis to ensure that cells grow in the appropriate location. AKT, in turn, regulates mediators of apoptosis, such as caspase-9 and Bcl-2-associated death promoter (BAD). Also, FAK activates AKT through PI3K and inhibits caspase-3 and apoptosis through PI3K/AKT/NF-κB (nuclear factor-kappa B) signaling (302). Lastly, Shc activates the MAPK pathway through growth factor receptor-bound protein 2 (GrB2) associations and can also activate PI3K/AKT (303). There ARE several ways in which AKT regulates apoptosis including the inhibition of caspase-9 and -3 (304) and the inhibition of the Bax conformational change thereby preventing Bax from translocating to the mitochondria (305). Currently, there is a trend in linking these observations to the activation of ER stress *in vivo*.

4.8. Research method to investigate SASP

New research focuses on exploring the contribution of senescence or SASP in the progression of PPHN and identifying key molecular effectors of this program. I have proposed employing an *in vitro* model of neonatal PPHN to: 1) deregulate senescence or SASP phenotypes and determine whether treatment with a combined exogenous antioxidant/NO therapy could attenuate SASP-induced immunomodulatory potential, and 2) determine whether such deregulation may reverse tissue remodeling in the hypertensive pulmonary circulation *in vitro* (Figure 4.4). Tissue culture data would be validated via the immunostaining of pulmonary artery sections recapitulated from a previously published porcine model of the hypoxic PHN (249, 274, 306). Senescence-associated β-galactosidase (SA β-gal) is a lysosomal enzyme marker that is upregulated in senescence and thereby enables the detection and quantitation of senescence induction.

The proposed approach models PHN research using PASM cells from a newborn piglet and exposing them to pulsatile stretch within a hypoxic environment in tissue culture (Figure 4.4). Repetitive stretch-relaxation cycles are applied at physiological rates comparable to the heart rate of a neonate. Normoxic (21% O2) and hypoxic (10% or 4% O2) pulmonary arterial myocytes from the newborn piglet are exposed for 72 hours to ± 5% stretch from basal length at a frequency of 1 Hz *in vitro*. In this model, normoxic cells treated with pulsatile stretch functions as the control state, while hypoxia in the absence of pulsatile stretch models the pulmonary hypertensive state. It is anticipated that pulsatile mechanical stretch downregulates

cell cycle progression by upregulating ROS generation and eventually upregulating senescence; hypoxia in the absence of mechanical stretch triggers the onset of excess SM proliferation. The focus is on demonstrating whether hypoxia provokes senescence or SASP independent of and together with the stretch. Additionally, the aim is to determine whether non-stretching hypoxic cells grow indefinitely, and whether increased ROS/RNS, senescence or SASP cooperate via a positive feedback loop to sustain survival in non-stretching dysfunctional vascular myocytes.

The application of the hypertensive *in vitro* model outlined in Figure 4.4 is particularly important in identifying the immunomodulatory potential of senescence or the SASP program in PPHN and characterizing senescence in response to a high level of oxidative and nitrosative stress. The goal is to determine whether treatment with exogenous antioxidants could attenuate the combined effects of hypoxia, loss of pulsatile stretch, and SASP-induced immunomodulation in the hypertensive pulmonary circulation and to attempt to reverse tissue remodeling secondary to such environmental cues in the presence of ROS/RNS scavengers. Examples of the available antioxidant therapy strategies include heme oxygenase-1 (HO-1). HO-1 catalyzes the degradation of heme to three enzymatic end-products as follows: carbon monoxide (CO), free Fe^{+2}, and biliverdin. Carbon monoxide and HO-1

A

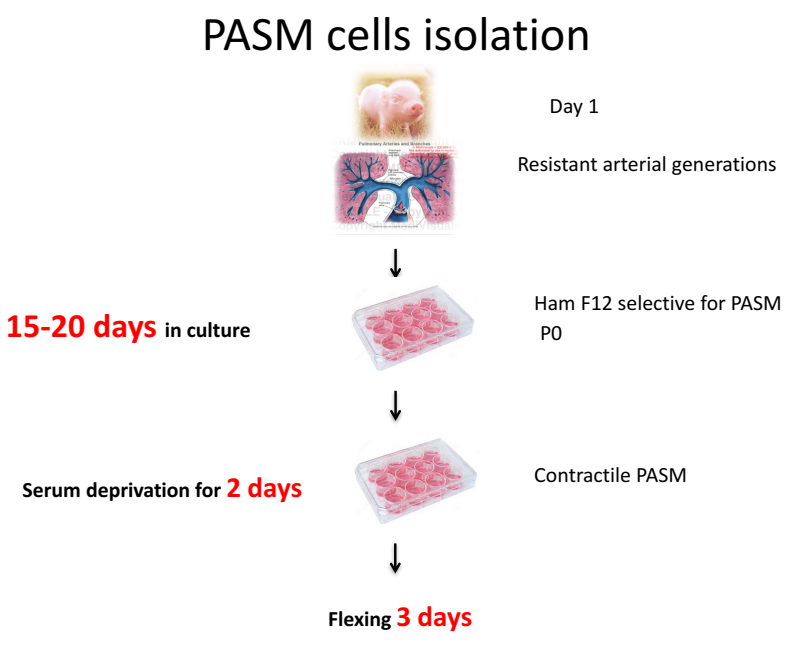

B

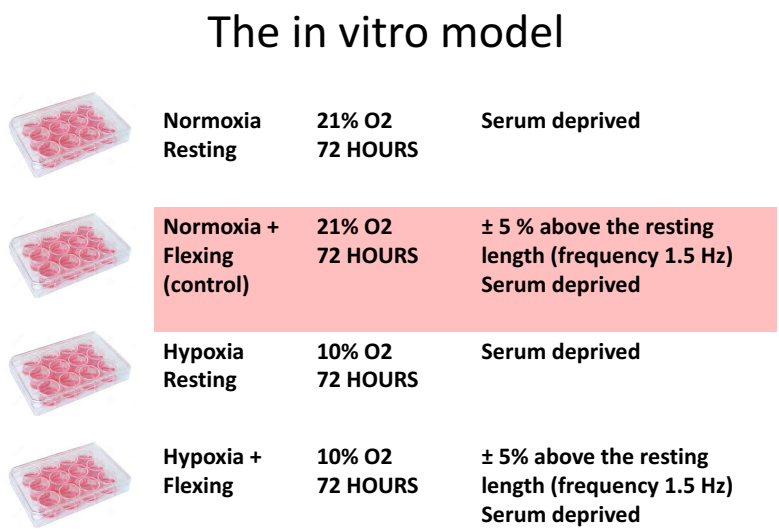

Figure 4.4. An *in vitro* model of neonatal PHN. (A) The method is PASM cell-specific. As collagenase disintegrates the ECM, non-muscle cells do not adhere in low Ca^{2+} conditions. Muscle cell isolation from the tissue does not seem to need high $CaCl_2$. A low gradient of $CaCl_2$ and F12-Ham is true optimal condition. (B) PASM cells from a newborn piglet are exposed to pulsatile stretch within a hypoxic or normoxic environment in tissue culture. Normoxic cells with the application of pulsatile stretch is the control state, while hypoxia in the absence of pulsatile stretch models the pulmonary hypertensive state (247).

are protective in PHN due to the relaxation of vascular tone and SM cell proliferation inhibition by CO (307).

The effect of hypoxia together with cyclic stretch on cell cycle progression can be examined using propidium iodide/5-Bromo-2´-Deoxyuridine (PI/BrdU) flow cytometry for investigating the cell cycle in PASM. If cell cycle progression is activated, demonstrating the expression and role of cell cycle regulators p53, pRb, cyclins (E and D) and CDK, CDKI, and transcriptional regulators E2F1, avian myelocytomatosis viral oncogene homolog c-myc and the Krüppel-like factor (KLF5) is key in initiating SM proliferation.

The proposed research approach is based on the previously published normobaric hypoxia models (249, 256, 308). The intent is to demonstrate the cumulative effects of hypoxia together with or independent of cyclic stretch on cell death and proliferative signaling in pulmonary arterial SM *in vitro*. In a hypoxic environment, the arterial SM cultures are exposed to repetitive circumferential stretch-relaxation cycles at rates comparable to physiological stretch overload *in vivo*. The porcine model uses pulmonary resistant arteries of the 2nd to 6th generation. The arteries are microdissected from the lungs of newborn (<24 h) piglets and recovered in cold Ca^{2+}-free physiological buffer. Minced vessels are then digested with collagenase and papain according to Shimoda et al. (306) (Figure 4.4). The cells are dispersed by gentle trituration and resuspended in Hams F-12 medium supplemented with 10% fetal bovine serum (FBS) and plated on collagen-coated Flexercell 6-well flexible culture dishes. Primary 70% confluent SM monolayers are established, then serum-starved with 1% insulin/transferrin/selenium for three days

to synchronize in a contractile phenotype before experimentation. Myocytes are then allocated to four study groups as follows: [i] normoxia/no stretch (control group; 21% O_2, 5% CO_2, balance N_2); [ii] normoxia/stretched (cyclic stretch to ±5% from resting length, frequency 1 Hz); [iii] hypoxia/no stretch (10% O_2); and [iv] hypoxia/stretched, as presented above in Figure 4.4. Myocytes in mechanically stretched groups are placed on the Flexercell Strain Unit, which applies uniform circumferential stretch to the collagen matrix to simulate the wall strain of vascular hypertension, for 72 hours in a dedicated hypoxic (10% O_2) or normoxic (21% O_2) incubator. Oxygen and carbon dioxide partial pressures, PO_2 and PCO_2, are maintained within 1% tolerance. After 72 hours of environmental exposure to hypoxia together with or independent of cyclic strain, cells are either fixed or cell lysates are collected in appropriate lysis buffers for quantifying mitochondrial and ER stress markers. The same model is amenable to studying cells in a hyperoxic environment (>21% O_2), (Figure 4.4).

4.9. Mitochondrial stress

BNIP3, BCL2/adenovirus E1B 19 kDa protein-interacting protein 3, induces delayed cell death by autophagic cell death. The pro-apoptotic function of BNIP3 has been proposed to depend on its membrane association at either mitochondrial or non-mitochondrial sites and through a selective interaction with Bcl2/Bcl-XL (B-cell lymphoma-extra large) via the NH-terminal (aa 1-49) region. The latter interaction is thought to regulate the induction of apoptosis by modulating the activity of BNIP3 or altering its conformation and accessibility to other cofactors (309). Full-length BNIP3

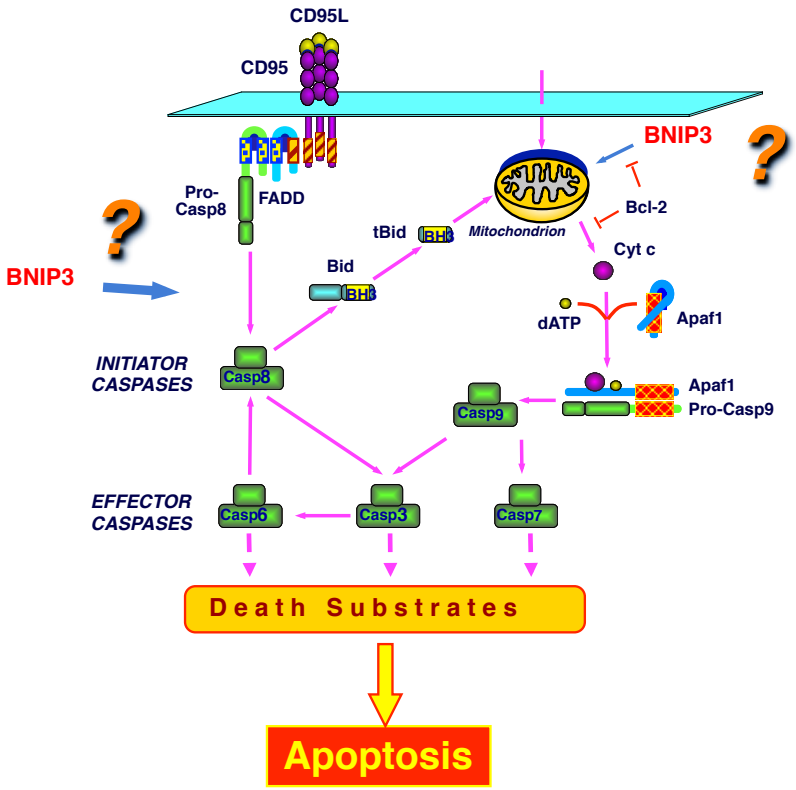

Figure 4.5. BNIP3 is a putative inducer of apoptosis. BNIP3 is a pro-apoptotic protein that interacts with viral anti-apoptotic proteins. The mammalian protein in Homo sapiens cDNA is 1,535 bp, of which the encoded protein is 194 aa, and the predicted molecular weight is 21.54 kD with a pI of 6.08; however, it migrates on the sodium dodecyl sulfate-polyacrylamide gels as a monomer of 30 kD and a homodimer of 60 kD. The BH3 domain contains Leu, Asp, and Ile as conserved residues. The BH3 domain of the Bcl2 family of proapoptotic proteins (Bik, Bid, Bim, Bax, and Bak) is essential for heterodimerization with antiapoptosis proteins. Examples include the following: adenovirus E1B 19 kD, Bcl2, Bcl-XL, *Caenorhabditis elegans* (CED-9), and Epstein–Barr virus (EBV)-encoded proteins (BHRF1) and targeting the green fluorescent heterologous protein GFP to the mitochondria. The carboxy terminus (31 aa) is required for the homodimerization as well as directing the expression to the mitochondria. All BNIP3 proteins contain PEST sequences. It is presumed that these proteins are degraded rapidly after expression in a stage-specific manner as a type of regulation to a lethal protein, and its degradation is controlled by the proteasome (247).

appears to be toxic to bacteria, as described previously for other pro-apoptotic Bcl2 family members, as shown in Figure 4.5. Hypoxia-inducible factor 1a (HIF1a) activates NIP3 expression (310). Under persistent oxygen deprivation conditions, NIP3 primes cells for apoptosis, but hypoxia alone is not a significant effector and cell death requires acidosis. The mechanisms that have been implicated in BNIP3-induced necrosis-like cell death include the loss of mitochondrial membrane potential, outer mitochondrial membrane permeability transition, and oxidative stress (311).

Activation of caspase, apoptotic protease activating factor 1 (Apaf-1), and cytochrome c release are not necessary for BNIP3-mediated apoptosis (312), as shown in Figure 4.5. BNIP3 proteins are rich in Ser/Thr residues, raising the possibility that these proteins can be regulated by phosphorylation in response to phosphorylation signals.

BNIP3 can overcome Bcl2 suppression of apoptosis. Possible mechanisms include acting on Bcl2 or other anti-apoptotic family members that regulate mitochondrial permeability transition pores or cytochrome c release. NIP3 has a different pattern of localization, resembling the pattern exhibited by the mitochondria, cytoplasmic membrane, or nuclear envelope region (313). The variant that lacks the transmembrane domain was mostly expressed as a free cytosolic protein. A minor component of the protein colocalized with the mitochondria, suggesting that it may interact by a mechanism other than membrane insertion (312, 314). NIP3 is sequestered to the nuclear envelope/ER regions by a 19-kDa protein, abrogating its mitochondrial function. The pro-apoptotic activity of BNIP3 is dependent on its transmembrane (TM) domain, as the protein is expressed in the

mitochondria, while the mutant lacking the TM domain or the carboxy terminus does not dimerize or localize to the mitochondria, which ablates its apoptotic activity (314). Mammalian NIP3-like protein X (Nix) (BNIP3L/BNIP3α/B5) and ceBNIP3 from C.

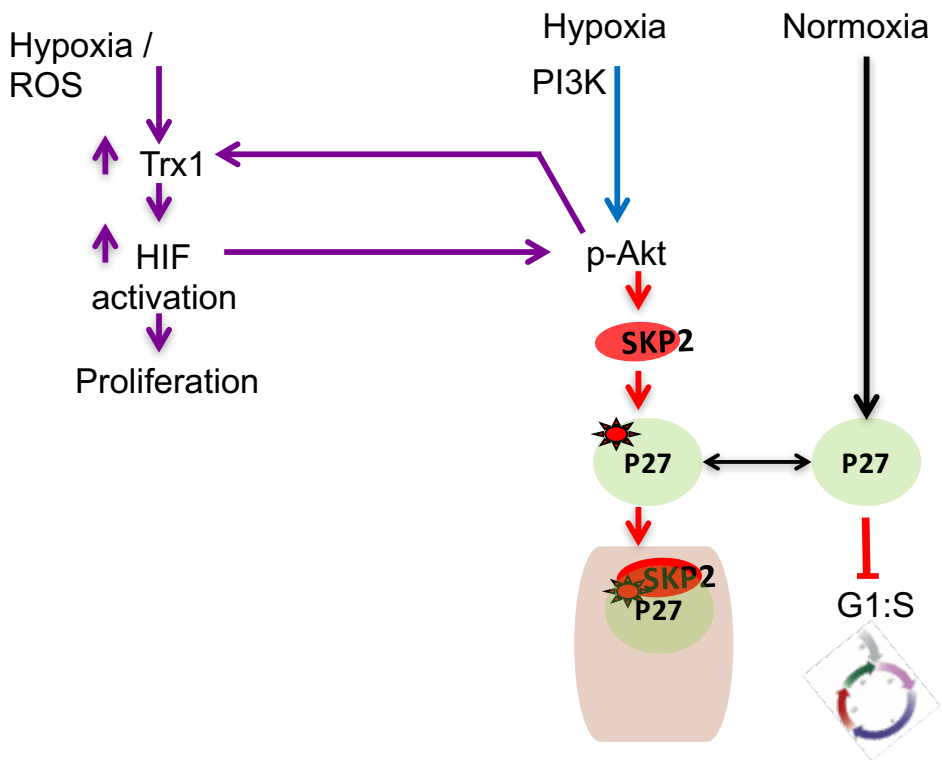

Figure 4.6. Hypoxia-induced PASM proliferation via the AKT/SKP2/p27-associated pathway. Hypoxia initiates PI3K signaling leading to AKT phosphorylation. The pro SKP2 acts in the ubiquitin-dependent proteolytic degradation of p27. The balance of cell proliferation and quiescence is regulated by p27 that inhibits G1 Cyclin/CDK complexes and blocks the cell in the G1:S. Trx1 is a redox protein disulfide reductase that links to AKT-dependent signaling in the mitochondria and cytosol. Nicotinamide adenine dinucleotide phosphate (NADPH) reduces and replenishes oxidized Trx1 from the disulfide to the dithiol state. Trx1 or its receptor TrxR1 are ubiquitously cytosolic, while Trx2 and TrxR2 are predominantly mitochondrial. Trx1 is a redox-dependent transcription factor for HIF-1α. HIF-1α is strongly implicated in PHN pathogenesis. Oxidative stress induced by hypoxia results in hydrogen peroxide (H_2O_2), which causes nuclear accumulation of Trx1. Upregulated Trx1-dependent HIF-1α signaling promotes proliferation with downstream effects on PI3K-AKT signaling in both basal and hypoxia-induced PASM. This effect is dependent on O_2 tension. This model represents the importance of p27 as key regulator of PASM proliferation through the hypoxia/PI3K/AKT pathway which links hypoxia and ROS to cell cycle activation. Skp2, S-phase kinase-associated protein 2 (247).

elegans are structurally and functionally similar to BNIP3. Mitochondrial localization is necessary for the induction of cell death. The mechanism by which these antiapoptosis proteins promote cell death remains to be elucidated.

PASM phenotypes are characterized by immunoblotting for protein markers of SM differentiation such as α-SM actin, β-actin and SM desmin. The basal level of cell cycle regulatory proteins is quantitated by immunoblotting using whole cell lysates and anti-p53, anti-pRb, anti-p27 and anti-p21.

Phosphatase and tensin homolog (PTEN) function relies on reversible oxidation/reduction. Thioredoxin1 (Trx1) regulates PTEN function by serving as the preferential electron donor to reduce oxidized PTEN. The impaired replenishment of ribonucleotide reductase with an electron from knocked-down Trx1 causes DNA damage and reduces PASM proliferation both in normoxia and hypoxia (315). The mechanism of Trx1 is shown in Figure 4.6.

Luo et al. (316) used the hypoxia-induced PHN model in mice to induce hyperplasia and demonstrated that heparin blocked the activation of guanosine-5'-diphosphate-Rho (GDP-Rho) into guanosine-5'-triphosphate-Rho (GTP-Rho) by inactivating guanosine nucleotide exchange factor H1 (GEFH1), which in turn inhibits the activation of Rho kinase 1 and 2 and downregulates both hypoxia-induced PH and sodium NH1 in mice PASM. Hypoxia increased Rho kinase expression and negated heparin's antiproliferative effect on PASM cells from mice and humans. They concluded that p27 is the only CDKI required for the inhibition of PASM proliferation by heparin. AKT regulates SKP2 and p27. AKT regulates the transcription, translation, and stability of SKP2, and eventually that of p27 directly and indirectly, as outlined in

Figure 4.6. In addition, Rho is regulated by PKC and PKA, which inhibit p160Rho kinase. The effect of Rho-kinase inhibitors is associated with decreased pulmonary artery expression of growth factors, cell proliferation markers, matrix protein generation, inflammatory cell infiltration, an increase in signals for apoptosis, and a negative effect on pulmonary artery cell growth, which prevents stress fiber formation and reduces nuclear ERK and tenascin-C expression.

4.10. Signal-induced cell cycle

Hypoxia and oxidative stress signaling integrate with mechanical stretch to induce the cell cycle via a mechanism that is yet to be identified (Figure 4.1). CDKs 2 and 4 activate cell cycle progression, whereas the CDKIs, namely p27kip1, p21cip1 and p16arf, regulate p53 and pRb by suppressing the transcription of the early genes of arterial myocytes and arresting growth. Using the stretch-hypoxia model presented below (Section 4.16.1), cell cycle progression can be addressed by quantitating the cell cycle distribution of p27 and p21 expression using RT-qPCR (for mRNA levels) and immunoblotting (for protein levels). To identify which treatment upregulates cell cycle entry and proliferation, cell cycle phases are quantitated and imaged using Laser Scanning Cytometry (LSC) to compare the effects of different treatments (hypoxia together with or independent of stretch; and normoxia together with or independent of stretch) in comparison with serum-deprived and serum-fed PASM or hASM, using cells selectively labeled for p53, pRb, p27, p21, and p16.

Correlating the level of expression with the degree of proliferation can be demonstrated directly using the statistical modules of LSC.

Importantly, the effects of hypoxia associated with cyclic stretch on mitochondrial function, cellular and mitochondrial ROS, and mitochondrial protein nitration are under current investigation. As mitochondrial mass can increase in the case of decreased mitochondrial function, mitochondria can be visualized with the fluorescent dyes MitoFluor Green or MitoTracker (317, 318). Current approaches for total cell ROS quantitation include dichlorofluorescene, superoxide radical quantitation by dihydroethidium fluorescence, mitochondrial superoxide quantification by MitoSOX staining, and mitochondrial protein nitration by immunoblotting of subcellular fractions using anti-nitrotyrosine. The above markers are amenable to quantitation using LSC in PASM cells while being co-incubated with selective ROS scavengers that are added daily to the cultures or diluent. The ROS scavengers include polyethylene glycol PEG-conjugated SOD, PEG-catalase, NO scavenger N-acetyl-cysteine, and peroxynitrite radical scavenger catalyst 5,10,15,20-tetrakis (4-sulfonatophenyl) porphyria to-iron (III) chloride (FeTTPS) (274).

E2F1, a downstream effector of mechanotransduction signaling, plays a critical role in governing DNA synthesis. It regulates CDK and hence the G1:S transition. P27 is an upstream factor of E2F1 and is downregulated in PASM isolated from sodium-hydrogen exchanger 1 NHE1-deficient mice with hypoxic PHN. Hypoxia disrupts pRb-E2F complexes resulting in the constitutive expression of E2F-responsive genes and premature S phase entry and DNA synthesis through an unknown mechanism (Figure 4.1).

Future research focuses on exploring the integrated effects of hypoxia associated with cyclic mechanical stretch on senescence or inflammation associated with SASP phenotypes. Induction of SASP is accomplished using exogenous oxidant stressors such as hydrogen peroxide (H_2O_2), 100% oxygen or higher doses of NO to subsequently study the DNA-damage response (DDR). Monolayers are deprived of serum, and cells are left to recover for ten days to allow the DDR to occur. Oxidants are expected to increase the rate of DNA damage and genetic instability, which will eventually trigger DNA damage checkpoint networks and p16 genes, thus activating the effectors of cell fate decision, p53 and pRb. Normally p53 is required for p21 inhibition of cell cycle progression, and pRb inhibits the transcriptional activation of E2F genes. Characterizing and identifying the expression of senescence markers can be demonstrated by SA β-gal staining in primary PASM monolayers, *in situ* using light microscopy, by SASP markers (IL-6 and IL-8) in conditioned medium, and by correlating the induction degree of senescence with the expression of cell cycle markers. The latter can be undertaken by the following i) RT-qPCR for their mRNA levels and immunoblotting for their protein levels; ii) detection of DNA damage foci by immunofluorescence using antibodies against the phosphorylated variant of histone gamma H2AX; and iii) confocal microscopy to detect PML bodies, which contribute to the E2F gene expression during senescence. Profiling the expression and examining the roles of the traditional senescence regulators, i.e., p53, pRb, ataxia-telangiectasia mutated (ATM), Checkpoint kinase 2 (CHK2), p19ARF, and cyclin-dependent kinase inhibitor 2A, multiple tumor suppressor 1 (p16INK4a) using small interfering RNA can be demonstrated. If the contribution of senescence or SASP

to the PPHN phenotype can be demonstrated, a therapeutic approach would be to rescue senescence by treating cells with permeable exogenous antioxidants.

The effect of oxygen tension on mitochondrial membrane potential has been measured as a function of the fluorescence of a mitochondria-specific cationic dye JC1; the dye accumulates in the mitochondria in relation to the membrane potential. The dye is monomeric at membrane potentials lower than 140 mV, but emits green light when the dye is excited at 490 nm (319). It also forms aggregates and emits red light when it is excited at 540 nm. Cells are grown in black clear bottom 96-well plates for the purpose of excitation and emission studies. The cells are then exposed to different oxygen tensions (hypoxia or hyperoxia) to measure the effect of oxygen tension on the mitochondrial oxygen potential. This is followed by treating the cells with either FeTTPs or medium. The procedure requires delivery of JC1 dye to cells in a HEPES (4-(2-hydroxyethyl)-1-piperazineethanesulfonic acid) buffer containing sodium chloride and high glucose or low glucose concentrations for 30 min at 37°C, following which the cells are washed. After washing the cells, the fluorescence in the wells is measured sequentially at 490/540 nm and 540/590 nm wavelengths using a fluorescence plate reader. The emission at 540 nm is green when excited at 490 nm, and the excitation at 540 nm results in green fluorescence at 590 nm. The changes in the ratio between measured red and green fluorescence intensities are calculated for each well after subtracting for the reagent and background.

Mitochondrial superoxide is measured by MitoSOX staining and mitochondrial protein nitration that involves immunoblotting of subcellular fractions using anti-nitrotyrosine. Substantial levels of ROS are produced by dysfunctional mitochondria,

which are distinguished by labeling the cells with specific fluorescent probes; i.e., MitoFluor Green for the increased mitochondrial mass as a compensatory mechanism for the lack of mitochondrial function, as reported in previous studies (317, 318).

4.11. Endoplasmic reticulum stress markers

The 78 kDa glucose-regulated protein (GRP78) expression pattern indicates early ER stress, and inositol-requiring enzyme 1α (IRE1α) expression, Protein kinase RNA-like ER kinase (PERK) phosphorylation, and activating transcription factor 6 (ATF6) cleavage indicates late ER stress. IRE1α and PERK activation are confirmed by examining X-box-binding protein 1 (XBP1) splicing, ATF4 expression, eIF2α phosphorylation and C *elegans* BP homologous protein (CHOP) expression (320). The above markers are amenable to quantitation using LSC in PASM cells subject to cyclic stretch coupled with or independent of hypoxia while being co-incubated with selective ROS scavengers that are added daily to the cultures or diluent. The ROS scavengers include PEG-SOD, PEG-catalase, the NO scavenger N-acetyl-cysteine, and FeTTPS (274).

Whole cell adenosine triphosphate (ATP) is a biomarker of altered respiratory chain homeostasis (275) and can be quantitated by measuring the luminescence of a reaction created by adding assay buffer to cell lysates and mixing them with the substrate and ATP enzyme in a 96-well plate. Relative light units are converted to ATP content using a standard curve determined by linear regression of emitted relative

luminescence for a log series of known ATP standards. The data are presented normalized to lysate protein concentration.

Other approaches use cells pre-incubated with GSK-PERK inhibitor (GSK2606414), and/or MannKind IRE1 inhibitor (Mck-8866), for 4 hr before mechanical stretch/environmental exposures and then incubated with the same concentrations of inhibitors during exposure to hypoxia together with or independent of the cyclic stretch. Cell lysates are collected for the determination of cleaved caspase-3 and poly (ADP-ribose) polymerase (PARP). In a secondary approach, IRE1, CHOP, and ATF6 are targeted with specific small hairpin shRNA. Stable IRE1, CHOP, and ATF6 knockdown myocytes are then exposed to hypoxia with or without cyclic stretch (320, 321).

4.12. Models of ROS regulation of vascular constrictor receptor sensitivity

The Fawn-Hooded rat is a genetic strain in which the adult animal develops severe PHN after exposure to a mild decrease in alveolar PO2; e.g., at high altitudes. In this model, altered serotonin metabolism increases lung ET_A and downregulates endothelial NO synthase. Fewer and larger alveoli, reduced pulmonary artery density, and decreased lung growth during the perinatal period are mechanisms that contribute to the progression of PHN in this model. Serotonin-induced PHN in bone morphogenic protein receptor II (BmpR-II) heterozygous mice mimic the human condition with limited success. The mutant animal exhibits hypoxia when lacking the receptor or develops PAH when overexpressing the receptor (322).

ET antagonists such as ET_A receptor-selective antagonist BQ-123 and Bosentan (dual ET_A and ET_B receptor antagonist) reduce the medial thickening of the pulmonary artery and lower pulmonary artery pressure in rats and human patients. The phosphodiesterase (PDE) 5 inhibitor Sildenafil attenuates vasoconstriction due to hypoxia and reduces right ventricle mass in humans (323).

Susceptibility to increased ROS-mediated lipid peroxidation in the neonatal pulmonary artery is high when exposed to a sudden rise in oxygen tension during treatment. Arachidonic acid metabolism is one among various biochemical approaches that is currently under investigation. Authors have shown that hypoxia and oxidative stress in the neonatal circulatory transition predispose the neonate to pulmonary artery constriction via the upregulation of thromboxane A2 signaling, a vasoconstrictive inflammatory prostanoid (258, 324). In contrast, prostaglandin I2 (PGI2) is a vasodilator. An increase in the thromboxane A2: PGI2 ratio is thus a biomarker of PHN (257, 325). F2-isoprostane is a marker of the lipid peroxidation of arachidonic acid, which stimulates endothelial cell proliferation and ET_A synthesis and may play a role in the pathogenesis of PAH (326). The hypoxia-mediated $(ONOO^-)^\bullet$ inhibition of SOD activity in myocytes promotes 8-isoprostane (274). 8-Isoprostane (8-iso-PGF2α) is a prostanoid ligand that mediates vasocontractility and inflammatory responses of the vascular thromboxane receptor (TR) (327) through TR coupling with G-protein-coupled receptor (GPCR). TR is sensitized by $(ONOO^-)^\bullet$ and hypoxia and is deactivated by phosphorylation associated with PGI2 receptor (isoprostane receptor) coupling to PKA (328). Current approaches (274) compare hypoxic and control arteries treated with exogenous ROS or $(ONOO^-)^\bullet$ scavenger *in*

vitro and *in vivo*. The dysfunctional environment associated with the SM or a hypoxic artery enriches receptor activation via attenuating the affinity of TR to PGI2 and subsequent receptor inhibitory dephosphorylation in response to vasodilator therapy and the augmentation of intracellular Ca^{2+} release. Research is emerging on the role of PKA and PKC activation and the cyclic AMP-regulated kinases such as the transmembrane protein adenylyl cyclase (i.e., interacts with Gαs of GPCR) in normalizing the TR response via activating PKA and PKC (308, 327). Cyclic guanosine monophosphate (cGMP) is an intracellular second messenger of NO and an indirect marker of natriuretic peptide production. The current approaches characterize the role of antioxidants and ROS on the induction of inflammatory and contractility prostanoid mediators by challenging pulmonary myocytes with daily doses of antioxidants for 72 hours; i.e., SOD or the permeable PEG-SOD, PEG-catalase, or an NO donor such as sodium nitroprusside. A parallel setting of experiments is treated with an $(ONOO^-)^\bullet$ scavenger during the same course of environmental stress, i.e., for 72 hours of hypoxia with or without mechanical stretch versus the control (normoxia with or independent of mechanical stretch or inducing cells with a potent stressor such as H_2O_2) for 1 hour. Then, the isoprostanoid intermediate of interest is quantified in the conditioned medium by enzyme-linked immunosorbent assay methods. The same approaches can be amenable to measuring contractility using isometric myography or to time-lapse imaging of lung slices from hypertensive and normotensive animals for quantifying the contractility of arterioles to isoprostanoids and the total contractility to potassium chloride. The same approaches can be amenable to measuring the effect of ROS on PKA signaling via the 5' AMP-activated

protein kinase (AMPK) pathway. This can be achieved by pre-treating cultures with antioxidants or H_2O_2 (as described above) plus the AMPK activator A769662 (328) or inhibitor compound C (329) for 27 hours followed by 2 hours of incubation with PKA inhibitor (H89). Direct PKA activity or PKA-mediated AMPK activity can be measured in cell lysates. These approaches can measure ROS-mediated thromboxane receptor sensitization. Additionally, soluble guanylate cyclase promotes the maturation of endothelium-dependent and -independent relaxation. Prostacyclin and its analogs (i.e., Iloprost, Beraprost, intravenous Epoprostenol) proved long-term beneficial vasodilatory effects compared to normal prostanoids because of a short half-life; improve survival in patients. These are vasoprotective vasodilators that inhibit platelet aggregation and PASM proliferation.

By connecting known pathways of ROS generation and ER stress, scientists attempt to uncover new targets for therapy, as ER stress intermediates can be manipulated pharmacologically to alter apoptosis in targeted cell populations. Prevention of irreversible fibrotic medial thickening in PHN, which is the factor most limiting to treatment responses, would help reduce mortality in infants with PHN and prolong the time interval for vasodilator therapies. This is a good model to observe the effects of hypoxia together with and independent of pulsatile stretch and the method/mechanism involved in the contractile force and the link to transcription; i.e., to inhibit E2F. When SM switches phenotypes, and when proliferation decreases the expression of contractile genes (i.e., downregulated actin) and changes contractile cells into migrating cells, how E2F expression changes the contractile phenotype can be observed. The contractile phenotype may be rescued when E2F is

inhibited and rescues pRb. The trend is to observe the transcription factors that drive that switch between phenotypes; i.e., c-fos expression of the proliferative phenotype. Does c-fos expression of the proliferative phenotype co-activate with myocardin (an SM marker that expresses in the heart) to activate the contractile phenotype gene expression? Does E2F inhibit myocardin activity in PASM cells? If yes, then how does this impact actin in PASM cells? For phenotype switching, some studies have investigated the ratio of myocardin to myocardin-related transcription factor A (MRTFA) in airway SM. Myocardin increases in the contractile phenotype, and MRTFA increases in the proliferative phenotype leading to changes in the actin dynamics. More research is required to determine how the response to E2F is linked to physiological function.

4.13. Quantitative evaluation of the cell fate decision

H_2O_2 increases the rate of mutations, which eventually triggers DNA damage checkpoint networks DDR and p16 genes. Selected cell lines can be used to quantify cell fate responses following DNA damage by exposing cells to different combinations of stressors, i.e., H_2O_2 and/or NO while being stretched together with or independent of hypoxia followed by 10 days of recovery. Using LSC, it is possible to quantify the proportion of individual cell lines that preferentially undergo apoptosis, necrosis, autophagy, senescence or mitotic catastrophe, as outlined in Figure 4.7. In this way, it is possible to compare a panel of oxidant-treated, hypoxia-treated, or mechanical stretch-treated to non-treated cell lines and normal controls and assess different cell fate pathways. ELISA and BrdU staining are used to detect heterochromatin foci,

higher and persistent DNA damage foci, increased SA-β galactosidase staining, increased PML expression, increased DNA segments with chromatin alterations reinforcing senescence (DNA SCARS: DNA segments with chromatin alterations reinforcing senescence), and increased p16, IL-6 and IL-8 levels. These assays allow the characterization of the molecular response of individual cell lines to the integrated action of pulsatile stretch, oxidative stress and hypoxia combinations, together or independent of each other. Senescence markers predict this response. Figure 4.7 presents a model that correlates resistance to therapy and cell fate decision.

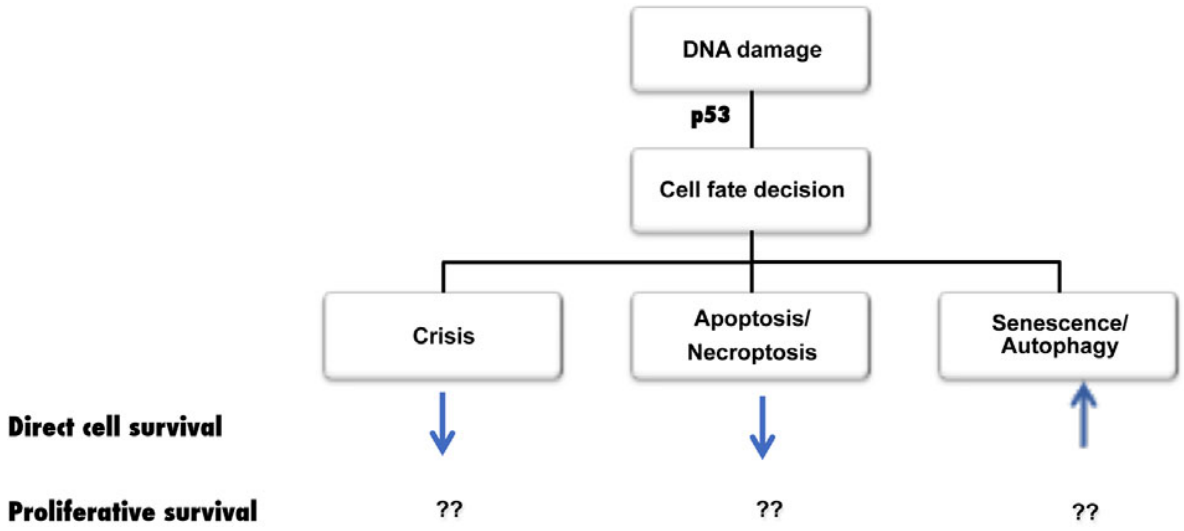

Figure 4.7. Correlation between resistance to therapy and cell fate decision is shown. Cell lines that commit to senescence can be used to assess direct and proliferative cell survival. Direct (96 hr) and proliferative cell survival (2–3 weeks) post-exposure to stressors reflect the ability of cells to survive the damage and to proliferate. The correlation between individual cell fates with direct or proliferative survival demonstrates if senescent SM cells have the potential to impact treatment outcomes. By comparing the proportions of direct cell survival with proliferative cell survival, it is possible to predict the cell fate taking into account the physiological conditions of the cell. The results will allow prediction of patient care through a better characterization of patient responses to current therapies and to design novel bioassays to search for small chemicals or cytokines that potentiate the senescence antiproliferative mechanism for future therapies (247).

The enzymatic activity of β-gal can be detected optimally at pH 4.0 using the chromogenic substrate 5-bromo-4-chloro-3-indolyl β D-galactopyranoside (X-gal). Cells that are positive for high β-gal stain blue-green using an inverted microscope. The assay is performed 120 hr post-transfection (i.e., untreated sample and/or control small interference RNA (siRNA)-treated sample) or after cell manipulation. The cell culture medium is aspirated, and cells are fixed with 4% paraformaldehyde for 5 min. After cell washes, 250 µl SA-β-gal staining solution is added to each well. Cells are incubated in the dark at 37 °C. The incubation time varies with the cell type. The reaction is terminated when the cells are stained blue-green, which is visualized under an inverted bright-field microscope. Using a 10X objective, images of cells are captured in each well and expressed as a percentage of the total cell number.

4.14. Biomechanical signaling crosstalk with cell cycle entry

The small G protein Rho kinase regulates the assembly and disassembly of actin filaments and ensures the integrity of the cytoskeleton, which is essential for ERK1/2-dependent gene transcription in response to stretch. The absence of stretch causes actin depolymerization and loss of the contractile phenotype. Rho inhibitor plays a significant role in cell cycle control by inhibiting G1 separation of the centrioles prematurely and completion of cytokinesis thus serving as a cell cycle checkpoint. Whether the inhibition of Rho A or Rho inhibitor is sufficient for the inhibition of myocyte proliferation is not well explored, and the role of hypoxia and pulsatile stretch in regulating such inhibition is also unknown.

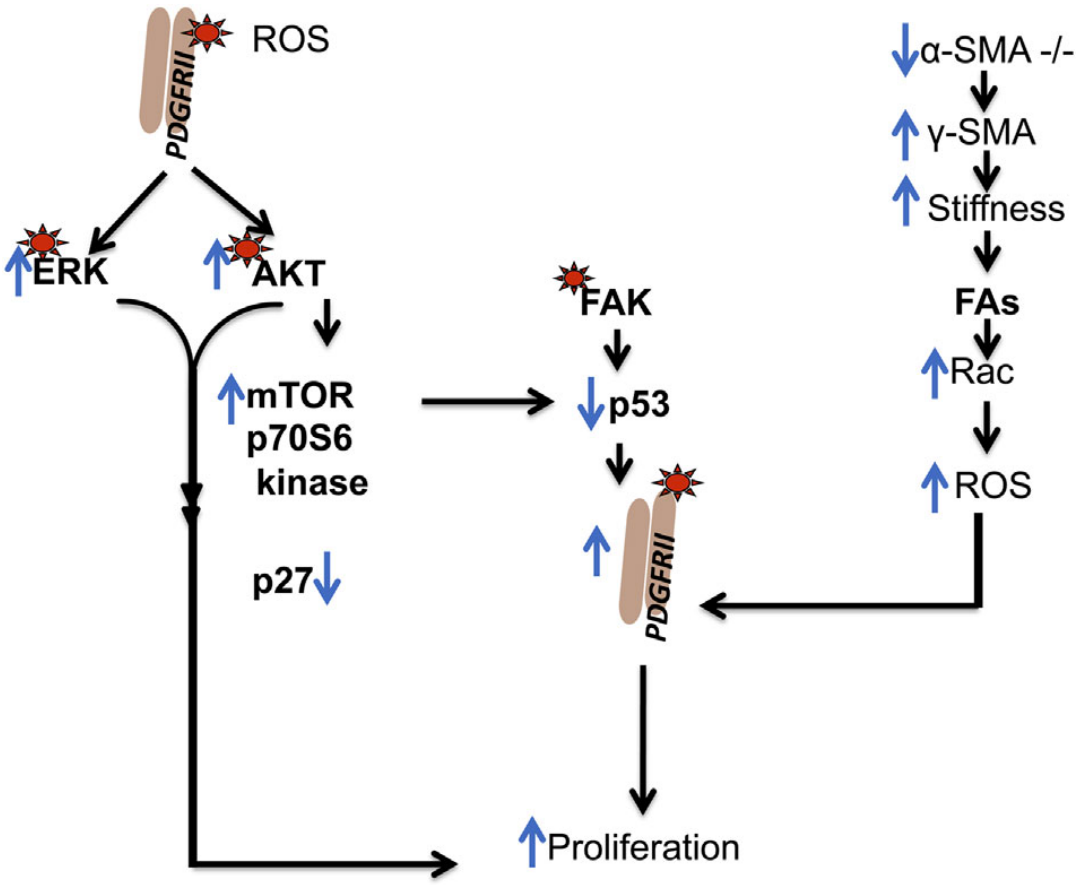

Figure 4.8. The link between the distribution of SMα-actin and SM hyperplasia in vascular diseases was studied by Papke et al (330) who used cells from SM-actin $22^{-/-}$ mouse. The group reported crosstalk between PDGFRB upregulated expression and activity. Activation of FAK and altered p53 localization caused SM hyperplasia in response to the loss of SMα-actin. In the actin null mutant cell, tension increases and activates FA maturation related to size and activity and influences their redistribution at the cell periphery compared to wild-type mice in which they were dispersed across the cell. SM-actin $22^{-/-}$ induced FAK (phosphorylated on Tyr297) was sufficient to suppress Rho and activate Ras-related C3 botulinum toxin substrate 1 (Rac1) independently upon Lysophosphatidic acid (LPA) stimulation, which induced proliferation mediated by increased ROS. Loss of SM-actin reduced p53 nuclear localization and increased PDGFRB expression and phosphorylation by a mechanism that involved FAK and mTOR activation, which increased the activation of PDGFRB. Upregulated mTOR was associated with increased phosphorylation of p70S6 kinase and abolished p27 activity indicative of AKT activation. In the same model, ROS-activated ligand-independent activation of PDGFRB occurs via the inhibition of the protein tyrosine phosphatase responsible for deregulating the active receptor (247).

PI3K is activated by growth factors and is involved in cell cycle progression. PI3K mediates SM proliferation after arterial injury and is required for insulin-like growth factor-1-induced vascular SM proliferation. AKT is a serine/threonine kinase downstream of PI3K and is involved in cell survival and replication in SM; hence, the PI3K/AKT pathway plays a critical role in pulmonary vascular remodeling. PI3K activation can activate AKT that in turn can modulate the Bcl-2 family and apoptosis and stimulate beta-catenin, which is thought to activate mTOR in regulating protein synthesis and cell cycle progression (Figure 4.8). Finally, induction of the stress-activated protein kinases p38 and JNK can result in modulation of DNA damage responses (331) and cell survival.

PDGFRB is activated in hypertensive pulmonary SM cells. Stretch-induced myocyte proliferation involves PDGF expression, PKC activation, Rho/Rho inhibitor, and superoxide production and induces expression and translocation of Egr1, c-Jun and fibronectin gene expression (Figure 4.9). Liu et al. (332) reported that chronic hypoxia increased PDGFRB phosphorylation. This activation was associated with PHN and induced adventitial fibroblast proliferation by activating JNK1 signaling that was mediated by a modest elevation in NADPH oxidase-derived H_2O_2 and $O^{\bullet -}$ radical formation as presented in (Figure 4.9). They suggested that the small increase in ROS generation might elicit sufficient signals that turn on replicative responses with a greater magnitude than a massive increase in ROS.

ERK1/2 are downstream of the PDGFRB in PHN and potential pathways that link PDGFR/ROS/MAPK to proliferation. Typically, PDGFRB activates Rho inhibitor, which changes Ca^{+2} sensitivity and thus has a potential for Ca^{+2} blocking. As a result,

fasudil inhibits PDGFRB-induced Rho activation, which in turn, elicits the activation of p21, p27, and the downregulation of proliferating cell nuclear antigen proliferating cell nuclear antigen (PCNA) and causes growth arrest. Rho inhibitor-mediated p27 degradation upregulates proliferation (Figure 4.10).

Rho regulates SMα-actin and SM hyperplasia in vascular diseases. Papke et al. (330) used cells from an SM-actin22 $^{-/-}$ mouse to study the crosstalk between PDGFRB upregulated expression and activity. Activation of FAK and altered p53 localization caused SM hyperplasia in response to the loss of SMα- actin. In actin-null mutant cells, tension increases and activates FA maturation in terms of size and activity and influences FA's redistribution at the cell periphery compared to wild-type mice, in which they were dispersed across the cell. SM-actin22 null mutant-induced FAK (phosphorylated on Tyr 297) was sufficient to suppress Rho and activate Rac1 independently upon LPA stimulation, which induced proliferation mediated by increased ROS.

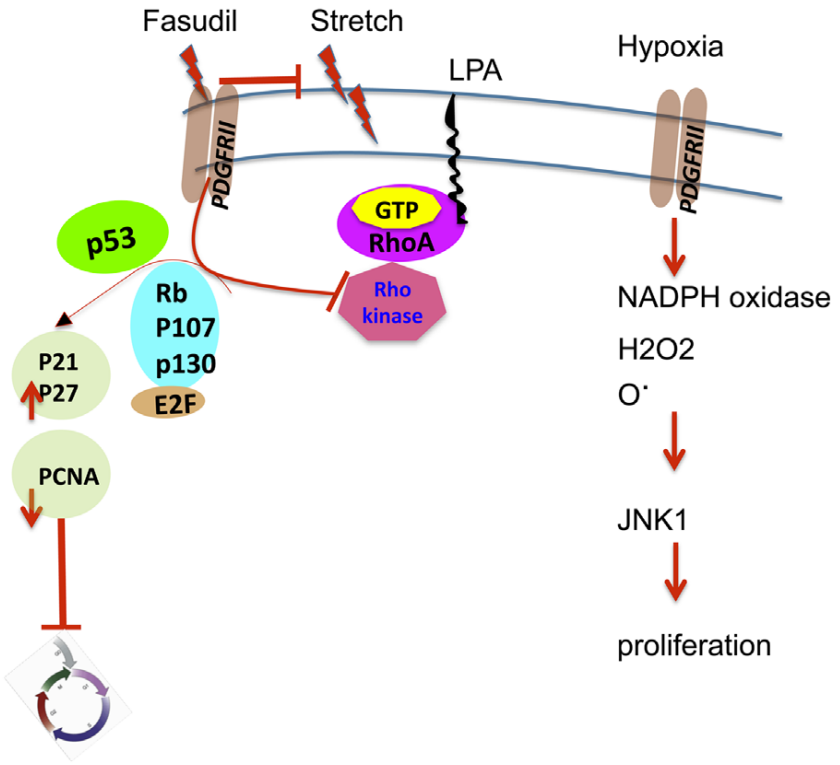

Figure 4.9. Chronic hypoxia elevates PDGFRB phosphorylation and activation is associated with PHN, specifically, hypoxia induces adventitial fibroblast proliferation by activating PDGFRB/JNK1 signaling that is mediated by modest elevation of NADPH oxidase-derived H_2O_2 and $O^{\bullet -}$ radical formation. The Rho/Rho kinase pathway contributes to growth factor-induced SM proliferation. Stretch-induced SM proliferation involves PDGF expression. Cyclins/CDK complexes regulate proliferation by phosphorylating and inactivating the transcriptional repressor Rb and allowing the expression of genes that trigger cell cycle progression. P16, p21, and p27 are key regulatory CDKIs. Normally, PDGFRB activates Rho kinase. In this model, the Rho kinase inhibior fasudil (the only clinical available selective Rho kinase inhibitor that also functions as an intracellular Ca^{+2} blocker) inhibits PDGFRB induced Rho kinase activation, and in turn elicits the activation of p21, p27 and downregulation of PCNA and growth arrest. Regulation of Rho inhibitor activity can be modulated by (i) arachidonic acid and protein oligomerization, which induces N-terminal transphosphorylation; (ii) RhoA upregulation of Rho kinase; (iii) the binding between the C-terminal of the Rho-binding domain to the N-terminal domain of Rho inhibitor inhibits Rho kinase activity. The p21 promoter region is reported to be bound to G9a (histone lysine methyltransferase; an epigenetic mark for gene suppression, DNA methyltransferase I and histone deacetylase I), which regulates the cell cycle (247).

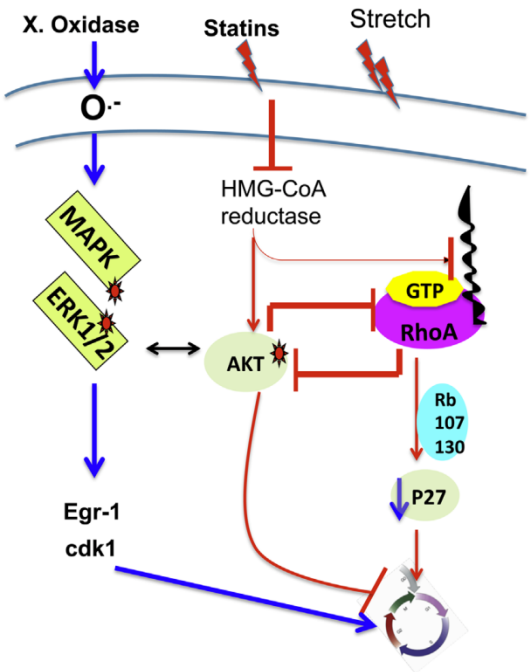

Figure 4.10. AKT is a serine/threonine kinase downstream of PI3K and is involved in cell survival and replication in SM. The PI3K/AKT pathway plays a critical role in vascular remodeling. Stretch increases the level of ERK1/2 and AKT phosphorylation. AKT phosphorylation positively regulates stretch-induced SM proliferation. Statins (cerivastatin and simvastatin) are used for the treatment of hypercholesterolemia. Statins prevent stretch-induced SM proliferation via inhibition of the RhoA/Rho kinase pathway in the saphenous vein by inducing the inhibition of mevalonate synthesis, which is a critical step in the synthesis and posttranslational modification of the geranyle-geranyle moiety that anchors Rho to the plasma memberane. Therefore, statins inhibit RhoA translocation to the plasma membrane and thus inactivate its binding to Rho kinase and prevent the downstream events. Cerivastatin significantly prevented stretch-induced membrane accumulation of RhoA, but not of P44/42 MAPK and AKT. Both activated AKT and inactivated RhoA have down regulatory effect on each other, but the mechanism is not well known. Mevalonate restored the preventive effect of cerivastatin on stretch-induced RhoA membrane accumulation. The effect of Rho inhibitors on the level of pAKT can be studied to demonstrate the crosstalk between Rho and AKT signaling and whether Rho/Rho regulates AKT. Whether the inhibition of RhoA is sufficient for the inhibition of stretch-induced proliferation in hypoxic PASM cells has not been studied. Rho/Rho kinase activation inhibits Rb, and Rho inhibitors and cerivastatin reduce Rb. Stretch-induced SM proliferation involves superoxide production and induces expression and translocation of Egr1. Egr1 is a redox-regulated early growth response transcription factor, it increases in the lung of neonatal pulmonary hypertensive calf in response to hypoxia, regulates downstream targets critical to proliferation and fibrosis and is implicated in vascular remodeling. The loss of extracellular SOD3 expression in cultured calf PASM cells mimics the hypoxia-induced extracellular ROS elevation observed *in vivo*. Xanthine oxidase (X. Oxidase) was given to the hypoxic PASM cells in culture. It was found that the loss of extracellular SOD was associated with an uprise of superoxide radical and this mediates up regulation of Egr1 via phosphorylation and activation MAPK/ERK1/2 and CDK1 activation (247).

In the following sections I describe an application for LSC in the quantification of the cumulative effects of hypoxia and cyclic mechanical strain on cytoskeleton remodeling in PASM and ASM cells in an *in vitro* model of PPHN.

4.15. Vascular effects of PPHN

PPHN is a rapid progressive vasculopathy, occurring at a developmentally crucial moment in perinatal circulatory transition because the pulmonary artery fails to relax (224, 333), (248) due to perinatal hypoxia, inflammation or direct lung injury (249), (334), (335, 336). This sporadically occurring, lethal disease is characterized by hypoxemia, pulmonary vascular constriction and arterial remodeling. Thirty percent of PPHN infants die or require ventilator assistance (251). End-stage PPHN histology is characterized by thickened vascular media and adventitia, smooth muscle (SM) hyperplasia and extracellular matrix deposition (337), impairing arterial distensibility (253), and resulting in a fixed and irreversible increase in pulmonary vascular resistance (333); see schematic in Figure 4.11.

The SM composition of the hypoxic pulmonary arterial wall is influenced by selective cell cycle re-entry and initiation of apoptotic signaling (280, 281). The effect of hypoxia on pulmonary apoptosis is phenotype-dependent. In synthetic myocytes, survival and proliferative signaling is enhanced by hypoxia (338). Survival and proliferative signaling promote vascular fibrosis; the fixed thickening of the arterial wall in turn increases resistance to vasodilator therapy such as NO (339).

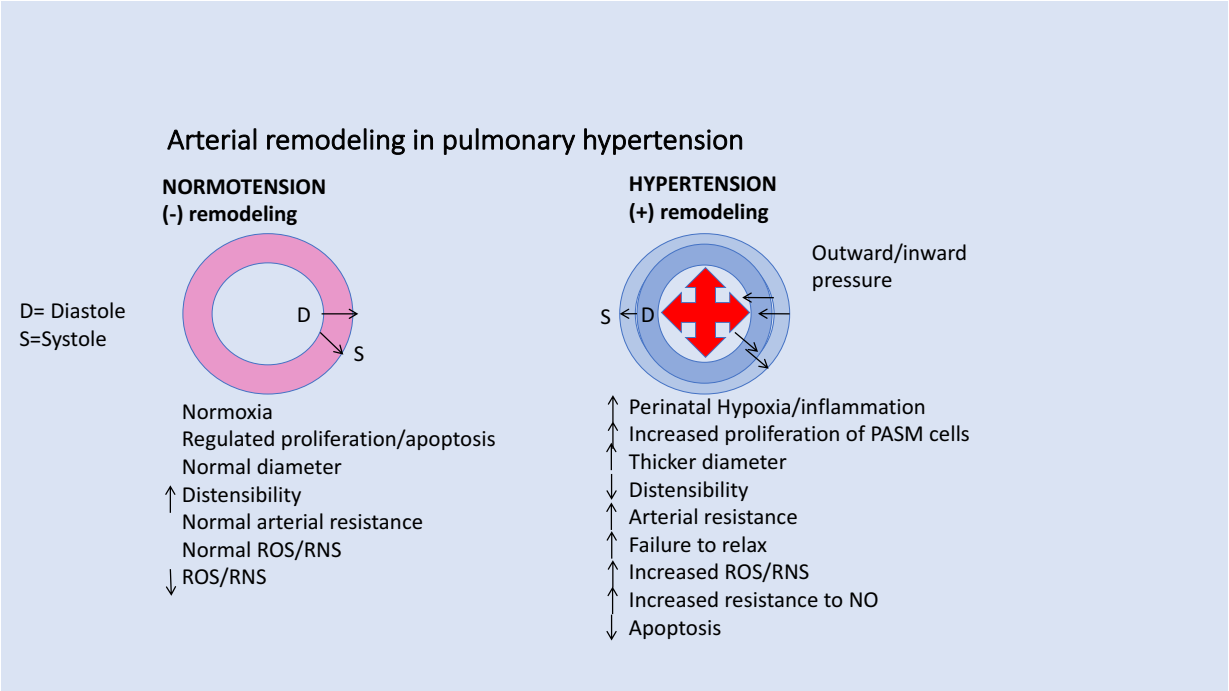

Figure 4.11. Arterial remodeling in PPHN. The perfusion in the pulmonary circuit depends on the cardiac effort (systole). One cardiac beat causes 10% stretch. In PH, one cardiac beat causes less than 10% stretch. The cytoskeleton reacts to stretch. With a small strain (± 5% from the resting length), there is heterogeneous response. With higher strain (±10% from the resting length), a huge response occurs, such as a ripping damage to the cytoskeleton. High strain is associated with cell death due to the loss of adherence to the membrane. The arterioles change their diameter in response to local conditions such as sympathetic or endocrine stimulation. Capillary walls permit exchange of oxygen and metabolites between blood and the surrounding interstitial fluids. Diffusion distance is short and exchange is quick because the wall is thin. A high filamentous to monomeric actin (F:G) ratio increases stiffness, resulting in a thicker vessel diameter, higher pressure in remodeled versus non-remodeled vessels. Pulsation is non-harmonized due to the loss of distensibility. Remodeling is associated with HTN, higher ROS, and lower antioxidant enzyme levels (Catalase, SOD 1,2,3, Glutatione peroxidase, NADPAH oxidases (NOX)). Copyright is owned by Johar and Bernstein (299).

Smooth muscle cells undergo cyclic mechanical stretch during the cardiac cycle. Hypoxia and NO cumulatively activate apoptosis of contractile pulmonary artery SM, causing a contraction of this subpopulation. In unresolved PPHN, pulsatile strain is exacerbated and it alters myocyte phenotype commitment (254).

Cyclic stretch triggers apoptosis in vascular myocytes (255). The effects of pulsatile strain on the vascular wall are phenotype dependent; stretch induces apoptosis selectively in contractile myocytes (255, 340). Vascular pulsation is thought to be important for stretch-induced SM dilation and maintenance of arterial homeostasis without initiation of dedifferentiation and mural fibrosis (341). How much stretch on the arterial wall, hypoxia and time are hypertensive and can lead to pulmonary overflow is not identified yet.

The altered cytoskeleton can be imaged at the cellular level by LSC. LSC quantifies fluorescence. The principle of quantifying nuclear fluorescence is as follow. In normal cells, Go-G1, S and G2 nuclei stained with dye will look similar. If apoptosis starts scribing into the cell population, the nucleus begins to shrink and then fragments into smaller pieces. In this case, the amount of dye present in a single nucleus does not change, but becomes more concentrated. Thus, the total integrated fluorescence for the population will not change, but the dye being localized in a smaller volume will exhibit an increase in each pixel's fluorescence while the total grey level values will be the same.

Reactive oxygen species are important signaling molecules connecting vascular stretch with cell cycle entry or arrest. Endothelial cell strain triggers release of mitochondrial ROS to the cytosol (273). Vascular myocytes generate mitochondrial

superoxide in response to stretch (342), activating biomechanical signaling pathways. This study was designed to demonstrate that LSC, a method that utilizes a fluidic matrix to grow cells, can be uniquely employed to link the actions of pulsatile stretch and hypoxia in a PAH oxidative environment and the occurrence of tissue remodeling.

4.16. Methods

4.16.1. The *in vitro* model

All experimental protocols performed involving tissues from animals were in accordance with the ethical standards of the University of Manitoba. The guidelines of the Canadian Council on Animal Care on the use of animals were followed and all approvals were obtained from the University of Manitoba animal care committee. This study model (as shown previously in Figure 4.4.) does not depend on cells coming from a remodeled *in vivo* environment. Rather, it requires that the newborn pulmonary vessels are superbly plastic. It is not possible to extrapolate results from already remodeled circuits because the *in vivo* phenotype is rapidly lost when cells are grown *in vitro*. For this reason, it is necessary to examine the induction of cell fate decisions immediately after the application of stressors to neonatal primary PASM or hASM cells *in vitro.* The resistant pulmonary arteries of 2nd to 6th generation are microdissected from lungs of newborn (<24h, N=3) piglets raised in normoxia (Fraction of inspired oxygen; FiO_2 = 0.21). Tissue is recovered in cold Ca^{2+}-free physiological buffer. Minced vessels are digested with collagenase and papain according to (306). Cells dispersed by gentle trituration are resuspended in Hams F-12 medium supplemented with 10% FBS, and plated on collagen coated flexer-cell 6-

well flexible culture dishes for 2 days prior to experimentation. Stable 70% confluent SM monolayers are established while serum-starved for 3 days (with 1% survival factor; insulin/transferrin/selenium, Sigma) to synchronize in a contractile phenotype. Serum starved contractile myocytes are allocated to four groups: [i] Normoxia resting (21% O_2, 5% CO_2, balance N_2), [ii] Normoxia mechanically stretched (cyclic stretch to total ± 5% from resting length, frequency 1 Hz), which serves as a control, [iii] Hypoxia (10% O_2) resting, and [iv] Hypoxia mechanically stretched as in (ii).

4.16.2. Application of cell stretching

Myocytes in mechanically stretched groups are placed on the Flexer-cell strain unit, which applies uniform circumferential stretch to the collagen matrix beneath the cells to simulate the wall strain of vascular HTN, for 72 hours in a dedicated hypoxic or normoxic incubator without loading. Pressure of carbon dioxide (PCO_2) and pressure of oxygen (PO_2) are maintained within 1% tolerance. All cells are seeded at a density of $70x10^3$ cells per well in a 6 well Flexer-cell plate and are observed to avoid confluence. After 72 hours of applying the stretch or rest, cells present in the medium are fixed with paraformaldehyde (PFA) for LSC application or cell lysates collected in appropriate lysis buffers for protein assays. In all cases, cells in P0 were used in the experiments described in this chapter. Cells are counted using a haemocytometer to correct for cells that have detached from the memberane before flexing (Figure 4.12). This model enables the assessment *in vivo* of the effect of a contractile force when applied to the vessel in a normal physiological status, in its optimal length, after it has been challenged by the treatment, and is either in the

relaxed or contracted mode out of the lung. The vessel can be fixed and sections prepared. The vascular wall can be immunostained and signaling compared in either state, however, this is beyond the scope of this chapter.

4.16.3. Hoechst nuclear staining for LSC

After challenging PASM cells with stimuli in the Flexer-cell plates, cells are fixed immediately with 4% PFA, then permeabilized with fresh phosphate-buffered saline (PBS) containing 3.0% Triton X-100. After washing the cells, the nuclei are counter stained by incubating with sterile PBS containing freshly prepared cold working Hoechst 33342 solution (PBS containing 10 µg/ml) for 3 min at room temperature, light protected. Cells are washed several times with PBS to improve the background. Membranes are excised from plates and cells are allowed to air dry with the cell side facing up, protected from light for 30-45 mins. Sections to be imaged are excised and mounted in mounting medium Prolong Diamond Antifade (appendix B, Figure B.1). After 30 mins, another 70 µl mounting medium and a cover slip are added in the dark to the cell's side facing up. Cells are kept at 4°C until imaging is performed.

4.16.4. The LSC scanning parameters

An LSC for quantitative imaging cytometry is a flow cytometer analogue adapted for both epifluorescent imaging and quantitative measurments of fluorescence in tissue sections and adherent cell systems. In addition, the system may be configured for quantitative analysis of chromatically stained tissue sections. An LSC was provided for my research work by the Children's Hospital Research Institute of Manitoba, Biology of Breathing Theme, Winnipeg, Manitoba, Canada. I used an Olympus 1X71 inverted microscope. The source of the lasers is gas (488 nm; 5-20 mW

adjustable) and solid state diode lasers (405 and 633 nm) for fluorescent excitations. The integral intensity of the blue fluorescence staining is quantified using the 20X objective for myocyte nuclei and 40X for cytosolic actin. Fluorescence is collected using photomultiplier 1 (PMT1). The colours assigned to the PMT1 tubes are i.e. 488 nm (green), 405 nm (blue) and 633 nm (long red). An example of the red and green signals in the form of contour analysis of cytoplasmic F:G-actin ratios in cultured hASM cells is presented in appendix B (Figure B.5). In nuclear staining, the blue channel is used to quantify Hoechst 33342 nuclear fluorescence (Figure 4.14. C, D and 4.15 E, F). For the blue emission, the laser used for excitation is the violet laser. The software used is iCys 3.4. The iCys provides true quantitative imaging by virtue of its high depth-of-focus. This is demonstrated by its ability to provide direct cell cycle measurement comparable to that of a flow cytometer. The PMT detector used is a 14-bit camera. For voltage, I used units of 1-10. The scattergram (X, Y position) creates a dot plot image of the scan area, with each dot representing an event (nucleus) (Figure 4.14 C, D and 4.15 A-F).

The LSC provides a means to visualize and quantify cellular events and processes by identifying the edges of stained regions. Total fluorescence from any colour channel found within the boundary of both the threshold and the integration contours is considered an event and is identified for quantification. The integral blue = the total summed fluorescence (total summed grey level) within the boundary of the integration contour. The gain is always left at 100. The step size is 1. Settings of voltage, offset, min and max, the scattergram, the histogram in regions of interest in

the nuclei and the cytoplasm, are standardized and the parameters of the scanning process, contouring, and the modules used are illustrated in appendix B.5.

4.16.5. Phantom contour analysis of cytoplasmic F:G-actin ratios in cultured hASM cells by Phalloidin/DNase-I staining using LSC

Human ASM cells (HC82) were grown in feeder medium, up to a 70% confluence prior to flexing. After challenging the cells with stimuli in the flexer-cell plates, cells were fixed immediately with 4% PFA in PBS for 15 mins. Cells were then washed to remove the residual fixative, then permeabilized with fresh Cyto-Tris buffered saline (TBS: 20 mM Tris base, 0.154 M NaCl, 2 mM EGTA, 2 mM $MgCl_2$, pH 7.2) containing 3.0% Triton X-100 buffer (Sigma 93443) for 15 mins. Cells were blocked for 1 hour at RT with 1% BSA in Cyto-TBS buffer, then washed with Cyto-TBS buffer. Cells were stained with 1% bovine serum albumin (BSA) in Cyto-TBS cocktail-containing Alexa Fluor Phalloidin 633 at 5:200 dilution (for F-actin in the myocytes cytosol Invitrogen Probes, red fluorescence, excitation range 632 nm and emission 647 nm) concurrently with DNase-I (488 nm) at 1:1000 dilution (for G-actin in the myocytes cytosol Invitrogen Probes, green fluorescence excitation range 488 nm and emission 525 nm) for 1 hour at RT in a humidified chamber. Cells were then washed with Cyto-TBS buffer while being shaken at low speed and nuclei were counter stained with Hoechst 33342 as described above. Cells were washed while being shaken at low speed in ddH_2O, followed by another longer wash to provide a better background. Membranes were excised from the plate, air-dried, mounted and assembled flat and in the dark, or were kept at 4°C until imaging was performed. F- and G-actin staining were quantified as red and green integral intensity by LSC at 40X

magnification, adjusted to F-actin and then the same parameters are used for G-actin. A lattice grid of phantom contours for the measurement of F:G-actin fluorescence is shown in (Figures 4.16, 4.17, 4.18 and 4.19). The blue laser was used to collect green fluorescence.

4.16.6. Isolation of cell associated phantoms (the first LSC method)

The scattergram (X, Y position) creates a dot plot image of the scan area, with each dot representing an event (actin fiber). Phantom means a visual illusion that can define regions with distinctive boundaries when no real surrounding edges exist. Isolation of nuclear-associated phantoms and cell associated phantoms is presented in (Figures 4.16-4.18 A-C).

4.16.7. Isolation of nuclear associated phantoms (the second LSC method)

An alternative method is available for the isolation of nuclear associated phantoms, using the experimental protocol's association module. By linking phantom contours with primary contours (blue channel – Hoechst nuclear fluorescence) through the association module, phantoms that were in direct physical contact with primary nuclear contours (associated), may be isolated as a distinct population – the cell associated nuclear phantoms. Associated events were displayed using a primary event scattergram and blotting nuclear (blue channel) fluorescence versus associated long red channel phantom fluorescence. This scattergram may be termed the association scattergram.

4.16.8. Bradford protein assay

Radioimmunoprecipitation assay (RIPA) buffer (150 mM NaCl, 0.1% Triton X-100, 0.5% Sodium deoxycholate, 0.1% sodium dodecyl sulfate (SDS), 50 mM Tris-HCl, pH 8) was used to prepare the whole cell lysates. 100 µl of the RIPA buffer was added

to 2 wells of a 6 well flexcell plate. Prior to usage (sodium fluoride (NaF) 50 mM, 200 mM phenyl methyl sulfonyl fluoride (PMSF) in dimethyl sulfoxide (DMSO), sodium orthovanadate (NaOV) 250 mM, Protease inhibitors (10 µL/1 ml buffer) and phosphatase inhibitor (10 µl/1 ml buffer)) were freshly added to the RIPA buffers, which was then filter-sterilized through 0.22 µM membrane. 2 µl lysates were diluted 1:100 for protein concentration and measured in 96 well plates at 595 nm using a spectrophotometer (Gen5 software). Using BSA (1 µg/µl) as a standard, Bradford reagent was used to draw a standard curve for protein concentration. A replicate of 3 wells out of 3 independent animals was used consistently for statistical analysis.

4.16.9. Expression of SM differentiation markers

PASM or hASM cells were examined by immunoblotting for protein markers of SM differentiation such as α-SM actin, β-actin and SM desmin (Figure 4.3). Quantification of the basal level of SM differentiation markers and cell cycle regulatory proteins by immunoblotting was done using whole cell lysates (20 µg/lane in 6x Laemmli buffer (SDS 12 g/100 ml, bromophenol blue 60 mg/100 ml, glycerol 47 ml, 12 ml of 0.5 M Tris pH 6.8, ddH_2O 12 ml), the protein lysate was added to 6x Laemmli buffer at 1:5 ratio and was boiled for 5 mins, cooled and then dithiothretol (DTT) (9.3 g/100 ml protein/Laemmli mixture) was added before loading. Protein bands were separated by SDS-polyacrylamide gel electrophoresis (SDS PAGE) using 12% gels and then transferred to polyvinylidene difluoride (PVDF) membrane. The PVDF was blocked using 5% milk in TBS-Tween, and then incubated with each of the following antibodies consecutively: mouse anti α-SM actin (Sigma A2547); rabbit anti desmin (Sigma); rabbit anti protein kinase B (AKT) and phosphorylated (pAKT) (Cell

Signaling); rabbit anti extracellular regulated kinase (ERK1), ERK2, pERK1/2 (Cell Signaling); mouse anti cellular Rous sarcoma virus protooncogen Src and p-Src (Cell Signaling). The membranes were stripped and re-probed with mouse anti β-actin to control for differences in protein loading (Sigma, diluted 1:5000 in 1% BSA in 1% TBS), followed by 2 hours incubation with the horse radish protein HRP-conjugated goat anti-mouse antibody or anti-rabbit secondary antibody (diluted 1:5000) in 1% free-fat milk in TBS-containing Tween at room temperature). All bands were visualized using the Lumi-light Western blotting substrate (Roche Diagnostics, Mannheim, Germany). The intensity of the bands was detected using the Fluorochem system and quantified with Alpha Ease FC, version 6, software.

4.16.10. Simultaneous quantification of whole cell ROS and superoxide anion by Dichlorofluorescein (DCF) and Dihydroethidium (DHE) fluorescence

Working solutions of DCF/DHE were prepared concurrently from stock solutions: stock cell permeable H2DCF-DA (Sigma, 0.0024 g in 50 µl DMSO; DHE (Sigma, 0.0015 g in 50 µl DMSO) avoiding light, to obtain 100 µM working solutions of DCF and DHE respectively. The DCF assay was modified after Wang and Joseph (343) and the DHE assay was modified after Munzel et al. (344), respectively, as follows. Attached cells were washed with 1X PBS twice, then treated with trypsin 0.75 ml/well. Incomplete (serum-free) F12 medium (0.75 ml) was added and cells were collected in microfuge tubes to a total volume of 1.5 ml, then centrifuged at 1000 rpm for 7 min. The pellet was resuspended in 1 ml incomplete F12 medium. One ml working DCF or DHE was added to each $1x10^6$ cells after normalizing for the cell number per treatment (hypoxia together or independent on stretch, normoxia together or independent on stretch). Cells were incubated at 37°C for 30 min,

centrifuged at 1000 rpm for 5 min; then washed 2X with 1X PBS to wash out the extracellular DCF or DHE. Cells were resuspended 1 ml F12 per 10^6 cells for the number of 3 well replicates per treatment. The intracellular DCF fluorescence was read at excitation 485 nm, emission 520 nm and gain 1500, at time 0, and every 30 minutes thereafter while being incubated at 37°C. The intracellular DHE fluorescence was read at excitation 488-510 nm, emission 590-620 nm and gain 1500, at time 0, and every 30 minutes thereafter while being incubated at 37°C.

4.16.11. Statistical analysis

Data are presented as mean ± standard deviation (SD). PASM cells were compared within each matched phenotype groups, i.e. (hypoxia together with stretch) and (hypoxia independent on stretch) were compared to (normoxia together with stretch) and (normoxia independent on stretch), respectively, by two-way ANOVA. DCF and DHE data were analysed with PRISM 6.0 (GraphPad Software, Inc. San Diego, CA). Two-way ANOVA followed by Bonferroni test for multiple comparisons was performed on 3 independent samples per group. Alpha (p) < 0.05 represents significance. The statistical analysis for the isolation of cytoplasmic phantom was confirmed by two methods using the iCys software.

4.17. Results

4.17.1. Cell count by haemocytometer

Haemocytometer was used to quantify cell detachment (or viability) during the incubation (Figure 4.12). This figure was insightful of the starting confluency after each treatment and pre-scanning. The highest cell detachment rate occurred in the

normoxic population, indicating that normoxic cells have a higher susceptibility to the adverse effects of strain than the hypoxic population. The relationship between cell death and survival in PASM cells in the normoxic population is inverse, normal and dynamic (strain-dependent, responsive), i.e., when cell death increases, survival decreases; strain promoted cell detachment or death. In the hypoxic population, the relationship between cell death and survival is inverse, but cell death (detachment) is strain-independent. The normoxic population is susceptible to the adverse effects of flexing more than the hypoxic population.

4.17.2. Immunoblot quantification of the basal level of SM diffrentiaiton markers

Immunoblot quantification of the basal level of SM differentiation markers, cell cycle regulatory proteins and their phospho-specific partners was done to characterize hASM cells and the expression of the contractile phenotype in starved cells and to compare this expression to the non-starved (synthetic phenotype) conditions as shown in Figure 4.13. The panel shows representative results of 3 separate experiments using Bio Rad 161-0374 molecular weight markers. Serum deprivation for 48 hours upregulated the basal expression of key proteins involved

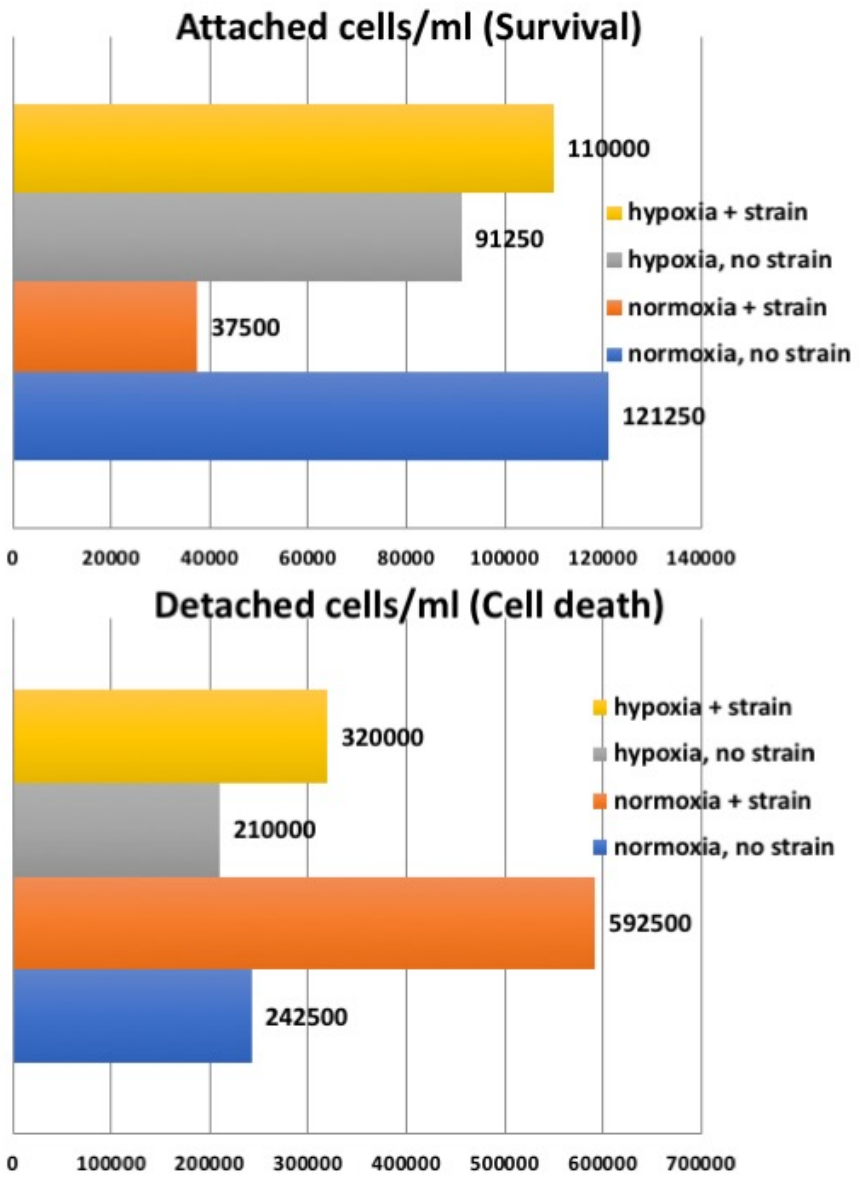

Figure 4.12. Cell count of the attached viable cells (upper) is compared to cell count of the detached dead cells (lower) graph. Seeding density is 70% prior to flexing in both experiments.

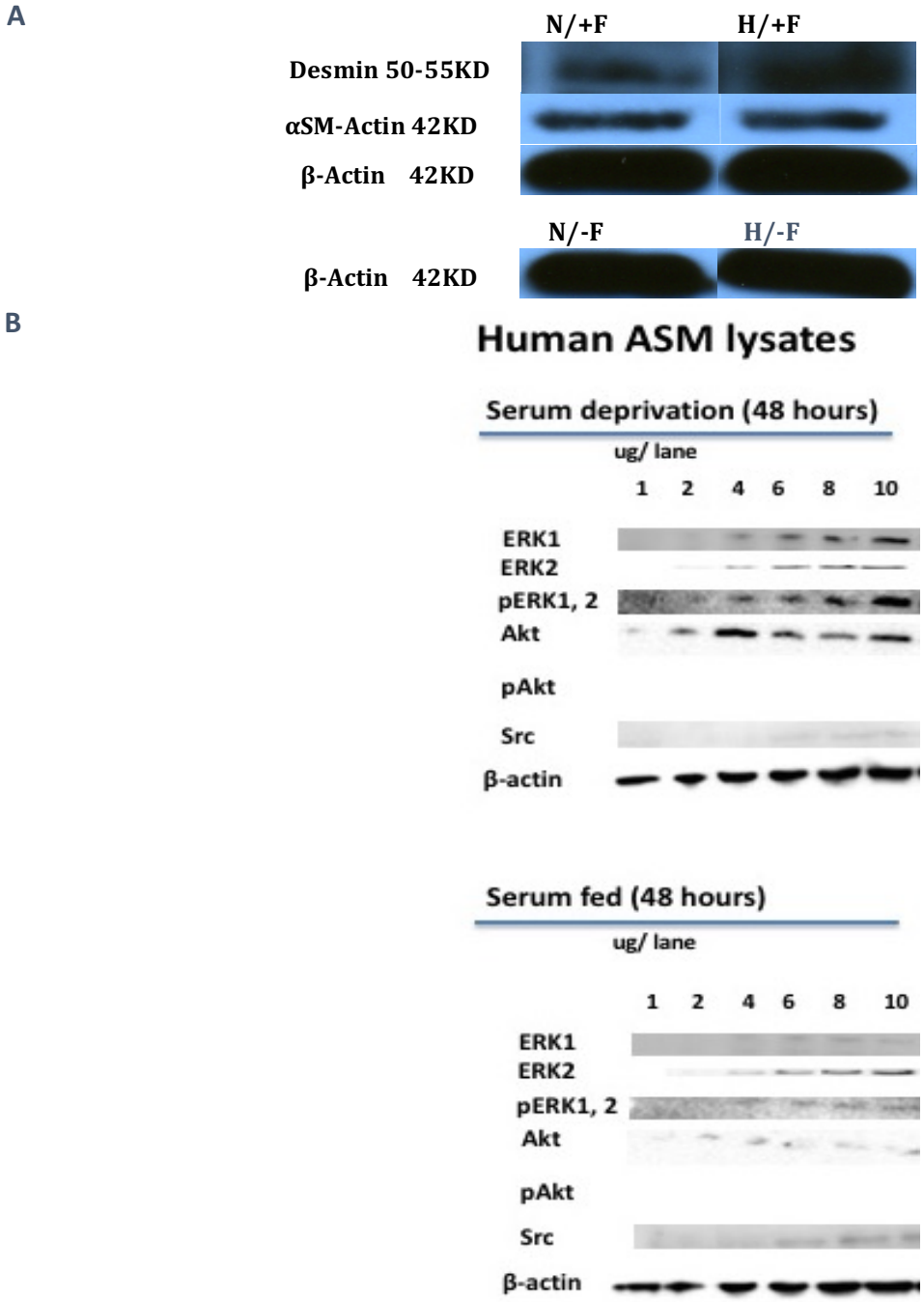

Figure 4.13. Examination of SM markers in hypertensive PASM (A) or normal hASM cells (B) to characterize the basal expression in SM cells. B) Levels of SM markers α-actin, β-actin, desmin in 20 µg cell lysate in relation to different conditions of hypoxia and flexing. N= Normoxia; F=Flexing; H=Hypoxia. B) Concentration gradient shows the basal levels of ERK1/2, pERK1/2, AKT, src but not pAKT, as they are expressed in serum fed and serum deprived hASM. β-actin is a reference protein. Cropped gels are presented for both panels. Full-length gels and blots are shown in appendix A.

in different biomechanical and hypoxia pathways and their phosphospecific partners except for src and psrc.

4.17.3. Cell cycle analysis of nuclear Hoechst staining in PASM cells

Nuclear condensation can be indicative of either mitotic (Figure 4.15 A, E and Figure B.4) or apoptotic processes (Figure 4.14 A, B). Interestingly, apoptosis is characteristic of hypoxic pulmonary vascular remodeling (338, 345-347). Apoptotic events represent a minor (1%) percentage of the total event population (Figure 4.15 E). The mitotic events are shown in Figure 4.15 A and represent the majority of the high max pixel population (Figure 4.15 F). Therefore, a small percentage of condensed nuclei have a morphology consistent with apoptosis occurring within the population of cultured cells (also shown in Figure 4.15 E). The normal growing population was predominantly (97%) in Go/G1 as shown in (Figure 4.14 C, D and Figure 4.15 E, F).

A

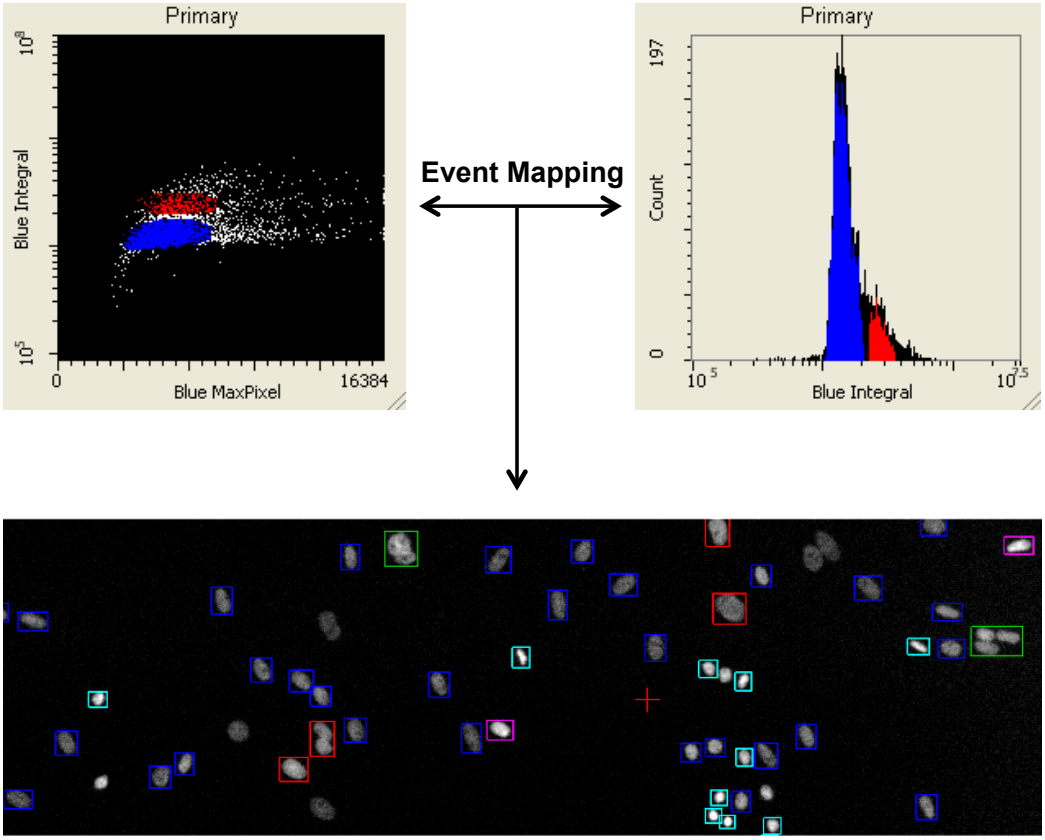

G0/G1 Events (Blue); G2 Events (Red)

B

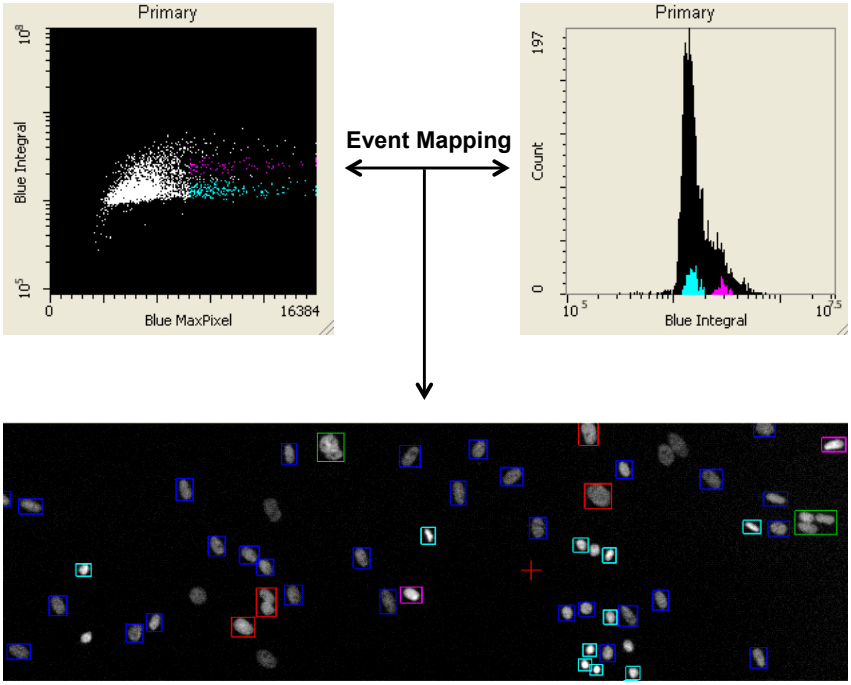

C

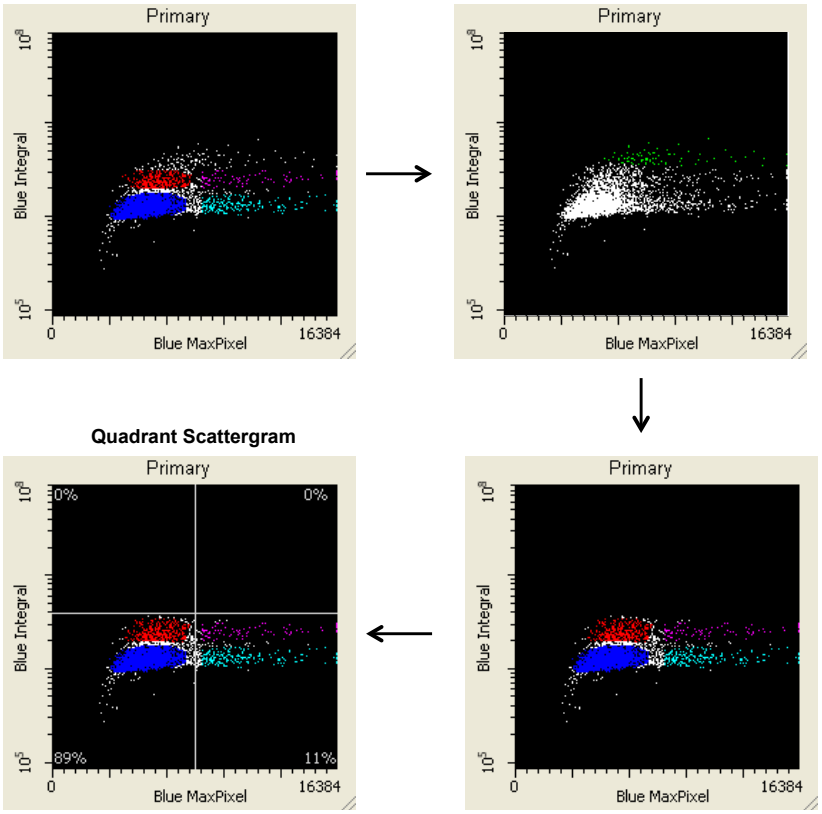
Primary
Blue Integral
Blue MaxPixel
0
16384
Quadrant Scattergram
0%
0%
89%
11%

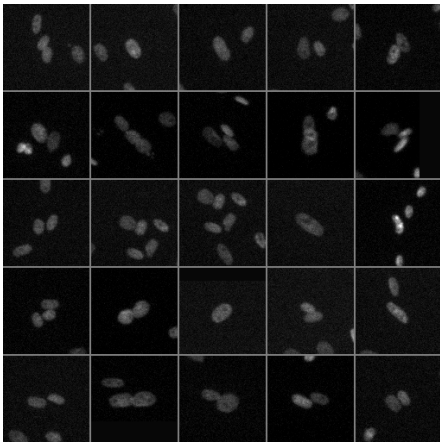
Gallery: Green Population

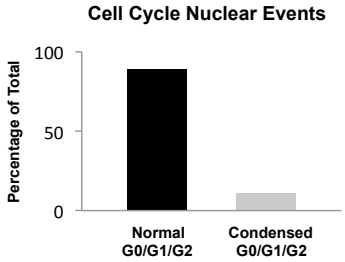
Cell Cycle Nuclear Events
Percentage of Total
100
50
0
Normal G0/G1/G2
Condensed G0/G1/G2

D

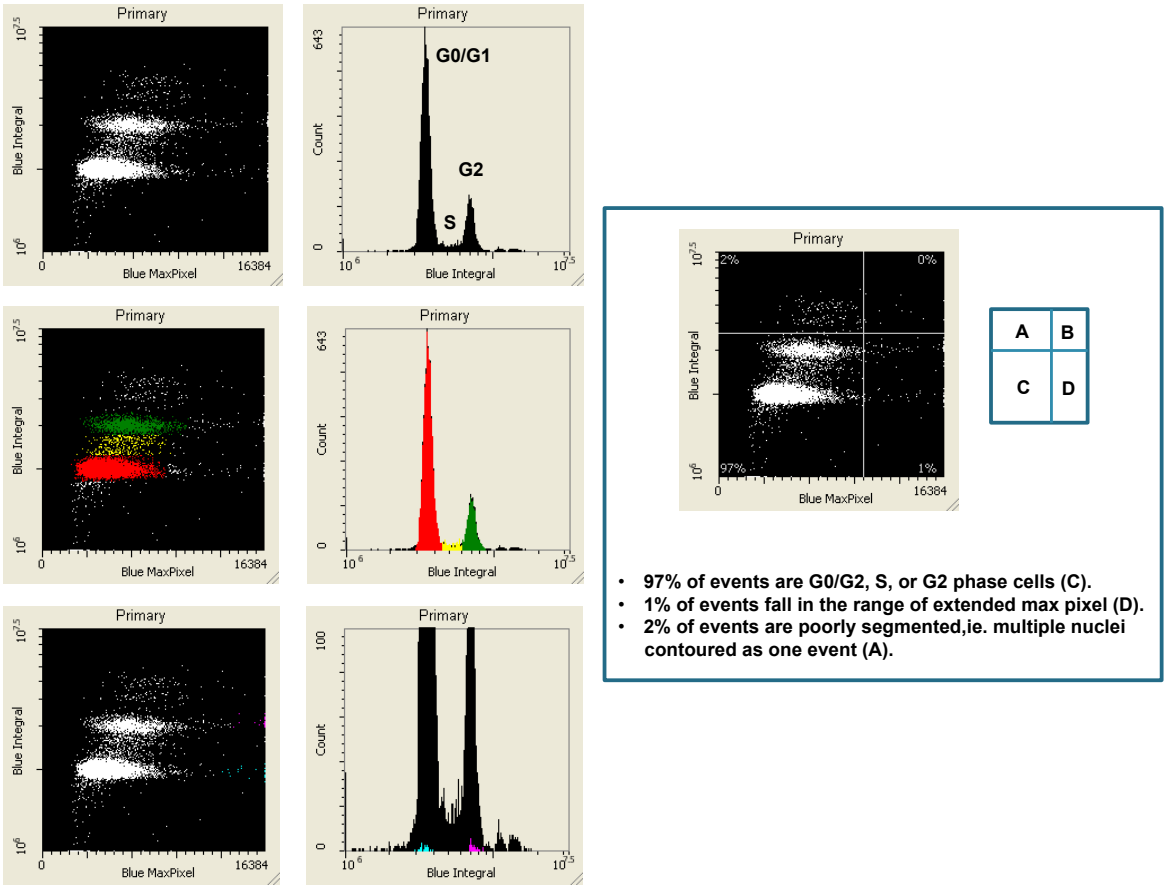

Figure 4.14. Cell cycle events. A) Event mapping of PASM cells, no treatment. Distinct event populations can be identified and colour coded within scattergrams or histograms and the colour-coded events mapped to their specific coordinates within recorded scan field images. B) Cell cycle events. Max pixel extensions of Go/G1 and G2 populations. Condensation of Go/G1 events is shown as cyan and of G2 events is in magenta. Nuclear condensation results in the cell cycle event populations with extended max pixel values in scatter gram plots. Nuclear condensation can be indicative of either mitotic or apoptotic processes. Event mapping shows that condensed nuclei have a morphology consistent with apoptosis occurring within the population of cultured cells. C) The horizontal/vertical division lines can be positioned manually, creating sectors of defined size (quadrants), D) the normal growing population in Go/G1 was predominant (97% of the total population).

A

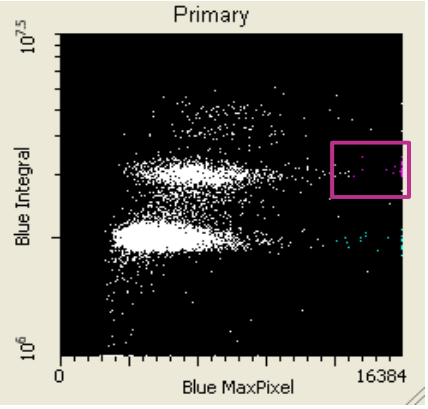

Majority of maxpixel events appear to be mitotic nuclei.

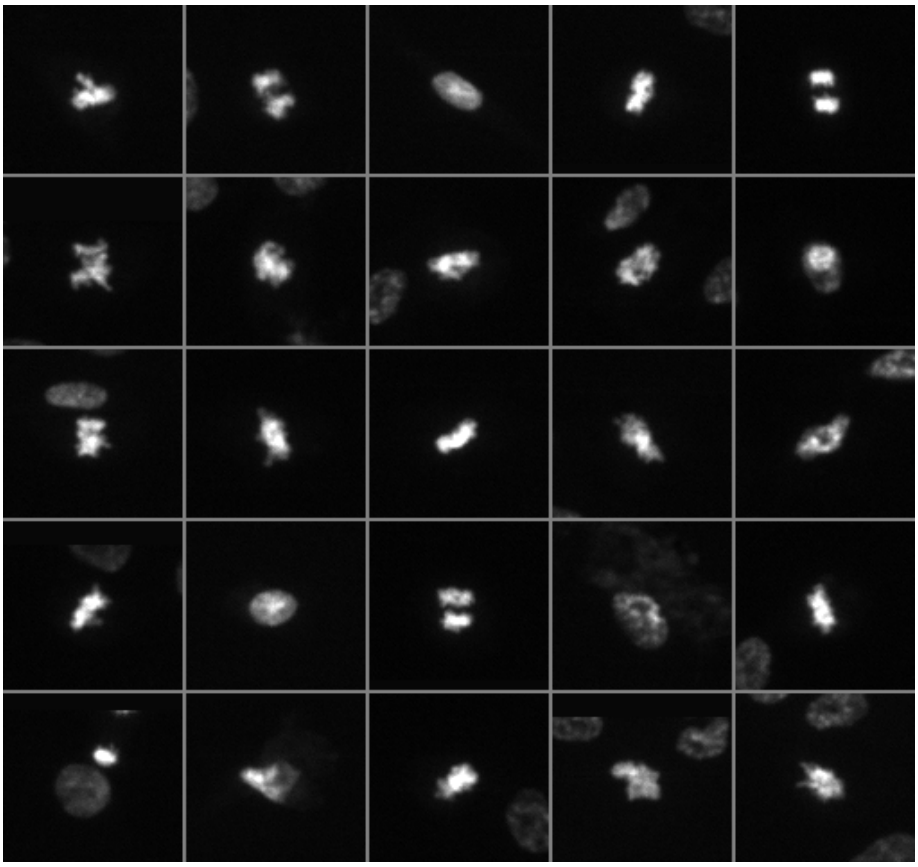

B

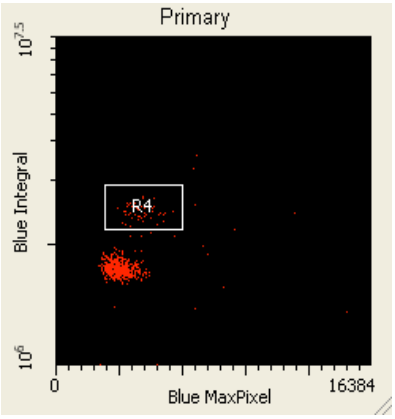

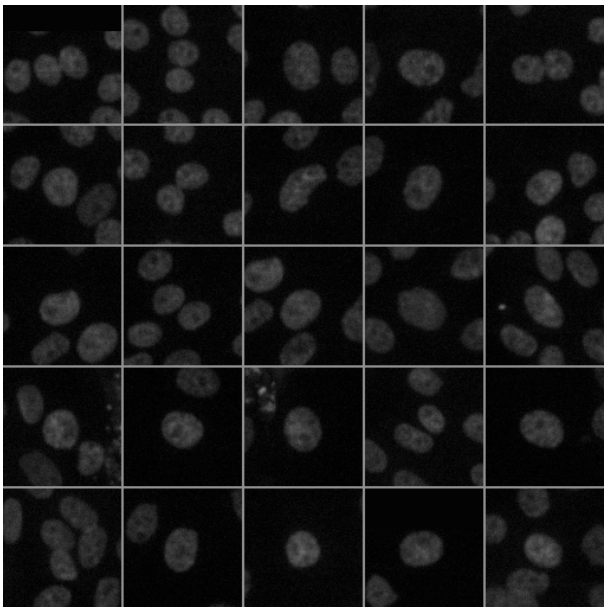

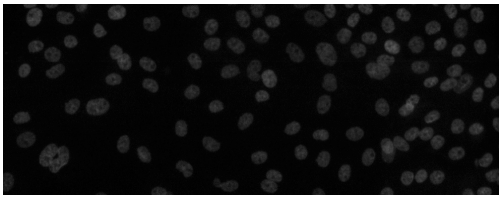

C

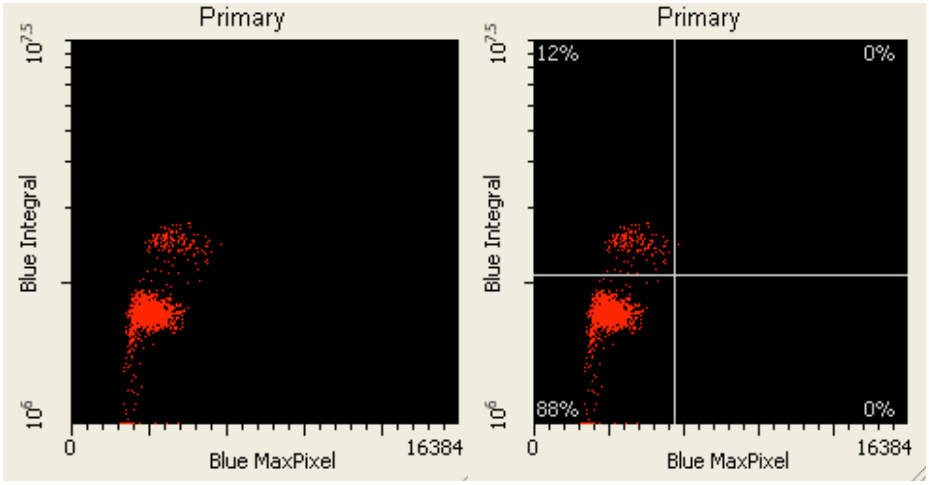
Primary
Blue Integral
Blue MaxPixel
0
16384
Primary
12%
0%
88%
0%

D

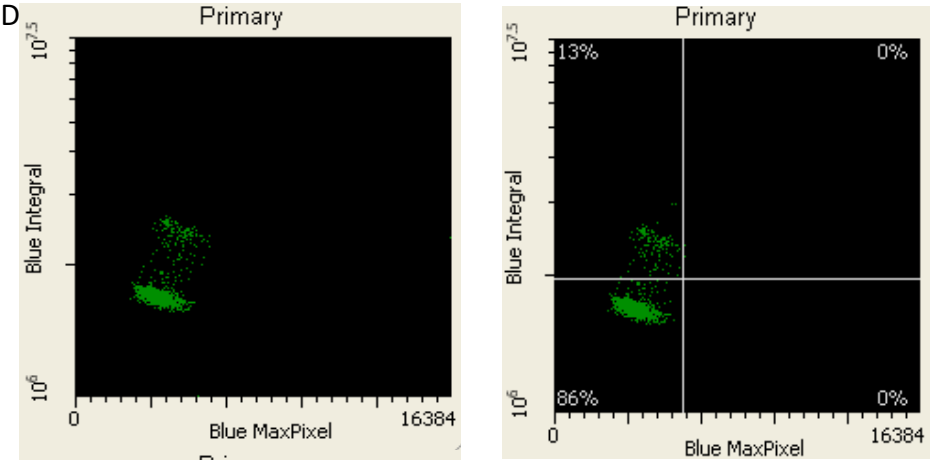
Primary
Blue Integral
Blue MaxPixel
0
16384
Primary
13%
0%
86%
0%

E

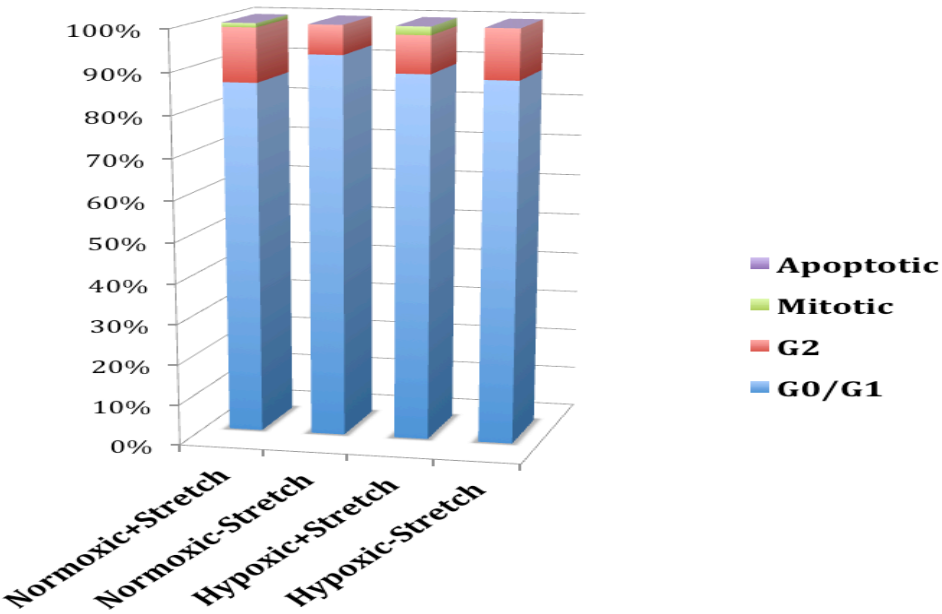
100%
90%
80%
70%
60%
50%
40%
30%
20%
10%
0%
Normoxic+Stretch
Normoxic-Stretch
Hypoxic+Stretch
Hypoxic-Stretch
Apoptotic
Mitotic
G2
G0/G1

F

Well	Label	G2 Primary Count R5	G0/G1 Primary Count R6	Condensed G0/G1 Primary Count R8	Condensed G2 Primary Count R10
1		362	2,164	201	86

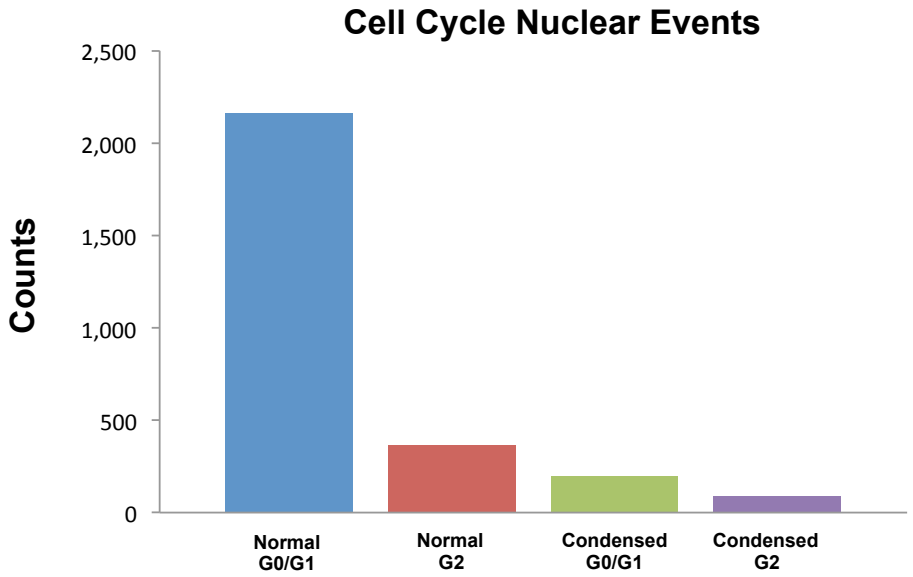

Figure 4.15. Quantification of cell cycle nuclear events by LSC. A) Gallery and field image of region 4 (R4) (G2 events). R4 is the region of interest (ROI). X, Y scattergram of hypoxia together with stretch representing regions of interest. B) Scattergram and quadrant statistics. Hypoxia without stretch; (The predominant proportion of normal cells is in Go/G1 phase 84% of total, and a small proportion is in G2 phase 15%. S phases: 1%. No apoptosis). C) Normoxia together with stretch. D) Normoxia without stretch. E) Apoptosis and cell cycle analysis. Hypoxia together with stretch: (Go/G1=88%, G2=12%, S=0%, apoptosis= 0%). Normoxia with stretch: (Go/G1 86%, G2 13%, M 1%). Normoxia without stretch: (Go/G1 93%, G2 7%). F) Statistics. The cytometer software contains a statistic package allowing for the selection of various statistical parameters for data analysis. For the present analysis, the statistical parameter "count" was used for the assessment of the percentage of nuclear events in various stages of the cell cycle. N=3 replicates.

The purpose of the LSC is to demonstrate the validity and reproducibility of its application in the quantification of the cumulative effects of hypoxia and cyclic mechanical stretch on cytoskeleton remodeling in PASM and hASM. The altered F:G-actin ratio as a measurable endpoint for cytoskeleton organization upon exposure of PASM or hASM cells to hypoxia together or independent on strain. The F:G-actin ratio is quantified by two LSC modules that can generate the same ratios, and hence are reproducible. Without some method of correction, used as is, quantification of G-actin fluorescence would include both nuclear and cytoplasmic signals. The LSC quantifies whole cell actin, and removes the nuclear G-actin fluorescence from the total G-actin fluorescence. To remove the nuclear G-actin fluorescence from the total G-actin fluorescence, cell associated phantoms must be separated further into nuclear and cytoplasmic populations. This is achieved through a scattergram blot of blue versus long red phantom fluorescence, the numerical values of such separation are shown in Figure 4.16 (B and C) and 4.17. Fluorescence quantification can be expressed either as the summed integrated fluorescence of all phantoms or as the mean integrated phantom fluorescence. LSC is a valid method for visualizing and quantifying actin depolymerization in hypertensive myocytes, as F:G-actin ratios scored 3.2 (sum) or 3.1 (mean) in cultured hASM cells by two alternative methods (Figures 4.17 and 4.19).

As was pointed to in the first section of chapter 4, pulsatile strain increases total endogenous ROS and superoxide anion release significantly in normoxic and hypoxic conditions in primary PASM fibers (Figure 4.11 and 4.20). The effect of strain

is predominant in increasing the superoxide release, only under hypoxic conditions (Figure 4.20).

4.17.4. Hypoxia and stretch-induced changes in oxidative metabolism

ROS are important signaling molecules connecting vascular stretch with cell cycle entry or arrest. Endothelial cell strain triggers release of mitochondrial ROS to the cytosol (273). Vascular myocytes generate mitochondrial superoxide in response to stretch (342), activating mechanotransduction signaling pathways. The effect of mechanical strain on the ability of pulmonary myocytes to handle oxidative stress in hypertensive environment is unknown. I aimed to demonstrate whether cyclic strain together or independent of hypoxia contribute to increased ROS in PASM cells using DCF-DA and DHE-based assays.

The changes in the emission of DCF and DHE, normalized to the control (normoxia together with stretch), are presented in Figure 4.20. I wanted to demonstrate the hypothesis that mechanical stretch and hypoxia alter the defence against ROS. The results obtained reveal that pulsatile strain increased total ROS and superoxide release significantly in normoxic and hypoxic conditions.

A

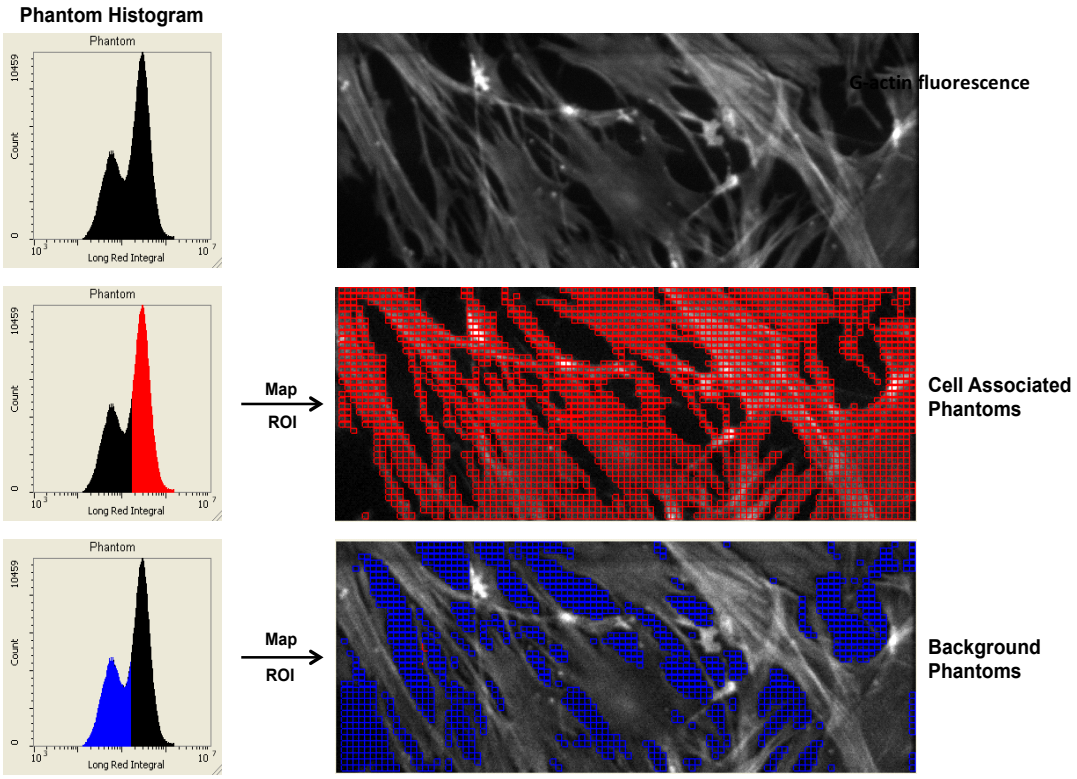
Phantom Histogram
Phantom
Count
10459
0
Long Red Integral
G-actin fluorescence
Map
ROI
Cell Associated
Phantoms
Background
Phantoms

B

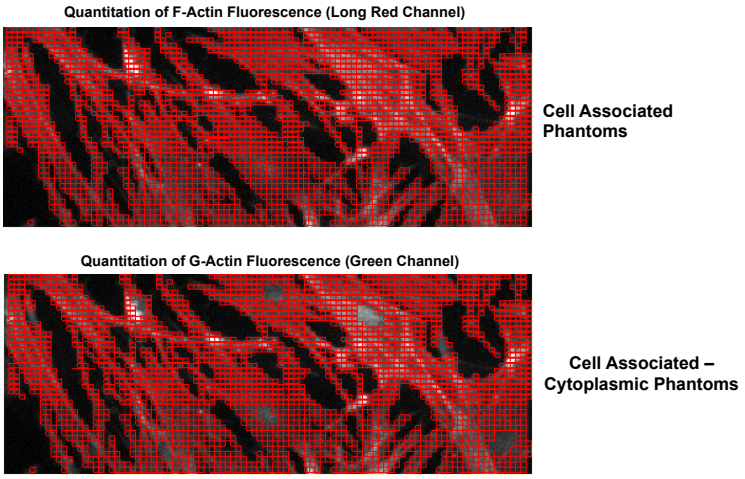
Quantitation of F-Actin Fluorescence (Long Red Channel)
Cell Associated
Phantoms
Quantitation of G-Actin Fluorescence (Green Channel)
Cell Associated –
Cytoplasmic Phantoms

C

Phantom Integral Long Red Sum	Phantom Integral Green Sum	F-Actin/G-Actin Ratio (Sum)
74,520,809,222	23,094,202,036	3.2
Phantom Integral Long Red Mean	Phantom Integral Green Mean	F-Actin/G-Actin Ratio (Mean)
344,232	111,163	3.1

Figure 4.16. Phantom contour analysis of cytoplasmic F:G-actin ratios in cultured primary PASM cells. A) Identification of background and cell associated phantom populations (long red channel). The cell associated phantom contour population is used for the quantification of F- and G-actin fluorescence. B) To remove the nuclear G-actin fluorescence from the total G-actin fluorescence, cell associated phantoms must be separated further into nuclear and cytoplasmic populations. This is achieved through a scattergram plot of blue versus long red phantom fluorescence, the numerical values of such separation are shown in C. C) Fluorescence quantification can be expressed either as the summed integrated fluorescence of all phantoms or as the mean integrated phantom fluorescence. ROI= region of interest.

A

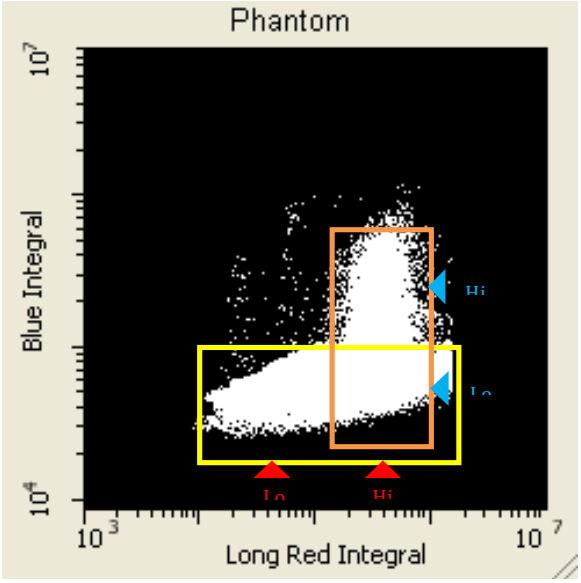

B

Phantom Histograms **Phantom Scattergrams**

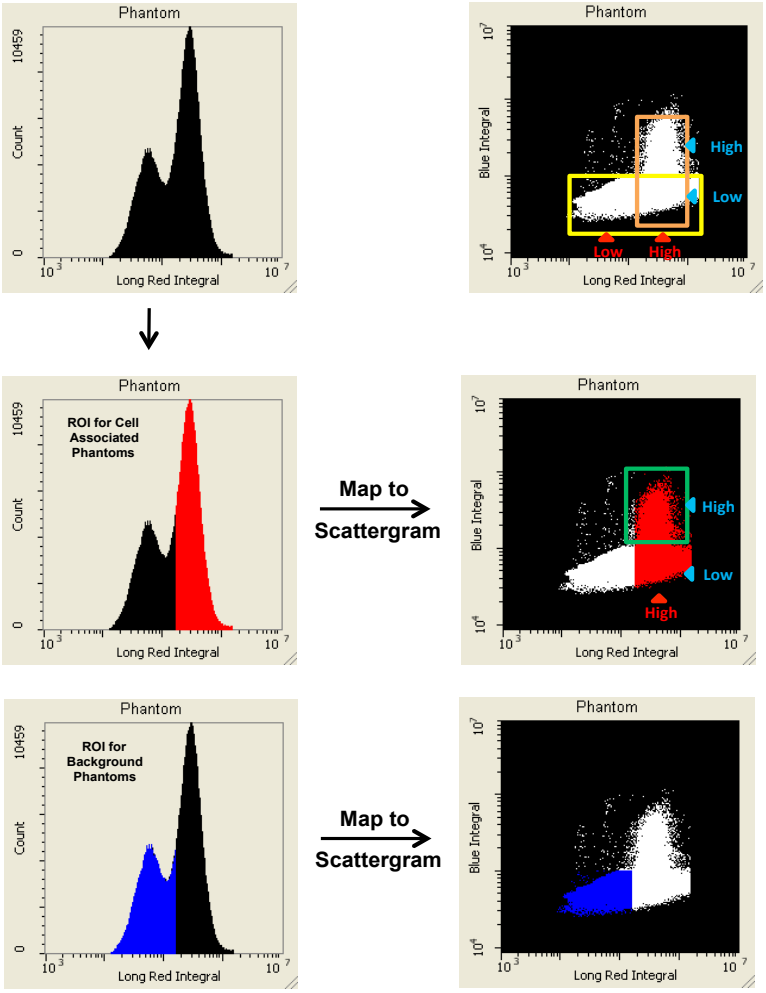

C

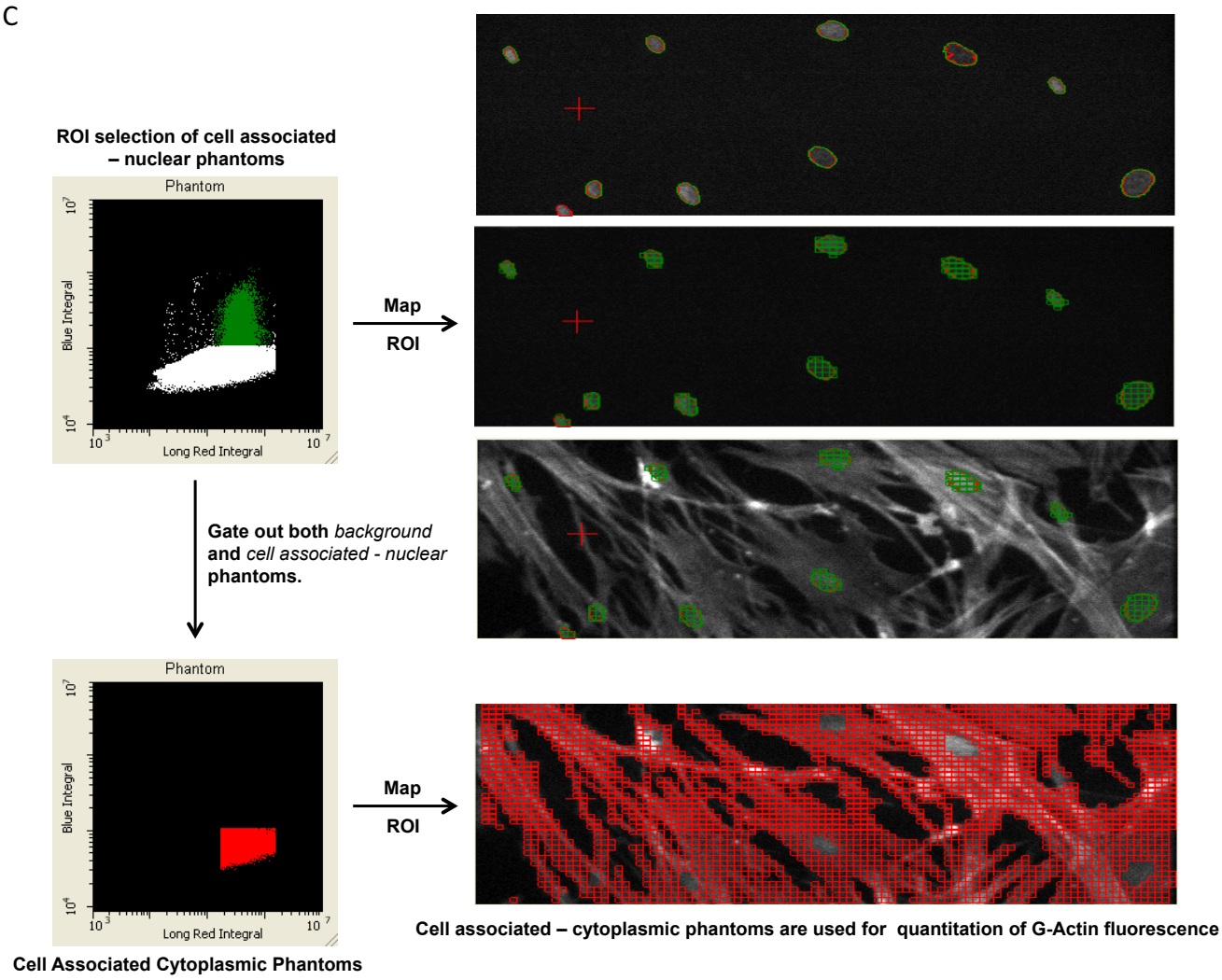

Figure 4.17. Isolation of nuclear associated phantoms. A) A scatter gram plot of blue (Hoechst) nuclear fluorescence versus long red (F-actin) cytoplasmic fluorescence reveals distinct phantom populations: Phantoms with low blue/low long red and low blue/high long red fluorescence (yellow box). Phantoms with low blue/high long red and high blue/high long red fluorescence (orange box). B) Cell associated phantoms previously identified in the phantom histogram, map to regions of low blue/high long red and high blue/high long red fluorescence within the phantom scatter gram. Phantoms with both high blue/high long red fluorescence (green box) are likely the cell associated- nuclear phantoms. ROI= region of interest.

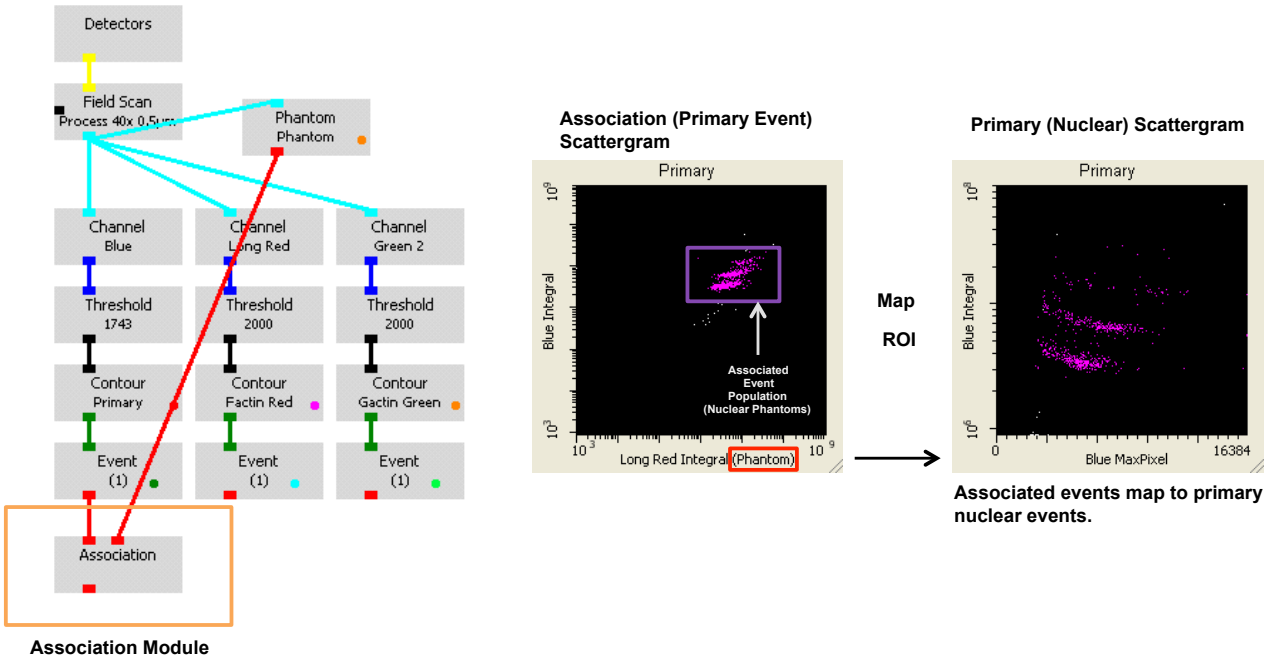

Figure 4.18. Nuclear associated phantom module. Phantoms links only phantom contours that are in direct contact with the primary contour (blue fluorescence) through the association module. The primary contour is the nucleolus phantom contour. The associated events are displayed using primary event scattergram and blotting nuclear (blue channel) fluorescence versus associated long red channel phantom fluorescence. This scattergram may be termed the association scattergram.

A

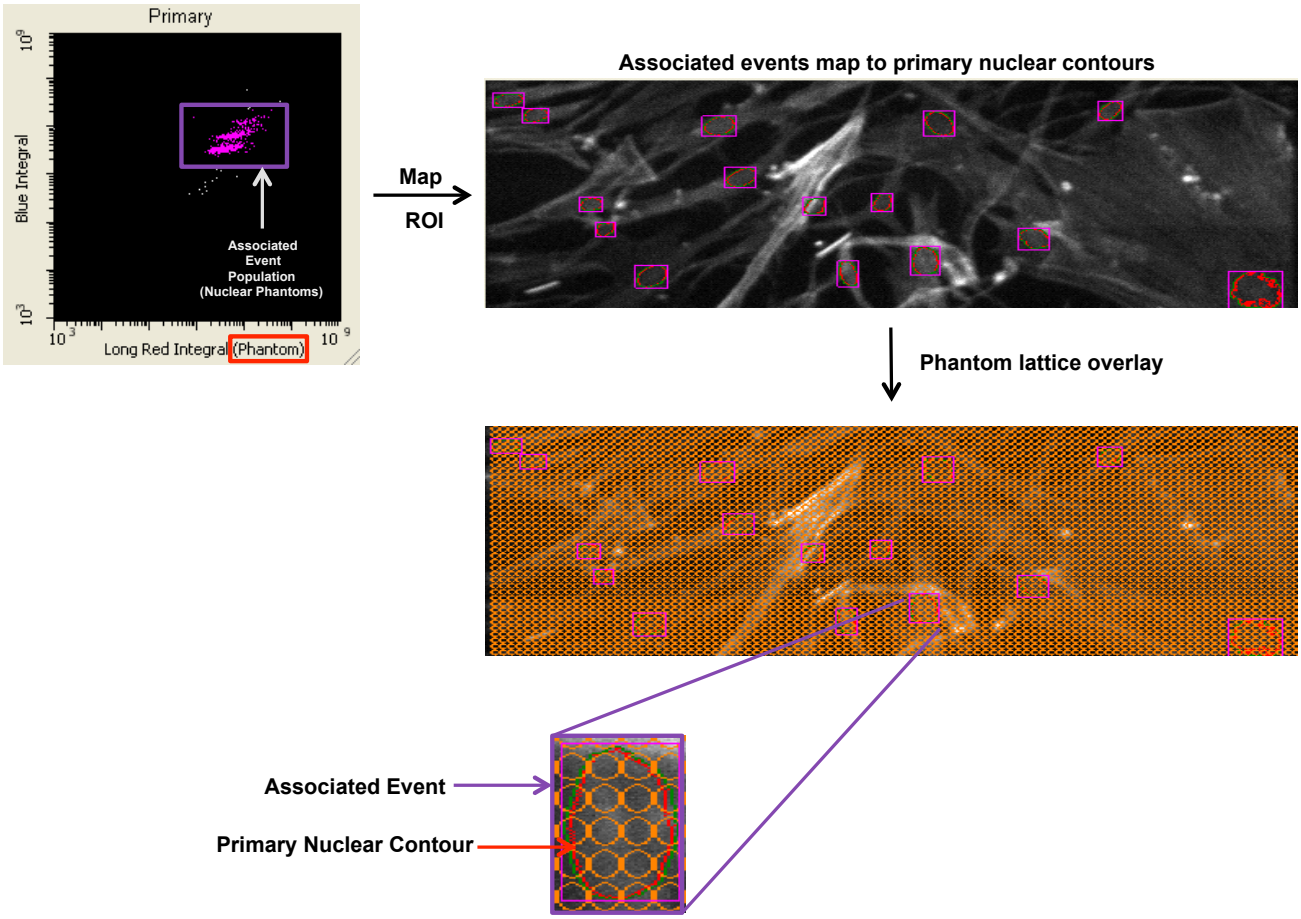
Primary
Blue Integral
Long Red Integral (Phantom)
Associated Event Population (Nuclear Phantoms)
Map ROI
Associated events map to primary nuclear contours
Phantom lattice overlay
Associated Event
Primary Nuclear Contour

B

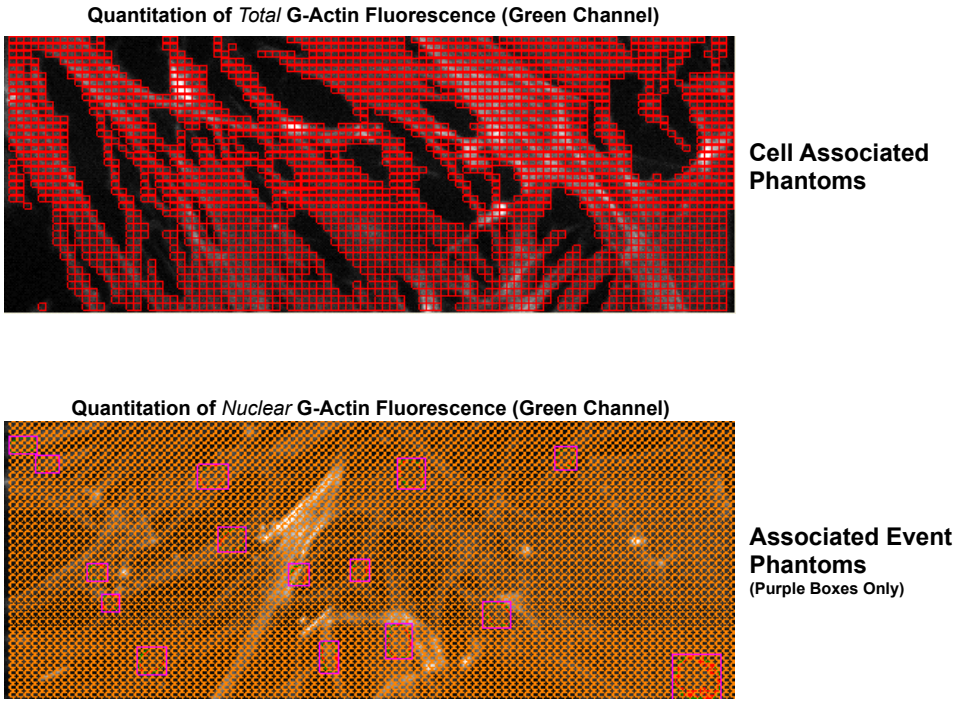

Total F-Actin	Total G-Actin	Nuclear G-Actin	Cytoplasmic G-Actin	
Phantom Integral Long Red Sum	Phantom Integral Green Sum (Total)	Phantom Integral Green Sum (Nuclear)	Corrected Phantom Integral Green Sum Total	F:G-Actin Ratio (Sum)*
74,520,809,222	26,136,680,654	3,142,947,131	22,993,733,523	3.2

Figure 4.19. A) An alternative method of isolation of nuclear associated phantoms. B) The associated event population contains only those phantom contours in direct contact with the primary nuclear contour. C) *using this method, phantom population is consistent with the cell-associated nuclear phantom population isolated by the previous methodology.

A) Total ROS in PASM cells by DCF assay

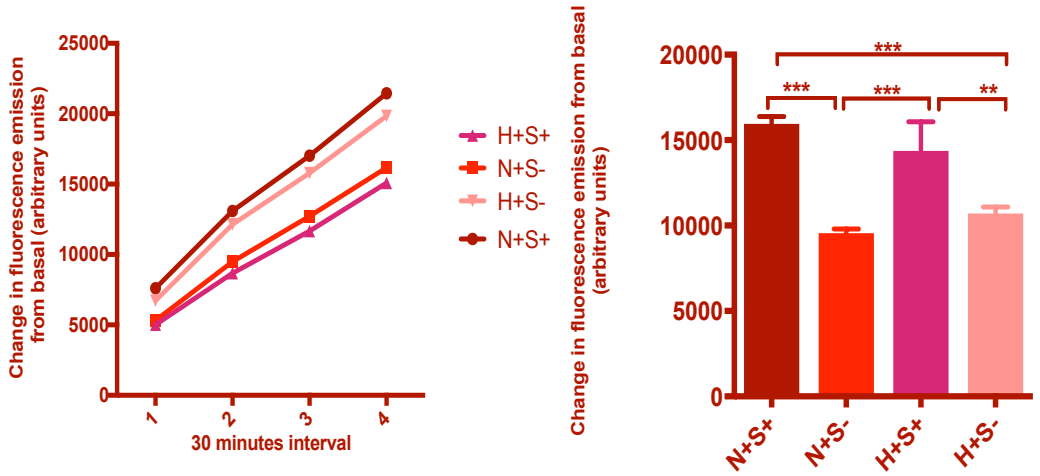

B) Endogenous superoxide anion in PASM cells by DHE assay

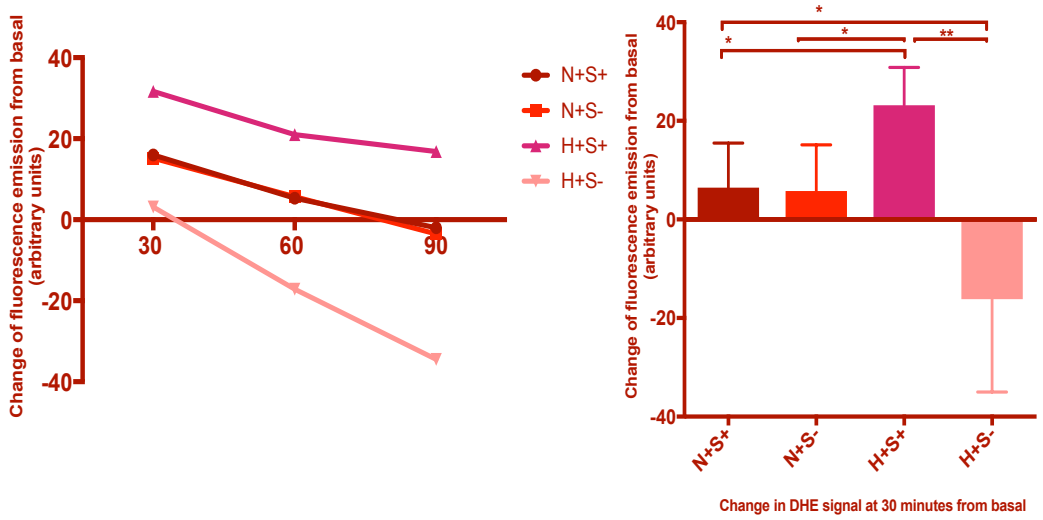

Figure 4.20. Pulsatile strain increased total ROS and superoxide release significantly in normoxic and hypoxic conditions. A) Total endogenous ROS is quantified by the change in DCF-DA fluorescence from primary PASM fibers. B) Endogenous superoxide radical is quantified by the change in DHE signal at 30 mins from basal induction. For both assays an average of $5x10^5$ stimulated cells/treatment was analyzed during two consecutive 30 min periods at 37°C at excitation 485 nm, emission 520 nm and gain 1500. P <0.05 represents significance, ***highly significant, Ratio to normoxic strain. N+S+=Normoxia together with stretch; N+S-= Normoxia independent on stretch; H+S+=Hypoxia together with stretch; H+S-=Hypoxia independent on stretch.

4.18. Discussion

4.18.1. Profound changes in PASM phenotypes

I characterized the utility of the LSC method in elucidating arterial cytoskeleton remodeling *in vitro*. I demonstrated that (a) LSC is a valid method that can be used in the analysis of nuclear and cytosolic fluorescence, (b) the cumulative effects of mechanical strain together with hypoxia promote ROS formation, (c) the molecular events in response to hypoxia and mechanical overload of the pulmonary circuit can be demonstrated *in vitro* by subjecting hypoxic cultured primary PASM to repetitive stretch-relaxation cycles at rates comparable to dynamic stretch *in vivo*, and (d) the altered cytoskeleton in the form of F:G-actin ratio can be imaged and quantified at the cellular level by LSC. LSC can remove the nuclear G-actin fluorescence from the total G-actin fluorescence. The findings obtained by LSC *in vitro* are amenable to validation in any *in vivo* model of interest.

Factors contributing to PAH include prolonged vasoconstriction, vascular remodeling, inflammatory cell migration, and *in situ* thrombosis leading to vascular lesions. The pulmonary circuit supplies the lung. SM in the *tunica media* constrict the diameter of the lumen in a process called vasoconstriction or increase the diameter in a process called vasodilation due to its composition of elastic and SM fibers. Contraction or relaxation in response to local stimuli is under the control of the sympathetic division of the autonomic nervous system. Any change in the vessel diameter affects both blood pressure and flow. The three layers; *intima, media* and *adventitia*, are connected by collagen fibers. Elasticity resists the pressure generated by the heart as it forces blood into the circuit. Elastic non-remodeled arteries are

stretched during systole, whereas during ventricular diastole blood pressure within the arteries fall and they recoil to force blood onward towards the capillaries.

The pulmonary arterial wall normally exists in a state of dynamic tension, stretching in systole and relaxing in diastole. SM cells undergo cyclic mechanical stretch during the cardiac cycle, critical for maintaining homeostatic signaling and balance between cell fate decisions. The pulsatile strain alters myocyte phenotype commitment (254) and induces the generation of ROS (348).

While hypertensive states are traditionally modelled by increased pulsatile mechanical stretch, a review of echocardiography and Magnetic Resonance Imaging (MRI) data indicates that in fact hypertensive states may be marked by an increased diastolic vascular diameter and loss of distensibility, with limited pulsatile deformation during systole (349-351). MRI is a useful method for imaging cardiovascular tissues and as a means for measuring the arterial diameter. When I stretch at the heart rate of 1.5 Hz (the physiological frequency; the same inspiration/exhalation frequency characteristic of the animal), I get ¼ of the response when using the non-physiological frequency. Although others could get a maximum deformation at faster rates (15-18%) (352-354) these are non-physiological rates. The maximum deformation I can get during pulsation is about ±5% of the resting vessel wall length. In PAH I can get less deformation. This is contradictory to the way controls are usually designated, wherein the control is static (unstrained), and the strained is hypertensive. The behaviour of the cells during stretch is comparable to the behaviour of the arterial wall according to the LSC. I used a fluidic matrix to grow cells, since cells grown on a solid matrix more closely resemble the hypertensive

state. Thus the presence of pulsation provides the homeostatic state and removal of pulsing produces the pathological state.

The data obtained support the concept that subjecting PASM cells from a normal neonatal (<24 hr age) pulmonary artery to *in vitro* stressors, it is possible to recapitulate the effect of the same stressors in the disease state. Normoxia together with ±5 % stretch from the resting length at a physiologically relevant pulsation rate is a control. Hypoxia and loss of pulsation is what is seen in PAH. I find the highest cell detachment (death) rate is reported among the normoxic population, indicative a normoxia-associated higher susceptibility to the adverse effects of strain than the hypoxic population (Figure 4.12).

4.18.2. F:G-actin ratio links remodeling to the phenotype

The F:G-actin is suggested as an endpoint in the cytoplasm because the greater the amount of G-actin that is present, the stronger is the hypertensive phenotype that is expressed as the cell loses the dynamic assembly of the cytoskeleton. To prove that stretched cells are comparable to cells seen in the vascular wall I took a structural approach that compared F to G actin in the cytosol using LSC. Serum deprivation for 48 hours upregulated the basal expression of key proteins involved in different biomechanical and hypoxia pathways and their phosphospecific partners except for Src (Figure 4.13).

4.18.3. Cell cycle entry and proliferation signaling

In this study, different treatments did not change the distribution of the cell cycle phases. The normal growing population is predominantly in Go/G1. This finding is consistent with other findings that showed no significant increase in PASM growth

under 5% and 10% hypoxia. For example, Santilli's studies reported that the cells in the medial wall of the artery normally exist under conditions of low oxygen (355-357). Santilli measured the concentration of transarterial wall oxygen in rabbit aortas by using an O_2 microelectrode and found the lowest O_2 concentrations in the medial wall of the artery, compared with the adventitia and lumen (344-346). The O_2 concentration was only approximatley 4% in the centre of the media, but 12% in the lumen and 8% in the adventitia. Scientists usually use 1-3% O_2 in studies related to proliferation (355-357).

Chronic hypoxia-induced hypertension is a well known model in which the decrease in alveolar oxygen pressure to <70 mmHg can induce a strong vasoconstrictor response, but this is variable among animal species. The greatest effect is in cattle, where short time chronic hypoxia causes acute vasoconstriction (358) while prolonged hypoxia results in remodeling of the distal pulmonary arterial branches (359, 360). With the level of hypoxia I use (FiO_2: 0.10), PO2 in tissues is not reaching half of 21% at 40 mmHg. By undertaking 10% O_2, it takes the tissues to a physiological pH. Previous studies standardized the model (256, 339). Saini-Chohan (361), showed that 10% O_2 *in vivo* causes significant remodeling of the pulmonary arterial media in just 72 hours. Those studies have also shown that 10% O_2 *in vitro* has a similar effect on proliferation of SM cells. Gradient hypoxia ranging from 1-4% and measurements of the actual amount of O_2 dissolved in the monolayer under test conditions can be observed and used to optimize the system.

P53 and pRb are key regulators of proliferation. p27 is a key regulator of PASM proliferation through the hypoxia/PI3K/AKT pathway and it converges on hypoxia and

ROS to promote cell cycle entry (316). Compared to normoxia, hypoxia induced significantly higher expression of desmin (Figure 4.13 A). Hypoxic and normoxic hASM express the same level of β-actin in the presence of stretch. The lack of stretch leads to much lower expression of β-actin, (Figure 4.13 A). Serum deprivation for 48 hours upregulates the basal expression of key proteins involved in different biomechanical and hypoxia pathways and their phosphospecific partners except for Src. This demonstrates that pulsatile stretch maintains the expression of SM-specific genes and contractility, and the absence of pulsatile stretch alters cytoskeleton assembly (Figure 4.13 B).

In hyperproliferative states such as PPHN, the plasticity of the resistant arteries is lost (253, 333) by an ongoing process of remodeling that implies there is a predominance of synthetic SM fibers (337). The elevated levels of hypoxemia and oxidative stress contribute to disease progression by inducing proliferation (338) and protecting against cell cycle arrest, i.e. apoptosis or senescence (280, 281). The role of actin polymerization in regulating cell cycle events in hypertensive PASM is currently unknown.

4.18.4. Oxidative and nitrosative stress

NO is a known vasodilator that can be exogenously inhaled to reduce pulmonary vascular resistance but not systemic vascular resistance (362). Depending on the concentration, >10 particle per million worsens arterial oxygenation, with higher doses being potentially toxic (363). Chemical reactions with O_2 or ROS release toxic nitrogen oxides and hydroxyl radicals that subsequently react with superoxide to form peroxynitrite radicals which elicit pulmonary cellular injury (278).

In the pulmonary artery, there are three sources of $O^{\bullet -}$ radical generation in response to hypoxia: 1) NADPH oxidase, 2) the mitochondrial electron transport chain, and 3) uncoupled endothelial nitric oxide synthase and xanthine oxidase (XO). A group in 2011 (364) disrupted extracellular SOD3 expression in cultured calf PASM cells as a way to mimic hypoxia-induced extracellular ROS elevation *in vivo*. They subsequently expressed XO in the hypoxic PASM cells in culture. They found that the loss of SOD3 was associated with an increase of the $O^{\bullet -}$ radical and this mediated up regulation of the early growth gene Egr1 via phosphorylation and activation of ERK1/2 and CDK1 (364).

Perfusion in the pulmonary circuit depends on the pressure of the blood ejected during each heartbeat (one cardiac output/ one pulse going through the heart). Each contraction causes 10% stretch. In PHN, one contraction causes less than 10% stretch (365). The cytoskeleton response to stretch with low levels of strain (±5%) is heterogeneous. With higher strain (±10%), a huge response occurs, such as ripping of the cytoskeleton (365). The flexer-cell is associated with cell death due to loss of adherence to the membrane. Capillary walls permit exchange between blood and the surrounding interstitial fluids. Diffusion distance is small, and exchange is quick because the wall is thin (274). A high F:G-actin ratio downstream of SOD increases stiffness, resulting in thicker vessel diameter, higher pressure in remodeled versus non-remodeled vessels, and pulsation is non-harmonized due to the loss of distensibility (274). Remodeling is associated with HTN, higher ROS, lower antioxidant enzyme levels such as catalase, SOD1,2,3, glutatione peroxidase and NADPH oxidase (274). Our current findings show that pulsatile strain increase total endogenous ROS

and superoxide anion release significantly in normoxic and hypoxic conditions in primary PASM fibers (Figure 4.20 A). The effect of strain was predominant in increasing the superoxide release only under hypoxic conditions (Figure 4.20 B). These data led us to assume that the increased generation of ROS is likely the mechanism that induces cell death in mechanically strained myocytes and that hypoxia independent of strain protects against such death.

Our use of phantom contours through the application of LSC gives a more accurate analysis of actin fluorescence than can be achieved through the use of peripheral contouring in previously published studies (298). Phantom integrates the fluorescence within each circle everywhere. I can measure which phantom is overlaid on top of each position. As F-actin fluorescence more thoroughly delineates cell boundaries, red channel F-actin fluorescence is used for the separation of the phantom contour lattice into background and cell associated populations. I generate a phantom histogram: the primary contour is the nucleus phantom contour. Once the cell associated phantom population has been established, these phantoms are used for the quantification of both F- and G-actin cellular fluorescence. The strategies described in Figures 4.16, 4.17, 4.18, and 4.19 can be employed to isolate and remove the nuclear G-actin signal. Fluorescence quantitation is expressed either as the summed integrated fluorescence of all phantoms or as the mean integrated phantom fluorescence. The results of the two methods are almost identical. The latter finding demonstrates that the LSC is capable of visualizing and quantifying actin depolymerization in hypertensive myocytes, as F:G-actin ratios scored 3.2 (sum) or

3.1 (mean) in cultured hASM cells. The absence of pulsatile stretch alters ROS, LDL peroxidation and F:G-actin, linking ROS to cytoskeleton disassembly. Although I established the validity of the LSC for this purpose, the inavailability of resources limited quantification of the induced F:G-actin ratio after the exposure to the four study treatments.

4.19. Conclusion

These experiments provide pilot data necessary to characterize, in broad terms, hypoxia and mechanical strain-induced regulation of the PPHN phenotypic vasculature in an animal model that manifests the disease in a similar pattern to human babies. Results obtained *in vitro* can be validated in a neonatal porcine model of hypoxic pulmonary hypertension.

4.20. Limitations and solutions

Limitations of LSC include: 1) avoiding background formation on the flexer-cell membrane as the background interferes with the fluorescence of the nucleus and cytosol. A single cell approach cannot apply. Adding an inhibitor can demonstrate higher levels of regulation. 2) DCF limitations include, in the narrative: first, H_2O_2-dependent oxidation of DCFH to DCF occurs slowly, if at all, in the absence of ferrous iron. Second, DCFH oxidation is reliant on metal-catalyzed oxidation reactions, thus mitochondrial heme-containing cytochromes, peroxidases and a variety of other organic acid or protein-complexed transition metals catalyze DCFH oxidation. Lastly, intracellular deacetylation of DCFH-diacetate to DCFH does not assure detection of

intracellular redox reactions of whatever chemical origin. Following deacetylation, DCFH can back-diffuse into the extracellular compartment to undergo further reactions. However, the above limitations affect both the experiment and the control, therefore, they do not invalidate my data.

CHAPTER 5: CONCLUSION

5.1. NGS and LSC are novel approaches that help understanding the diseases models

I have examined the process of lung toxicity in the context of embryonic lung development and described the nuclear and cytoplasmic changes in chromatin and metabolic consequences of pulmonary disease of the newborn, all of which encompass embryonic remodeling and unabated stress on lung development.

These linkages indicate that there need to be more intensive studies of lung responses to high levels of cytotoxic stressors, and this thesis describes the findings obtained from two models of developmental lung disorders that continue to impair lung function postpartum and cause high mortality rates among neonates. The expressed goal of this research, then, was to examine nitrofen-induced CDH and PPHN in the context of the hypothesis that aberrant cellular remodeling during development leads to abnormal lung growth and occurs via changes in miRNA and cytoskeletal modifications.

Pulmonary artery hyperplasia is the result of proliferation of the PASM, and the induction of proliferation by hypoxia in the fetus and the newborn is the primary cause of PPHN. In this work, I explored two models of PAH, identifying changes in RNA levels in an animal model of CDH using NGS technology, and in an *in vitro* model of PPHN using LSC to open new avenues for research of cytoskeleton remodelling in PAH.

Oxidative and nitrosative stress that persists in excess of homeostatic balancing reactions leads to impaired remodeling and abnormal lung growth due to tissue hypoplasia or pulmonary artery hyperplasia. Underlying these processes is oxidative stress, which if unresolved leads to programmed cell death that involves apoptosis and autophagy because of ER impairment.

MiRNA deep sequencing technology has become a platform for the discovery of important miRNAs affecting various regulatory signals that control pivotal processes in all tissues, including development and differentiation (58, 59). MiRNAs operate as negative or positive post-transcriptional regulators of gene expression, and converging lines of evidence have suggested a role for miRNA silencing in ER stress signaling (45).

In this thesis, the contribution of miRNAs to lung development and disease and possible future implications in the field of lung biology was examined. I used NGS technology to characterize transcriptome differences between control lungs and nitrofen-induced hypoplastic lungs in embryonic lung tissues prior to the development of the diaphragmatic defect. I found that transcriptome changes contributed to abnormal lung development in the nitrofen rat model of CDH that is analogous to that in human CDH *in silico*.

NGS is suitable to the research question because it is more sensitive; it enables high throughput screening of thousands of genes and miRNAs; it identifies the whole transcriptome and other RNA species simultaneously; this makes it very useful to the research question in proving that the transcriptome changes contribute to abnormal

lung development in nitrofen-induced CDH lung. In contrast, RT-qPCR and dPCR validate and quality check limited number of reads, and thus are limited with respect to NGS.

Although many approaches using miRNA inhibitors or mimics showed significant results, the constituents used in these studies are not suitable for *in vivo* miRNA inhibition or ectopic expression.

By comparing the differentially expressed transcriptome of nitrofen-induced hypoplastic lungs versus control lungs in E13 rat embryos before the development of embryonic diaphragmatic defects, it was possible to identify the expression profile of miRNA and mRNA genes associated with CDH. I validated the dataset by both RT-qPCR and dPCR, and conducted GO, miRNA target analysis, and orthologous miRNA sequence matching for the deregulated miRNAs *in silico*. Numerous mRNA and miRNAs were expressed in nitrofen-induced hypoplastic lungs, sixty-four of which were homologous to known human miRNAs. MiRNA pathways most relevant to nitrofen-induced lung hypoplasia include PI3K, TGF-β, and cell cycle kinases.

Loss of E-cadherin is a hallmark of the epithelial to mesenchymal transition and synergizes the dedifferentiation capacity of the cell. I have shown that nitrofen-induces upregulation of rno-miR-296-3p. In parallel, there is downregulation of members of the miR-200 family upon nitrofen treatment by > 2 fold relative to the control. A previous study from Xu et al. (237) in the nitrofen rat model demonstrated that TGF-β1 protein was stronger in CDH lungs. CYP26B1 fine tunes the activity of RA,

which is converted by retinol to more functional retinyl esters. I report that nitrofen inhibits CYP26B1 and lecithin retinol acyltransferase (LRAT). This corroborates findings that RA is diminished upon nitrofen exposure. CYP26B1 and LRAT correlate positively with miR-142-5p expression, whereas miR-592 negatively correlates with CYP26B1 expression. This is consistent with previous evidence from clinical studies that showed retinol levels to be lower in babies born with CDH (240). Finally, our study has characterized the transcriptome associated with nitrofen-induced abnormal lung development using NGS technology. Our data highlight the importance of PI3K, TGF-β, RA, and cell cycle kinase signaling in nitrofen-induced rat lung hypoplasia. However, these expression data need to be confirmed through measurements of the signaling intermediates directly via Western blotting or similar methods.

Mechanical wall strain caused by cardiac pulsation integrates with hypoxia to generate rapidly progressive myocyte cytoskeleton disassembly and failure to exert force generation. A review of the current available research methods, models and markers of PPHN showed there was relevance to processes associated with oxidative and nitrosative stress as well as cell fate commitment, with an emphasis on apoptosis and proliferation (247). Although these associations are not immediately related to the work on nitrofen-induced rat lung hypoplasia that is important for understanding neonatal PHN, nevertheless, it is an *in vivo* view of the dynamics of neonatal PHN.

As indicated in this thesis, miRNAs have a critical role in this process, but a histopathological view of these disturbances is required to understand the mechanical parameters that relate to increases in vascular resistance.

Further elucidation of the current research methods is necessary in order to determine which markers and related signaling pathways are relevant to the development of PHN as a result of oxidative and nitrosative stress.

New research focuses on exploring the contribution of senescence or SASP in the progression of PHN and identifying key molecular effectors of this program. It is therefore proposed that addressing this issue directly may be achieved by employing an *in vitro* model of neonatal PHN to: 1) deregulate senescence or SASP phenotypes and determine whether treatment with a combined exogenous antioxidant/NO therapy could attenuate SASP-induced immunomodulatory potential, and 2) determine whether such deregulation may reverse tissue remodeling in the hypertensive pulmonary circulation *in vitro*. This concept is supported by reports examining the immunostaining of pulmonary artery sections recapitulated from a previously published porcine model of the hypoxic HTN (249, 274, 306). The lysosomal enzyme marker SA β-gal is upregulated in senescence and thereby enables the detection and quantitation of senescence induction.

This work is unique in demonstrating that LSC, a method utilizing a fluidic matrix to grow cells, is appropriate for identifying a role for pulsatile stretch in PAH tissue remodeling. Furthermore, this work explains how hypoxia and mechanical strain induce the HTN phenotype in the vasculature of animals that manifest the

disease in a manner similar to human babies. The findings obtained by LSC *in vitro* are amenable to validation in any model of interest *in vivo*.

Previous studies have used immunoblotting for studying cell fate decisions. Western blotting is inadequate as it does not quantitatively provide the phenotype characteristics. LSC overcomes the limitations of cell count by BrdU incorporation using flow cytometry, hence LCS is favourable from the following prospectives: 1) LSC can be applied *in situ*, 2) PASM cells are challenging in terms of losing their adhesion characteristics when they are lifted, hence LSC is favourable compared to flow cytometry as it maintains cell shape and integrity, 3) LSC allows signal quantification by immunostaining after subjecting cells to any stressors simultaneously, i.e. pulsatile stretch with or without hypoxia, 4) LSC is very sensitive and reproducible, allowing exploration of very subtle differences which would be lost by Western blotting due to inter-experimental variability, 5) LSC can be applied to cells or tissues by immunostaining compared to Western blotting or flow cytometry, which utilize only cell lysates or cells, respectively, 6) LSC can measure fluorescence in any compartment of the cell by identifying contouring around intracellular organelles, 7) LSC allows 3-dimensional measurement of markers at the cell surface and intracellularly, 8) LSC can correlate function with signaling, i.e. the more G-actin, the stronger is the phenotype as the cell loses the dynamic assembly of the cytoskeleton, 9) phantom module selection by LSC allows quantification of cytoplasmic F:G-actin ratio as an indicator of the effect of pulsatile strain with or without hypoxia on PASM depolymerization in a visual way that is unavailable by Western blotting. Western blotting allows quantifying the F:G-actin ratio by fractionation; a laborious method.

The LSC method does not inform about the upstream triggers of hypoxia and mechanical strain or how they crosstalk, or what is the link to the cell cycle. It does, however, allow the investigator to correlate actin depolymerization with the phenotype characteristics quantitatively and in a visual format, and indicates that stretched cells are comparable to cells that are seen in the vascular wall. Echocardiographic pulmonary artery diameter fix dilated (non-stretching) patients would benefit from antioxidant therapy. This is a novel approach using a unique *in vitro* model of the *in vivo* pulmonary vasculature in hypertensive disease. By connecting known pathways of ROS generation and apoptosis with other cell fate decisions such as cellular senescence and inflammatory signaling, I hope in the future to uncover new targets for therapy of vascular remodeling in PPHN. Prevention of irreversible fibrotic medial thickening in PPHN (the factor most limiting treatment responses) would help reduce mortality in infants with PPHN and prolong the window of opportunity for vasodilator therapies.

5.2. How can this information be applied clinically?

My approach has provided and can provide in the future greater understanding of the physiology and pathophysiology of the developing lung. Lung development is a complicated process integrating cell differentiation, morphogenesis, and regeneration and these processes are controlled, in part, by miRNAs. I have presented a summary on the potential role of miRNAs contributing to lung development and a variety of lung diseases. The insights gained from lung

biology research will provide the road map to address the potential role of miRNAs in lung organogenesis and develop novel therapeutics to target specific lung diseases. In the future, pharmaceutical and genetic therapeutic approaches will be employed to examine the role of miRNAs in lung pathobiology. Further, miRNAs could serve as potential targets for lung specific therapy, diagnostic tools for the treatment of various lung diseases, and to develop therapeutics for the novel targets. Thus, understanding the intricacies in miRNA-lung biology will guide us as new therapeutic strategies and approaches are developed for personalized medicine.

Although my study does not address whether altered mRNA production is a cause or an effect of miRNA-altered expression, the presence of a relationship between the two provides a starting point for future studies. Additional experimental work, including luciferase reporter gene assays and mutagenesis of predicted miRNA-binding sites, will be useful to examine these interactions further.

I describe a new approach for a unique *in vitro* model of the *in vivo* pulmonary vasculature in hypertensive disease. The *in vitro* model is reproducible and clinically relevant to human pulmonary vascular pathophysiology. My approach demonstrates an LSC method that utilizes a fluidic matrix to grow cells and describes the role of pulsatile stretch in pulmonary artery hypertension tissue remodeling.

This overview of the current and future research addresses a clinically important question with carefully targeted fundamental biophysical and biomechanical research at the cellular, molecular, and organ system levels. The new approaches validate the currently identified targets in animal models and support

movement towards translational research for future therapeutic interventions. Developing new PHN therapies that specifically use components of the immune system to restore vascular homeostasis rather than attempting to reverse remodeling after the fact, is warranted. Identifying the concerted interplay between ROS/RNS generation, senescence, and inflammatory signaling will lead to therapeutic targets to combat vascular remodeling in PHN. Prevention of fibrotic thickning will help reduce mortality and morbidity in infants with PHN and prolong the window of opportunity for vasodilator therapies. Identifying new measures to ensure treatment of PHN at an earlier stage achieves the greatest benefit regarding survival. The *in vitro* model currently under investigation and described in this thesis is designed to mimic human disease. This approach may have positive implications for the treatment of PPHN. The above evidence can be tested via clinical trials. Finally, tissue microarrays from PPHN patients can be obtained to correlate the presence of senescence biomarkers with clinical progression, survival, and in response to treatment in different stages of PPHN progression.

CHAPTER 6: FUTURE RESEARCH

Although this study addresses primarily whether cyclic strain is associated or independent of hypoxia in the context of apoptosis, the question of whether mechanical stretch when combined with hypoxia upregulates DNA synthesis remains unaddressed. I did not attempt to study each treatment independently, since I studied instead their interactions. In the absence of pulsatile strain one expects more oxidative stress, i.e. high LDL peroxidation, but how this links to F:G-actin and to the cell cycle is yet to be investigated.

Targeting selected mRNA reads by siRNA approaches *in vitro* will allow a demonstration of physiological relevance in the context of lung development and surfactant production. Using miR 200 b KO mouse model, Khoshgoo et al. (366) demonstrated a role for ADPR in surfactant production and function, and suggested a role for miR 200 b in ADPR production. Adipocyte differentiation-related protein (ADPR) is a protein marker of lung lipofibroblasts with confirmed lower expression in CDH hypoplastic lungs. Recently, Khoshgoo et al. (44) demonstrated *in situ* hybridization combined with immunohistochemistry to determine the co-expression of miR 200 b and ADRP in hypoplastic lungs. They observed a disrupted ADPR expression around the developing airway in the lipofibroblast cells concurrently with the lowest expression of miR 200 b.

Phylogenetic inference analysis and similarity search: gene and species trees that were assigned the highest scores will be used to study conservation in structure and function, to distant rat from human in terms of responding to nitrofen and its effect on the relationship between genes.

Future research should examine whether the inhibition of p53 or p16 signaling will suppress the senescence phenotype using lentivirus-delivered shRNA-mediated p53 or p16 depletion in PASM cells challenged with stretch, hypoxia or both. Additionally, the growth suppressive mechanisms underlying control cells compared to PASM cells challenged with the same stressors need to be investigated; e.g., testing the requirement of components of the DNA damage response pathway other than p53 (such as p21, ATM, and CHK2) or pRb (such as p16) in the proliferative phenotype. Additionally, research that addresses whether the inhibition of ERK1/2 signaling will suppress hypoxia stretch-induced proliferation using lentivirus-delivered shRNA-mediated ERK1/2 depletion (ligand and receptor) or that uses the expression of a dominant-negative mutant of the essential receptor is required. Whether the cells that are made deficient in ERK1/2 acquire resistance to proliferation can be studied using simple growth assays. It is expected that cells subjected to stretch or hypoxia will grow compared to control. The above-selected genes can be targeted by lentivirus-mediated stable RNAi to study their differential roles in modulating other signaling networks that could be involved in proliferation. In addition to hypoxia together with or independent of mechanical strain, cells can be further stressed by treatment with oxidants or exposure to 100% oxygen to precipitate cell cycle exit and DNA damage; rescue can also be attempted by

treatment with superoxide or peroxynitrite scavengers. The study of inflammasome activation can be pursued if secretion of IL-1β and IL-18 is first identified. In terms of apoptosis and cell cycle arrest, more research is required to examine how transcription factors p53, pRb, and E2F regulate the contractile phenotype of smooth muscle cells.

Additionally, proliferation can be assayed by Ki-67 staining to confirm the LSC data. Apoptosis is determined conventionally by PI/BrdU fluorescence-activated cell sorting (FACS). According to whether the type of cell death is intrinsic or extrinsic, apoptosis markers such as annexin V, caspase 3 and 9 activation, Bax/Bcl-2 ratio, Bax/Bcl-XL ratio, Bax localization (immunocytochemistry and subcellular fractionation), mitochondrial permeability by JC1 fluorescence, cytochrome c by subcellular fractionation followed by Western blotting can be examined as confirmatory methods, however, this is beyond the scope of this study.

CHAPTER 7: LITERATURE CITED

1.Kelsen SG. The Unfolded Protein Response in Chronic Obstructive Pulmonary Disease. Ann Am Thorac Soc. 2016;13 Suppl 2:S138-45.

2.Fulda S, Gorman AM, Hori O, Samali A. Cellular stress responses: cell survival and cell death. Int J Cell Biol. 2010;2010:214074.

3.Khoshgoo N, Kholdebarin R, Iwasiow BM, Keijzer R. MicroRNAs and lung development. Pediatr Pulmonol. 2013;48(4):317-23.

4.Herriges M, Morrisey EE. Lung development: orchestrating the generation and regeneration of a complex organ. Development. 2014;141(3):502-13.

5.Sessa R, Hata A. Role of microRNAs in lung development and pulmonary diseases. Pulm Circ. 2013;3(2):315-28.

6.Williams AE, Moschos SA, Perry MM, Barnes PJ, Lindsay MA. Maternally imprinted microRNAs are differentially expressed during mouse and human lung development. Dev Dyn. 2007;236(2):572-80.

7.Bhaskaran M, Wang Y, Zhang H, Weng T, Baviskar P, Guo Y, Gou D, Liu L. MicroRNA-127 modulates fetal lung development. Physiol Genomics. 2009;37(3):268-78.

8.Dong J, Jiang G, Asmann YW, Tomaszek S, Jen J, Kislinger T, Wigle DA. MicroRNA networks in mouse lung organogenesis. PLoS One. 2010;5(5):e10854.

9.Savério Bellusci, Justin Grindley, Hisayo Emoto, Nobuyuki Itoh, Brigid LM Hogan. Fibroblast Growth Factor 10 (FGF10) and branching morphogenesis in the embryonic mouse lung. Development 1997;124:4867-4878

10.Human Embryology organogenesis. Module 18 Respiration react. 18.1 Phases of lung development http://www.embryology.ch/anglais/rrespiratory/phasen01.html

11.Massaro D, Massaro GD. Invited Review: pulmonary alveoli: formation, the "call for oxygen," and other regulators. Am J Physiol Lung Cell Mol Physiol. 2002;282(3):L345-58.

12.Kotecha S, Barbato A, Bush A, Claus F, Davenport M, Delacourt C, Deprest J, Eber E, Frenckner B, Greenough A, Nicholson AG, Anton-Pacheco JL, Midulla F. Congenital diaphragmatic hernia. Eur Respir J. 2012;39(4):820-9.

13.Stege G, Fenton A, Jaffray B. Nihilism in the 1990s: the true mortality of congenital diaphragmatic hernia. Pediatrics. 2003;112(3 Pt 1):532-5.

14.Keijzer R, Puri P. Congenital diaphragmatic hernia. Semin Pediatr Surg. 2010;19(3):180-5.

15.Veenma DC, de Klein A, Tibboel D. Developmental and genetic aspects of congenital diaphragmatic hernia. Pediatric pulmonology. 2012;47(6):534-45.

16.Tonks A, Wyldes M, Somerset DA, Dent K, Abhyankar A, Bagchi I, Lander A, Roberts E, Kilby MD. Congenital malformations of the diaphragm: findings of the West Midlands Congenital Anomaly Register 1995 to 2000. Prenat Diagn. 2004;24(8):596-604.

17.Holder AM, Klaassens M, Tibboel D, de Klein A, Lee B, Scott DA. Genetic factors in congenital diaphragmatic hernia. Am J Hum Genet. 2007;80(5):825-45.

18.Brown Medical School. Digital Pathology Brown University, c/o Rhode Island Hospital 593 Eddy Street APC11-42A Providence, RI 02903: http://www.brown.edu/Courses/Digital_Path/systemic_path/pulmonary/L35.JPG; 2005.

19.Roubliova XI, Lewi PJ, Verbeken EK, Vaast P, Jani JC, Lu H, Tibboel D, Deprest JA. The effect of maternal betamethasone and fetal tracheal occlusion on pulmonary vascular morphometry in fetal rabbits with surgically induced diaphragmatic hernia: a placebo controlled morphologic study. Prenat Diagn. 2009;29(7):674-81.

20.Flemmer AW, Jani JC, Bergmann F, Muensterer OJ, Gallot D, Hajek K, Sugawara J, Till H, Deprest JA. Lung tissue mechanics predict lung hypoplasia in a rabbit model for congenital diaphragmatic hernia. Pediatr Pulmonol. 2007;42(6):505-12.

21.Jani JC, Flemmer AW, Bergmann F, Gallot D, Roubliova X, Muensterer OJ, Hajek K, Deprest JA. The effect of fetal tracheal occlusion on lung tissue mechanics and tissue composition. Pediatr Pulmonol. 2009;44(2):112-21.

22.Cilley RE, Zgleszewski SE, Krummel TM, Chinoy MR. Nitrofen dose-dependent gestational day-specific murine lung hypoplasia and left-sided diaphragmatic hernia. Am J Physiol. 1997;272(2 Pt 1):L362-71.

23.Migliazza L, Otten C, Xia H, Rodriguez JI, Diez-Pardo JA, Tovar JA. Cardiovascular malformations in congenital diaphragmatic hernia: human and experimental studies. J Pediatr Surg. 1999;34(9):1352-8.

24.Mey J, Babiuk RP, Clugston R, Zhang W, Greer JJ. Retinal dehydrogenase-2 is inhibited by compounds that induce congenital diaphragmatic hernias in rodents The American journal of pathology 2003;162:673-679

25.Sbragia L, Nassr AC, Goncalves FL, Schmidt AF, Zuliani CC, Garcia PV, Gallindo RM, Pereira LA. VEGF receptor expression decreases during lung development in congenital diaphragmatic hernia induced by nitrofen. Braz J Med Biol Res. 2014;47(2):171-8.

26.Gonzalez-Reyes S, Fernandez-Dumont V, Martinez-Calonge W, Martinez L, Hernandez F, Tovar J. Pax3 mRNA is decreased in the hearts of rats with experimental diaphragmatic hernia.

Pediatric surgery international 2005;21:203-207

27.Keijzer R, Liu J, Deimling J, Tibboel D, Post M. Dual-hit hypothesis explains pulmonary hypoplasia in the nitrofen model of congenital diaphragmatic hernia. Am J Pathol. 2000;156(4):1299-306.

28.Kling DE, Schnitzer JJ. Vitamin A deficiency (VAD), teratogenic, and surgical models of congenital diaphragmatic hernia (CDH). Am J Med Genet C Semin Med Genet. 2007;145C(2):139-57.

29.Clugston RD, Zhang W, Alvarez S, De Lera AR, Greer JJ. Understanding abnormal retinoid signaling as a causative mechanism in congenital diaphragmatic hernia Am J Respir Cell Mol Biol 2010;42:276-85.

30.Babiuk RP, Thebaud B, Greer JJ. Reductions in the incidence of nitrofen-induced diaphragmatic hernia by vitamin A and retinoic acid. Am J Physiol Lung Cell Mol Physiol. 2004;286(5):L970-3.

31.Noble BR, Babiuk RP, Clugston RD, Underhill TM, Sun H, Kawaguchi R, Walfish PG, Blomhoff R, Gundersen TE, Greer JJ. Mechanisms of action of the congenital diaphragmatic hernia-inducing teratogen nitrofen. Am J Physiol Lung Cell Mol Physiol. 2007;293(4):L1079-87.

32.Mendelsohn C, Lohnes D, Decimo D, Lufkin T, LeMeur M, Chambon P, Mark M. Function of the retinoic acid receptors (RARs) during development (II). Multiple abnormalities at various stages of organogenesis in RAR double mutants. Development. 1994;120(10):2749-71.

33.Mendelsohn C, Larkin S, Mark M, LeMeur M, Clifford J, Zelent A, Chambon P. RAR beta isoforms: distinct transcriptional control by retinoic acid and specific spatial patterns of promoter activity during mouse embryonic development. Mech Dev. 1994;45(3):227-41.

34.You LR, Takamoto N, Yu CT, Tanaka T, Kodama T, Demayo FJ, et al. Mouse lacking COUP-TFII as an animal model of Bochdalek-type congenital diaphragmatic hernia. Proc Natl Acad Sci USA. 102;102:16351–16356.

35.Klaassens M, van Dooren M, Eussen HJ, Douben H, den Dekker AT, Lee C, Donahoe PK, Galjaard RJ, Goemaere N, de Krijger RR, Wouters C, Wauters J, Oostra BA, Tibboel D, de Klein A. Congenital diaphragmatic hernia and chromosome 15q26: determination of a candidate region by use of fluorescent in situ hybridization and array-based comparative genomic hybridization. Am J Hum Genet 2005;76:877-82.

36.Jay PY, Bielinska M, Erlich JM, Mannisto S, Pu WT, Heikinheimo M, Wilson DB. Impaired mesenchymal cell function in Gata4 mutant mice leads to diaphragmatic hernias and primary lung defects. Dev Biol. 2007;301(2):602-14.

37.Ackerman KG, Herron BJ, Vargas SO, et al. Fog2 is required for normal diaphragm and lung development in mice and humans. PLoS Genet 2005;1:58-65.

38.Bleyl SB, Moshrefi A, Shaw GM, Saijoh Y, Schoenwolf GC, Pennacchio LA, Slavotinek AM. Candidate genes for congenital diaphragmatic hernia from animal models: sequencing of FOG2 and PDGFRalpha reveals rare variants in diaphragmatic hernia patients. Eur J Hum Genet. 2007;15(9):950-8.

39.Slavotinek AM, Moshrefi A, Davis R, et al. Array comparative genomic hybridization in patients with congenital diaphragmatic hernia: mapping of four CDH-critical regions and sequencing of candidate genes at 15q26.1-15q26.2. Eur J Hum Genet 2006;14:999-1008.

40.Clugston RD, Klattig J, Englert C, Clagett-Dame M, Martinovic J, Benachi A, Greer JJ. Teratogeninduced, dietary and genetic models of congenital diaphragmatic hernia share a common mechanism of pathogenesis. Am J Pathol 2006;69:1541-9.

41.Bates MD, Dunagan DT, Welch LC, Kaul A, Harvey RP. The Hlx homeobox transcription factor is required early in enteric nervous system development. BMC Dev Biol 6:33.

42.Katz AL, Wiswell TE, Baumgart S. Contemporary controversies in the management of congenital diaphragmatic hernia. Clin Perinatol. 1998;25:219–248.

43.Deprest J, Gratacos E, Nicolaides KH. Fetoscopic tracheal occlusion (FETO) for severe congenital diaphragmatic hernia: evolution of a technique and preliminary results. Ultrasound Obstet Gynecol. 2004;24(2):121-6.

44.Khoshgoo N, Kholdebarin R, Pereira-Terra P, Mahood TH, Falk L, Day CA, Iwasiow BM, Zhu F, Mulhall D, Fraser C, Correia-Pinto J, Keijzer R. Prenatal microRNA miR-200b Therapy Improves Nitrofen-induced Pulmonary Hypoplasia Associated With Congenital Diaphragmatic Hernia. Ann Surg. 2017;DOI: 10.1097/SLA.0000000000002595 PMID: 29135495.

45.Maurel M, Chevet E. Endoplasmic reticulum stress signaling: the microRNA connection. Am J Physiol Cell Physiol. 2013;304(12):C1117-26.

46.Dengjel J, Kratchmarova I, Blagoev B. Mapping Protein–Protein Interactions by Quantitative Proteomics. In: Cutillas P, Timms J (eds) LC-MS/MS in Proteomics. Methods in Molecular Biology (Methods and Protocols). 658. Humana Press, Totowa, NJ2010.

47.Watanabe Y, Tomita M, Kanai A. Computational methods for microRNA target prediction. Methods Enzymol. 2007;427:65-86.

48.Masuda K, Kishimoto T. Identification of RNA-binding Proteins. Bio-Protocol. 2016;6(17).

49.Haring M, Offermann S, Danker T, Horst I, Peterhansel C, Stam M. Chromatin immunoprecipitation: optimization, quantitative analysis and data normalization. Plant Methods. 2007;3(3:11):11.

50.Yoon JH, Abdelmohsen K, Srikantan S, Yang X, Martindale JL, De S, Huarte M, Zhan M, Becker KG, Gorospe M. LincRNA-p21 suppresses target mRNA translation. Mol Cell. 2012;47(4):648-55.

51.Wang Z. The Guideline of the Design and Validation of MiRNA Mimics. In: Wu W. (eds) MicroRNA and Cancer. Methods in Molecular Biology (Methods and Protocols), vol 676. Humana Press, Totowa, NJ. 2011.

52.Kidd KK, Sgaramella-Zonta LA. Phylogenetic analysis: concepts and methods. Am J Hum Genet. 1971;23(3):235-52.

53.Rhinn M, Dolle P. Retinoic acid signalling during development. Development. 2012;139(5):843-58.

54.Huang H, Xie C, Sun X, Ritchie RP, Zhang J, Chen YE. miR-10a Contributes to Retinoid Acid-induced Smooth Muscle Cell Differentiation. The Journal of Biological Chemistry. 2010; 285 (13): 9383-9389.

55.Ørom UA, Nielsen FC, Lund AH. MicroRNA-10a Binds the 50UTR of Ribosomal Protein mRNAs and Enhances Their Translation. Cell 2008;30, 460–471.

56.Gregory PA, Bert AG, Paterson EL, Barry SC, Tsykin A, Farshid G, Vadas MA, Khew-Goodall Y, Goodall GJ. The miR-200 family and miR-205 regulate epithelial to mesenchymal transition by targeting ZEB1 and SIP1. Nat Cell Biol. 2008;10(5):593-601.

57.Bartel DP. MicroRNAs: target recognition and regulatory functions. Cell. 2009;136(2):215-33.

58.Burgos KL, Javaherian A, Bomprezzi R, Ghaffari L, Rhodes S, Courtright A, Tembe W, Kim S, Metpally R, Van Keuren-Jensen K. Identification of extracellular miRNA in human cerebrospinal fluid by next-generation sequencing. RNA. 2013;19(5):712-22.

59.Oshlack A, Robinson MD, Young MD. From RNA-seq reads to differential expression results. Genome Biol. 2010;11(12):220.

60.Seitz H, Youngson N, Lin SP, Dalbert S, Paulsen M, Bachellerie JP, Ferguson-Smith AC, Cavaille J. Imprinted microRNA genes transcribed antisense to a reciprocally imprinted retrotransposon-like gene. Nat Genet. 2003;34(3):261-2.

61.Pillai RS, Bhattacharyya SN, Artus CG, Zoller T, Cougot N, Basyuk E, Bertrand E, Filipowicz W. Inhibition of translational initiation by Let-7 MicroRNA in human cells. Science. 2005;309(5740):1573-6.

62.Hutvagner G, Zamore PD. A microRNA in a multiple-turnover RNAi enzyme complex. Science. 2002;297(5589):2056-60.

63.Ambros V. The functions of animal microRNAs. Nature. 2004;431(7006):350-5.

64.Boehm M, Slack F. A developmental timing microRNA and its target regulate life span in C. elegans. Science. 2005;310(5756):1954-7.

65.Chen X, Liang H, Zhang J, Zen K, Zhang CY. Secreted microRNAs: a new form of intercellular communication. Trends Cell Biol. 2012;22(3):125-32.

66.Costinean S, Zanesi N, Pekarsky Y, Tili E, Volinia S, Heerema N, Croce CM. Pre-B cell proliferation and lymphoblastic leukemia/high-grade lymphoma in E(mu)-miR155 transgenic mice. Proc Natl Acad Sci U S A. 2006;103(18):7024-9.

67.Esau C, Kang X, Peralta E, Hanson E, Marcusson EG, Ravichandran LV, Sun Y, Koo S, Perera RJ, Jain R, Dean NM, Freier SM, Bennett CF, Lollo B, Griffey R. MicroRNA-143 regulates adipocyte differentiation. J Biol Chem. 2004;279(50):52361-5.

68.Xu P, Guo M, Hay BA. MicroRNAs and the regulation of cell death. Trends Genet. 2004;20(12):617-24.

69.Sanger miRBase version 21. http://wwwmirbaseorg/blog/2014/06/mirbase-21-finally-arrives/.

70.Nana-Sinkam SP, Hunter MG, Nuovo GJ, Schmittgen TD, Gelinas R, Galas D, Marsh CB. Integrating the MicroRNome into the study of lung disease. Am J Respir Crit Care Med. 2009;179(1):4-10.

71.Oglesby IK, McElvaney NG, Greene CM. MicroRNAs in inflammatory lung disease--master regulators or target practice? Respir Res. 2010;11:148.

72.Sayed D, Abdellatif M. MicroRNAs in development and disease. Physiol Rev. 2011;91(3):827-87.

73.Tomankova T, Petrek M, Kriegova E. Involvement of microRNAs in physiological and pathological processes in the lung. Respir Res. 2010;11:159.

74.Yi R, Qin Y, Macara IG, Cullen BR. Exportin-5 mediates the nuclear export of pre-microRNAs and short hairpin RNAs. Genes Dev. 2003;17(24):3011-6.

75.Lund E, Guttinger S, Calado A, Dahlberg JE, Kutay U. Nuclear export of microRNA precursors. Science. 2004;303(5654):95-8.

76.Kim VN. MicroRNA biogenesis: coordinated cropping and dicing. Nat Rev Mol Cell Biol. 2005;6(5):376-85.

77.Giraldez AJ, Mishima Y, Rihel J, Grocock RJ, Van Dongen S, Inoue K, Enright AJ, Schier AF. Zebrafish MiR-430 promotes deadenylation and clearance of maternal mRNAs. Science. 2006;312(5770):75-9.

78.Wu L, Fan J, Belasco JG. MicroRNAs direct rapid deadenylation of mRNA. Proc Natl Acad Sci U S A. 2006;103(11):4034-9.

79.Wightman B, Ha I, Ruvkun G. Posttranscriptional regulation of the heterochronic gene lin-14

by lin-4 mediates temporal pattern formation in C. elegans. Cell. 1993;75(5):855-62.

80.Olsen PH, Ambros V. The lin-4 regulatory RNA controls developmental timing in Caenorhabditis elegans by blocking LIN-14 protein synthesis after the initiation of translation. Dev Biol. 1999;216(2):671-80.

81.Doench JG, Sharp PA. Specificity of microRNA target selection in translational repression. Genes Dev. 2004;18(5):504-11.

82.Hergenreider E, Heydt S, Treguer K, Boettger T, Horrevoets AJ, Zeiher AM, Scheffer MP, Frangakis AS, Yin X, Mayr M, Braun T, Urbich C, Boon RA, Dimmeler S. Atheroprotective communication between endothelial cells and smooth muscle cells through miRNAs. Nat Cell Biol. 2012;14(3):249-56.

83.Salmena L, Poliseno L, Tay Y, Kats L, Pandolfi PP. A ceRNA hypothesis: the Rosetta Stone of a hidden RNA language? Cell. 2011;146(3):353-8.

84.Karreth FA, Tay Y, Perna D, Ala U, Tan SM, Rust AG, DeNicola G, Webster KA, Weiss D, Perez-Mancera PA, Krauthammer M, Halaban R, Provero P, Adams DJ, Tuveson DA, Pandolfi PP. In vivo identification of tumor- suppressive PTEN ceRNAs in an oncogenic BRAF-induced mouse model of melanoma. Cell. 2011;147(2):382-95.

85.Rutnam ZJ, Du WW, Yang W, Yang X, Yang BB. The pseudogene TUSC2P promotes TUSC2 function by binding multiple microRNAs. Nat Commun. 2014;5:2914.

86.Askarian-Amiri ME, Crawford J, French JD, Smart CE, Smith MA, Clark MB, Ru K, Mercer TR, Thompson ER, Lakhani SR, Vargas AC, Campbell IG, Brown MA, Dinger ME, Mattick JS. SNORD-host RNA Zfas1 is a regulator of mammary development and a potential marker for breast cancer. RNA. 2011;17(5):878-91.

87.Cabili MN, Trapnell C, Goff L, Koziol M, Tazon-Vega B, Regev A, Rinn JL. Integrative annotation of human large intergenic noncoding RNAs reveals global properties and specific subclasses. Genes Dev. 2011;25(18):1915-27.

88.Kretz M, Webster DE, Flockhart RJ, Lee CS, Zehnder A, Lopez-Pajares V, Qu K, Zheng GX, Chow J, Kim GE, Rinn JL, Chang HY, Siprashvili Z, Khavari PA. Suppression of progenitor differentiation requires the long noncoding RNA ANCR. Genes Dev. 2012;26(4):338-43.

89.Lu Y, Thomson JM, Wong HY, Hammond SM, Hogan BL. Transgenic over-expression of the microRNA miR-17-92 cluster promotes proliferation and inhibits differentiation of lung epithelial progenitor cells. Dev Biol. 2007;310(2):442-53.

90.Lu Y, Okubo T, Rawlins E, Hogan BL. Epithelial progenitor cells of the embryonic lung and the role of microRNAs in their proliferation. Proc Am Thorac Soc. 2008;5(3):300-4.

91.Yanaihara N, Caplen N, Bowman E, Seike M, Kumamoto K, Yi M, Stephens RM, Okamoto A, Yokota J, Tanaka T, Calin GA, Liu CG, Croce CM, Harris CC. Unique microRNA molecular profiles

in lung cancer diagnosis and prognosis. Cancer Cell. 2006;9(3):189-98.

92.Navarro A, Marrades RM, Vinolas N, Quera A, Agusti C, Huerta A, Ramirez J, Torres A, Monzo M. MicroRNAs expressed during lung cancer development are expressed in human pseudoglandular lung embryogenesis. Oncology. 2009;76(3):162-9.

93.Carraro G, El-Hashash A, Guidolin D, Tiozzo C, Turcatel G, Young BM, De Langhe SP, Bellusci S, Shi W, Parnigotto PP, Warburton D. miR-17 family of microRNAs controls FGF10-mediated embryonic lung epithelial branching morphogenesis through MAPK14 and STAT3 regulation of E-Cadherin distribution. Dev Biol. 2009;333(2):238-50.

94.Ventura A, Young AG, Winslow MM, Lintault L, Meissner A, Erkeland SJ, Newman J, Bronson RT, Crowley D, Stone JR, Jaenisch R, Sharp PA, Jacks T. Targeted deletion reveals essential and overlapping functions of the miR-17 through 92 family of miRNA clusters. Cell. 2008;132(5):875-86.

95.Hayashita Y, Osada H, Tatematsu Y, Yamada H, Yanagisawa K, Tomida S, Yatabe Y, Kawahara K, Sekido Y, Takahashi T. A polycistronic microRNA cluster, miR-17-92, is overexpressed in human lung cancers and enhances cell proliferation. Cancer Res. 2005;65(21):9628-32.

96.White AC, Xu J, Yin Y, Smith C, Schmid G, Ornitz DM. FGF9 and SHH signaling coordinate lung growth and development through regulation of distinct mesenchymal domains. Development. 2006;133(8):1507-17.

97.Harris KS, Zhang Z, McManus MT, Harfe BD, Sun X. Dicer function is essential for lung epithelium morphogenesis. Proc Natl Acad Sci U S A. 2006;103(7):2208-13.

98.Lu J, Qian J, Chen F, Tang X, Li C, Cardoso WV. Differential expression of components of the microRNA machinery during mouse organogenesis. Biochem Biophys Res Commun. 2005;334(2):319-23.

99.Fabbri M, Garzon R, Cimmino A, Liu Z, Zanesi N, Callegari E, Liu S, Alder H, Costinean S, Fernandez-Cymering C, Volinia S, Guler G, Morrison CD, Chan KK, Marcucci G, Calin GA, Huebner K, Croce CM. MicroRNA-29 family reverts aberrant methylation in lung cancer by targeting DNA methyltransferases 3A and 3B. Proc Natl Acad Sci U S A. 2007;104(40):15805-10.

100.Jones PA, Takai D. The role of DNA methylation in mammalian epigenetics. Science. 2001;293(5532):1068-70.

101.Choudhary C, Kumar C, Gnad F, Nielsen ML, Rehman M, Walther TC, Olsen JV, Mann M. Lysine acetylation targets protein complexes and co-regulates major cellular functions. Science. 2009;325(5942):834-40.

102.Ito K, Caramori G, Lim S, Oates T, Chung KF, Barnes PJ, Adcock IM. Expression and activity of histone deacetylases in human asthmatic airways. Am J Respir Crit Care Med. 2002;166(3):392-6.

103.Banerjee A, Trivedi CM, Damera G, Jiang M, Jester W, Hoshi T, Epstein JA, Panettieri RA, Jr. Trichostatin A abrogates airway constriction, but not inflammation, in murine and human asthma models. Am J Respir Cell Mol Biol. 2012;46(2):132-8.

104.Wang Y, Tian Y, Morley MP, Lu MM, Demayo FJ, Olson EN, Morrisey EE. Development and regeneration of Sox2+ endoderm progenitors are regulated by a Hdac1/2-Bmp4/Rb1 regulatory pathway. Dev Cell. 2013;24(4):345-58.

105.Londhe VA, Sundar IK, Lopez B, Maisonet TM, Yu Y, Aghai ZH, Rahman I. Hyperoxia impairs alveolar formation and induces senescence through decreased histone deacetylase activity and up-regulation of p21 in neonatal mouse lung. Pediatr Res. 2011;69(5 Pt 1):371-7.

106.Zhu L, Li H, Tang J, Zhu J, Zhang Y. Hyperoxia arrests alveolar development through suppression of histone deacetylases in neonatal rats. Pediatr Pulmonol. 2012;47(3):264-74.

107.Benlhabib H, Mendelson CR. Epigenetic regulation of surfactant protein A gene (SP-A) expression in fetal lung reveals a critical role for Suv39h methyltransferases during development and hypoxia. Mol Cell Biol. 2011;31(10):1949-58.

108.Dakhlallah D, Batte K, Wang Y, Cantemir-Stone CZ, Yan P, Nuovo G, Mikhail A, Hitchcock CL, Wright VP, Nana-Sinkam SP, Piper MG, Marsh CB. Epigenetic regulation of miR-17~92 contributes to the pathogenesis of pulmonary fibrosis. Am J Respir Crit Care Med. 2013;187(4):397-405.

109.Woltering JM, Durston AJ. MiR-10 represses HoxB1a and HoxB3a in zebrafish. PLoS One. 2008;3(1):e1396.

110.Tzur G, Levy A, Meiri E, Barad O, Spector Y, Bentwich Z, Mizrahi L, Katzenellenbogen M, Ben-Shushan E, Reubinoff BE, Galun E. MicroRNA expression patterns and function in endodermal differentiation of human embryonic stem cells. PLoS One. 2008;3(11):e3726.

111.Ovcharenko D, Kelnar K, Johnson C, Leng N, Brown D. Genome-scale microRNA and small interfering RNA screens identify small RNA modulators of TRAIL-induced apoptosis pathway. Cancer Res. 2007;67(22):10782-8.

112.Noren Hooten N, Abdelmohsen K, Gorospe M, Ejiogu N, Zonderman AB, Evans MK. microRNA expression patterns reveal differential expression of target genes with age. PLoS One. 2010;5(5):e10724.

113.Huang H, Xie C, Sun X, Ritchie RP, Zhang J, Chen YE. miR-10a contributes to retinoid acid-induced smooth muscle cell differentiation. J Biol Chem. 2010;285(13):9383-9.

114.Tian Y, Zhang Y, Hurd L, Hannenhalli S, Liu F, Lu MM, Morrisey EE. Regulation of lung endoderm progenitor cell behavior by miR302/367. Development. 2011;138(7):1235-45.

115.Zhang Y, Goss AM, Cohen ED, Kadzik R, Lepore JJ, Muthukumaraswamy K, Yang J, DeMayo FJ, Whitsett JA, Parmacek MS, Morrisey EE. A Gata6-Wnt pathway required for epithelial stem

cell development and airway regeneration. Nat Genet. 2008;40(7):862-70.

116.Lize M, Herr C, Klimke A, Bals R, Dobbelstein M. MicroRNA-449a levels increase by several orders of magnitude during mucociliary differentiation of airway epithelia. Cell Cycle. 2010;9(22):4579-83.

117.Lize M, Pilarski S, Dobbelstein M. E2F1-inducible microRNA 449a/b suppresses cell proliferation and promotes apoptosis. Cell Death Differ. 2010;17(3):452-8.

118.Marcet B, Chevalier B, Luxardi G, Coraux C, Zaragosi LE, Cibois M, Robbe-Sermesant K, Jolly T, Cardinaud B, Moreilhon C, Giovannini-Chami L, Nawrocki-Raby B, Birembaut P, Waldmann R, Kodjabachian L, Barbry P. Control of vertebrate multiciliogenesis by miR-449 through direct repression of the Delta/Notch pathway. Nat Cell Biol. 2011;13(6):693-9.

119.Tellez CS, Juri DE, Do K, Bernauer AM, Thomas CL, Damiani LA, Tessema M, Leng S, Belinsky SA. EMT and stem cell-like properties associated with miR-205 and miR-200 epigenetic silencing are early manifestations during carcinogen-induced transformation of human lung epithelial cells. Cancer Res. 2011;71(8):3087-97.

120.Johnson SM, Grosshans H, Shingara J, Byrom M, Jarvis R, Cheng A, Labourier E, Reinert KL, Brown D, Slack FJ. RAS is regulated by the let-7 microRNA family. Cell. 2005;120(5):635-47.

121.Kumar MS, Erkeland SJ, Pester RE, Chen CY, Ebert MS, Sharp PA, Jacks T. Suppression of non-small cell lung tumor development by the let-7 microRNA family. Proc Natl Acad Sci U S A. 2008;105(10):3903-8.

122.Pieraccioli M, Imbastari F, Antonov A, Melino G, Raschella G. Activation of miR200 by c-Myb depends on ZEB1 expression and miR200 promoter methylation. Cell Cycle. 2013;12(14):2309-20.

123.Li X, Roslan S, Johnstone CN, Wright JA, Bracken CP, Anderson M, Bert AG, Selth LA, Anderson RL, Goodall GJ, Gregory PA, Khew-Goodall Y. MiR-200 can repress breast cancer metastasis through ZEB1-independent but moesin-dependent pathways. Oncogene. 2014;33(31):4077-88.

124.Pacurari M, Addison JB, Bondalapati N, Wan YW, Luo D, Qian Y, Castranova V, Ivanov AV, Guo NL. The microRNA-200 family targets multiple non-small cell lung cancer prognostic markers in H1299 cells and BEAS-2B cells. Int J Oncol. 2013;43(2):548-60.

125.Yang S, Banerjee S, de Freitas A, Sanders YY, Ding Q, Matalon S, Thannickal VJ, Abraham E, Liu G. Participation of miR-200 in pulmonary fibrosis. Am J Pathol. 2012;180(2):484-93.

126.Rodriguez A, Vigorito E, Clare S, Warren MV, Couttet P, Soond DR, van Dongen S, Grocock RJ, Das PP, Miska EA, Vetrie D, Okkenhaug K, Enright AJ, Dougan G, Turner M, Bradley A. Requirement of bic/microRNA-155 for normal immune function. Science. 2007;316(5824):608-11.

127.Rao R, Rieder SA, Nagarkatti P, Nagarkatti M. Staphylococcal enterotoxin B-induced microRNA-155 targets SOCS1 to promote acute inflammatory lung injury. Infect Immun. 2014;82(7):2971-9.

128.Johnson CD, Esquela-Kerscher A, Stefani G, Byrom M, Kelnar K, Ovcharenko D, Wilson M, Wang X, Shelton J, Shingara J, Chin L, Brown D, Slack FJ. The let-7 microRNA represses cell proliferation pathways in human cells. Cancer Res. 2007;67(16):7713-22.

129.Takamizawa J, Konishi H, Yanagisawa K, Tomida S, Osada H, Endoh H, Harano T, Yatabe Y, Nagino M, Nimura Y, Mitsudomi T, Takahashi T. Reduced expression of the let-7 microRNAs in human lung cancers in association with shortened postoperative survival. Cancer Res. 2004;64(11):3753-6.

130.Mattes J, Collison A, Plank M, Phipps S, Foster PS. Antagonism of microRNA-126 suppresses the effector function of TH2 cells and the development of allergic airways disease. Proc Natl Acad Sci U S A. 2009;106(44):18704-9.

131.Comer BS, Camoretti-Mercado B, Kogut PC, Halayko AJ, Solway J, Gerthoffer WT. Cyclooxygenase-2 and microRNA-155 expression are elevated in asthmatic airway smooth muscle cells. Am J Respir Cell Mol Biol. 2015;52(4):438-47.

132.Milosevic J, Pandit K, Magister M, Rabinovich E, Ellwanger DC, Yu G, Vuga LJ, Weksler B, Benos PV, Gibson KF, McMillan M, Kahn M, Kaminski N. Profibrotic role of miR-154 in pulmonary fibrosis. Am J Respir Cell Mol Biol. 2012;47(6):879-87.

133.Cushing L, Kuang PP, Qian J, Shao F, Wu J, Little F, Thannickal VJ, Cardoso WV, Lu J. miR-29 is a major regulator of genes associated with pulmonary fibrosis. Am J Respir Cell Mol Biol. 2011;45(2):287-94.

134.Yang T, Liang Y, Lin Q, Liu J, Luo F, Li X, Zhou H, Zhuang S, Zhang H. miR-29 mediates TGFbeta1-induced extracellular matrix synthesis through activation of PI3K-AKT pathway in human lung fibroblasts. J Cell Biochem. 2013;114(6):1336-42.

135.Kim J, Kang Y, Kojima Y, Lighthouse JK, Hu X, Aldred MA, McLean DL, Park H, Comhair SA, Greif DM, Erzurum SC, Chun HJ. An endothelial apelin-FGF link mediated by miR-424 and miR-503 is disrupted in pulmonary arterial hypertension. Nat Med. 2013;19(1):74-82.

136.Yang S, Banerjee S, Freitas A, Cui H, Xie N, Abraham E, Liu G. miR-21 regulates chronic hypoxia-induced pulmonary vascular remodeling. Am J Physiol Lung Cell Mol Physiol. 2012;302(6):L521-9.

137.Jemal A, Siegel R, Ward E, Hao Y, Xu J, Thun MJ. Cancer statistics, 2009. CA Cancer J Clin. 2009;59(4):225-49.

138.Ebi H, Sato T, Sugito N, Hosono Y, Yatabe Y, Matsuyama Y, Yamaguchi T, Osada H, Suzuki M, Takahashi T. Counterbalance between RB inactivation and miR-17-92 overexpression in reactive oxygen species and DNA damage induction in lung cancers. Oncogene.

2009;28(38):3371-9.

139.Liu X, Sempere LF, Ouyang H, Memoli VA, Andrew AS, Luo Y, Demidenko E, Korc M, Shi W, Preis M, Dragnev KH, Li H, Direnzo J, Bak M, Freemantle SJ, Kauppinen S, Dmitrovsky E. MicroRNA-31 functions as an oncogenic microRNA in mouse and human lung cancer cells by repressing specific tumor suppressors. J Clin Invest. 2010;120(4):1298-309.

140.Bernstein E, Kim SY, Carmell MA, Murchison EP, Alcorn H, Li MZ, Mills AA, Elledge SJ, Anderson KV, Hannon GJ. Dicer is essential for mouse development. Nat Genet. 2003;35(3):215-7.

141.Kumar MS, Lu J, Mercer KL, Golub TR, Jacks T. Impaired microRNA processing enhances cellular transformation and tumorigenesis. Nat Genet. 2007;39(5):673-7.

142.Zhang M, Shi J, Huang Y, Lai L. Expression of canonical WNT/beta-CATENIN signaling components in the developing human lung. BMC Dev Biol. 2012;12:21.

143.Mujahid S, Nielsen HC, Volpe MV. MiR-221 and miR-130a regulate lung airway and vascular development. PLoS One. 2013;8(2):e55911.

144.Selman M, Pardo A, Kaminski N. Idiopathic pulmonary fibrosis: aberrant recapitulation of developmental programs? PLoS Med. 2008;5(3):e62.

145.Xu YD, Hua J, Mui A, O'Connor R, Grotendorst G, Khalil N. Release of biologically active TGF-beta1 by alveolar epithelial cells results in pulmonary fibrosis. Am J Physiol Lung Cell Mol Physiol. 2003;285(3):L527-39.

146.Fabian SL, Penchev RR, St-Jacques B, Rao AN, Sipila P, West KA, McMahon AP, Humphreys BD. Hedgehog-Gli pathway activation during kidney fibrosis. Am J Pathol. 2012;180(4):1441-53.

147.Willis BC, Borok Z. TGF-beta-induced EMT: mechanisms and implications for fibrotic lung disease. Am J Physiol Lung Cell Mol Physiol. 2007;293(3):L525-34.

148.Pandit KV, Corcoran D, Yousef H, Yarlagadda M, Tzouvelekis A, Gibson KF, Konishi K, Yousem SA, Singh M, Handley D, Richards T, Selman M, Watkins SC, Pardo A, Ben-Yehudah A, Bouros D, Eickelberg O, Ray P, Benos PV, Kaminski N. Inhibition and role of let-7d in idiopathic pulmonary fibrosis. Am J Respir Crit Care Med. 2010;182(2):220-9.

149.Pandit KV, Milosevic J, Kaminski N. MicroRNAs in idiopathic pulmonary fibrosis. Transl Res. 2011;157(4):191-9.

150.Liu G, Friggeri A, Yang Y, Milosevic J, Ding Q, Thannickal VJ, Kaminski N, Abraham E. miR-21 mediates fibrogenic activation of pulmonary fibroblasts and lung fibrosis. J Exp Med. 2010;207(8):1589-97.

151.Lino Cardenas CL, Henaoui IS, Courcot E, Roderburg C, Cauffiez C, Aubert S, Copin MC, Wallaert B, Glowacki F, Dewaeles E, Milosevic J, Maurizio J, Tedrow J, Marcet B, Lo-Guidice JM,

Kaminski N, Barbry P, Luedde T, Perrais M, Mari B, Pottier N. miR-199a-5p Is upregulated during fibrogenic response to tissue injury and mediates TGFbeta-induced lung fibroblast activation by targeting caveolin-1. PLoS Genet. 2013;9(2):e1003291.

152.Weaver M, Yingling JM, Dunn NR, Bellusci S, Hogan BL. Bmp signaling regulates proximal-distal differentiation of endoderm in mouse lung development. Development. 1999;126(18):4005-15.

153.Li Y, Gordon J, Manley NR, Litingtung Y, Chiang C. Bmp4 is required for tracheal formation: a novel mouse model for tracheal agenesis. Dev Biol. 2008;322(1):145-55.

154.Litingtung Y, Lei L, Westphal H, Chiang C. Sonic hedgehog is essential to foregut development. Nat Genet. 1998;20(1):58-61.

155.Radzikinas K, Aven L, Jiang Z, Tran T, Paez-Cortez J, Boppidi K, Lu J, Fine A, Ai X. A Shh/miR-206/BDNF cascade coordinates innervation and formation of airway smooth muscle. J Neurosci. 2011;31(43):15407-15.

156.Sala FG, Del Moral PM, Tiozzo C, Alam DA, Warburton D, Grikscheit T, Veltmaat JM, Bellusci S. FGF10 controls the patterning of the tracheal cartilage rings via Shh. Development. 2011;138(2):273-82.

157.Taganov KD, Boldin MP, Chang KJ, Baltimore D. NF-kappaB-dependent induction of microRNA miR-146, an inhibitor targeted to signaling proteins of innate immune responses. Proc Natl Acad Sci U S A. 2006;103(33):12481-6.

158.Tili E, Michaille JJ, Cimino A, Costinean S, Dumitru CD, Adair B, Fabbri M, Alder H, Liu CG, Calin GA, Croce CM. Modulation of miR-155 and miR-125b levels following lipopolysaccharide/TNF-alpha stimulation and their possible roles in regulating the response to endotoxin shock. J Immunol. 2007;179(8):5082-9.

159.Moschos SA, Williams AE, Perry MM, Birrell MA, Belvisi MG, Lindsay MA. Expression profiling in vivo demonstrates rapid changes in lung microRNA levels following lipopolysaccharide-induced inflammation but not in the anti-inflammatory action of glucocorticoids. BMC Genomics. 2007;8:240.

160.Murphy AJ, Guyre PM, Pioli PA. Estradiol suppresses NF-kappa B activation through coordinated regulation of let-7a and miR-125b in primary human macrophages. J Immunol. 2010;184(9):5029-37.

161.Perry MM, Moschos SA, Williams AE, Shepherd NJ, Larner-Svensson HM, Lindsay MA. Rapid changes in microRNA-146a expression negatively regulate the IL-1beta-induced inflammatory response in human lung alveolar epithelial cells. J Immunol. 2008;180(8):5689-98.

162.Metzger RJ, Klein OD, Martin GR, Krasnow MA. The branching programme of mouse lung development. Nature. 2008;453(7196):745-50.

163.Bhattacharyya S, Balakathiresan NS, Dalgard C, Gutti U, Armistead D, Jozwik C, Srivastava M, Pollard HB, Biswas R. Elevated miR-155 promotes inflammation in cystic fibrosis by driving hyperexpression of interleukin-8. J Biol Chem. 2011;286(13):11604-15.

164.Kuo YC, Li YS, Zhou J, Shih YR, Miller M, Broide D, Lee OK, Chien S. Human mesenchymal stem cells suppress the stretch-induced inflammatory miR-155 and cytokines in bronchial epithelial cells. PLoS One. 2013;8(8):e71342.

165.Hu R, Pan W, Fedulov AV, Jester W, Jones MR, Weiss ST, Panettieri RA, Jr., Tantisira K, Lu Q. MicroRNA-10a controls airway smooth muscle cell proliferation via direct targeting of the PI3 kinase pathway. FASEB J. 2014;28(5):2347-57.

166.Lu TX, Munitz A, Rothenberg ME. MicroRNA-21 is up-regulated in allergic airway inflammation and regulates IL-12p35 expression. J Immunol. 2009;182(8):4994-5002.

167.Chiba Y, Misawa M. MicroRNAs and their therapeutic potential for human diseases: MiR-133a and bronchial smooth muscle hyperresponsiveness in asthma. J Pharmacol Sci. 2010;114(3):264-8.

168.McLaughlin VV, Archer SL, Badesch DB, Barst RJ, Farber HW, Lindner JR, Mathier MA, McGoon MD, Park MH, Rosenson RS, Rubin LJ, Tapson VF, Varga J, American College of Cardiology Foundation Task Force on Expert Consensus D, American Heart A, American College of Chest P, American Thoracic Society I, Pulmonary Hypertension A. ACCF/AHA 2009 expert consensus document on pulmonary hypertension a report of the American College of Cardiology Foundation Task Force on Expert Consensus Documents and the American Heart Association developed in collaboration with the American College of Chest Physicians; American Thoracic Society, Inc.; and the Pulmonary Hypertension Association. J Am Coll Cardiol. 2009;53(17):1573-619.

169.Simon MA. Right ventricular adaptation to pressure overload. Curr Opin Crit Care. 2010;16(3):237-43.

170.Courboulin A, Paulin R, Giguere NJ, Saksouk N, Perreault T, Meloche J, Paquet ER, Biardel S, Provencher S, Cote J, Simard MJ, Bonnet S. Role for miR-204 in human pulmonary arterial hypertension. J Exp Med. 2011;208(3):535-48.

171.Caruso P, MacLean MR, Khanin R, McClure J, Soon E, Southgate M, MacDonald RA, Greig JA, Robertson KE, Masson R, Denby L, Dempsie Y, Long L, Morrell NW, Baker AH. Dynamic changes in lung microRNA profiles during the development of pulmonary hypertension due to chronic hypoxia and monocrotaline. Arterioscler Thromb Vasc Biol. 2010;30(4):716-23.

172.Parikh VN, Jin RC, Rabello S, Gulbahce N, White K, Hale A, Cottrill KA, Shaik RS, Waxman AB, Zhang YY, Maron BA, Hartner JC, Fujiwara Y, Orkin SH, Haley KJ, Barabasi AL, Loscalzo J, Chan SY. MicroRNA-21 integrates pathogenic signaling to control pulmonary hypertension: results of a network bioinformatics approach. Circulation. 2012;125(12):1520-32.

173.Cheng Y, Liu X, Yang J, Lin Y, Xu DZ, Lu Q, Deitch EA, Huo Y, Delphin ES, Zhang C. MicroRNA-145, a novel smooth muscle cell phenotypic marker and modulator, controls vascular neointimal lesion formation. Circ Res. 2009;105(2):158-66.

174.Elia L, Quintavalle M, Zhang J, Contu R, Cossu L, Latronico MV, Peterson KL, Indolfi C, Catalucci D, Chen J, Courtneidge SA, Condorelli G. The knockout of miR-143 and -145 alters smooth muscle cell maintenance and vascular homeostasis in mice: correlates with human disease. Cell Death Differ. 2009;16(12):1590-8.

175.Caruso P, Dempsie Y, Stevens HC, McDonald RA, Long L, Lu R, White K, Mair KM, McClure JD, Southwood M, Upton P, Xin M, van Rooij E, Olson EN, Morrell NW, MacLean MR, Baker AH. A role for miR-145 in pulmonary arterial hypertension: evidence from mouse models and patient samples. Circ Res. 2012;111(3):290-300.

176.Fichtlscherer S, De Rosa S, Fox H, Schwietz T, Fischer A, Liebetrau C, Weber M, Hamm CW, Roxe T, Muller-Ardogan M, Bonauer A, Zeiher AM, Dimmeler S. Circulating microRNAs in patients with coronary artery disease. Circ Res. 2010;107(5):677-84.

177.Wei C, Henderson H, Spradley C, Li L, Kim IK, Kumar S, Hong N, Arroliga AC, Gupta S. Circulating miRNAs as potential marker for pulmonary hypertension. PLoS One. 2013;8(5):e64396.

178.Bader AG, Brown D, Winkler M. The promise of microRNA replacement therapy. Cancer Res. 2010;70(18):7027-30.

179.Trang P, Medina PP, Wiggins JF, Ruffino L, Kelnar K, Omotola M, Homer R, Brown D, Bader AG, Weidhaas JB, Slack FJ. Regression of murine lung tumors by the let-7 microRNA. Oncogene. 2010;29(11):1580-7.

180.Wiggins JF, Ruffino L, Kelnar K, Omotola M, Patrawala L, Brown D, Bader AG. Development of a lung cancer therapeutic based on the tumor suppressor microRNA-34. Cancer Res. 2010;70(14):5923-30.

181.Krutzfeldt J, Rajewsky N, Braich R, Rajeev KG, Tuschl T, Manoharan M, Stoffel M. Silencing of microRNAs in vivo with 'antagomirs'. Nature. 2005;438(7068):685-9.

182.Garzon R, Marcucci G, Croce CM. Targeting microRNAs in cancer: rationale, strategies and challenges. Nat Rev Drug Discov. 2010;9(10):775-89.

183.Rayner KJ, Esau CC, Hussain FN, McDaniel AL, Marshall SM, van Gils JM, Ray TD, Sheedy FJ, Goedeke L, Liu X, Khatsenko OG, Kaimal V, Lees CJ, Fernandez-Hernando C, Fisher EA, Temel RE, Moore KJ. Inhibition of miR-33a/b in non-human primates raises plasma HDL and lowers VLDL triglycerides. Nature. 2011;478(7369):404-7.

184.Xiao J, Meng XM, Huang XR, Chung AC, Feng YL, Hui DS, Yu CM, Sung JJ, Lan HY. miR-29 inhibits bleomycin-induced pulmonary fibrosis in mice. Mol Ther. 2012;20(6):1251-60.

185.Johar D, Siragam V, Mahood TH, Keijzer R. New insights into lung development and diseases: the role of microRNAs. Biochem Cell Biol. 2015;93(2):139-48.

186.van Loenhout RB, Tibboel D, Post M, Keijzer R. Congenital diaphragmatic hernia: comparison of animal models and relevance to the human situation. Neonatology. 2009;96(3):137-49.

187.Manson JM. Mechanism of nitrofen teratogenesis. Environ Health Perspect. 1986;70:137-47.

188.Allan DW, Greer JJ. Pathogenesis of nitrofen-induced congenital diaphragmatic hernia in fetal rats. J Appl Physiol (1985). 1997;83(2):338-47.

189.Inui M, Martello G, Piccolo S. MicroRNA control of signal transduction. Nat Rev Mol Cell Biol. 2010;11(4):252-63.

190.Yates LA, Norbury CJ, Gilbert RJ. The long and short of microRNA. Cell. 2013;153(3):516-9.

191.Mahood TH, Johar DR, Iwasiow BM, Xu W, Keijzer R. The transcriptome of nitrofen-induced pulmonary hypoplasia in the rat model of congenital diaphragmatic hernia. Pediatr Res. 2016;79(5):766-75.

192.Cilley RE, Zgleszewski SE, Krummel TM, Chinoy MR. Nitrofen dose-dependent gestational day-specific murine lung hypoplasia and left-sided diaphragmatic hernia. Am J Physiol. 1997;272:L362–L371.

193.Kluth D, Kangah R, Reich P, Tenbrinck R, Tibboel D, Lambrecht W. Nitrofen-induced diaphragmatic hernias in rats: an animal model. J Pediatr Surg. 1990;25:850–854.

194.Tenbrinck R, Tibboel D, Gaillard JL, Kluth D, Bos AP, Lachmann B, Molenaar JC. Experimentally induced congenital diaphragmatic hernia in rats. J Pediatr Surg. 1990;25:426–429.

195.Robinson MD, McCarthy DJ, Smyth GK. edgeR: a Bioconductor package for differential expression analysis of digital gene expression data. Bioinformatics. 2010;26(1):139-40.

196.Gerlach D, Kriventseva EV, Rahman N, Vejnar CE, Zdobnov EM. miROrtho: computational survey of microRNA genes. Nucleic Acids Res. 2009;37(Database issue):D111-7.

197.Ye J, Coulouris G, Zaretskaya I, Cutcutache I, Rozen S, Madden TL. Primer-BLAST: a tool to design target-specific primers for polymerase chain reaction. BMC Bioinformatics. 2012;13:134.

198.Kent WJ, Sugnet CW, Furey TS, Roskin KM, Pringle TH, Zahler AM, Haussler D. The human genome browser at UCSC. Genome Res. 2002;12(6):996-1006.

199.Mi H, Muruganujan A, Thomas PD. PANTHER in 2013: modeling the evolution of gene function, and other gene attributes, in the context of phylogenetic trees. Nucleic Acids Res.

2013;41(Database issue):D377-86.

200.Kanehisa M, Goto S, Sato Y, Kawashima M, Furumichi M, Tanabe M. Data, information, knowledge and principle: back to metabolism in KEGG. Nucleic Acids Res. 2014;42(Database issue):D199-205.

201.Kozomara A, Griffiths-Jones S. miRBase: annotating high confidence microRNAs using deep sequencing data. Nucleic Acids Res. 2014;42(Database issue):D68-73.

202.Landgraf P, Rusu M, Sheridan R, Sewer A, Iovino N, Aravin A, Pfeffer S, Rice A, Kamphorst AO, Landthaler M, Lin C, Socci ND, Hermida L, Fulci V, Chiaretti S, Foa R, Schliwka J, Fuchs U, Novosel A, Muller RU, Schermer B, Bissels U, Inman J, Phan Q, Chien M, Weir DB, Choksi R, De Vita G, Frezzetti D, Trompeter HI, Hornung V, Teng G, Hartmann G, Palkovits M, Di Lauro R, Wernet P, Macino G, Rogler CE, Nagle JW, Ju J, Papavasiliou FN, Benzing T, Lichter P, Tam W, Brownstein MJ, Bosio A, Borkhardt A, Russo JJ, Sander C, Zavolan M, Tuschl T. A mammalian microRNA expression atlas based on small RNA library sequencing. Cell. 2007;129(7):1401-14.

203.Houbaviy HB, Murray MF, Sharp PA. Embryonic stem cell-specific MicroRNAs. Dev Cell. 2003;5(2):351-8.

204.Meng QL, Liu F, Yang XY, Liu XM, Zhang X, Zhang C, Zhang ZD. Identification of latent tuberculosis infection-related microRNAs in human U937 macrophages expressing Mycobacterium tuberculosis Hsp16.3. BMC Microbiol. 2014;14:37.

205.Suh MR, Lee Y, Kim JY, Kim SK, Moon SH, Lee JY, Cha KY, Chung HM, Yoon HS, Moon SY, Kim VN, Kim KS. Human embryonic stem cells express a unique set of microRNAs. Dev Biol. 2004;270(2):488-98.

206.Xie C, Jiang XH, Zhang JT, Sun TT, Dong JD, Sanders AJ, Diao RY, Wang Y, Fok KL, Tsang LL, Yu MK, Zhang XH, Chung YW, Ye L, Zhao MY, Guo JH, Xiao ZJ, Lan HY, Ng CF, Lau KM, Cai ZM, Jiang WG, Chan HC. CFTR suppresses tumor progression through miR-193b targeting urokinase plasminogen activator (uPA) in prostate cancer. Oncogene. 2013;32(18):2282-91, 2291 e1-7.

207.Meunier J, Lemoine F, Soumillon M, Liechti A, Weier M, Guschanski K, Hu H, Khaitovich P, Kaessmann H. Birth and expression evolution of mammalian microRNA genes. Genome Res. 2013;23(1):34-45.

208.Swarbrick A, Woods SL, Shaw A, Balakrishnan A, Phua Y, Nguyen A, Chanthery Y, Lim L, Ashton LJ, Judson RL, et al. miR-380-5p represses p53 to control cellular survival and is associated with poor outcome in MYCN amplified neuroblastoma. Nature medicine 2010;16(10):1134-1140.

209.Schee K, Lorenz S, Worren MM, Gunther CC, Holden M, Hovig E, Fodstad O, Meza-Zepeda LA, Flatmark K. Deep Sequencing the MicroRNA Transcriptome in Colorectal Cancer. PLoS One. 2013;8(6):e66165.

210.Cazzoli R, Buttitta F, Di Nicola M, Malatesta S, Marchetti A, Rom WN, Pass HI. microRNAs

derived from circulating exosomes as noninvasive biomarkers for screening and diagnosing lung cancer. J Thorac Oncol. 2013;8(9):1156-62.

211.Guo L, Yang Y, Liu J, Wang L, Li J, Wang Y, Liu Y, Gu S, Gan H, Cai J, Yuan JX, Wang J, Wang C. Differentially expressed plasma microRNAs and the potential regulatory function of Let-7b in chronic thromboembolic pulmonary hypertension. PLoS One. 2014;9(6):e101055.

212.Kai Y, Peng W, Ling W, Jiebing H, Zhuan B. Reciprocal effects between microRNA-140-5p and ADAM10 suppress migration and invasion of human tongue cancer cells Biochemical and biophysical research communications. 2014;448(3):308-314.

213.Jinushi T, Shibayama Y, Kinoshita I, Oizumi S, Jinushi M, Aota T, Takahashi T, Horita S, Dosaka-Akita H, Iseki K. Low expression levels of microRNA-124-5p correlated with poor prognosis in colorectal cancer via targeting of SMC4. Cancer Med. 2014;3(6):1544-52.

214.Vaira V, Roncoroni L, Barisani D, Gaudioso G, Bosari S, Bulfamante G, Doneda L, Conte D, Tomba C, Bardella MT, Ferrero S, Locatelli M, Elli L. microRNA profiles in coeliac patients distinguish different clinical phenotypes and are modulated by gliadin peptides in primary duodenal fibroblasts. Clin Sci (Lond). 2014;126(6):417-23.

215.Uchino K, Takeshita F, Takahashi RU, Kosaka N, Fujiwara K, Naruoka H, Sonoke S, Yano J, Sasaki H, Nozawa S, et al. Therapeutic effects of microRNA-582-5p and -3p on the inhibition of bladder cancer progression: molecular therapy. The journal of the American Society of Gene Therapy 2013;21(3):610-619.

216.Wu X, Bhayani MK, Dodge CT, Nicoloso MS, Chen Y, Yan X, Adachi M, Thomas L, Galer CE, Jiffar T, Pickering CR, Kupferman ME, Myers JN, Calin GA, Lai SY. Coordinated targeting of the EGFR signaling axis by microRNA-27a*. Oncotarget. 2013;4(9):1388-98.

217.Persson H, Kvist A, Rego N, Staaf J, Vallon-Christersson J, Luts L, Loman N, Jonsson G, Naya H, Hoglund M, et al. 2011. Cancer research Identification of new microRNAs in paired normal and tumor breast tissue suggests a dual role for the ERBB2/Her2 gene;71(1):78-86.

218.Chen X, Pan M, Han L, Lu H, Hao X, Dong Q. miR-338-3p suppresses neuroblastoma proliferation, invasion and migration through targeting PREX2a FEBS letters 2013;587 (22):3729-3737.

219.Gao W, Gu Y, Li Z, Cai H, Peng Q, Tu M, Kondo Y, Shinjo K, Zhu Y, Zhang J, et al. miR-615-5p is epigenetically inactivated and functions as a tumor suppressor in pancreatic ductal adenocarcinoma. Oncogene 2015;26(34 (13)):1629-40.

220.Wang B, Herman-Edelstein M, Koh P, Burns W, Jandeleit-Dahm K, Watson A, Saleem M, Goodall GJ, Twigg SM, Cooper ME, Kantharidis P. E-cadherin expression is regulated by miR-192/215 by a mechanism that is independent of the profibrotic effects of transforming growth factor-beta. Diabetes. 2010;59(7):1794-802.

221.Hassan F, Nuovo GJ, Crawford M, Boyaka PN, Kirkby S, Nana-Sinkam SP, Cormet-Boyaka E.

MiR-101 and miR-144 regulate the expression of the CFTR chloride channel in the lung. PLoS One. 2012;7(11):e50837.

222.Jansson MD, Damas ND, Lees M, Jacobsen A, Lund AH. miR-339-5p regulates the p53 tumor-suppressor pathway by targeting MDM2. Oncogene. 2015;34(15):1908-18.

223.Vilming Elgaaen B, Olstad OK, Haug KB, Brusletto B, Sandvik L, Staff AC, Gautvik KM, Davidson B. Global miRNA expression analysis of serous and clear cell ovarian carcinomas identifies differentially expressed miRNAs including miR-200c-3p as a prognostic marker. BMC Cancer. 2014;14:80.

224.Bao W, Holt LJ, Prince RD, Jones GX, Aravindhan K, Szapacs M, Barbour AM, Jolivette LJ, Lepore JJ, Willette RN, DeAngelis E, Jucker BM. Novel fusion of GLP-1 with a domain antibody to serum albumin prolongs protection against myocardial ischemia/reperfusion injury in the rat. Cardiovasc Diabetol. 2013;12:148.

225.Voellenkle C, Rooij J, Guffanti A, Brini E, Fasanaro P, Isaia E, Croft L, David M, Capogrossi MC, Moles A, Felsani A, Martelli F. Deep-sequencing of endothelial cells exposed to hypoxia reveals the complexity of known and novel microRNAs. RNA. 2012;18(3):472-84.

226.Kitahara Y, Nakamura K, Kogure K, Minegishi T. Role of microRNA-136-3p on the expression of luteinizing hormone-human chorionic gonadotropin receptor mRNA in rat ovaries. Biol Reprod. 2013;89(5):114.

227.Wang Y, Huang C, Reddy Chintagari N, Bhaskaran M, Weng T, Guo Y, Xiao X, Liu L. miR-375 regulates rat alveolar epithelial cell trans-differentiation by inhibiting Wnt/beta-catenin pathway. Nucleic Acids Res. 2013;41(6):3833-44.

228.Sheng Y, Ding S, Chen K, Chen J, Wang S, Zou C, Zhang J, Cao Y, Huang A, Tang H. Functional analysis of miR-101-3p and Rap1b involved in hepatitis B virus-related hepatocellular carcinoma pathogenesis. Biochem Cell Biol. 2014;92(2):152-62.

229.Ambros V, Bartel B, Bartel DP, Burge CB, Carrington JC, Chen X, Dreyfuss G, Eddy SR, Griffiths-Jones S, Marshall M, Matzke M, Ruvkun G, Tuschl T. A uniform system for microRNA annotation. RNA. 2003;9(3):277-9.

230.Davis-Dusenbery BN, Chan MC, Reno KE, Weisman AS, Layne MD, Lagna G, Hata A. down-regulation of Kruppel-like factor-4 (KLF4) by microRNA-143/145 is critical for modulation of vascular smooth muscle cell phenotype by transforming growth factor-beta and bone morphogenetic protein 4. J Biol Chem. 2011;286(32):28097-110.

231.Chinoy MR, Chi X, Cilley RE. Down-regulation of regulatory proteins for differentiation and proliferation in murine fetal hypoplastic lungs: altered mesenchymal-epithelial interactions. Pediatr Pulmonol. 2001;32(2):129-41.

232.Tong QS, Zheng LD, Tang ST, Jiang GS, Ruan QL, Zeng FQ, Dong JH. Nitrofen suppresses cell proliferation and promotes mitochondria-mediated apoptosis in type II pneumocytes. Acta

Pharmacol Sin. 2007;28(5):672-84.

233.Jin FG, Li WP, Mu DG, Chu DL, Fu EQ, Xie YH, Lu JL, Sun YN. Joint application of 7 interventional pulmonology methods in early diagnosis of lung cancer. Zhonghua Yi Xue Za Zhi. 2009;89(24):1667-71.

234.Halappanavar S, Wu D, Williams A, Kuo B, Godschalk RW, Van Schooten FJ, Yauk CL. Pulmonary gene and microRNA expression changes in mice exposed to benzo(a)pyrene by oral gavage. Toxicology. 2011;285(3):133-41.

235.Popova AP, Bozyk PD, Goldsmith AM, Linn MJ, Lei J, Bentley JK, Hershenson MB. Autocrine production of TGF-beta1 promotes myofibroblastic differentiation of neonatal lung mesenchymal stem cells. Am J Physiol Lung Cell Mol Physiol. 2010;298(6):L735-43.

236.Jesudason EC, Smith NP, Connell MG, Spiller DG, White MR, Fernig DG, Losty PD. Peristalsis of airway smooth muscle is developmentally regulated and uncoupled from hypoplastic lung growth. Am J Physiol Lung Cell Mol Physiol. 2006;291(4):L559-65.

237.Xu C, Chen ZX, Liu WY, Wang YX, Xiong ZX. [A series of observation on the expression of TGF-beta1 in the lung of nitrofen-induced congenital diaphragmatic hernia rat model]. Zhonghua Wai Ke Za Zhi. 2009;47(4):301-4.

238.Chen MH, MacGowan A, Ward S, Bavik C, Greer JJ. The activation of the retinoic acid response element is inhibited in an animal model of congenital diaphragmatic hernia. Biol Neonate. 2003;83(3):157-61.

239.Pavez Lorie E, Li H, Vahlquist A, Torma H. The involvement of cytochrome p450 (CYP) 26 in the retinoic acid metabolism of human epidermal keratinocytes. Biochim Biophys Acta. 2009;1791(3):220-8.

240.Beurskens LW, Tibboel D, Lindemans J, Duvekot JJ, Cohen-Overbeek TE, Veenma DC, de Klein A, Greer JJ, Steegers-Theunissen RP. Retinol status of newborn infants is associated with congenital diaphragmatic hernia. Pediatrics. 2010;126(4):712-20.

241.Weiss FU, Marques IJ, Woltering JM, Vlecken DH, Aghdassi A, Partecke LI, Heidecke CD, Lerch MM, Bagowski CP. Retinoic acid receptor antagonists inhibit miR-10a expression and block metastatic behavior of pancreatic cancer. Gastroenterology. 2009;137(6):2136-45 e1-7.

242.Volpe MV, Martin A, Vosatka RJ, Mazzoni CL, Nielsen HC. Hoxb-5 expression in the developing mouse lung suggests a role in branching morphogenesis and epithelial cell fate. Histochem Cell Biol. 1997;108(6):495-504.

243.Ma L, Teruya-Feldstein J, Weinberg RA. Tumour invasion and metastasis initiated by microRNA-10b in breast cancer. Nature. 2007;449(7163):682-8.

244.Tang H, Hornstein E, Stolovich M, Levy G, Livingstone M, Templeton D, Avruch J, Meyuhas O. Amino acid-induced translation of TOP mRNAs is fully dependent on phosphatidylinositol 3-

kinase-mediated signaling, is partially inhibited by rapamycin, and is independent of S6K1 and rpS6 phosphorylation. Mol Cell Biol. 2001;21(24):8671-83.

245.Doi T, Ruttenstock E, Dingemann J, Puri P. Spatiotemporal alteration in phosphatidylinositide 3-kinase-serine/threonine protein kinase B signaling in the nitrofen-induced hypoplastic lung. J Pediatr Surg. 2010;45(2):366-71.

246.Janssen WJ, McPhillips KA, Dickinson MG, Linderman DJ, Morimoto K, Xiao YQ, Oldham KM, Vandivier RW, Henson PM, Gardai SJ. Surfactant proteins A and D suppress alveolar macrophage phagocytosis via interaction with SIRP alpha. Am J Respir Crit Care Med. 2008;178(2):158-67.

247.Johar D. Cytoskeletal remodeling and regulation of cell fate in the hypertensive neonatal pulmonary artery in response to stress. J Cell Physiol. 2018;233(3):2146-2161.

248.Lakshminrusimha S, Steinhorn RH. Pulmonary vascular biology during neonatal transition. Clin Perinatol. 1999;26(3):601-19.

249.Haworth SG. Development of the normal and hypertensive pulmonary vasculature. Exp Physiol. 1995;80(5):843-53.

250.Farrow KN, Fliman P, Steinhorn RH. The diseases treated with ECMO: focus on PPHN. Semin Perinatol. 2005;29(1):8-14.

251.Hernandez-Diaz S, Van Marter LJ, Werler MM, Louik C, Mitchell AA. Risk factors for persistent pulmonary hypertension of the newborn. Pediatrics. 2007;120(2):e272-82.

252.Dakshinamurti S. Pathophysiologic mechanisms of persistent pulmonary hypertension of the newborn. Pediatric pulmonology. 2005;39(6):492-503.

253.Tozzi CA, Christiansen DL, Poiani GJ, Riley DJ. Excess collagen in hypertensive pulmonary arteries decreases vascular distensibility. Am J Respir Crit Care Med. 1994;149(5):1317-26.

254.Qu MJ, Liu B, Wang HQ, Yan ZQ, Shen BR, Jiang ZL. Frequency-dependent phenotype modulation of vascular smooth muscle cells under cyclic mechanical strain. J Vasc Res. 2007;44(5):345-53.

255.Sotoudeh M, Li YS, Yajima N, Chang CC, Tsou TC, Wang Y, Usami S, Ratcliffe A, Chien S, Shyy JY. Induction of apoptosis in vascular smooth muscle cells by mechanical stretch. Am J Physiol Heart Circ Physiol. 2002;282(5):H1709-16.

256.Haworth SG, Hislop AA. Effect of hypoxia on adaptation of the pulmonary circulation to extra-uterine life in the pig. Cardiovasc Res. 1982;16(6):293-303.

257.Fike CD, Kaplowitz MR, Pfister SL. Arachidonic acid metabolites and an early stage of pulmonary hypertension in chronically hypoxic newborn pigs. Am J Physiol Lung Cell Mol Physiol. 2003;284(2):L316-23.

258.Jankov RP, Belcastro R, Ovcina E, Lee J, Massaeli H, Lye SJ, Tanswell AK. Thromboxane A(2) receptors mediate pulmonary hypertension in 60% oxygen-exposed newborn rats by a cyclooxygenase-independent mechanism. Am J Respir Crit Care Med. 2002;166(2):208-14.

259.Steinhorn RH, Albert G, Swartz DD, Russell JA, Levine CR, Davis JM. Recombinant human superoxide dismutase enhances the effect of inhaled nitric oxide in persistent pulmonary hypertension. Am J Respir Crit Care Med. 2001;164(5):834-9.

260.El-Ferzli GT, Philips JB, 3rd, Bulger A, Ambalavanan N. Evaluation of a pumpless lung assist device in hypoxia-induced pulmonary hypertension in juvenile piglets. Pediatr Res. 2009;66(6):677-81.

261.Bisgard GE, Will JA. Glucagon and aminophylline as pulmonary vasodilators in the calf with hypoxic pulmonary hypertension. Chest. 1977;71(2 suppl):263-5.

262.Jane-Wit D, Chun HJ. Mechanisms of dysfunction in senescent pulmonary endothelium. J Gerontol A Biol Sci Med Sci. 2012;67(3):236-41.

263.Saker M, Lipskaia L, Marcos E, Abid S, Parpaleix A, Houssaini A, Validire P, Girard P, Noureddine H, Boyer L, Vienney N, Amsellem V, Marguerit L, Maitre B, Derumeaux G, Dubois-Rande JL, Jourdan-Lesaux C, Delcroix M, Quarck R, Adnot S. Osteopontin, a Key Mediator Expressed by Senescent Pulmonary Vascular Cells in Pulmonary Hypertension. Arterioscler Thromb Vasc Biol. 2016;36(9):1879-90.

264.Kurz DJ, Decary S, Hong Y, Erusalimsky JD. Senescence-associated (beta)-galactosidase reflects an increase in lysosomal mass during replicative ageing of human endothelial cells. J Cell Sci. 2000;113 (Pt 20):3613-22.

265.Campisi J, Andersen JK, Kapahi P, Melov S. Cellular senescence: a link between cancer and age-related degenerative disease? Semin Cancer Biol. 2011;21(6):354-9.

266.Kumar M, Seeger W, Voswinckel R. Senescence-associated secretory phenotype and its possible role in chronic obstructive pulmonary disease. Am J Respir Cell Mol Biol. 2014;51(3):323-33.

267.Araya J, Kojima J, Takasaka N, Ito S, Fujii S, Hara H, Yanagisawa H, Kobayashi K, Tsurushige C, Kawaishi M, Kamiya N, Hirano J, Odaka M, Morikawa T, Nishimura SL, Kawabata Y, Hano H, Nakayama K, Kuwano K. Insufficient autophagy in idiopathic pulmonary fibrosis. Am J Physiol Lung Cell Mol Physiol. 2013;304(1):L56-69.

268.Rochette PJ, Brash DE. Human telomeres are hypersensitive to UV-induced DNA Damage and refractory to repair. PLoS Genet. 2010;6(4):e1000926.

269.Zhang YH, Zhao CQ, Jiang LS, Dai LY. Cyclic stretch-induced apoptosis in rat annulus fibrosus cells is mediated in part by endoplasmic reticulum stress through nitric oxide production. Eur Spine J. 2011;20(8):1233-43.

270.Rasheva VI, Domingos PM. Cellular responses to endoplasmic reticulum stress and apoptosis. Apoptosis. 2009;14(8):996-1007.

271.Nishitani WS, Saif TA, Wang Y. Calcium signaling in live cells on elastic gels under mechanical vibration at subcellular levels. PLoS One. 2011;6(10):e26181.

272.Cheng WP, Wang BW, Chen SC, Chang H, Shyu KG. Mechanical stretch induces the apoptosis regulator PUMA in vascular smooth muscle cells. Cardiovasc Res. 2012;93(1):181-9.

273.Ali MH, Pearlstein DP, Mathieu CE, Schumacker PT. Mitochondrial requirement for endothelial responses to cyclic strain: implications for mechanotransduction. Am J Physiol Lung Cell Mol Physiol. 2004;287(3):L486-96.

274.Gong Y, Yi M, Fediuk J, Lizotte PP, Dakshinamurti S. Hypoxic neonatal pulmonary arterial myocytes are sensitized to ROS-generated 8-isoprostane. Free Radic Biol Med. 2010;48(7):882-94.

275.Mark Evans A, Ward JP. Hypoxic pulmonary vasoconstriction--invited article. Adv Exp Med Biol. 2009;648:351-60.

276.Waypa GB, Schumacker PT. Oxygen sensing in hypoxic pulmonary vasoconstriction: using new tools to answer an age-old question. Exp Physiol. 2008;93(1):133-8.

277.Groenendyk J, Sreenivasaiah PK, Kim DH, Agellon LB, Michalak M. Biology of endoplasmic reticulum stress in the heart. Circ Res. 2010;107(10):1185-97.

278.Gotoh T, Mori M. Nitric oxide and endoplasmic reticulum stress. Arterioscler Thromb Vasc Biol. 2006;26(7):1439-46.

279.Minamino T, Kitakaze M. ER stress in cardiovascular disease. J Mol Cell Cardiol. 2010;48(6):1105-10.

280.Wohrley JD, Frid MG, Moiseeva EP, Orton EC, Belknap JK, Stenmark KR. Hypoxia selectively induces proliferation in a specific subpopulation of smooth muscle cells in the bovine neonatal pulmonary arterial media. J Clin Invest. 1995;96(1):273-81.

281.Hall SM, Hislop AA, Wu Z, Haworth SG. Remodelling of the pulmonary arteries during recovery from pulmonary hypertension induced by neonatal hypoxia. The Journal of pathology. 2004;203(1):575-583.

282.Burridge K, Chrzanowska-Wodnicka M. Focal adhesions, contractility, and signaling. Annu Rev Cell Dev Biol. 1996;12:463-518.

283.Laboureau J, Dubertret L, Lebreton-De Coster C, Coulomb B. ERK activation by mechanical strain is regulated by the small G proteins rac-1 and rhoA. Experimental dermatology. 2004;13(2):70-7.

284.Klein EA, Campbell LE, Kothapalli D, Fournier AK, Assoian RK. Joint requirement for Rac and ERK activities underlies the mid-G1 phase induction of cyclin D1 and S phase entry in both epithelial and mesenchymal cells. J Biol Chem. 2008;283(45):30911-8.

285.Barman SA, Zhu S, White RE. RhoA/Rho-kinase signaling: a therapeutic target in pulmonary hypertension. Vasc Health Risk Manag. 2009;5:663-71.

286.Croft DR, Crighton D, Samuel MS, Lourenco FC, Munro J, Wood J, Bensaad K, Vousden KH, Sansom OJ, Ryan KM, Olson MF. p53-mediated transcriptional regulation and activation of the actin cytoskeleton regulatory RhoC to LIMK2 signaling pathway promotes cell survival. Cell research. 2011;21(4):666-82.

287.Boudreau NJ, Jones PL. Extracellular matrix and integrin signalling: the shape of things to come. Biochem J. 1999;339 (Pt 3):481-8.

288.Sieg DJ, Hauck CR, Ilic D, Klingbeil CK, Schaefer E, Damsky CH, Schlaepfer DD. FAK integrates growth-factor and integrin signals to promote cell migration. Nat Cell Biol. 2000;2(5):249-56.

289.Sieg DJ, Hauck CR, Schlaepfer DD. Required role of focal adhesion kinase (FAK) for integrin-stimulated cell migration. J Cell Sci. 1999;112 (Pt 16):2677-91.

290.Frisch SM, Vuori K, Ruoslahti E, Chan-Hui PY. Control of adhesion-dependent cell survival by focal adhesion kinase. J Cell Biol. 1996;134(3):793-9.

291.Giancotti FG, Ruoslahti E. Integrin signaling. Science. 1999;285(5430):1028-32.

292.Wary KK, Mainiero F, Isakoff SJ, Marcantonio EE, Giancotti FG. The adaptor protein Shc couples a class of integrins to the control of cell cycle progression. Cell. 1996;87(4):733-43.

293.Schlaepfer DD, Broome MA, Hunter T. Fibronectin-stimulated signaling from a focal adhesion kinase-c-Src complex: involvement of the Grb2, p130cas, and Nck adaptor proteins. Mol Cell Biol. 1997;17(3):1702-13.

294.Pozzi A, Wary KK, Giancotti FG, Gardner HA. Integrin alpha1beta1 mediates a unique collagen-dependent proliferation pathway in vivo. J Cell Biol. 1998;142(2):587-94.

295.Eliceiri BP, Klemke R, Stromblad S, Cheresh DA. Integrin alphavbeta3 requirement for sustained mitogen-activated protein kinase activity during angiogenesis. J Cell Biol. 1998;140(5):1255-63.

296.Schlaepfer DD, Hauck CR, Sieg DJ. Signaling through focal adhesion kinase. Prog Biophys Mol Biol. 1999;71(3-4):435-78.

297.Renshaw MW, Price LS, Schwartz MA. Focal adhesion kinase mediates the integrin signaling requirement for growth factor activation of MAP kinase. J Cell Biol. 1999;147(3):611-8.

298.Fediuk J, Gutsol A, Nolette N, Dakshinamurti S. Thromboxane-induced actin polymerization

in hypoxic pulmonary artery is independent of Rho. Am J Physiol Lung Cell Mol Physiol. 2012;302(1):L13-26.

299.Johar D, Bernstein LH. A targeted approach toward more accurate assessment of hypertension. Egyptian Journal of Chest Diseases and Tuberculosis 2017;66 517–536.

300.Stromblad S, Becker JC, Yebra M, Brooks PC, Cheresh DA. Suppression of p53 activity and p21WAF1/CIP1 expression by vascular cell integrin alphaVbeta3 during angiogenesis. J Clin Invest. 1996;98(2):426-33.

301.Frisch SM, Francis H. Disruption of epithelial cell-matrix interactions induces apoptosis. J Cell Biol. 1994;124(4):619-26.

302.Sonoda Y, Matsumoto Y, Funakoshi M, Yamamoto D, Hanks SK, Kasahara T. Anti-apoptotic role of focal adhesion kinase (FAK). Induction of inhibitor-of-apoptosis proteins and apoptosis suppression by the overexpression of FAK in a human leukemic cell line, HL-60. J Biol Chem. 2000;275(21):16309-15.

303.Gu H, Maeda H, Moon JJ, Lord JD, Yoakim M, Nelson BH, Neel BG. New role for Shc in activation of the phosphatidylinositol 3-kinase/Akt pathway. Mol Cell Biol. 2000;20(19):7109-20.

304.Zhou H, Li XM, Meinkoth J, Pittman RN. Akt regulates cell survival and apoptosis at a postmitochondrial level. J Cell Biol. 2000;151(3):483-94.

305.Yamaguchi H, Wang HG. The protein kinase PKB/Akt regulates cell survival and apoptosis by inhibiting Bax conformational change. Oncogene. 2001;20(53):7779-86.

306.Shimoda LA, Manalo DJ, Sham JS, Semenza GL, Sylvester JT. Partial HIF-1alpha deficiency impairs pulmonary arterial myocyte electrophysiological responses to hypoxia. Am J Physiol Lung Cell Mol Physiol. 2001;281(1):L202-8.

307.Vergadi E, Chang MS, Lee C, Liang OD, Liu X, Fernandez-Gonzalez A, Mitsialis SA, Kourembanas S. Early macrophage recruitment and alternative activation are critical for the later development of hypoxia-induced pulmonary hypertension. Circulation. 2011;123(18):1986-95.

308.Hinton M, Gutsol A, Dakshinamurti S. Thromboxane hypersensitivity in hypoxic pulmonary artery myocytes: altered TP receptor localization and kinetics. Am J Physiol Lung Cell Mol Physiol. 2007;292(3):L654-63.

309.Lawrie CM, Sulistijo ES, MacKenzie KR. Intermonomer hydrogen bonds enhance GxxxG-driven dimerization of the BNIP3 transmembrane domain: roles for sequence context in helix-helix association in membranes. J Mol Biol. 2010;396(4):924-36.

310.Guo K, Searfoss G, Krolikowski D, Pagnoni M, Franks C, Clark K, Yu KT, Jaye M, Ivashchenko Y. Hypoxia induces the expression of the pro-apoptotic gene BNIP3. Cell Death Differ.

2001;8(4):367-76.

311.Kutrasiak LA, Hernandez OM, Bishopric NH, Webster KA. Hypoxia and acidosis activate cardiac myocyte death through the BCL2 family protein BNIP3. Proc Nat Acad Sci. 2002;99(20):12825-30.

312.Ghavami S, Eshraghi M, Kadkhoda K, Mutawe MM, Maddika S, Bay GH, Wesselborg S, Halayko AJ, Klonisch T, Los M. Role of BNIP3 in TNF-induced cell death--TNF upregulates BNIP3 expression. Biochim Biophys Acta. 2009;1793(3):546-60.

313.Yasuda M, Theodorakis P, Subramanian T, Chinnadurai G. Adenovirus E1B-19K/BCL-2 interacting protein BNIP3 contains a BH3 domain and a mitochondrial targeting sequence. J Biol Chem. 1998;273(20):12415-21.

314.Chen G, Ray R, Dubik D, Shi L, Cizeau J, Bleackley RC, Saxena S, Gietz RD, Greenberg AH. The E1B 19K/Bcl-2-binding protein Nip3 is a dimeric mitochondrial protein that activates apoptosis. J Exp Med. 1997;186(12):1975-83.

315.Chen B, Nelin VE, Locy ML, Jin Y, Tipple TE. Thioredoxin-1 mediates hypoxia-induced pulmonary artery smooth muscle cell proliferation. Am J Physiol Lung Cell Mol Physiol. 2013;305(5):L389-95.

316.Luo Y, Xu DQ, Dong HY, Zhang B, Liu Y, Niu W, Dong MQ, Li ZC. Tanshinone IIA inhibits hypoxia-induced pulmonary artery smooth muscle cell proliferation via Akt/Skp2/p27-associated pathway. PLoS One. 2013;8(2):e56774.

317.Poot M, Pierce RH. Detection of changes in mitochondrial function during apoptosis by simultaneous staining with multiple fluorescent dyes and correlated multiparameter flow cytometry. Cytometry. 1999;35(4):311-7.

318.Moiseeva O, Bourdeau V, Roux A, Deschenes-Simard X, Ferbeyre G. Mitochondrial dysfunction contributes to oncogene-induced senescence. Mol Cell Biol. 2009;29(16):4495-507.

319.Perelman A, Wachtel C, Cohen M, Haupt S, Shapiro H, Tzur A. JC-1: alternative excitation wavelengths facilitate mitochondrial membrane potential cytometry. Cell Death Dis. 2012;3:e430.

320.Ghavami S, Yeganeh B, Stelmack GL, Kashani HH, Sharma P, Cunnington R, Rattan S, Bathe K, Klonisch T, Dixon IM, Freed DH, Halayko AJ. Apoptosis, autophagy and ER stress in mevalonate cascade inhibition-induced cell death of human atrial fibroblasts. Cell Death Dis. 2012;3:e330.

321.Ghavami S, Mutawe MM, Schaafsma D, Yeganeh B, Unruh H, Klonisch T, Halayko AJ. Geranylgeranyl transferase 1 modulates autophagy and apoptosis in human airway smooth muscle. Am J Physiol Lung Cell Mol Physiol. 2012;302(4):L420-8.

322.Le Cras TD, Kim DH, Markham NE, Abman AS. Early abnormalities of pulmonary vascular

development in the Fawn-Hooded rat raised at Denver's altitude. Am J Physiol Lung Cell Mol Physiol. 2000;279(2):L283-91.

323.Farrow KN, Lakshminrusimha S, Czech L, Groh BS, Gugino SF, Davis JM, Russell JA, Steinhorn RH. SOD and inhaled nitric oxide normalize phosphodiesterase 5 expression and activity in neonatal lambs with persistent pulmonary hypertension. Am J Physiol Lung Cell Mol Physiol. 2010;299(1):L109-16.

324.Fike CD, Pfister SL, Kaplowitz MR, Madden JA. Cyclooxygenase contracting factors and altered pulmonary vascular responses in chronically hypoxic newborn pigs. J Appl Physiol (1985). 2002;92(1):67-74.

325.Sood BG, Delaney-Black V, Glibetic M, Aranda JV, Chen X, Shankaran S. PGE2/TXB2 imbalance in neonatal hypoxemic respiratory failure. Acta Paediatr. 2007;96(5):669-73.

326.Al-Naamani N, Trammell AW, Safdar Z. Circulating Biomarkers in Pulmonary Arterial Hypertension. Adv Pulm Hypertension. 2015;14(1):21-27.

327.Reid HM, Kinsella BT. The alpha, but not the beta, isoform of the human thromboxane A2 receptor is a target for nitric oxide-mediated desensitization. Independent modulation of Tp alpha signaling by nitric oxide and prostacyclin. J Biol Chem. 2003;278(51):51190-202.

328.Vane JR, Botting RM. Pharmacodynamic profile of prostacyclin. Am J Cardiol. 1995;75(3):3A-10A.

329.Jin J, Mullen TD, Hou Q, Bielawski J, Bielawska A, Zhang X, Obeid LM, Hannun YA, Hsu YT. AMPK inhibitor Compound C stimulates ceramide production and promotes Bax redistribution and apoptosis in MCF7 breast carcinoma cells. J Lipid Res. 2009;50(12):2389-97.

330.Papke CL, Cao J, Kwartler CS, Villamizar C, Byanova KL, Lim SM, Sreenivasappa H, Fischer G, Pham J, Rees M, Wang M, Chaponnier C, Gabbiani G, Khakoo AY, Chandra J, Trache A, Zimmer W, Milewicz DM. Smooth muscle hyperplasia due to loss of smooth muscle alpha-actin is driven by activation of focal adhesion kinase, altered p53 localization and increased levels of platelet-derived growth factor receptor-beta. Hum Mol Genet. 2013;22(15):3123-37.

331.Heron-Milhavet L, Karas M, Goldsmith CM, Baum BJ, LeRoith D. Insulin-like growth factor-I (IGF-I) receptor activation rescues UV-damaged cells through a p38 signaling pathway. Potential role of the IGF-I receptor in DNA repair. J Biol Chem. 2001;276(21):18185-92.

332.Liu AJ, Ling F, Wang D, Wang Q, Lu XD, Liu YL. Fasudil inhibits platelet-derived growth factor-induced human pulmonary artery smooth muscle cell proliferation by up-regulation of p27kip(1) via the ERK signal pathway. Chin Med J (Engl). 2011;124(19):3098-104.

333.Hall SM, Gorenflo M, Reader J, Lawson D, Haworth SG. Neonatal pulmonary hypertension prevents reorganisation of the pulmonary arterial smooth muscle cytoskeleton after birth. J Anat. 2000;196 (Pt 3):391-403.

334.Walsh-Sukys MC, Tyson JE, Wright LL, Bauer CR, Korones SB, Stevenson DK, Verter J, Stoll BJ, Lemons JA, Papile LA, Shankaran S, Donovan EF, Oh W, Ehrenkranz RA, Fanaroff AA. Persistent pulmonary hypertension of the newborn in the era before nitric oxide: practice variation and outcomes. Pediatrics. 2000;105(1 Pt 1):14-20.

335.Baquero H, Soliz A, Neira F, Venegas ME, Sola A. Oral sildenafil in infants with persistent pulmonary hypertension of the newborn: a pilot randomized blinded study. Pediatrics. 2006;117(4):1077-83.

336.Walsh MC, Stork EK. Persistent pulmonary hypertension of the newborn. Rational therapy based on pathophysiology. Clin Perinatol. 2001;28(3):609-27, vii.

337.McLeod KA, Gerlis LM, Williams GJ. Morphology of the elastic pulmonary arteries in pulmonary hypertension: a quantitative study. Cardiology in the young. 1999;9(4):364-70.

338.Postolow F, Fediuk J, Nolette N, Hinton M, Dakshinamurti S. Hypoxia and nitric oxide exposure promote apoptotic signaling in contractile pulmonary arterial smooth muscle but not in pulmonary epithelium. Pediatr Pulmonol. 2011;46(12):1194-208.

339.Fike CD, Kaplowitz MR. Effect of chronic hypoxia on pulmonary vascular pressures in isolated lungs of newborn pigs. J Appl Physiol (1985). 1994;77(6):2853-62.

340.Su BY, Shontz KM, Flavahan NA, Nowicki PT. The effect of phenotype on mechanical stretch-induced vascular smooth muscle cell apoptosis. Journal of vascular research. 2006;43(3):229-237.

341.Kass DA. Ventricular arterial stiffening: integrating the pathophysiology. Hypertension. 2005;46(1):185-93.

342.Inoue N, Kawashima S, Hirata KI, Rikitake Y, Takeshita S, Yamochi W, Akita H, Yokoyama M. Stretch force on vascular smooth muscle cells enhances oxidation of LDL via superoxide production. Am J Physiol. 1998;274(6 Pt 2):H1928-32.

343.Wang H, Joseph JA. Quantifying cellular oxidative stress by dichlorofluorescein assay using microplate reader. Free Radic Biol Med. 1999;27(5-6):612-6.

344.Munzel T, Afanas'ev IB, Kleschyov AL, Harrison DG. Detection of superoxide in vascular tissue. Arterioscler Thromb Vasc Biol. 2002;22(11):1761-8.

345.Carmelle V. Remillard, Jason XJ Yuan. Activation of K channels: an essential pathway in programmed cell death. Am J Physiol Lung Cell Mol Physiol 2004;286(L49–L67).

346.Jian Chen MM, Yan-Xia Wang, Ming-Qing Dong, Bo Zhang, Ying Luo, Wen Niu, Zhi-Chao Li. Reoxygenation Reverses Hypoxic Pulmonary Arterial Remodeling by Inducing Smooth Muscle Cell Apoptosis via Reactive Oxygen Species–Mediated Mitochondrial Dysfunction. J Am Heart Assoc. 2017;6:e005602.

347.Suzuki YJ, Ibrahim YF, Shults NV. Apoptosis-based therapy to treat pulmonary arterial hypertension. J Rare Dis Res Treat. 2016;1(2):17-24.

348.Birukov KG. Cyclic stretch, reactive oxygen species, and vascular remodeling. Antioxidants & redox signaling. 2009;11(7):1651-67.

349.Ertan C, Tarakci N, Ozeke O, Demir AD. Pulmonary artery distensibility in chronic obstructive pulmonary disease. Echocardiography. 2013;30(8):940-4.

350.Kolipaka A, Woodrum D, Araoz PA, Ehman RL. MR elastography of the in vivo abdominal aorta: a feasibility study for comparing aortic stiffness between hypertensives and normotensives. Journal of magnetic resonance imaging : JMRI. 2012;35(3):582-6.

351.Lau EM, Iyer N, Ilsar R, Bailey BP, Adams MR, Celermajer DS. Abnormal pulmonary artery stiffness in pulmonary arterial hypertension: in vivo study with intravascular ultrasound. PLoS One. 2012;7(3):e33331.

352.Wedgwood S, Lakshminrusimha S, Schumacker PT, Steinhorn RH. Cyclic stretch stimulates mitochondrial reactive oxygen species and Nox4 signaling in pulmonary artery smooth muscle cells. Am J Physiol Lung Cell Mol Physiol. 2015;309(2):L196-203.

353.Dick AS, Ivanovska J, Kantores C, Belcastro R, Keith Tanswell A, Jankov RP. Cyclic stretch stimulates nitric oxide synthase-1-dependent peroxynitrite formation by neonatal rat pulmonary artery smooth muscle. Free Radic Biol Med. 2013;61:310-9.

354.Monica RS, Stephen W, Lyubov C, Gina AK, Satyan L, S. PT, S. RH, N.F. K. Cyclic Stretch Induces Inducible Nitric Oxide Synthase and Soluble Guanylate Cyclase in Pulmonary Artery Smooth Muscle Cells. Int J Mol Sci. 2013;14(2):4334–4348.

355.Santilli SM, Wernsing SE, Lee ES. The effect of supplemental oxygen on the transarterial wall oxygen gradients at a prosthetic vascular graft to artery anastomosis in the rabbit. Annals of vascular surgery. 2001;15(4):435-42.

356.Santilli SM, Tretinyak AS, Lee ES. Transarterial wall oxygen gradients at the deployment site of an intra-arterial stent in the rabbit. Am J Physiol Heart Circ Physiol. 2000;279(4):H1518-25.

357.Santilli SM, Wernsing SE, Lee ES. Transarterial wall oxygen gradients at a prosthetic vascular graft to artery anastomosis in the rabbit. Journal of vascular surgery. 2000;31(6):1229-39.

358.Newman JH, Holt TN, Hedges LK, Womack B, Memon SS, Willers ED, Wheeler L, Phillips JA, 3rd, Hamid R. High-altitude pulmonary hypertension in cattle (brisket disease): Candidate genes and gene expression profiling of peripheral blood mononuclear cells. Pulm Circ. 2011;1(4):462-9.

359.Bartsch P, Mairbaurl H, Swenson ER, Maggiorini M. High altitude pulmonary oedema. Swiss Med Wkly. 2003;133(27-28):377-84.

360.Glover GH, Newsou L. Further studies on brisket disease. J Agricultural Res. 1918;15: 409.

361.Saini-Chohan HK, Dakshinamurti S, Taylor WA, Shen GX, Murphy R, Sparagna GC, Hatch GM. Persistent pulmonary hypertension results in reduced tetralinoleoyl-cardiolipin and mitochondrial complex II + III during the development of right ventricular hypertrophy in the neonatal pig heart. Am J Physiol Heart Circ Physiol. 2011;301(4):H1415-24.

362.Peliowski A. Canadian Paediatric Society, Fetus and Newborn Committee. Inhaled nitric oxide use in newborns. Paediatrics & Child Health. 2012;17(2):95-97.

363.Kinsella JP, Neish SR, Shaffer E, Abman SH. Low-dose inhalation nitric oxide in persistent pulmonary hypertension of the newborn. Lancet. 1992;340(8823):819-20.

364.Hartney T, Birari R, Venkataraman S, Villegas L, Martinez M, Black SM, Stenmark KR, Nozik-Grayck E. Xanthine oxidase-derived ROS upregulate Egr-1 via ERK1/2 in PA smooth muscle cells; model to test impact of extracellular ROS in chronic hypoxia. PLoS One. 2011;6(11):e27531.

365.Saini-Chohan HK, Dakshinamurti S, Taylor WA, Shen GX, Murphy R, Sparagna GC, Hatch GM. Persistent pulmonary hypertension results in reduced tetralinoleoyl-cardiolipin and mitochondrial complex II Am J Physiol Heart Circ Physiol 2011;301: H1415–H1424.

366.Khoshgoo N, Visser R, Falk L, Day CA, Ameis D, Iwasiow BM, Zhu F, Ozturk A, Basu S, Pind M, Fresnosa A, Jackson M, Siragam VK, Stelmack G, Hicks GG, Halayko AJ, Keijzer R. MicroRNA-200b regulates distal airway development by maintaining epithelial integrity. Sci Rep. 2017;7(1):6382.

CHAPTER 8: APPENDICES

8. Appendix A: Full length gels showing bands used in the thesis figures

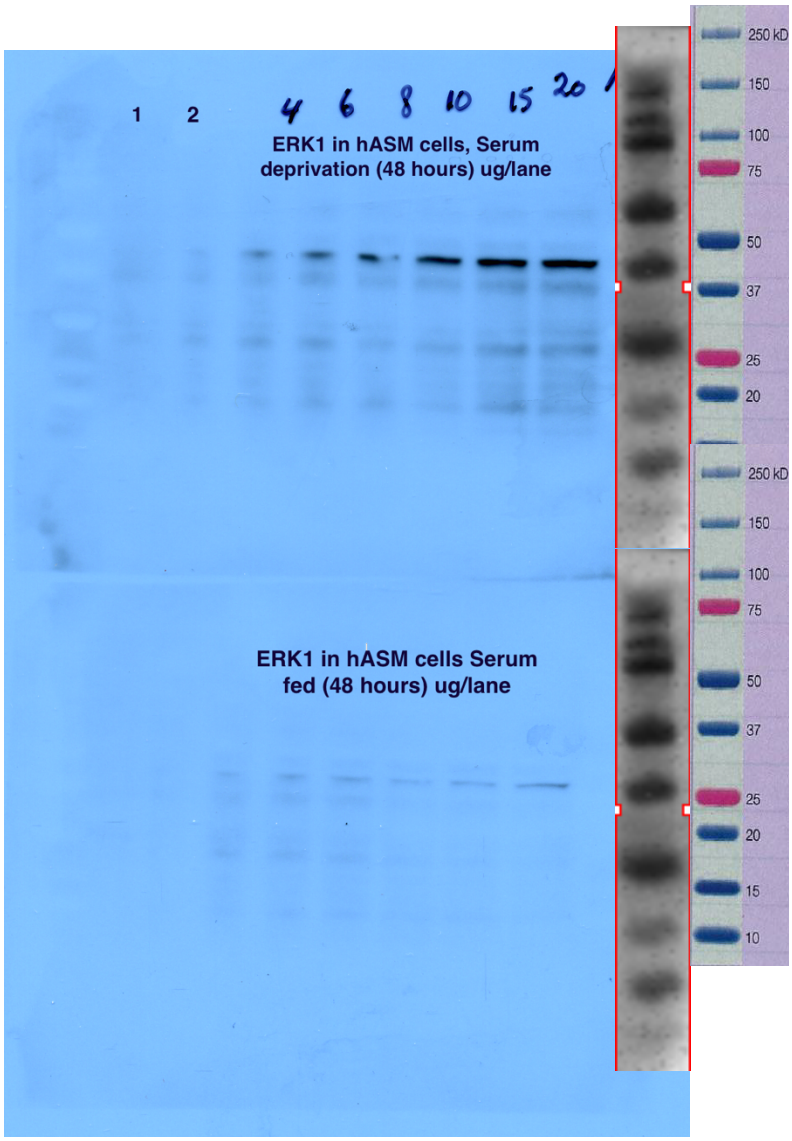

Figure A.1 Characterization of SM markers in hypertensive hASM cells. Concentration gradient shows the basal levels of ERK1 as it is expressed in serum fed and serum deprived hASM. Serum deprivation for 48 hours upregulated the basal expression ERK1. Full-length gel. Exposure: 2 mins. ERK 1=44 kDa.

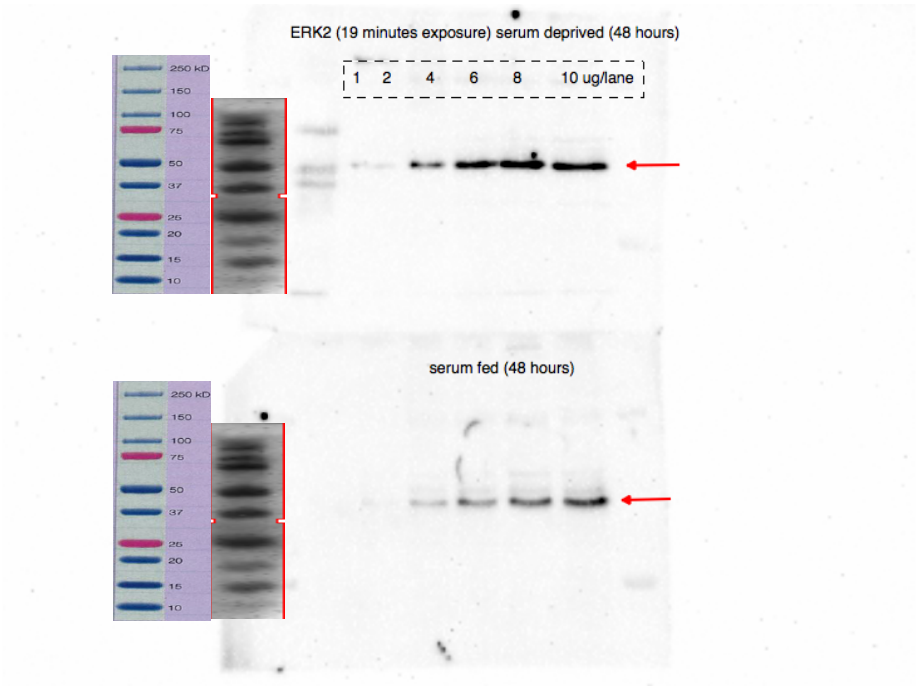

Figure A.2 Characterization of SM markers in hypertensive hASM cells. The concentration gradient shows the basal levels of ERK2 as it is expressed in serum fed and serum deprived hASM. Serum deprivation for 48 hours upregulated the basal expression of ERK2. Full-length gel. Exposure: 2 mins. ERK2= 42 kDa.

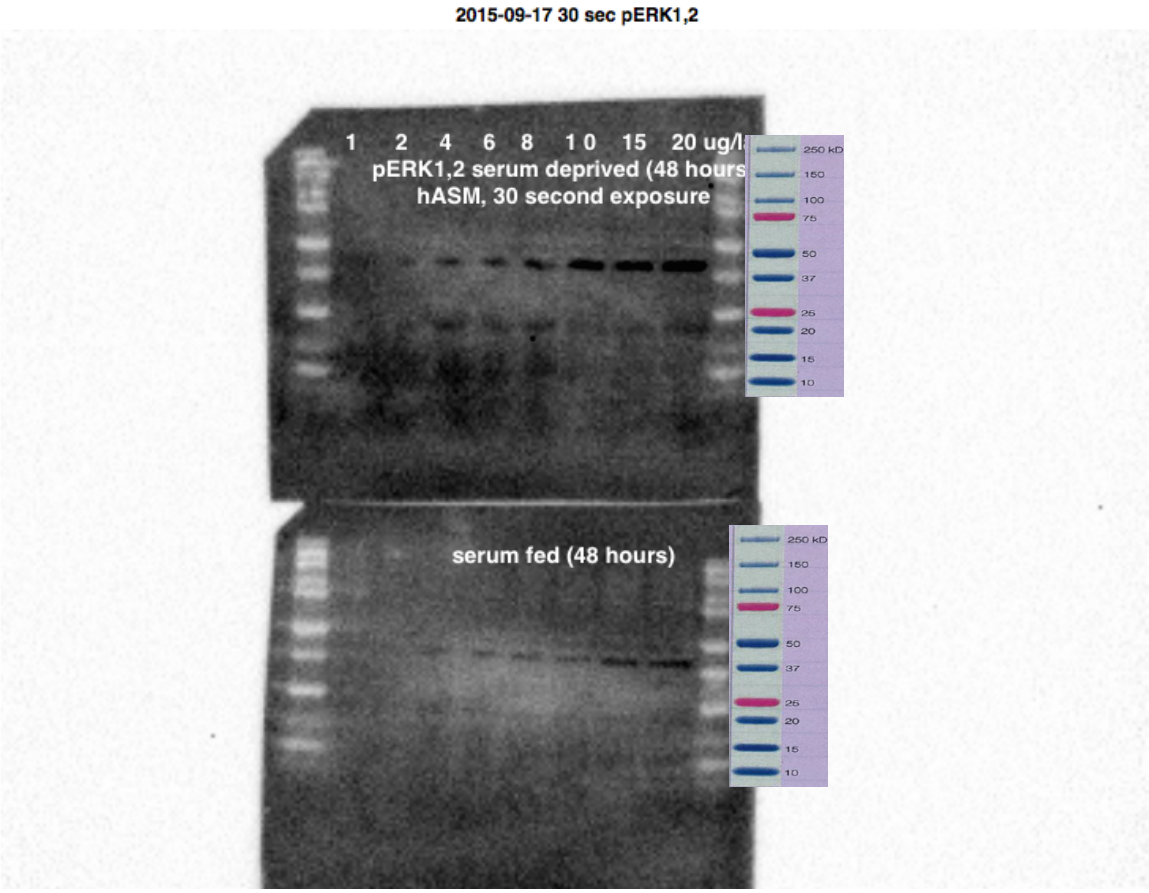

Figure A.3 Characterization of SM markers in hypertensive hASM cells. The concentration gradient shows the basal levels of pERK1/2 as they are expressed in serum fed and serum deprived hASM. Serum deprivation for 48 hours upregulated the basal expression of pERK1/2. Full-length gel. Exposure: 30 sec. pERK1/2 appear on PAGE as two close bands of 44-42 kDa.

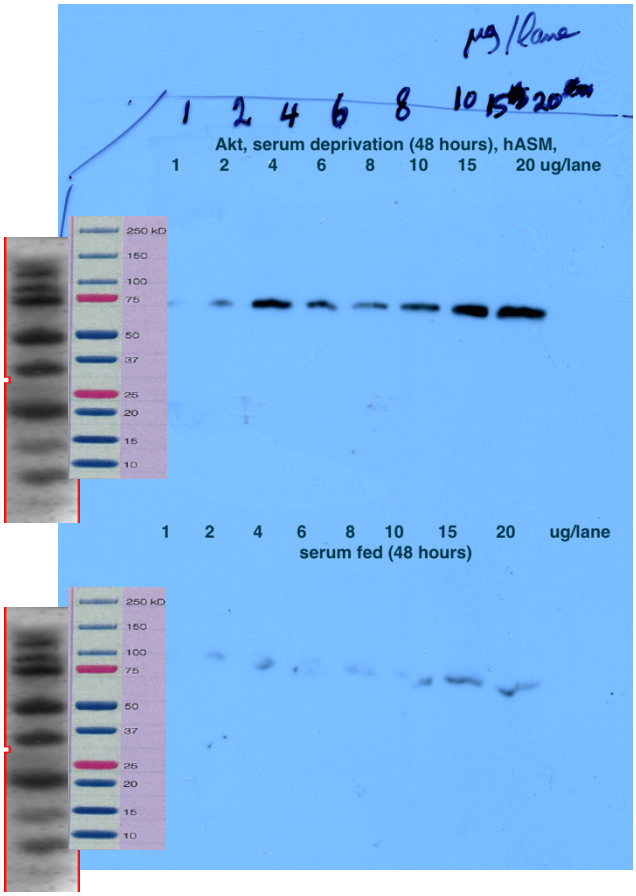

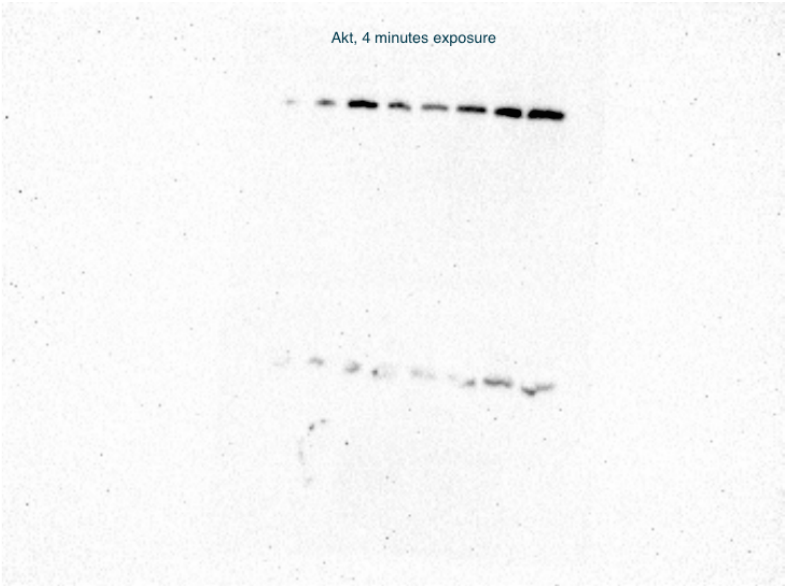

Figure A.4 Characterization of SM markers in hypertensive hASM cells. The concentration gradient shows the basal levels of AKT as it is expressed in serum fed and serum deprived hASM. Serum deprivation for 48 hours upregulated the basal expression of AKT. Full-length gel. Exposure: 4 mins. AKT=65 kDa.

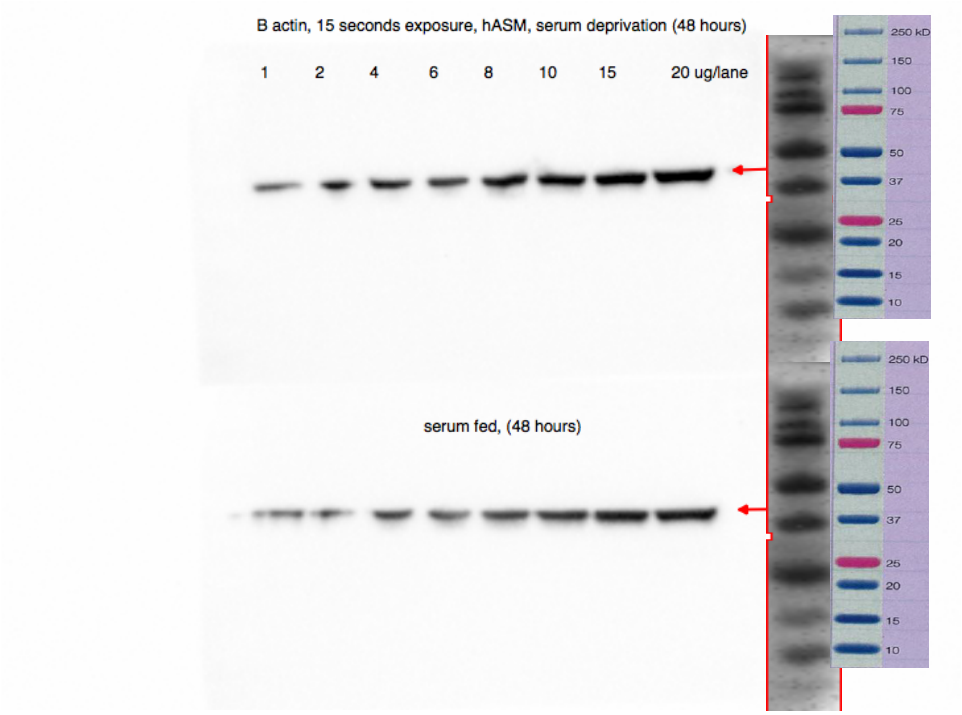

Figure A.5 Characterization of SM markers in hypertensive hASM cells. The concentration gradient shows the basal levels of β-actin as it is expressed in serum fed and serum deprived hASM. Serum deprivation for 48 hours upregulated the basal expression of β-actin. Full-length gel. Exposure: 15 sec. β-actin= 42 kDa.

Desmin in PASM lysates (20 µg/lane)

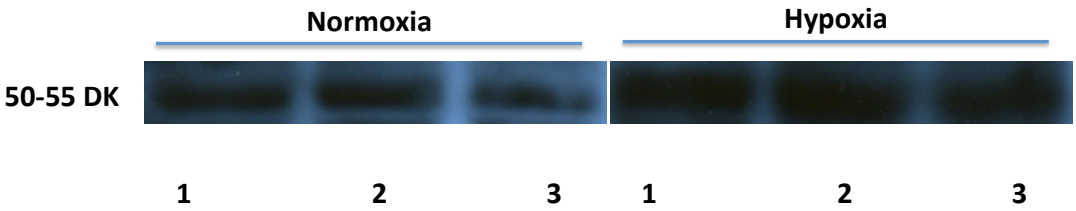

Band IDV	N	H
1	62018.00	110079.00
2	106109.00	124745.00
3	101268.00	178582.00
AVERAGE	89798.33	137802.00

Corrected IDV	N	H
1	0.69	0.80
2	1.18	0.91
3	1.13	1.30
AVERAGE	1.00	1.00

Figure A.6 Characterization of SM markers in hypertensive hASM cells. The data shows the basal levels of desmin as it is expressed in serum fed and serum deprived hASM. Serum deprivation for 48 hours upregulated the basal expression of desmin. Full-length gel. Exposure: 15 sec.

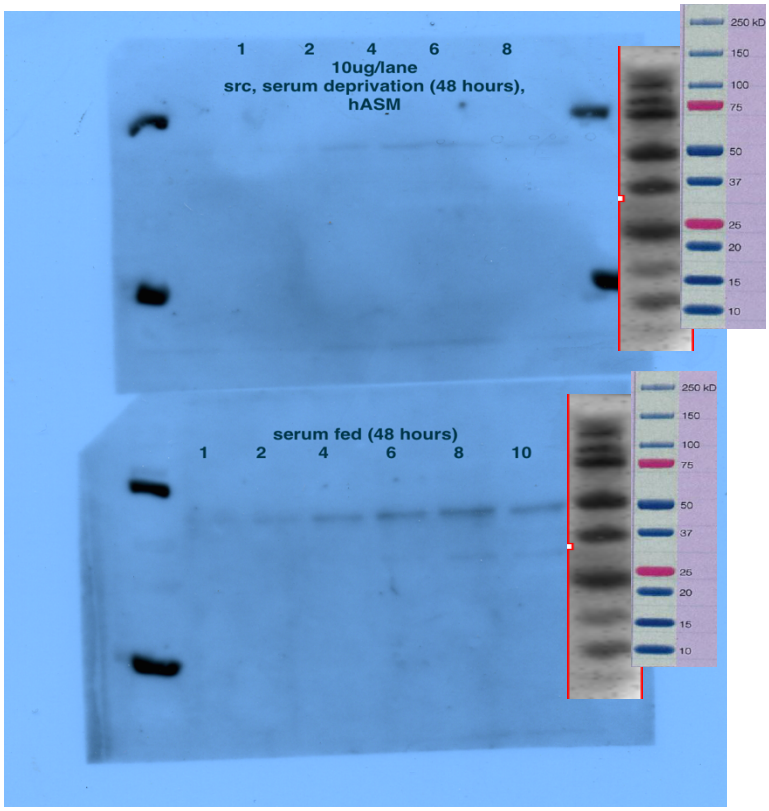

Figure A.7 Characterization of SM markers in hypertensive hASM cells. The data shows the basal levels of Src as it is expressed in serum fed and serum deprived hASM. Serum deprivation for 48 hours downregulated the basal expression of Src. Full-length gel. Exposure: 15 sec. Src=55 kDa.

8. Appendix B: Operating the LSC

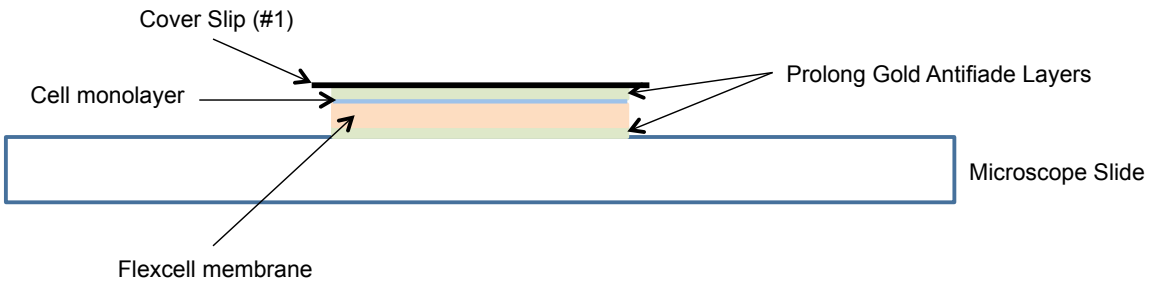

Figure B.1. Slide preparation. The membrane is affixed by mounting medium where cells side up.

8.1. The basic set up of LSC

8.1.1. The filed image

Under the protocol, four windows come up as the basic set up. One window is called “Carrier window”, the 2nd is the “Protocol window”, the 3rd is the “Field image window”. A fourth one is the “Well image”, (Figure B2). The Well image gives an image of the entire scan area (Figure B2 A). The field image shows an image of any scan field that I have selected, it can be a circle, rectangle, etc. Once the scan area is set and scanning starts, the laser will move and scan a section of this total area. Scan area is broken up into a series of scan fields. A well image of blue channels: Hoechst 33342 nuclear fluorescence from porcine PASM cells grown on Flexer-cell plates is presented in (Figure B2).

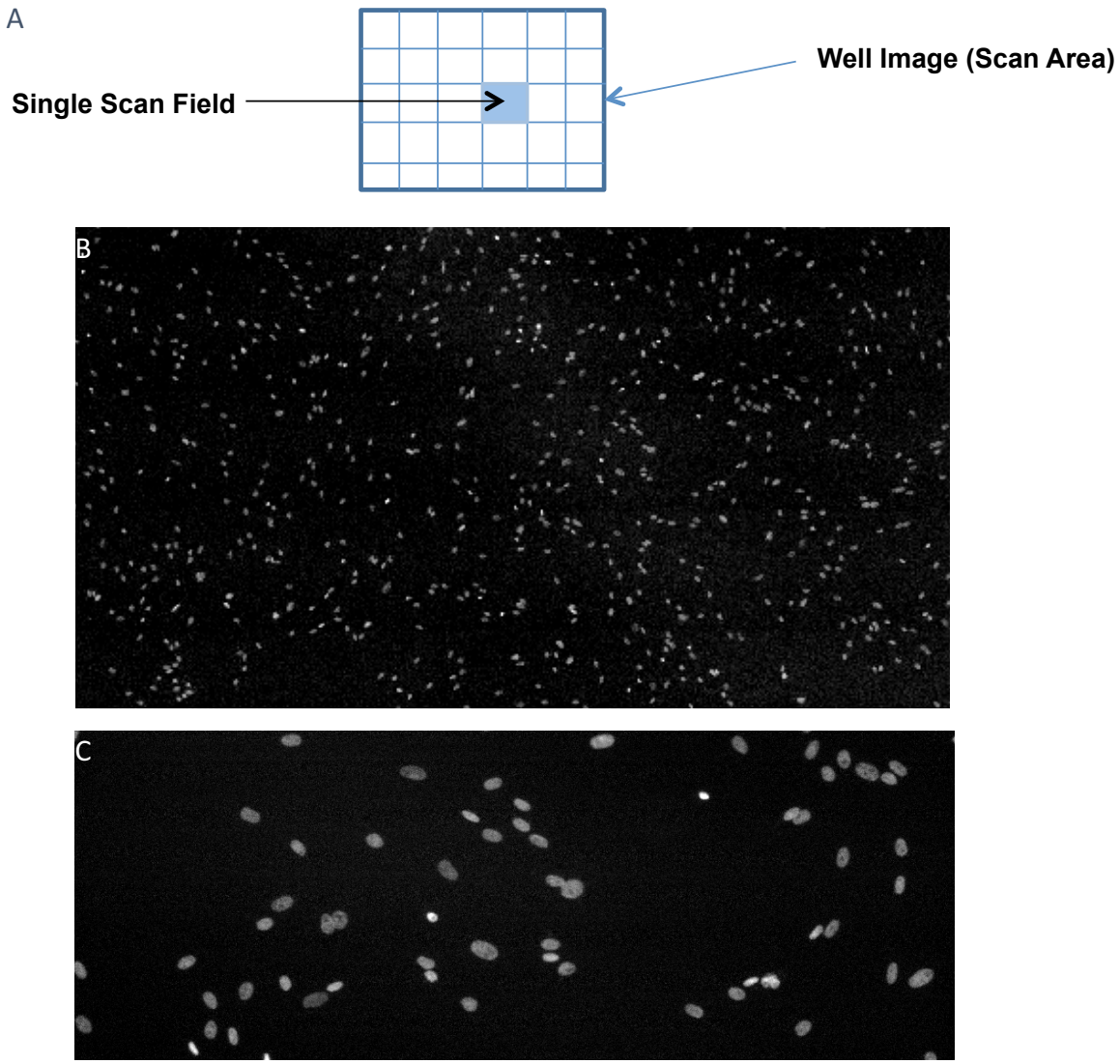

Figure B.2. Well image. A) Well image representative of the total area scanned with laser cytometer is a composite of single scan field images. B) a well image of blue channels: Hoechst 33342 nuclear fluorescence from porcine PASM cells grown on flexer-cell plates. C) A larger view of a single scan field showing Hoechst nuclear fluorescence.

8.1.2. Contouring fluorescence

Contouring represents software generated "regions of interest" that surround areas of sample fluorescence for the purpose of quantification. Total fluorescence from any colour channel will be integrated within the boundary of a contour. Once contoured, the contoured fluorescence is known as an event and is registered for quantification, (Figure B3). There are two contours around the nucleolus. The Threshold: a counter module that looks at fluorescence and attempts to draw a circle around a region of interest. The contour module is associated with the threshold contour. There is also the integration contour, a background and a peripheral contour. Within that area of interest the fluorescence is integrated. The contour module is colour-coded (e.g. red), referenced and the event module is colour coded (e.g. green). Each contour type has a hierarchy associated with it. It means that there is an object (e.g. nucleus), and I draw a point of interest around in such way as to integrate the fluorescence within the point of interest.

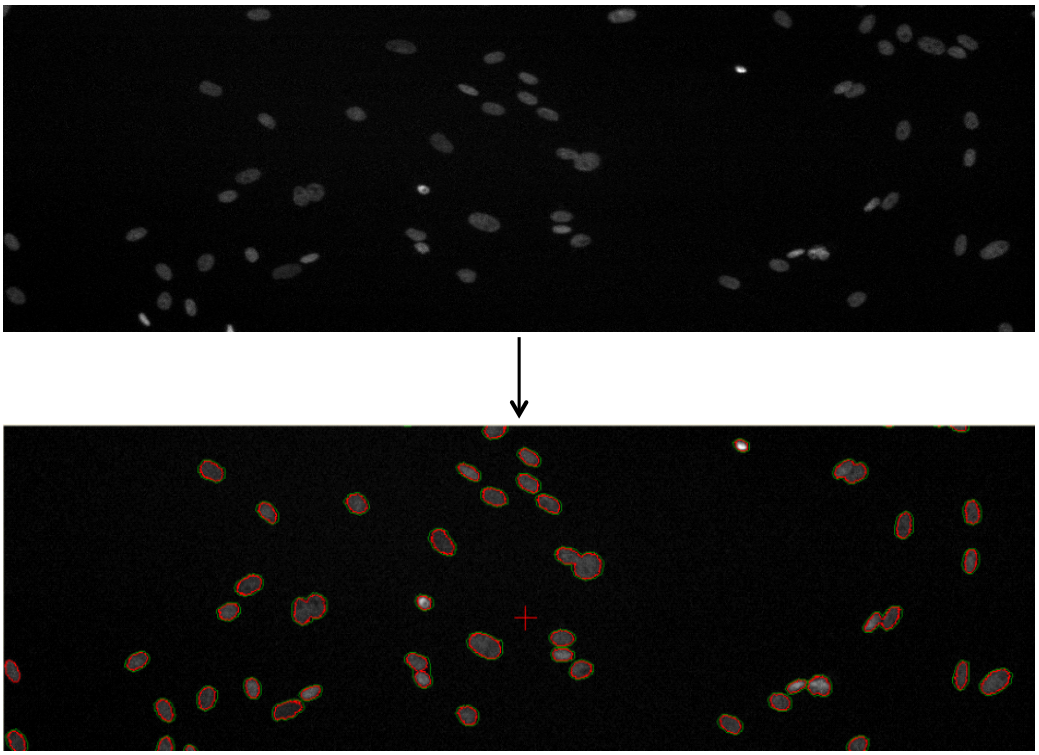

Figure B.3. Events before and after contouring. Blue channels: Hoechst 33342 nuclear fluorescence from porcine PASM cells grown on flexer-cell plates. How effectively I contour the threshold is controlled by the threshold module. Each one of the events is a separate quantitative measurement. The threshold contour (red) does not represent a boundary in which fluorescence is quantified. The true boundary for which fluorescence is quantified is defined by the integration contours (green). The reason is that sometimes the threshold contour does not outline the object all that effectively. The threshold is all or none. I cannot set contours for individual nuclei; I use a setting that is an average for all the events. The nucleolus has a brightness of three X. The other nucleolus is 0.5X in terms of brightness. The contour for the second nucleolus is not as precise, and lies inside the nucleus. Thus, some of the fluorescence is not included in the measurement. This can be corrected through the integration contour. The integration is drawn X pixels away from the threshold contour. To get the instrument to effectively contour the fluorescence and avoid getting noise, the threshold is set to a level at which the computer represents the fluorescent signal. The module image is a half-tone image of the filed where the pixels are either black or white. By changing the scale, either white, black or in between, allows the software to judge which signals are noise and which are not. Setting the slider as a rough starting point is trying to reduce the noise to a minimum value without starting to lose the image of the nuclei. To judge what noise value is appropriate, right clicking on the image brings up the profile of the grey level value of the pixels. Placing the cursor on the threshold contour provides the value which can be used to distinguish between signal and noise. With this information, the integration contour can be set to a value sufficiently different from the threshold contour such that all the fluorescence will be collected. The integration contour represents the boundary in which the fluorescence is quantitated.

8.2. Field scans

8.2.1. Selecting an objective and X step

These two parameters determine the overall dimension of the scan field, which determines the overall number of field images contained in our well image. The laser beam moves in X steps. An X step is an X axis stage stepping, down to 0.05 microns for improved sample resolution. A higher magnification couples with a smaller X step (affixed microns) gives a higher-resolution image. However, higher resolution is not required for better quantification. The resolution will be dictated by what I try to contour. For example, high resolution is not need for nuclei, but is for quantification of a smaller structure in the nucleus. Performing a contour at 40 X would be required in this case, at 0.25X step. Multiple channels identify which data set is going to be associated with which color.

8.2.2. Focus parameters

Focus offset looks for differences in refractive indices between one image and another to find where the focus point should be. Focus offset thus enables correction of blurry images. In this way, fluorescence images with a wide range of focus can be collected, and their quantification will be accurate even if the image is not (Figure B4).

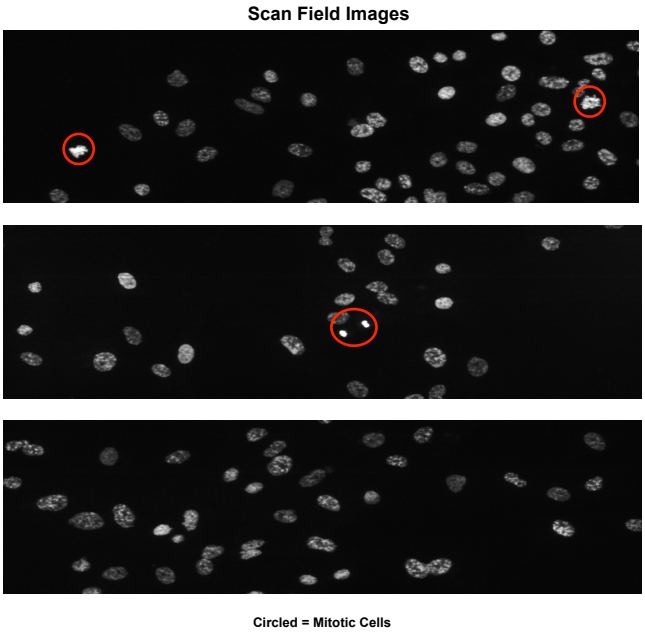

Figure B.4. Scan field images: mitotic events. Laser control voltage gain and offset will correspond to the image brightness. Mitotic nuclei are circled red. Nuclear fluorescence from porcine PASM cells grown on flexer-cell plates is obtained using Hoechst 33342 stain excited by the blue laser. Fluorescence is collected using PMT1. To get brighter fluorescence, the sensitivity of the detector is manipulated. The gain is always left in a 100. Additionally, I have to determine i) the field scan parameters, ii) the objective (25X for myocyte nuclei, 40X for cytosolic actin) and iii) the step size. It may also be necessary to modulate the offset, which is for the background fluorescence (how bright the background to the signal). Offset may be either a negative or a positive value. The PMT detector is a monochrome system that senses the grey level. Therefore, the computer is used to colour the image. This is just for visualization since it does not affect quantification; up to 5 colours can be selected.

8.3. The protocol window

This unit consists of a series of modules that, when connected together, control various aspects of the hardware that are required to perform the experiment. The protocol tap contains all of the parameters of the experiment, including how the analysis is going to be detected. An example of the red and green signals in the form of contour analysis of cytoplasmic F:G-actin ratios in cultured hASM cells is presented in Figure B5. The F-actin contour is the red signal and the G-actin contour is the green.

8.3.1. Modules

Each module of the protocol contains parameters that have some control over how the analysis is carried out. The detector module contains all the parameters affecting the detector. The field scan contains parameters describing the field image (e.g. focus parameters, the data parameters, the bit data, the actual image creation, what objectives, and the actual size of our scan field). If there are multiple channels, a colour has to be defined for each fluorescent colour. There is a single detector module, and a single field module. If three fluorescent colours are to be detected, the channel detects each colour that has to be identified. Then the threshold module, the contour module, the event module, the association module must be optimized (Figure B5).

8.3.2. Detector dynamics

A number of detector parameters must be set, including: i) which laser to use, ii) the colours to assigned to the photomultiplier (PMT) tubes (i.e. 488 nm - green, 405 nm - blue and 633 nm - long red), iii) the step size, which determines resolution, iv) the size of the scan field in microns, and v) the field size (Figure B5). At 20x25, the

field size is 1786 pixels. This information also indicates how many pixels are found in the scan field and the dimensions of the scan field (µM). With the 20X objectives and an X step of 0.5, this scan field would be 1000 pixels across and 760 high or 500 µM across and 380 µM high. These values change if an X step of 0.2 is used. In this example, the number of pixels (760) is the same, but image size is larger (Figure B5).

8.3.3. The object

A large area with low resolution gives a big imaging area. The resolution is controlled by X step size. The best resolution is obtained with the 10X objective, which uses the tiniest step size. The larger the step size the lower the resolution. If there is a nuclear structure that requires visualization, the 40X objective should be selected. In contrast, the 20X objective is sufficient with a step size of 1 if quantification of nuclear fluorescence is the aim. The scan field under these conditions will have a decent number of nuclei for accurate quantification.

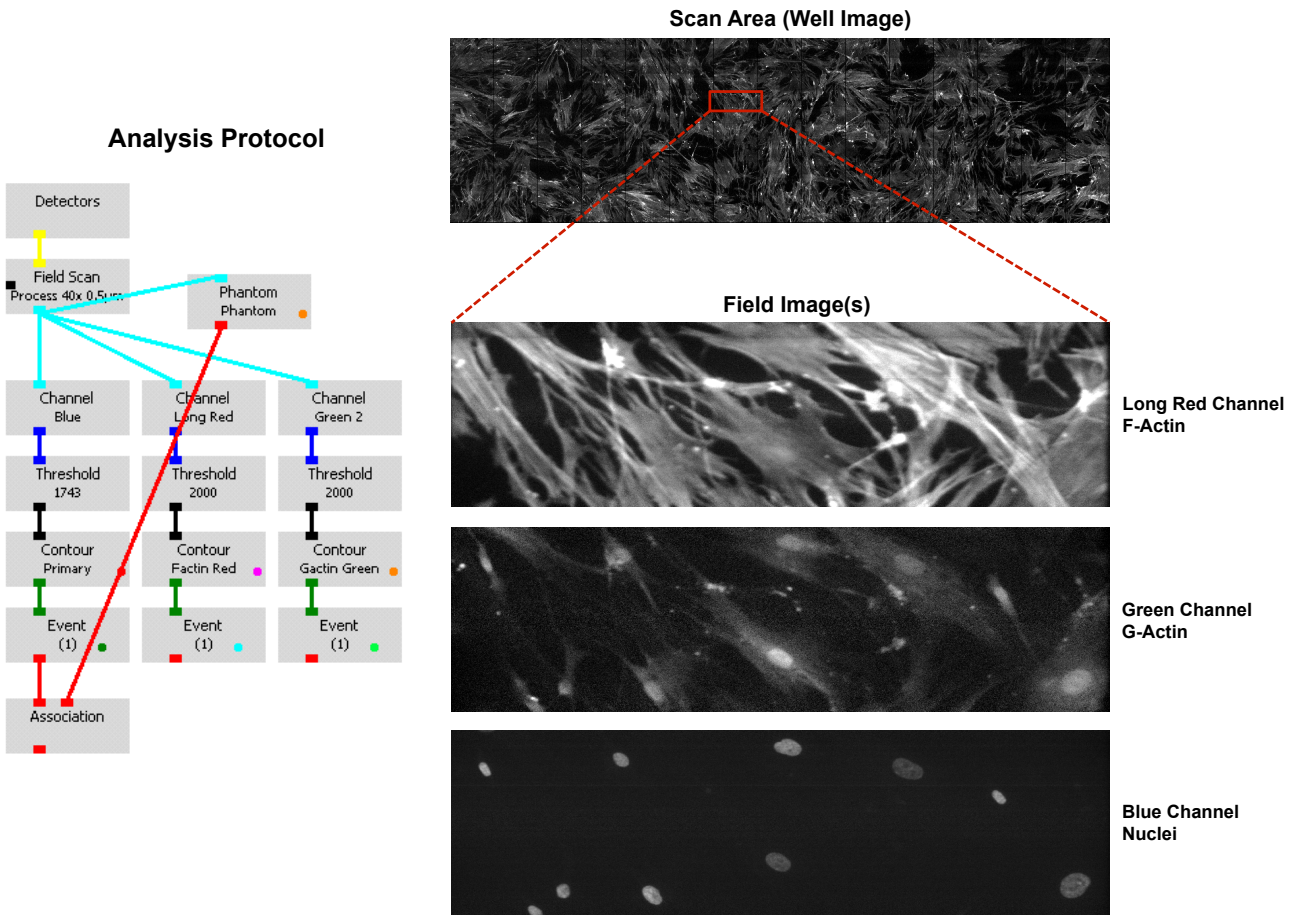

Figure B.5. Phantom contour analysis of cytoplasmic F:G-actin ratios in cultured hASM cells (HC82). Multiple channels are collected, with each assigned a separate colour. The F-actin contour is the red signal and the green is the G-actin. Phantom means a visual illusion that can define regions with distinctive boundaries when no real surrounding edges exist. Phantom contours are events generated by iCys from circular contours applied over the laser-scanned image. An Association module allows you to associate two event components generated with either an event module or a phantom module. There is primary and sub contour protocols. A one primary protocol is designed to analyze data using a single contour, and includes a phantom contour. The one primary, one sub protocol analyzes data using two contours. These are combined in the association module. The one primary, two sub contour protocol analyzes for a primary contour as well as two sub-contours, including an association among the three. It also provides a phantom contour module. I can break the connection with a module, but cannot connect the black module to a green module because they are colour coded, to make sure that they are in the right order, that are logistically related to one another by color code. Channel module cannot be connected to phantom because it is nonmeaningful. I can also disable a module down the chain event. If I want an association module I can click on and bring the association module and connect it with the primary event, which is the contour of the nucleus, and correlate it with phantoms.

8.3.4. The Histogram and the Scattergram

Cytometer “events” can be displayed in either Scattergram or Histogram format and events within either format may be “gated” so as to select specific populations of events within these formats. Gated events may be displayed separately or removed (“gated out”) from the largest event population. The histogram is one-dimensional blot as a function of how many events are recorded at that particular measurement value. The scattergram is a two parameter blot (Figure B6). Coordinate scattergrams display contoured events within scan areas according to their designated X, Y coordinates. The coordinate scattergram is effectively a "dot blot" reproduction of the scan area well image (Figures 4.14 C, D and 4.15 C, D).

8.3.5. Min/Max

Re-scanning is a second measurement where it is possible to change the contour after the initial data grab, but not at the same time when the data are collected. Large debris affect the results because they will be included in the integration. In this case contouring does not work. In the contour module, it is possible to use the minimum and maximum area to contour the nucleus, since most nuclei do not get bigger than a certain area. The max areais set to 200 μm^2, and the image re-updated to remove large debris.

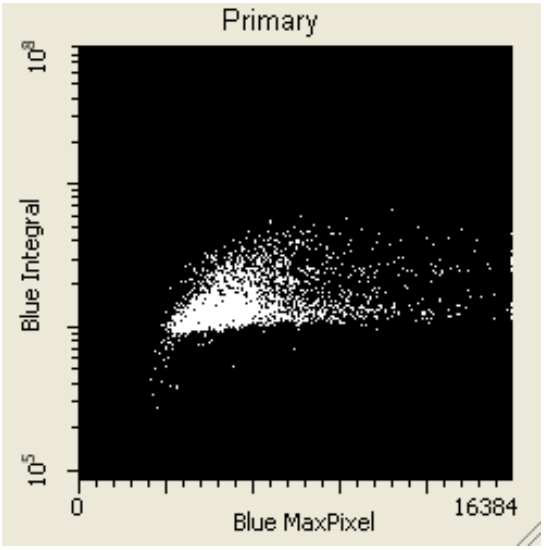

Scattergram Format

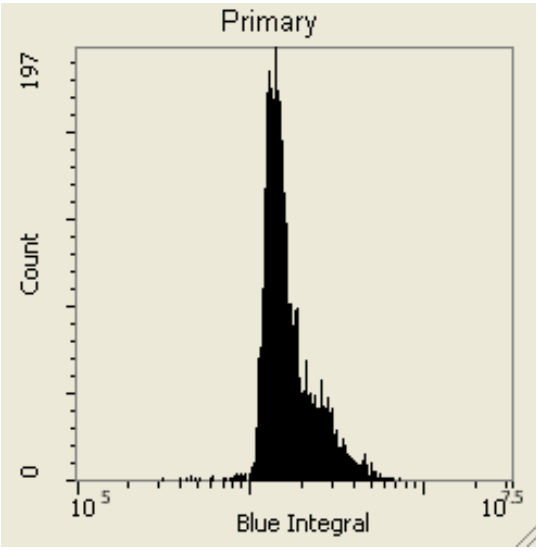

Histogram Format

Figure B.6. Event data from Hoechst stained, non-treated normal nuclei of PASM grown in flex-plates. The event that I attempt to contour is called the primary event. In case of Hoechst, the nucleus is a primary event. The integrated fluorescence (intensity of the blue fluorescence) within each nucleus is placed on the Y axis. The X axis is the max pixel value of the blue fluorescence. The histogram provides the blue integration value (rather than an area, which is the default) on a log scale. Although it is possible to use a linear scale, the logarithmic scale is preferred if most of the data falls within a broad range. The integral blue = the total summed fluorescence (total summed grey level) within the boundary of the integration contour. The scattergram (X, Y position) creates a dot plot image of the scan area, with each dot representing an event (nucleus or actin fibers). Different populations can be colour coded blue, red or yellow to help identify which nuclei are associated with the population I interest in.

8.3.6. Galleries

Images of specific events found within identified (and colour coded) event populations may be displayed as a "gallery" of images (Figure B7).

A

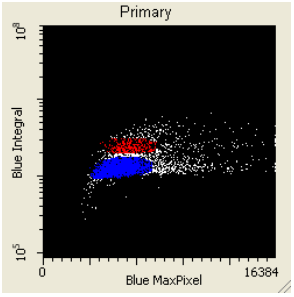

Gallery of Blue Population: G0/G1 Nuclei

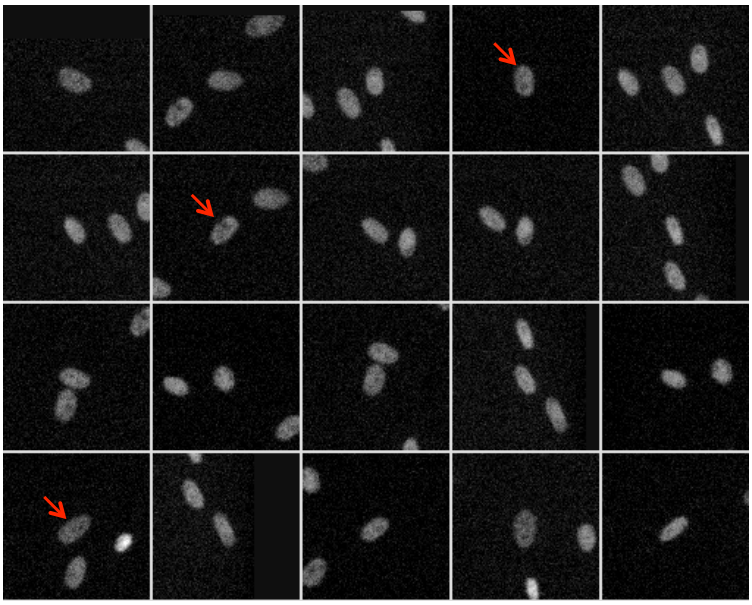

B

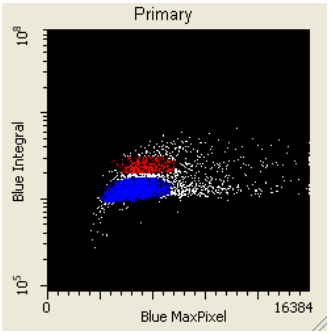

Gallery of Red Population: G2 Nuclei

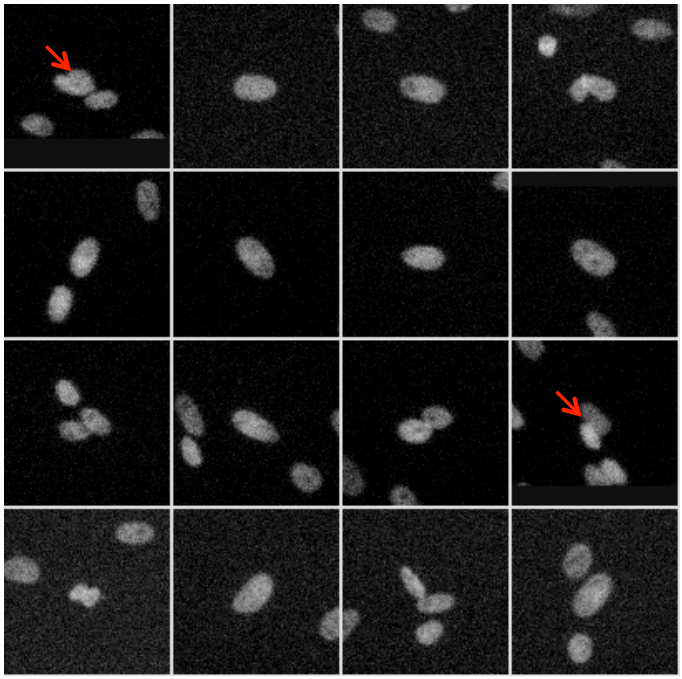

C

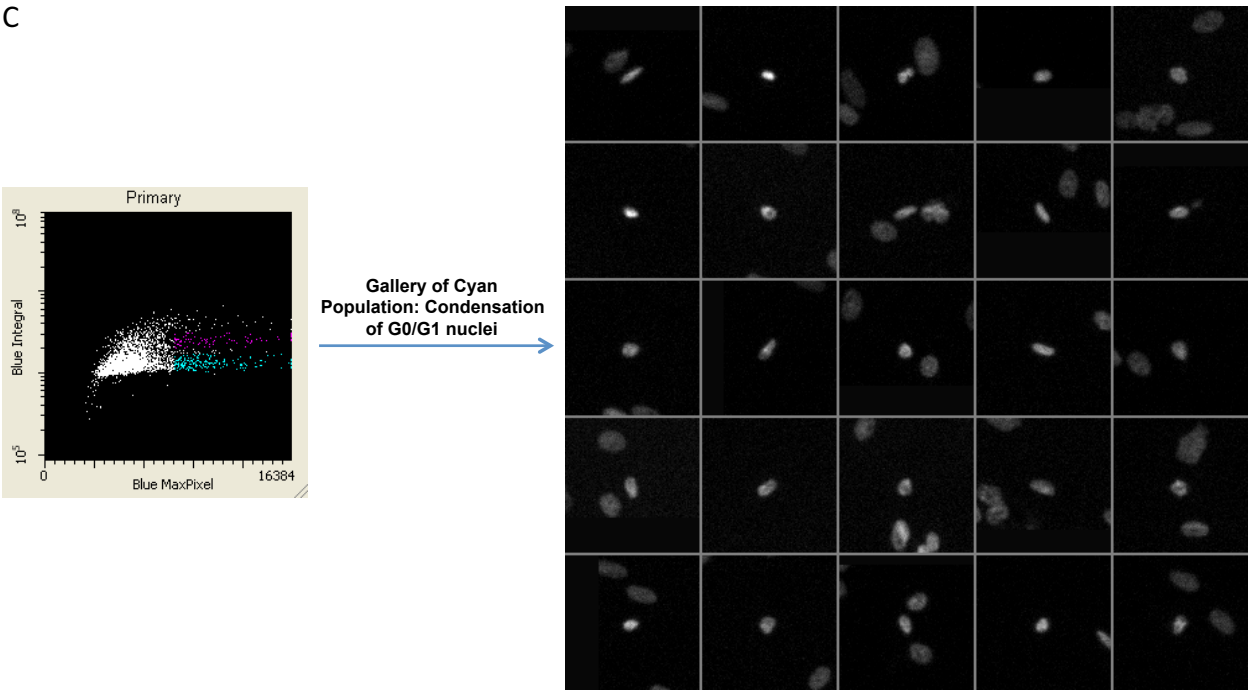

D

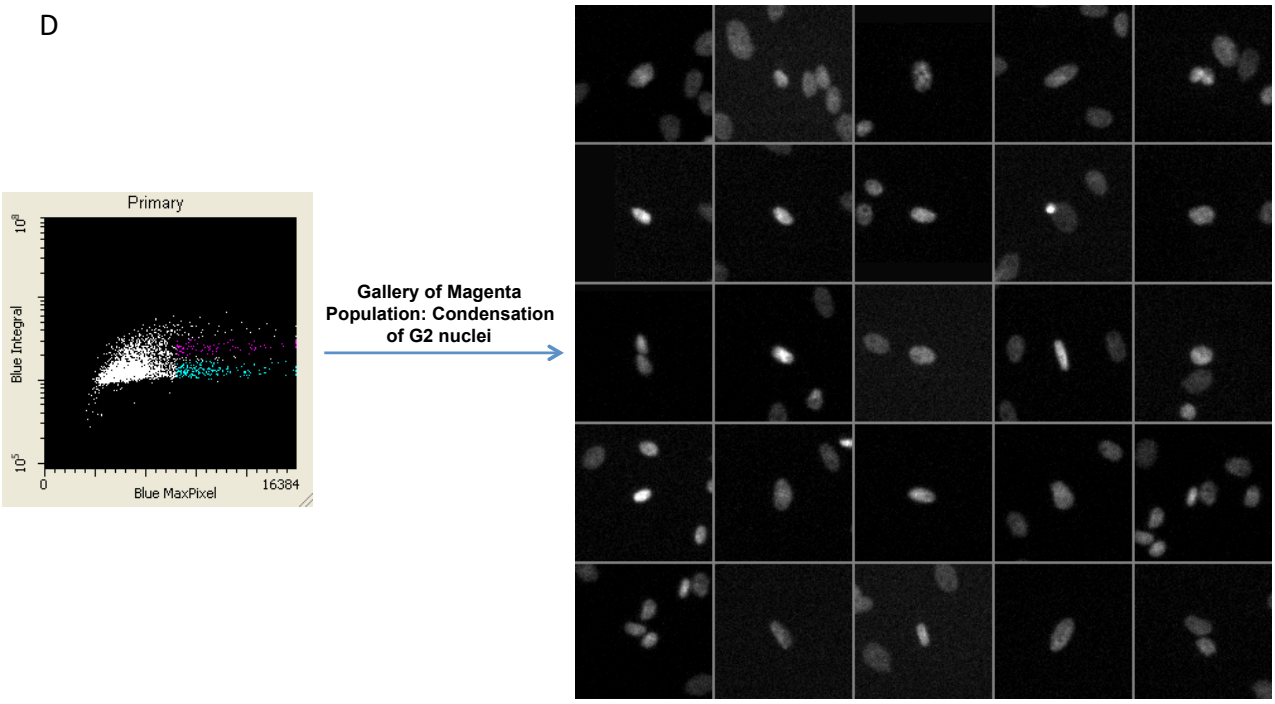

Figure B.7. Galleries. A) Gallery of cell cycle events in non-treated hASM cells (HC82). Multiple events may be found within any single gallery image. However, the event of interest is always that event located at the centre of the gallery image (arrows); B) Event population exhibits some contamination with contours of multiple nuclei. This is known as a problem with "segmentation" and results when fluorescent events are too closely spaced to be contoured effectively as single event arrows. C) hASM cells (HC82), no treatment. Gallery of cyan population: condensation of Go/G1 nuclei; D) gallery of magenta population: condensation of G2 nuclei.

8.4. Quadrants

Histograms identify which nucleus is associated with the population I am interested in. Setting the scattergram mode to "Quadrants" allows for division of the scatter gram plot into discreet sectors. The percentage of the total event population falling within each sector (quadrant) is automatically displayed (Figure 4.14 C, D). The quadrants associated with the negative control are also displayed (Figure 4.15 C, D).

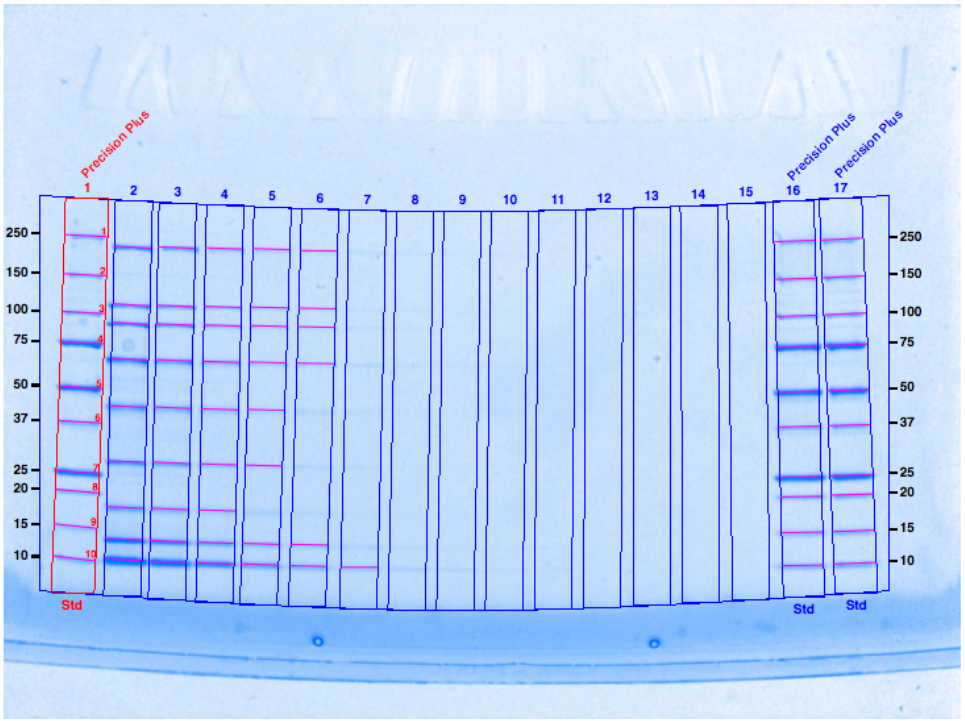

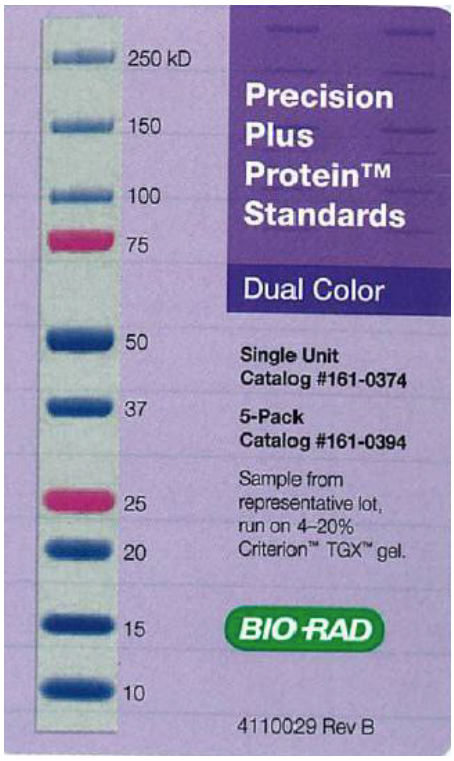

Figure B.8. Coomassie molecular ladder BioRad Precision Plus gel and specification.